Energy Research and Development Division
FINAL PROJECT REPORT

DEVELOPMENT AND EVALUATION OF GAS FUEL INTERCHANGEABILITY CRITERIA AND METHODOLOGIES

Appendices A - H

Prepared for: California Energy Commission
Prepared by: University of California, Irvine

MAY 2014
CEC-500-2015-063-AP

LIST OF APPENDICES

Appendix A: Review of Fuel Composition

Appendix B: Review of Existing Interchange Parameters and Methodologies

Appendix C: Alkane Ignition Delay Correlations

Appendix D: Details and Heat Transfer Analysis of JSR

Appendix E: Topical Report – Flame Speed Test Results and Analysis

Appendix F: Topical Report – Diffusion Transport Porperty Calculator

Appendix G: Topical Report – Flame Structure Tests and Interpretation

Appendix H: Topical Report – Reduced Order Kinetic Mechanisms for Alternative Fuels

APPENDIX A:
Review of Fuel Composition

Smaller appendices are attached to the main report. Longer appendices may be published separately under different publication numbers.

A.1 Gaseous Fuel Classes

A.1.1 Fossil-Fuel-Derived Natural Gas

A.1.1.1 Pipeline Natural Gas

"Standard" pipeline natural gas will have inherent variation, depending on from where it is extracted and its history in the natural gas pipeline infrastructure. Extensive work by the Gas Research Institute (GRI) to define the variability in the standard pipeline gas found throughout the United States has been relied upon as an indicator of the typical variability (Liss et al. 1992). This variation is summarized in Table A-1. Because higher molecular weight hydrocarbons have a substantially lower auto ignition temperature, they can lead to autoignition in the fuel-mixing region of the lean premixed combustion systems or catalytic combustion systems. In addition, the liquid droplets can create locally high concentrations of higher hydrocarbons.

A second implication of varying concentrations of higher hydrocarbons is the effect of the components on the flame position and stability. In this case, the kinetic reaction rate of the higher hydrocarbons is substantially higher than that of methane, resulting in changes of the flame speeds and therefore flame location.

In the case of any lean premixed combustion systems, the role of higher hydrocarbons in affecting system performance is potentially disastrous, due to the possibility of reaction within the premixer (Lieuwen et al. 2008).

Table A-1: Concentration of Fuel Constituents for Natural Gas in the United States

		Mean	Minimum *	Maximum *	10th Percentile	90th Percentile
Methane	Mole %	93.9	74.5	98.1	89.6	96.5
Ethane	Mole %	3.2	0.5	13.3	1.5	4.8
Propane	Mole %	0.7	0	2.6	0.2	1.2
C 4 +	Mole %	0.4	0	2.1	0.1	0.6
$CO_2 + N_2$	Mole %	2.6	0	10	1	4.3
Heating Value	MJ/m^3	38.46	36.14	41.97	37.48	39.03
Heating Value	BTU/scf	1033	970	1127	1006	1048
Specific Gravity		0.598	0.562	0.698	0.576	0.623
Wobbe Number	MJ/m^3	49.79	44.76	52.85	49.59	50.55
Wobbe Number	BTU/scf	1336	1201	1418	1331	1357
Air/Fuel Ratio	Mass	16.4	13.7	17.1	15.9	16.8
Air/Fuel Ratio	Volume	9.7	9.1	10.6	9.4	9.9
Molecular Weight	g/mol	17.3	16.4	20.2	16.7	18
Critical Compression Ratio		13.8	12.5	14.2	13.4	14
Methane Number		90	73.1	96.2	84.9	93.5
Lower Flammability Limit	Volume %	5	4.56	5.25	4.84	5.07
Hydrogen:Carbon Ratio		3.92	3.68	3.97	3.82	3.95
* without peakshaving						

Note: C 4 + = alkanes including butane and higher hydrocarbons; CO_2 = carbon dioxide; N_2 = nitrogen.

Source: Singer 2006; Liss et al. 1992.

It is noteworthy that the data shown are more than 25 years old. It is not clear to what extent the composition of natural gas throughout the United States might be different today as a result of gas production and/or other changes in the infrastructure; however, the results are still likely very relevant in describing the fuel variation. Table A-2 shows the variation in natural gas composition within California. Not surprisingly, the composition within the state varies less than it does throughout the entire United States.

Table A-2: Variation in California Natural Gas

Species	Mean	Minimum	Maximum
Methane	93.5	91.3	96.9
Ethane	3.1	0.5	5.2
Propane	0.6	0.1	1.1
C_4+	0.3	0	0.7
Inerts (CO_2 + N_2)	2.6	1.4	4.2

Source: Liss et al. 1992

One extreme scenario not included in Table A-2 is the case of "peak shaving," which involves the injection of propane/air mixtures into the pipeline to maintain the energy throughput of pipeline gas in times of peak demand. This practice, illustrated in Figure A-1, is analogous to peak shaving for electricity where, for economics and reliability, local generation is brought on line to offset high rates or limited supplies. In the case of peak shaving with gaseous fuels, the propane content of the pipeline natural gas can exceed 20 percent (Liss et al. 1992). This practice is most common in regions where natural gas flow may be limited during high use, such as in cold winter periods in the Northeast. With the advent of distributed generation systems and the increased need for energy reliability, the notion of incorporating backup fuels is becoming more important, and may well contribute to the specification of fuels used in the future.

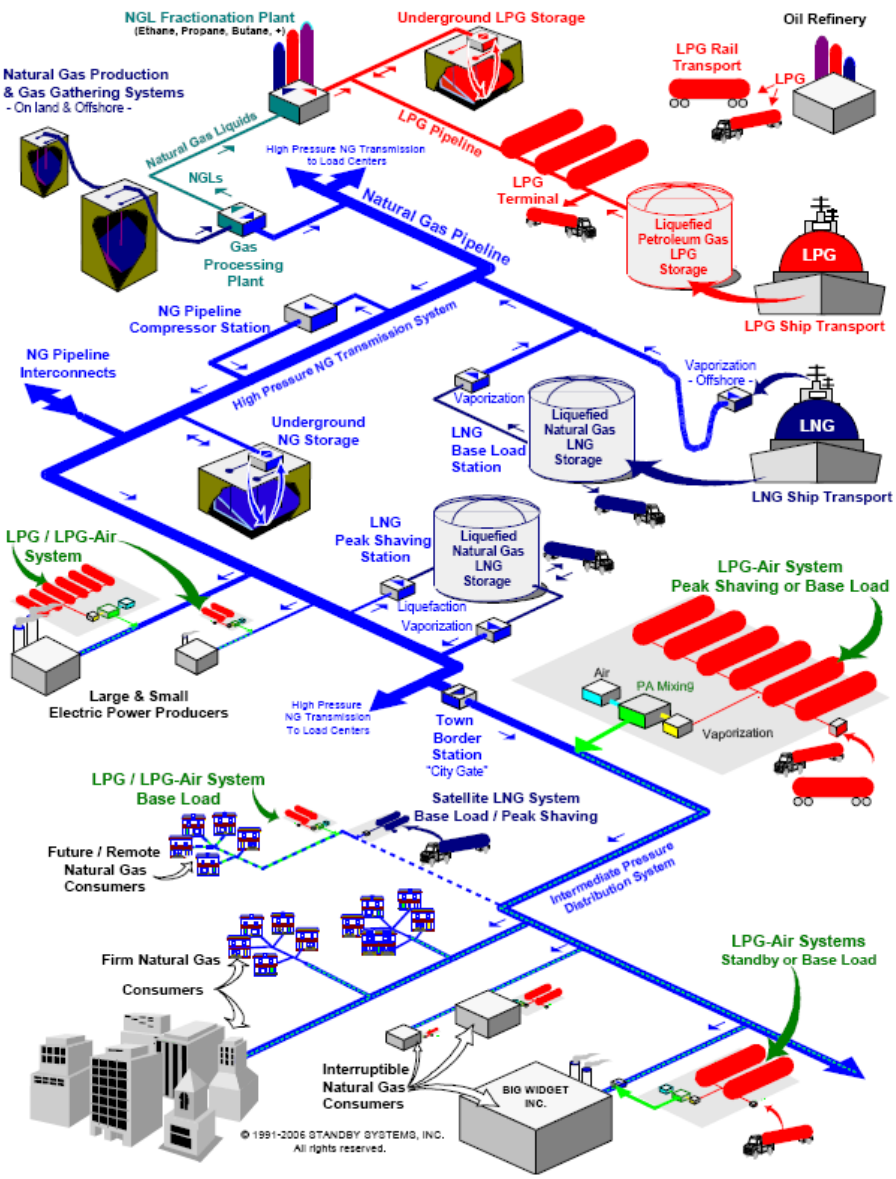

Source: Standby Systems, Inc., http://standby.com/propane/pdf/pps_ovw_e4.pdf; accessed March 2013.

Figure A-1: North American Gas Energy Grid: Natural Gas and LPG

In California, the typical backup fuel is diesel fuel or synthetic diesel. However, many power generation devices (especially smaller output devices) do not have "dual fuel capability"; that is, the capability to run "seamlessly" on the normal fuel (e.g., natural gas) and the backup. Of course, in California, the use of diesel fuel even for backup generation has been identified as a potentially significant air quality impact (Ryan et al. 2002), though some studies suggest the general impact is perhaps 50 percent less than originally projected by the U.S. Environmental Protection Agency (U.S. EPA) (Shah et al. 2006). Regardless, alternative backup fuels such as propane would be a good strategy to consider in terms of (1) ease of dual-fuel operability, since both fuels would be gaseous, and (2) reduced pollutant emissions.

Finally, it is worth noting that pipeline natural gas can also contain carbon dioxide and nitrogen, which can affect the position of the flame in a lean premixed combustion system (CO_2 can also affect the behavior of a catalyst in a catalytic combustion system). If CO_2 is present, it can affect the combustion processes through its high heat capacity and by its ability to suppress the oxidation of carbon monoxide.

Natural gas will also contain some moisture, although usually by the time it is delivered it is almost completely dry. At the levels likely to be present, water probably will have little effect; however, it can be explored if a satisfactory means of introducing moisture can be established.

Another factor associated with natural gas is the sulfur content. There are very large reserves of natural gas in the United States; however, the "sweet" gases are preferentially depleted, leaving increasingly "sour" gases for future use. Today the sour natural gases, those containing hydrogen sulfide or other organosulfur compounds, are being extracted and diluted with sweet or sulfur-free gases to maintain the desired low levels of sulfur in the gas. In the near future, sulfur removal will become necessary, and this will mean that all natural gases will tend toward having the maximum allowable sulfur levels. It is not clear what these maximum levels may be in the future, but today, based on gas transfer contracts, levels are between 10 to 20 grains per 100 cubic feet (ft^3) (0.22–0.45 grams per cubic meter [m^3]). Of course, sulfurous compounds are added to natural gas as an odorant for safety purposes.

A.1.1.2 Unconventional Natural Gas

In addition to the changing composition of natural gases from conventional sources, an increase in use of natural gas obtained from what can be termed "non-conventional sources" is occurring. One example is gas obtained from coal seams. This "coalbed methane" can be obtained as virtually pure methane by pre-draining coal seams before mining occurs. This removal of methane before mining starts is considered to be an essential part of mine safety because it reduces the amount of methane released during the mining operations.

Methane can also be extracted (often diluted with air) from "gobs" or collections of collapsed roof rubble found in mined-out areas. Similar methane-and-air mixtures can be extracted from coal seams during mining operations. In this type of extraction the gas is removed via bore-holes drilled horizontally into the coal seam, just ahead of the active working face. These latter two gas types usually consist of methane and air mixed. The concentration of methane in these gas streams can be controlled, if desired, to levels close to 90 percent. Such gases often meet the minimum heating values for pipeline-quality natural gas and are usually well within all contaminant-level requirements. These gases, however, add air to the natural mixtures in the pipelines, and this can result in the formation of sulfur-based acid gases or condensed-phase (liquid) acids if mixed with other natural gases containing sulfur compounds.

In recent years, "shale gas" has gained attention as a potential sustaining source of natural gas. The shale gas reserves in the Northeast and in Texas have been opened by new drilling techniques developed and mastered over the last 10 years. The viability of these extraction methods has resulted in a more than 70 percent increase in the natural gas reserves from 2000 to 2010 (U.S. Energy Information Administration 2013). Shale gas is mainly methane; however, it is

evident that appreciable quantities of ethane can be present. Reports of ethane levels to 16 percent have appeared with associated Wobbe Indices well above 1,400 (George and Bowles 2011). Also, some of the fields have appreciable quantities of propane and C4+ (e.g., Eagle Ford reserve gas, as measured by El Paso Energy) (George and Bowles 2011). This gas would generally be treated to bring the Wobbe Index into compliance with the pipeline specification; but if it were used locally, the higher hydrocarbons could pose operability issues. Generally, it seems that the compositions observed do not vary substantially beyond that reflected in Table A-1.

Beyond compositional variation introduced with shale gas is consideration for the environmental impact of the extraction methods (hydraulic fracturing) which require considerable water use and involves injection of several chemicals, including benzene, to help fracture the shale to release the gas. The environmental impact of this water/chemical use may well affect the overall feasibility of shale gas. Some state regions have already indicated they will not allow drilling in fear of affecting their own water supplies. Some energy companies have also responded to this concern (e.g., Chesapeake Energy Corporation in New York has bowed to environmentalist pressure regarding drilling for gas in the Marcellus Shale formation located in the New York/Pennsylvania region). Further, since the energy market is global, the increased U.S. reserves do not necessarily mean supplies are "endless," as the producers of shale gas will consider exporting this gas as worldwide pricing dictates.

While beyond the scope of the current effort, it may be desired to include an investigation of contaminants likely to be found in "non-conventional" natural gas and natural gas mixtures.

A.1.1.3 High Liquefied Natural Gas (LNG) Import Scenarios

Scenarios for supplementing the natural gas supply with imported liquefied natural gas, while no longer as likely with the discovery of shale gas, received attention as a means to overcome what were then depleting reserves of natural gas. This led to significant effort to assess the impact of such scenarios on a wide range of combustion devices (NGC + Interchangeability Work Group 2005). The variation in composition expected with high LNG import scenarios would feature more C_4+ (i.e., propane and other higher hydrocarbons) content than that expected for any natural gas, as summarized by the GRI report (Liss et al. 1992). The exact range of values is dependent on the origin of the LNG. As shown in Table A-3, the amount of the C_4+ values anticipated could exceed the maximum levels in the legacy U.S. pipeline gas (Table A-1) by more than 50 percent.

Table A-3: Fuel Composition from Various Sources around the World

		Methane	Ethane	Propane	C4+	LHV	HHV	Wobbe
		mol %	mol %	mol %	mol %	BTU/scf	BTU/scf	Index
Typical US		95.7	3.2	0.7	0.4	949	1052	1379
Known GT Experience		89.6	8	1.5	0.9	1006	1112	1412
	Brunei	89.76	4.75	3.2	2.29	1036	1144	1429
	Trinidad	96.14	3.4	0.39	0.07	940	1041	1374
	Algeria	87.83	8.61	1.18	0.32	991	1099	1405
	Indonesia	90.18	6.41	2.38	1.03	1010		1279
	Nigeria	90.53	5.05	2.95	1.47	1017		1283
LNG Source	Qatar	89.27	7.07	2.5	1.16	1018	1126	1419
	Abu Dhabai	85.96	12.57	1.33	0.14	1020	1127	1420
	Malaysia	87.64	6.88	3.98	1.5	1045	1155	1434
	Australia	86.41	9.04	3.6	0.95	1036	1145	1429
	Oman	86.61	8.31	3.32	1.76	1051	1161	1438

Source: (NGC + Interchangeability Work Group 2005)

Notes: HHV = higher heating value; scf = standard cubic foot; GT = Gas Turbine

In California, debates over environmental and safety aspects of LNG terminals have led to delays in developing tie points within the state. However, a terminal in Mexico (Costa Azul) has been developed and has been receiving LNG since mid-2008. As suggested above, terminals once envisioned to receive LNG from abroad are now being considered as a means to export natural gas from the United States.

A.2 Fossil Fuel Associated Gas

A.2.1 Associated Gas

Associated with oil extraction is often the outgassing of gases which are typically comprised of hydrocarbons similar to that found in natural gas. Generally speaking, these gases will have greater amounts of higher hydrocarbons than typical natural gas. These "associated gases" (i.e., associated with oil extraction) can be used as a fuel. In contrast, gases derived in gaseous form from gas wells are known as "non-associated gas" or "raw gas." The associated gases will likely appear similar to those found in the LNG scenarios in Table A-3, though they can vary substantially, depending on the location. Associated gases may be flared or vented in practice, which results in substantial greenhouse gas (GHG) forcing and wastes a potential fuel. In North America, associated gas represents a significant potential natural gas resource (Rojey et al. 1997). The amount is increasing in connection with shale gas extraction. For example, the Bakken oil extraction results in 0.7 billion cubic feet per day (bcf/d) of associated gas, of which more than 30 percent is flared (Fielden 2012).

A.2.2 Refinery Gas

Fuel refining leads to the production of off-gases that can potentially be used to produce power. The composition of these gases is different from LNG-type fuels in that they contain high quantities of hydrogen. Table A-4 shows typical compositions of these gases. In California, refining operations do generate such gases, and strategies for using these for energy production are already being pursued, though generally motivated by the necessity to avoid flaring. The

relative emissions performance of current systems used for consuming such gases can likely be improved if advanced combustion technology can be utilized.

A.2.3 Coke Oven Gas

Steel making generates off-gases from the coke by-product. While containing similar constituents as refinery off-gases, these have higher hydrogen versus methane content (~55 percent/~25 percent on a dry basis) along with an associated lower Wobbe Index (~650 Btu/scf, LHV basis) (Tillman and Harding 2004). These applications may not be highly relevant to California, as limited steel production occurs within the state. But covering these compositions in the test plan may be germane for general applicability.

Table A-4: Refinery Off-Gas Composition

Component	Vol % (dry basis)
H_2	25.7
CO	1.5
CH_4	37.4
N_2	2.9
C_2	27.5
C_3	2.9
C_4	1.7
C_5	0.4
LHV (Btu/ft^3)	984

Source: Rao et al. 1996.

A.3 Renewable Methane-Based Fuels

A.3.1 Landfill Gas[1]

When a landfill is capped, landfill gas (LFG) is generated as organic portions of the municipal solid wastes (MSW) decompose. Traditionally, landfill gas is not controlled, and the expected period over which landfill gas will be produced may range from 50 to 100 years. However, a usable landfill gas production rate lasts for only 10 to 15 years. A *bioreactor* is a controlled landfill in which water and other nutrient sources are added into the MSW to increase the landfill gas production rate.

Landfill gas is produced as a result of anaerobic ("in absence of air") decomposition of organic wastes. The organic portions of a landfill's MSW, including paper and paperboard, yard wastes, and food wastes, decompose through biochemical reactions where anaerobic conditions exist. The composition of the landfill gas varies with the characteristics of the waste, age of the landfill, weather conditions, and others. In general, landfill gas contains 50 percent methane (CH_4), 45 percent carbon dioxide (CO_2), and also other traces of gas such as nitrogen (N_2), oxygen (O_2), hydrogen sulfite (H_2S), and water vapor (Tillman and Harding 2004). However, the gas composition varies with the nature of the organic material and also with time. Indeed

[1] Adapted from California Energy Commission. Landfill Gas Power Plants. http://www.energy.ca.gov/biomass/landfill_gas.html.

variation in methane levels from 35 to 65 percent is common (Tillman and Harding 2004). In addition, while the capping process seeks to eliminate air, leaks can lead to nitrogen and oxygen levels of up to 20 percent and 2.5 percent, respectively. The other issues associated with landfills are contaminants. Sulfur compounds can range from negligible to 1,700 parts per million (ppm), and other compounds like siloxanes can be significant. In recent years, attempts to convert landfill gas to energy have required varying degrees of care relative to gas cleanup, to prevent damage or coating of critical power generation device parts.

California leads the nation in both solid-waste generation and the number of landfill gas-to-electricity (LFGTE) facilities. For example, the Puente Hills landfill, operated by the Los Angeles County Sanitation District, produces approximately 46.5 megawatts (MW) of power and is the largest LFGTE facility in the United States. Over 3,000 landfills exist in California. Approximately 300 of them remain active. Statewide, 75 LFGTE projects can be found, including 42 projects converting LFG to electricity, 7 projects converting LFG to heat, and 2 projects upgrading LFG into pipeline gas. The total electrical generation capacity from the existing 42 landfill gas to electricity projects is about 211 MW. The technologies used to convert LFG into electricity in California include gas turbine, steam turbine, reciprocating engine, and combined-cycle systems.

In California, 70 landfills have been flaring gas. These have the potential to produce approximately 66 MW of electricity. The three large flaring landfills (LFGTE potential > 5 MW), including Calabasas LF, Sunshine Canyon, and Operating Industries (OII) (Federal National Priorities List [NPL] Site), have installed gas turbines and are now generating > 30 MW of electricity.

In California, as of 2010, 91 landfills were generating more than 350 MW of energy from landfill gas. An additional 39 sites have shut down, pulling 81 MW of energy generation offline. A remaining 239 landfills have the potential to produce energy from the LFG produced. These landfills have the potential to produce approximately 31 MW of electricity. The 5 landfills that range in LFGTE potential between 1 MW and 1.5 MW have a total potential electrical capacity of approximately 7 MW. From the 56 venting landfills with LFGTE potential that are between 100 kilowatts (kW) and 1 MW in size, approximately 19 MW of total potential electrical capacity exists. The rest of 103 landfills have a combined potential electrical capacity of approximately 5 MW (U.S. Environmental Protection Agency 2012).

Landfill gas does represent an opportunity for upgrade and injection into existing natural gas pipelines. However, as pointed out by the California Energy Commission (Energy Commission), the cost of appropriate cleanup and pressurization for pipeline injection may not be favorable from an economic or overall efficiency benefit viewpoint without additional market or policy forcing functions. However, California's Renewable Portfolio Standards and SB1505[2] (which mandates that hydrogen fuel for vehicles be a minimum of 33 percent renewable) are spurring California utilities and fuel providers to explore potential uses of landfill gas.

[2] Senate Bill 1505, Lowenthal, Chapter 877, Statutes of 2006.

When landfill gas is vented, the GHG implications are serious, as methane is a much stronger greenhouse effect forcing species than CO_2. However, conversion of the LFG to power generates CO_2 and also, potentially, criteria pollutants. While the benefits of generating power from this otherwise "wasted fuel" are apparent, regulatory pressures are requiring a significant reduction in criteria emissions. As a result, improvements in combustion technology using these gases are needed.

A.3.2 Wastewater Treatment[3]

As it does in landfills, organic matter in wastewater streams also contains potential fuel value. While in landfills, the methane generated is due to slow decay of matter; this process can be enhanced with use of "digestion" strategies. Essentially, these processes can accelerate the breakdown of organic material and generation of methane gases. Most common is the use of anaerobic digestion (AD), which is a biological process in which biodegradable organic matter is decomposed by bacteria into biogas, which consists of CH_4, CO_2, and other trace amounts of gases. That biogas can be used to generate heat and electricity. Other important factors, such as temperature, moisture and nutrient contents, and pH are also critical for AD's success. In terms of temperature, either mesophilic AD (30°C–40°C, or 86°F–104°F) or thermophilic AD (50°C–60°C, or 122°F–140°F) can be used. In general, AD at lower temperature is more common, but thermophilic temperature has the advantage of reducing reaction time, which corresponds to the reduction of digester volume. Moisture content greater than 85 percent is suitable for anaerobic digestion.

Types of anaerobic digesters include Covered Lagoon, Batch Digester, Plug-Flow Digester, Completely Stirred Tank Reactor (CSTR), Upflow Anaerobic Sludge Blanket (UASB), Anaerobic Sequencing Batch Reactor (ASBR), and others.

Due to the nature of the digestion processes, the composition of fuel gas from these systems varies far less than from landfills and tends to have overall higher methane content.

Anaerobic digester technology is well developed worldwide, with an estimated 5.3–6.3 gigawatts (GW) installed. Traditional, small, farm-based digesters have been used in China, India, and elsewhere for centuries. The number of digesters of this type and scale is estimated to exceed 6 million. European Union (EU) companies are world leaders in development of the AD technology. Currently, the EU has a total generating capacity of 307 MW from AD technology. The countries in the EU with the largest development figures are Germany (150 MW), Denmark (40 MW), Italy (30 MW), and Austria and Sweden (both 20 MW). Germany led the small on-farm digesters for odor control. Italy developed a series of farm AD systems. Larger, centralized anaerobic digestion plants, which utilize animal manure and industry waste in a single facility, are a newer development. These are most prevalent in Denmark, where there are 18 plants (worldwide there are 50 or so, all within Europe). Municipal solid waste digestion is the newest area for anaerobic digestion. The most recent is for source-separated feedstocks, for which there are estimated to be over 150 commercial-scale

[3] Adapted from California Energy Commission. Anaerobic Digestion. http://www.energy.ca.gov/biomass/anaerobic.html.

plants. These plants have a combined capacity in excess of 6 million tons per year, and the number of plants planned is increasing rapidly.

Obvious opportunities in California include sewage processing and agricultural waste streams, and these are discussed next.

A.3.2.1 Sewage Treatment[4]

According to the California Energy Commission, 242 sewage wastewater treatment plants exist in California. Anaerobic digesters exist in a number of sewage treatment plants. About 38 MW of electrical power is generated from 10 existing sewage wastewater treatment plants. Twelve sewage treatment plants utilize the biogas to produce hot water or heat the digester. The rest of the 220 sewage wastewater treatment plants either do not recover biogas produced from anaerobic digester or do not have anaerobic digesters on site. About 36 MW of electrical potential can be recovered from those 220 sewage wastewater plants. Except for two medium sites (capable of generating between 1,000 kW and 5,000 kW) most of the sewage treatment sites have a small electrical potential (<1,000 kW). Some have even smaller potential: 168 sewage treatment plants have a biogas-to-electricity potential of less than 200 kW.

A.3.2.2 Agriculture/Dairy Waste Digestion[5]

According to the California Energy Commission, tax incentives of the late 1970s and early 1980s encouraged the construction of approximately 18 commercial farm-scaled digesters for energy production in California. Apparently, less than half these systems are running regularly. Only 0.37 MW of power is generated from the existing 5 digesters in California, although the total potential for animal waste-to-energy in California dairies is over 105 MW. Energy can be produced from different types of livestock wastes in California, including dairy, swine, poultry, turkey, sheep and lamb wastes. California dairies have 1.4 million milk cows and are the second leading state in total number of milk cows. There are 2,308 dairy farms in California, with an average size of 602 cows. Currently, only less than 1 percent of the livestock manure generated in California is utilized for power generation.

A.3.2.3 Other Applications

It is also possible to consider comingling of organic matter from waste streams (e.g., food waste from restaurants or personal residences) in anaerobic digesters. This could tremendously increase the feedstock available and thus maximize the production of alternative fuel. This same material could also be submitted to landfills, but the enhanced gas production by the digester provides a much shorter time frame for the production of waste to fuel.

A.4 Synthesis Gas

In recent years, strategies for clean use of the abundant domestic coal resources for low-emission energy production have gained attention. Examples include Integrated Gasification

---

[4] Adapted from California Energy Commission. Anaerobic Digestion. (This information is no longer available online since the Energy Commission redesigned its website.)

[5] See footnote 4.

Combined Cycle (IGCC) systems. In these cases, processing of raw fuel can be performed to achieve gaseous high-hydrogen fuels for direct use in gas turbine engines. Hydrogen gas (H_2) is a diatomic molecule composed of elemental hydrogen, and it exists in the atmosphere as a colorless, odorless gas. A shift toward using pure hydrogen fuel can be seen due to its high energy density and nearly zero emissions in comparison to carbon-based fuels (Stiegel and Ramezan 2006).

In addition to pure hydrogen, "syngas," or synthesis gas, mixtures primarily composed of H_2 and CO can also be obtained. Other names for syngas include *producer gas, town gas, blue water gas,* and *coal gas,* depending on its formation. Syngas first emerged in the early twentieth century for the production of methane, synthesis of ammonia, development of Fischer-Tropsch synthesis, and the hydroformylation of olefins (Wender 1996).

Hydrogen and syngas can be manufactured from any hydrogen feedstock using processes such as reformation, oxidation, gasification, and pyrolysis. When looking at syngas compositions, the primary focus is on the H_2/CO ratio, which is dependent on the production method as well as the feedstock used. Steam reformation of methane produces syngas with a H_2/CO ratio of approximately 3:1, whereas the composition of syngas from gasified coal has a ratio on the order of 1:1 (Spath and Dayton 2003).

Many of the widespread uses of syngas include its use in the synthesis of other chemicals or fuels, as well as direct use as a fuel. The major commercial uses of syngas include the manufacturing of hydrogen, the manufacturing of methanol (especially for the synthesis of methyl t-butyl ether [MTBE]), the synthesis of Fischer-Tropsch liquid fuels, and the hydroformylation (oxo) reaction of olefins, with the main uses of hydrogen being similar. The direct use of hydrogen and syngas as a fuel in a gas turbine combustor is also gaining recognition as a clean and viable source of power. The same is true for vehicles. While the widespread use of hydrogen "begs the question" of the infrastructure requirements, scenarios whereby hydrogen or high-hydrogen-content fuels are widely available are being seriously considered and appear to have a significant potential for reducing pollutants (Stephens-Romero et al. 2009). If a foothold is gained in the transportation sector, it will likely serve as a springboard for energy generation using these fuels as well.

It is conceivable that renewably derived hydrogen from intermittent sources could be stored and then injected into the gas pipeline to effectively "store" the energy produced. This is being pursued in Germany by companies like E.ON.

A.4.1 Natural Gas Derived

A large source of syngas production is from natural gas, which ranges from 87 to 96 percent methane in the United States (Wender 1996). Any production that uses methane as the raw fuel produces syngas as an intermediate, and the production of syngas is the only reaction that breaks down CH_4 into H_2 and CO with a limited amount of unfavorable CO_2 (Notari 1991). Some of these processes include: (1) steam reformation, (2) CO_2 reformation, (3) direct reformation, (4) partial oxidation, and (5) autothermal reformation (Choudhary et al. 2006).

2.5.1.1 Steam Reformation

Figure A-2 shows the schematic for conventional catalytic steam reformation. In the primary reformer, CH_4 is reacted with water over a nickel/aluminum oxide (Ni/Al_2O_3) catalyst at 900°C (1,650°F) and at pressures of 15–30 atmospheres (atm) to produce syngas with a H_2/CO ratio of about 3:1, with the reaction shown in Equation A-1:

$$CH_4 + H_2O \rightarrow CO + 3H_2 \quad \Delta H = +42.9 \text{ kilocalories per mole (kcal/mol)}$$ **Equation A-1**

The remaining stream is then reacted in the secondary reformer with O_2 over a Ni/Al_2O_3 catalyst, followed by one high and one low temperature water gas shift (WGS) reactor, as shown in Equation A-2:

$$CO + H_2O \rightarrow CO_2 + H_2 \qquad \Delta H = -9.8 \text{ kcal/mol}$$ **Equation A-2**

The purpose of the WGS reactors is to modify the H_2/CO ratio of the reformate stream before the syngas moves on to purification. For processes with the goal of producing pure hydrogen, the WGS reactors are used to fully oxidize any remaining CO into CO_2.

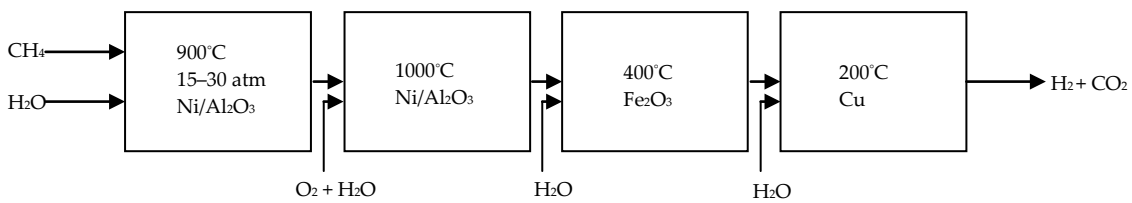

Source: Bharadwaj and Schmidt 1995.

Figure A-2: Block Diagram of a Conventional Catalytic Steam Reformer

A.4.1.1 CO_2 reformation

Syngas produced from steam catalytic reformation contains excess H_2 that is ultimately wasted. By using CO_2 to reform CH_4 instead of steam, more favorable gas mixtures can be achieved with the reaction in Equation A-3:

$$CH_4 + CO_2 \rightarrow 2CO + 2H_2 \qquad \Delta H = +70.5 \text{ kcal/mol}$$ **Equation A-3**

The remaining CO can then be oxidized into CO_2 using WGS reactors. Carbon dioxide reforming studies have been performed using nickel oxide (NiO), copper oxide (CuO), and iron oxide (Fe_2O_3) catalysts (Sodesawa et al. 1979) and further studies have shown that using excess CO_2 can inhibit the formation of carbon in the reformer process (Gadalla and Bower 1988).

A.4.1.2 Direct oxidation

Direct CH_4/O_2 oxidation has developed due to the disadvantages of conventional steam reformation: (1) the process is endothermic, (2) At 3:1, the H_2/CO ratio is higher than desired for Fischer-Tropsch synthesis, (3) corrosion effects caused by steam are evident, and (4) additional

cost is associated with the handling of excess H_2O. The direct oxidation of methane is described by the reaction shown in Equation A-4:

$$CH_4 + \frac{1}{2}O_2 \rightarrow CO + 2H_2 \qquad \Delta H = -8.5 \text{ kcal/mol}$$

Equation A-4

The conversion to syngas with direct oxidation is a much faster reaction than reformation. This suggests single-step processing, resulting in a smaller reactor, with the disadvantage of a flammable mixture of CH_4/O_2 (Bharadwaj and Schmidt 1995). Although the above reaction results in a H_2/CO syngas mixture, oxidation with air instead of pure O_2 can result in the formation of other exhaust gases.

A.4.1.3 Partial oxidation

In 1946, the first investigations of the partial oxidation of CH_4/O_2 began. A reduced 10 percent refractory-supported Ni catalyst was used and operated in the range of 750°C –900°C (1,380°F–1,650°F) at atmospheric pressure. It was shown that an initial exothermic reaction is caused by the complete consumption of a limited amount of O_2, as shown in Equation A-5:

$$CH_4 + O_2 \rightarrow CO_2 + 2H_2O \qquad \Delta H = -10.5 \text{ kcal/mol}$$

Equation A-5

The above reaction was then followed by an endothermic reaction of the remaining CH_4, reforming it with CO_2 and/or H_2O that is produced in the exothermic step (Equation A-6):

$$CH_4 + H_2O \rightarrow CO + 3H_2 \qquad \Delta H = +54.0 \text{ kcal/mol}$$

$$CH_4 + CO_2 \rightarrow 2CO + 2H_2 \qquad \Delta H = +62.4 \text{ kcal/mol}$$

Equation A-6

Currently, methods exist for both catalytic partial oxidation (CPOX) and non-catalytic partial oxidation (POX) (Bharadwaj and Schmidt 1995).

A.4.1.4 Autothermal reforming

Developed in the 1970s, autothermal reforming combines homogenous partial oxidation with steam reformation. The schematic for an autothermal reformer is shown in Figure A-3. Preheated streams of $O_2 + H_2O$ and $CH_4 + H_2O$ are fed into a burner where the CH_4 is partially oxidized, with the addition of H_2O to decrease the formation of carbon and help promote the premixing of CH_4 and O_2. After the homogeneous oxidation step, steam reformation occurs over a nickel catalyst at 1,000°C–1,200°C (1,830°F–2,190°F). This results in a product stream of varying composition, depending on the H_2O/CH_4 and CO_2/CH_4 ratios of the inlet streams (Bharadwaj and Schmidt 1995).

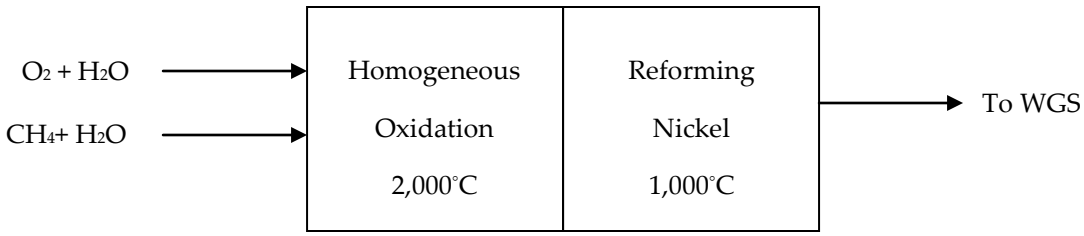

Source: Bharadwaj and Schmidt 1995.

Figure A-3: Block Diagram of Autothermal Reforming of CH_4

A.4.2 Coal

Coal is made up of energy-containing compounds as well as contaminants that must be removed in a cleanup process after conversion to syngas and/or hydrogen. The three categories of coal gasifiers are identified as entrained flow, fluidized bed, and moving bed (or fixed bed) gasifiers. In 2005, it was reported that 20 percent of coal gasification plants in the world were used to produce electricity, while the rest produced chemicals such as ammonia and methanol, as well as syngas (Minchener 2005). Conversion from coal produces syngas with a H_2/CO ratio of approximately 1:1, described by Equation A-7:

$$C + H_2O \rightarrow H_2 + CO \qquad \Delta H = +31.1 \text{ kcal/mol}$$

Equation A-7

In entrained flow gasifiers, pulverized coal particles and gasification agents (steam and oxygen or air) flow concurrently at high speed. The reaction takes place at 1,200°C–1,600°C (2,190°F–2,910°F) at pressures ranging from 20–80 atm. For this type of gasification, the coal feed can either be dry or wet, and the produced syngas requires considerable cooling before going through the cleanup process (Minchener 2005).

Fluidized bed gasifiers involve coal particles being suspended in the steam and oxygen/air gas flow, in which the coal feed is mixed with the particles undergoing gasification. The coal is fed into the upward flowing gas stream that fluidizes the bed during gasification. The reaction temperature ranges in fluidized bed gasifiers is lower than entrained flow gasifiers at 900°C–1,050°C (1,650°F–1,920°F), and is uniformly distributed due to back-mixing. But this mixing of coal and partially gasified particles also contributes to the problem of incomplete carbon conversion (Collot 2006).

Moving bed (or fixed bed) gasification involves the slow flowing of gases through the bed of the coal feed. The two classifications of moving bed gasifiers are slagging and dry ash, in which higher steam-to-oxygen ratios create lower reaction temperatures of approximately 1,000°C (1,830°F). One advantage to this type of gasification is the flexibility for use of coals with an ash content of up to 35 percent (Anjaneyulu et al. 1993).

A.4.3 Petroleum Coke

Coking technologies produce a solid, carbonaceous material from the processing of heavy and extra heavy oils called *petroleum coke,* or *petcoke* (Trommer et al. 2005). With increasing use of crude oil worldwide and within California, a resulting increase of this by-product is inevitable,

introducing another issue involving its disposal. The gasification technologies discussed in previous sections also are used to process petcoke, to promote further conversion to syngas and hydrogen, as well as to help eliminate some of this increasing refinery waste (Zou et al. 2007).

Steam gasification of petroleum coke is an endothermic process and is described in the net reaction in Equation A-8:

$$CH_xO_y + (1- y)H_2O \rightarrow (x/2 + 1 - y)H_2 + CO$$ **Equation A-8**

where x and y are the elemental molar ratios of H/C and O/C in the petcoke, respectively (Z'Graggen et al. 2007). The quality of the resulting syngas depends on the chemical composition of the petcoke, which is dependent on the refining processes. The following are the major competing reaction groups involved in the steam gasification of petcoke to hydrogen:

1. Steam Gasification: $C_{(gr)} + H_2O \rightarrow CO + H_2$
2. Boudouard Equilibrium: $2CO \rightarrow C_{(gr)} + CO_2$
3. Methanation: $C_{(gr)} + 2H_2 \rightarrow CH_4$
4. Steam Reformation: $CH_4 + H_2O \rightarrow CO + 3H_2$
5. Water Gas Shift: $CO + H_2O \rightarrow CO_2 + H_2$

These sets of reactions are all strongly dependent on temperature, C/O ratio, and pressure, and they ultimately determine the composition of the product gas. Another example of petcoke-to-syngas processing is by CO_2 gasification. From the above set of reactions, the steam gasification equation is replaced with the CO_2 gasification equation: $C_{(gr)} + CO_2 \rightarrow 2CO$ (Tyler and Smith 1975).

Gasification of petcoke is not limited to only steam and CO_2 gasification. Despite the particular gasification agent used, the resulting advantages include a decrease in oil refinery waste, as well as the production of useful syngas or hydrogen.

A.4.4 Biomass

For California, the use of gasified biomass represents a significant opportunity as a renewable fuel source which has the synergy of reducing landfill utilization while providing energy generation with a reduced carbon signature. It is noted that the landfill route for biomass disposal can ultimately lead to generation of a renewable fuel stream, but the time scale is much longer. Also, some biomass waste can be digested to produce fuels. However, gasification may make more sense, depending on the feedstock available. Biomass is a renewable material that contains considerable amounts of H, C, and O, and can be converted into syngas with pyrolysis or gasification (Ni et al. 2006). Like coal, biomass can have a wide range of compositional variation. The gasification and pyrolysis processes are detailed in Figure A-4.

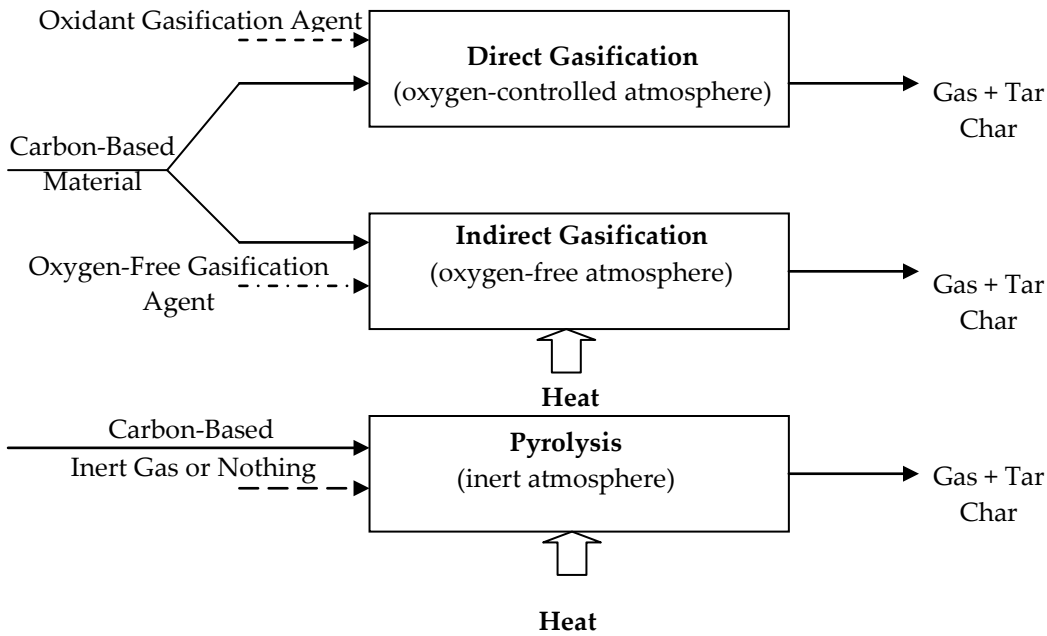

Source: Belgiorno et al. 2003.

Figure A-4 Block Diagram of the Gasification and Pyrolysis Processes

In the process of *direct gasification,* the feedstock is partially oxidized using an oxidizing gasification agent, and the temperature is self-maintained through the reactions (Belgiorno et al. 2003). *Indirect gasification* involves the use of an oxygen-free gasification agent, and an external energy source is needed to maintain the reaction temperature. *Pyrolysis* is a specific type of indirect gasification in which the gasification agent is either an inert gas or is absent from the reaction altogether (Hauserman et al. 1997).

Pyrolysis involves heating the biomass or other feedstock to temperatures of 375°C–525°C (700°F–980°F) at pressures of 1–5 atm in the absence of air, and can be classified into the two categories of slow and fast pyrolysis. In slow pyrolysis, the biomass is heated at a slow rate, resulting in the production of char, vapor, and gas. Previous studies have shown that the actual product composition is dependent on the feedstock and temperature (Maschio et al. 1994). In fast pyrolysis, the feedstock is heated rapidly without air, resulting in gas-, liquid-, and solid-phase products. Gaseous products from fast pyrolysis include varying compositions of H_2, CH_4, CO, and CO_2 (Equation A-9) (Ni et al. 2006).

$$\text{Biomass + heat} \rightarrow H_2 + CH_4 + CO + CO_2 + \text{other products}$$

Equation A-9

Methane can then be converted to more syngas and subsequent hydrogen with a reformation process and WGS reaction, as described in Section 2.5.1.

Gasification is a thermo-chemical process in which a solid or liquid feedstock is converted into a combustible gas product with the use of a gasification agent. The gaseous product may contain H_2, CO, CO_2, CH_4, H_2O, small amounts of higher hydrocarbons, inert gases from the gasification

agent, and contaminants (Bridgewater 1994). The conversion of solid biomass occurs with the reaction shown in Equation A-10 (Ni et al. 2006).

$$\text{Biomass} + \text{heat} + \text{steam} \rightarrow H_2 + CO + CO_2 + CH_4 + \text{hydrocarbons} + \text{char} \qquad \textbf{Equation A-10}$$

One of the major issues associated with biomass gasification occurs with the high nitrogen content of the syngas produced from air gasification. To eliminate this problem, pure oxygen gasification can be used, but the cost of producing the pure oxygen is estimated at around 20 percent of the total cost for a gasification plant (Belgiorno et al. 2003). Other issues with biomass gasification include dealing with any tar and ash formation in the product (Ni et al. 2006).

A.4.5 Compositional Considerations

Because of the numerous feedstock and processing methods used in obtaining syngas, it is expected that the resultant gases will have varying fuel composition. Syngas compositions vary not only with raw material (e.g., biomass, petroleum coke, coal), but also within each grouping, due to the composition of the actual feedstock. For example, successful uses of syngas-fired turbines have been demonstrated, and each facility operates a specific fuel composition, dependent on the coal feed. Some syngas facilities have been shown to operate on fuels with hydrogen compositions of greater than 90 percent, although they have not attempted to implement advanced combustion technology for low emissions. The current IGCC projects of GE Power Systems include plants that operate on a wide range of compositions, as shown in Table A-5. As shown in the table, many other constituents besides H_2 and CO can exist in the syngas, including diluents such as CO_2, N_2, and H_2O. Similarly, the syngas produced from biomass is strongly dependent on the type and composition, corresponding to another range of constituent concentrations.

Because the composition of syngas varies so widely with production, the concept of determining a matrix engrossing all possible constituent ranges for the project was eliminated. Instead, fuel compositions were determined by likely future scenarios that involve the use of high-hydrogen fuels. One representative composition was selected for each of the following scenarios in addition to pure hydrogen:

- Process and refinery gas
- Large-scale IGCC power plant (> 50 MW)
- Small-scale IGCC power plant (< 50 MW)
- Nitrogen dilution for NO_x abatement

Table A-5: Minimum and Maximum Concentrations for Syngas from GE Power Systems IGCC Plants

Constituent	Minimum %	Maximum %
H_2	8.6	61.9

CO	22.3	55.4
CO_2	1.6	30.0
CH_4	0.1	8.2%
N_2 + Ar	0.2	49.3
H_2O	0	39.8

Source: Jones and Shilling 2003.

Table A-6 shows the representative syngas composition on a dry, volumetric basis as produced by appropriate gasification methods. Pure hydrogen represents the case where carbon sequestration is utilized, though it is becoming apparent that 90 percent carbon removal may be a reasonable upper limit (meaning the fuel would be 90 percent hydrogen and balance methane). The process and refinery gas blend reflects the interest of smaller-scale combustion systems, while the gasified coal/petcoke is indicative of current IGCC central power plants. Note that for these larger-scale applications, expectations are that an air separation unit (ASU) will be used and, as a result, the gasifier will be fed with oxygen as opposed to air. In a smaller unit, the air separation unit may not be cost effective, so gasification with air is more likely. Finally, diluted fuel is representative of syngas diluted with nitrogen, which is the current practice for combustion systems.

Table A-6: Dry, Clean Compositions (Volumetric Basis)

SOURCE	H_2	CO	CH_4	CO_2	N_2	LHV (Btu/ft^3)	Wobbe Index
Pure H_2	100	0	0	0	0	265	1,006
Coal/Petcoke (O_2-blown)	37	46	1	14	2	247	289
Biomass (air-blown)	17	17	5	13	48	142	152
N_2 Dilution	23	31	1	10	35	165	183

References

Anjaneyulu, T., K. Prasad, K. Rao, and R. Vaidyeswaran. 1993. "Gasification Characteristics of Coal in a Moving Bed Pressure Gasifier." *Fuel Processing Technology* 35(3): 259–274.

Belgiorno, V., G. De Feo, C. Della Rocca, and R. Napoli. 2003. "Energy from Gasification of Solid Wastes." *Waste Management* 23: 1–15.

Bharadwaj, S., and L. Schmidt. 1995. "Catalytic Partial Oxidation of Natural Gas to Syngas." *Fuel Processing Technologies* 42: 109–127.

Bridgewater, A. 1994. "Catalysis in Thermal Biomass Conversion." *Applied Catalysis A: General* 116: 5–47.

Choudhary, V., K. Mondal, and T. Choudhary. 2006. "Oxy-CO_2 Reforming of Methane to Syngas Over CoOx/MGO/SA-5205 Catalyst." *Energy Fuels* 20: 2484–2488.

Collot, A. 2006. "Matching Gasification Technologies to Coal Properties." *International Journal of Coal Geology* 65: 191–212.

Fielden, S. 2012. "Why Will Bakken Flaring Not Fade Away." *RBN Energy* 6 September. http://rbnenergy.com/why-will-bakken-flaring-not-fade-away.

Gadalla, A., and B. Bower. 1988. "The Role of Catalyst Support of the Activity of Nickel for Reforming Methane with Carbon Dioxide." *Chemical Engineering Science* 43(11): 3049–3062.

George, D., and E. J. Bowles. 2011. Shale Gas Measurement and Associated Issues. July. 238(7).

Hauserman, W., N. Giordano, M. Lagana, and V. Recupero. 1997. "Biomass Gasifiers for Fuel Cell Systems." *La Chimica e L'Industria* 79(2): 199–207.

Jones, R., and N. Shilling. 2003. *IGCC Gas Turbines for Refinery Applications, Report GER-4219,* Schenectady: GE Power Systems.

Lieuwen, T., V. G. McDonell, D. Santavicca, and T. Sattelmayer. 2008. "Burner Development and Operability Issues Associated with Steading Flowing Syngas Fired Combustors." *Combustion Science and Technology* 180: 1169–1192.

Liss, W., et al. 1992. *Variability of Natural Gas Composition in Select Major Metropolitan Areas of the United States.* Chicago: Gas Research Institute.

Maschio, G., A. Lucchesi, and G. Stoppato. 1994. "Production of Syngas from Biomass." *Bioresource Technology* 48: 119–126.

Minchener, A. 2005. "Coal Gasification for Advanced Power Generation." *Fuel* 84: 2222–2235.

NGC+ Interchangeability Work Group. 2005. *White Paper on Natural Gas Interchangeability and Non-Combustion End Use.* NGC+ Interchangeability Work Group.

Ni, M., D. Leung, M. Leung, and K. Sumathy. 2006. "An Overview of Hydrogen Production from Biomass." *Fuel Processing Technology* 87(5): 461–472.

Notari, B. 1991. C-1 Chemistry: A Critical Review. *Catalytic Science and Technology* 1: 55–76.

Rao, A., D. Francuz, and E. West. 1996. *Refinery Gas Waste Heat Energy Conversion.* Houston: International Joint Power Generation Conference.

Rojey, A., et al. 1997. *Natural Gas Production, Processing, Transport.* Translation of 1994 Book ed. Paris: Editions Technip.

Ryan, N., K. Larsen, and P. Black. 2002. *Smaller, Closer, Dirtier, Diesel Backup Generators in California.* Environmental Defense Fund.

Shah, S., et al. 2006. "Emissions of Regulated Pollutants from In-use Backup Generators." *Atmospheric Environment* 40(22): 4199–4209.

Sodesawa, T., A. Dobashi, and F. Nozaki. 1979. "Catalytic Reaction of Methane with Carbon Dioxide." *Reaction Kinetics and Catalysis Letters* 12(1): 107–111.

Spath, P., and D. Dayton. 2003. *Preliminary Screening—Technical and Economic Assessment of Synthesis Gas to Fuels and Chemicals with Emphasis on the Potential for Biomass-Derived Syngas.* Golden, Colorado: National Renewable Energy Laboratory.

Stephens-Romero, S., et al. 2009. "Determining Air Quality and Greenhouse Gas Impacts of Hydrogen Infrastructure and Fuel Cell Vehicles." *Environmental Science and Technology* 43(23): 9022–9029.

Stiegel, G., and M. Ramezan. 2006. "Hydrogen From Coal Gasification: An Economical Pathway to a Sustainable Energy Future." *International Journal of Coal Geology* 65: 173–190.

Tillman, D., and N. Harding. 2004. *Fuels of Opportunity: Characteristics and Uses in Combustion Systems.* Oxford: Elsevier.

Trommer, D., et al. 2005. "Hydrogen Production by Steam-Gasification of Petroleum Coke Using Concentrated Solar Power: I. Thermodynamic and Kinetic Analyses." *International Journal of Hydrogen Energy* 30: 605–618.

Tyler, R., and I. Smith. 1975. "Reactivity of Petroleum Coke to Carbon Dioxide between 1030 and 1180 K." *Fuel* 54: 99–104.

U.S. Energy Information Administration. 2013. *U.S. Natural Gas Proved Reserves.* http://www.eia.gov/dnav/ng/hist/rngr11nus_1a.htm.

U.S. Environmental Protection Agency. 2012. *Landfill Methane Outreach Program.* http://www.epa.gov/lmop/.

Wender, I. 1996. "Reactions of Synthesis Gas." *Fuel Processing Technology* 48: 189–297.

Zou, J., et al. 2007. "Modeling Reaction Kinetics of Petroleum Coke Gasification with CO_2." *Chemical Engineering and Processing* 46: 630–636.

Z'Graggen, A., et al. 2007. "Hydrogen Production by Steam-Gasification of Petroleum Coke Using Concentrated Solar Power: III. Reactor Experimentation with Slurry Feeding." *International Journal of Hydrogen Energy* 32(8): 992–996.

APPENDIX B:
Review of Existing Interchange Parameters and Methodologies

The review of potential interchange parameters is divided into major sections. The first section reviews "supply side" parameters, which are those associated with fuel usage. Next examined are parameters that are associated with influence of fuel composition on "operability." In this context "operability" is meant to encompass flashback, blowoff, and autoignition. A by-product/related element is combustion dynamics, which are relevant to combustion systems but beyond the scope of this project. Finally, parameters associated with predicting the influence of fuel composition on pollutant emissions are examined.

B.1 Historical Natural Gas Parameters

A number of historic interchange parameters have been developed for fuel composition impacts. These are reviewed briefly here, but more details can be found elsewhere (NGC+ Interchangeability Work Group 2005; Singer 2006). Other examples summarizing these parameters can also be found (Ferguson et al. 2008).

B.1.1 Wobbe Index

The most commonly used parameter is the Wobbe Index, shown in Equation B-1:

$$WI = \frac{HV}{\sqrt{SG}} \qquad \textbf{Equation B-1}$$

where

HV is the fuel heating value
SG is the fuel specific gravity

The Wobbe Index is an important parameter associated with fuel systems, as it provides an indication of how much fuel containing energy can be passed through a given orifice at a given pressure drop. However it is well established that the Wobbe Index is not related directly to key combustion parameters such as flashback, flame temperature, etc. As a result, though widely documented and used, it should not really be expected to explain how fuel composition will affect combustion systems. Nonetheless it needs to be examined relative to its ability to infer operability and emissions behavior. It is important to note whether the Wobbe Index is reported on a higher heating value (HHV) or lower heating value (LHV) basis. In practice, HHV is rarely achieved, as it requires condensation of the water in the exhaust stream prior to exiting the system.

B.1.1.1 Example

The Wobbe Index has long been used as a gauge against which to compare how a given device's fuel management system can perform. This is illustrated by Figure B-1 , which shows that a given fuel control system may need to be changed if the Wobbe Index of a fuel falls beyond a

certain range. In addition, it has been observed to correlate with some aspects of combustion behavior, as illustrated by Figure B-2 and Figure B-3 which are discussed in following sections.

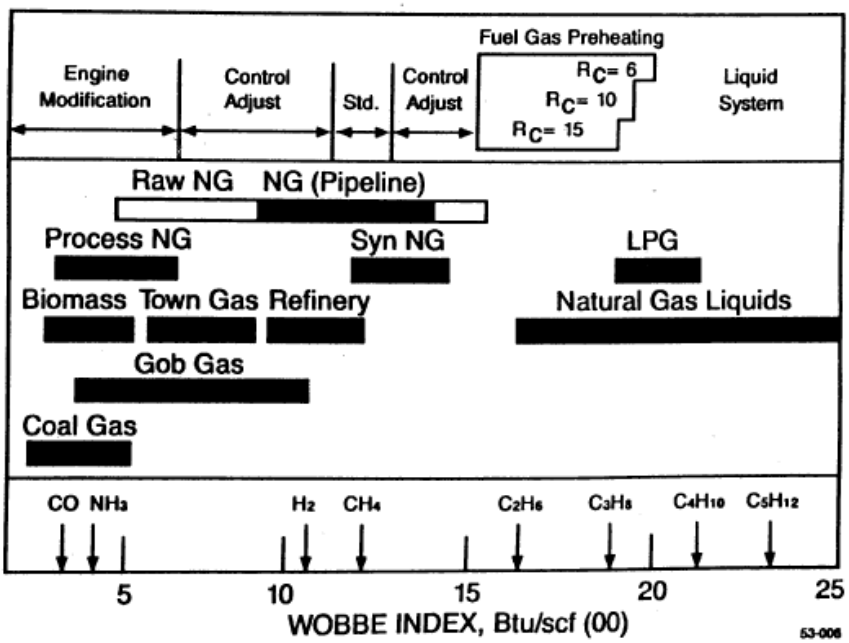

Source: Meier et al. 1986.

Figure B-1: Wobbe Index as an Indicator of Fuel System Adjustment Requirements

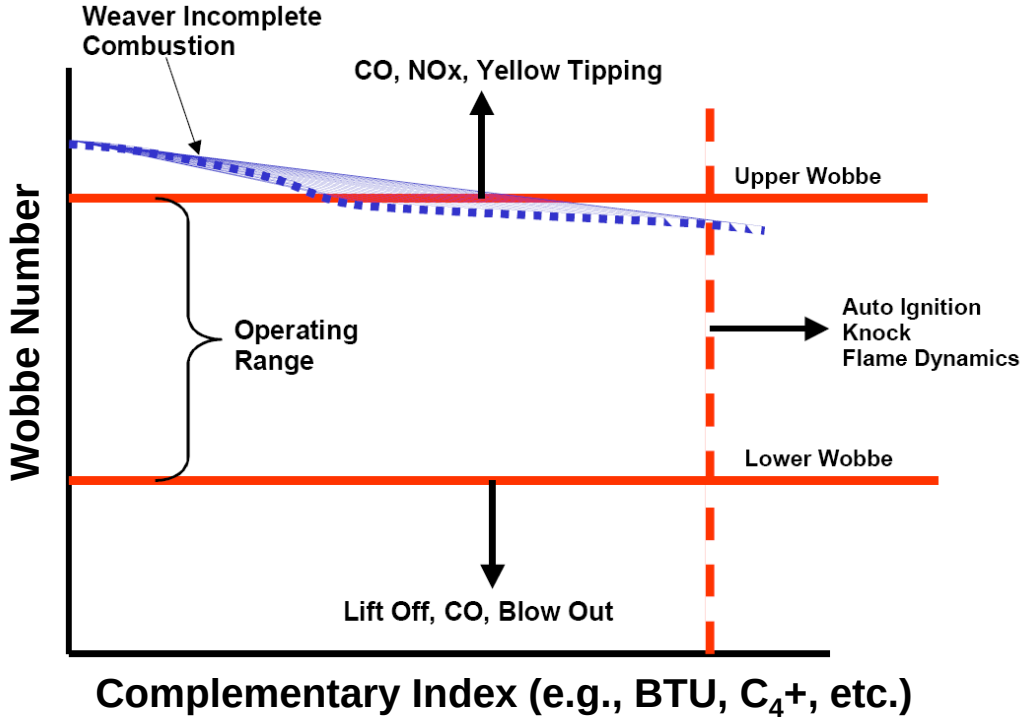

Source: NGC+ Interchangeability Work Group 2005.

Figure B-2: Example of Interchange Space Parameters

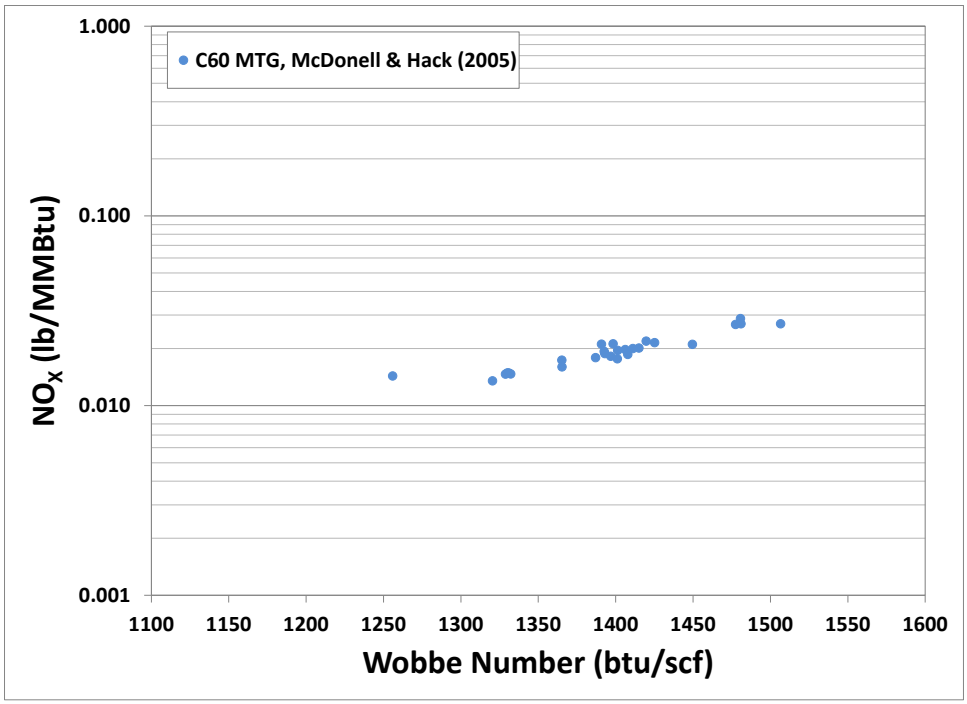

Source: Hack and McDonell 2008.

Figure B-3: Example of NOx/Wobbe Index Correlation

B.1.2 Modified Wobbe Index

The "modified" Wobbe Index (MWI) has been adopted by some practitioners. It utilizes the lower heating value (which is arguably more relevant to industrial combustion systems and gas turbines that will generally not have sufficient heat recovery in the exhaust systems to recover the enthalpy of evaporation (i.e., generally these systems have "non-condensing" exhaust systems). Further, it takes the step of incorporating fuel temperature which is, in effect, a means to modify the volumetric flow for a given situation. The MWI is given as Equation B-2

$$MWI = \frac{LHV}{\sqrt{T_{gas}}\sqrt{SG}}$$ **Equation B-2**

where

LHV is the fuel lower heating value
Tgas is the fuel temperature (absolute)
SG is the specific gravity of the fuel relative to air at ISO conditions

B.1.2.1 Example

The MWI has been used extensively by GE (GE Power Systems 2002) as part of their "OpFlex™" "Wide Wobbe" systems for gas turbines. By modifying the fuel temperature, the system can limit the MWI to workable ranges for a given system.

B.1.3 American Gas Association (AGA) Parameters

In 1946, the American Gas Association (AGA) carried out extensive experimental research on fuel gas interchangeability (American Gas Association 1946). AGA Tests were done on a specially developed partial premixing Bunsen-type burner and focused on establishing criteria for blending "supplemental" or "peaking gases" with baseload supplies or adjustment gases; those adjustment gases were the three most historically representative natural gases available in the United States at that time (Halchuk and Wilson 2005). Based on this experimental work, AGA developed several empirical indices to address the effects of fuel interchange on yellow tipping, flame lifting,, and flashback.

Table B-1 is a calculation sheet to determine the stability parameters of the adjustment fuel. " A " is the stoichiometric volume of air per unitary volume of gas, and " F " and " T " are the empirical determined lifting and yellow tip constants, respectively; these constants are defined for pure components of the fuel. "G" is the fuel mole fraction. The table also shows the formulas to calculate the constants for the adjustment. Since the constants A , F , and T are defined for pure substances, the same table can be used to calculate the parameters of the substitute gas. Table B-2 summarizes the formulas to define the stability parameter.

Table B-1: Gas Interchangeability Calculation Sheet

Analysis of Gas Decimal Volume	Fuel Mole Fraction	Air Required for Combustion (ft^3 air/ft^3 gas)		Lifting Constant		Yellow Tip Constant	
Symbol	G	A		F		T	
Nomenclature (adjustment gas)	G_a		$A_a = A \times G_a$		$F_a = F \times G_a$		$T_a = T \times G_a$
H_2		2.38		0.6		0	
CO		2.38		1.407		0	
CH_4		9.53		0.67		2.18	
C_3H_8 (propane)		23.82		1.931		9.8	
O_2		-4.76		2.9		-4.76	
CO_2				1.08			
N_2				0.688			
Total	1						

Note: A subscript "a" indicates the primary or "adjustment" gas, while terms with the "s" subscript are for the "substitute" gas.

Source: NGC+ Interchangeability Work Group 2005.

Table B-2: AGA Gas Interchangeability Parameters

Variable	Adjustment Gas	Substitute Gas
Air Theoretically required for Complete Combustion per 100Btu	$a_a = \frac{100A_a}{h_a}$	$a_s = \frac{100A_s}{h_s}$
Primary Air Factor:	$f_a = \frac{1000\sqrt{d_a}}{h_a}$	$f_s = \frac{1000\sqrt{d_s}}{h_s}$
Lifting Limit Constant:	$K_a = \frac{F_a}{d_a}$	$K_s = \frac{F_s}{d_s}$
Yellow Tip Limit:	$Y_a = \frac{100T_a}{A_a + 7E_a - 26.3O_{2a}}$	$Y_s = \frac{100T_s}{A_s + 7E_s - 26.3O_{2s}}$

Note: "d" is the specific gravity, "h" is the heating value; "E" is the total fraction of inert gases; $O_{2a,s}$ is the total fraction of oxygen in the fuel·

Source: NGC+ Interchangeability Work Group 2005.

Once the adjustment and substitute gas mixtures are identified and their respective parameters are defined, the stability indices can be calculated with equations B-3, B-4, and B-5:

Lifting Interchangeability Index:

$$I_L = \frac{K_a}{\frac{f_a a_s}{f_s a_a}\left(K_s - \log\left(\frac{f_a}{f_s}\right)\right)}$$

Equation B-3

Flashback Interchangeability Index:

$$I_F = K_s f_s \frac{\sqrt{\frac{h_s}{1000}}}{K_a f_a}$$

Equation B-4

Yellow Tip Interchangeability Index:

$$I_Y = \frac{f_s a_a Y_a}{f_a a_s Y_s}$$

Equation B-5

AGA developed a set of preferable and objectionable limits for each of the three adjustment natural gases, and those limits are presented in Table B-3. Two fuels are interchangeable if their lifting and flashback indices fall under the preferable values of 1.0 and 1.18, respectively; also the yellow tipping index must be above 1.0 in order to be interchangeable with regard to this criterion.

Table B-3: Limits of Interchangeability for Various Baseload Natural Gases

Interchange -ability Index	High Heating Value Natural Gas		High Methane Value Natural Gas		High Inert Natural Gas	
	Preferable	Objectionable	Preferable	Objectionable	Preferable	Objectionable

I_L	Under 1.0	Above 1.12	Under 1.0	Above 1.06	Under 1.0	Above 1.03
I_F	Under 1.18	Above 1.2	Under 1.18	Above 1.2	Under 1.18	Above 1.2
I_Y	Above 1.0	Under 0.7	Above 1.0	Under 0.8	Above 1.0	Under 0.9

Source: American Gas Association 1946.

A link between AGA criteria, the Wobbe Index, and Heating Value of the gas can be combined in a two-dimensional plot, as exemplified in Figure B-4. By calculating the AGA parameters for many different natural gases and reflecting a fail or a pass with color, a region of stability can be found. In this case, AGA indices set three boundaries, for lifting, yellow tipping, and flashback.

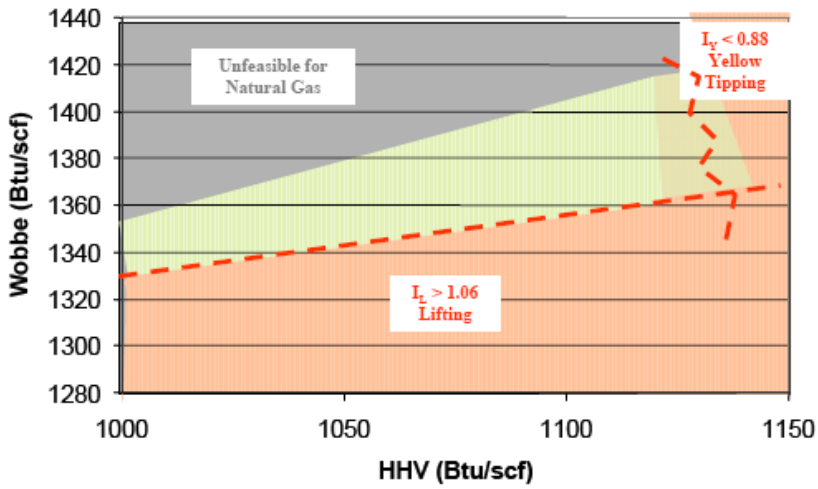

Source: NGC+ Interchangeability Work Group 2005.

Figure B-4: Stability Diagram Using AGA Indices. In this Case the Reference Gas Had the Following Composition C1 = 95%, C2 = 4%, C3 = 0.25%, N2 = 0.75%.

Since AGA indices were developed using a simple Bunsen-type flame and considered only the most common natural gases at the time when the work was published, these indices may not be applicable to the typical complex turbulent premixed flames found in current practical systems. The inaccuracies expected from applying AGA indices to current fuels may be even greater, since current fuels of interest include coal-derived syngas, landfill and biomass gases, imported LNG, and hydrogen-augmented fuels whose composition is completely different than those natural gases used to set the stability criteria. Nonetheless, these indices were considered as the most advanced methods and effective tools to predict interchangeability in the United States and should be considered as a starting point.

B.1.3.1 Example

As an example, consider the case when interchanging pure methane (adjustment gas: 100 percent CH_4) with a mixture of 70 percent CH_4 and 30 percent H_2 (substitute gas).

Other information related to these example fuels is presented in Table B-4.

Table B-4: Properties for an Example Fuel Calculation

Fuel mixture (vol.)	100% CH_4	70% CH_4 and 30% H_2
Relative density	$d_a = 0.55$	$d_s = 0.41$
Higher heating value (Btu/scf)	$h_a = 1011$	$h_s = 805.2$

Using the calculation sheets presented in Table B-1, the constants for adjustment gas (Table B-5) and substitute gas (Table B-6) are calculated. The gray shading is used to indicate the cells where the calculations are carried out.

Table B-5: Calculation of the Interchangeability Constants for the Adjustment Gas

Analysis of Gas Decimal Volume	Fuel Mol Fraction	Air Required for Combustion (ft^3 air/ft^3 gas)		Lifting Constant		Yellow Tip Constant	
Symbol	G	A		F		T	
Nomenclature (adjustment gas)	G_a		$A_a = A \times G_a$		$F_a = F \times G_a$		$T_a = T \times G_a$
H_2	0	2.38	0	0.6	0	0	0
CH_4	1	9.53	9.53	0.67	0.67	2.18	2.18
Total	1	$A_a =$	9.53	$F_a =$	0.67	$T_a =$	2.18

Table B-6: Calculation of the Interchangeability Constants for the Substitute Gas

Analysis of Gas Decimal Volume	Fuel Mol Fraction	Air Required for Combustion (ft^3 air/ft^3 gas)		Lifting Constant		Yellow Tip Constant	
Symbol	G	A		F		T	
Nomenclature (adjustment gas)	G_s		$A_s = A \times G_s$		$F_s = F \times G_s$		$T_s = T \times G_s$
H_2	0.3	2.38	0.714	0.6	0.18	0	0
CH_4	0.7	9.53	6.671	0.67	0.496	2.18	1.5226
Total	1	$A_s =$	7.385	$F_s =$	0.649	$T_s =$	1.5226

Using the results collected in Table B-5 and Table B-6, and the properties of the fuel, the corresponding calculations of the parameters are presented in Table B-7.

Table B-7: AGA Parameters-Calculation Sheet

Variable	Adjustment Gas	Substitute Gas
Air Theoretically required for Complete Combustion per 100Btu	$a_a = \frac{100A_a}{h_a} = \frac{100 \times 9.53}{1011} = 0.9426$	$a_s = \frac{100A_s}{h_s} = \frac{100 \times 7.385}{805.2} = 0.917$
Primary Air Factor:	$f_a = \frac{1000\sqrt{d_a}}{h_a} = \frac{1000 \times \sqrt{0.55}}{1011} = 0.7335$	$f_s = \frac{1000\sqrt{d_s}}{h_s} = \frac{1000 \times \sqrt{0.41}}{805.2} = 0.7952$
Lifting Limit Constant:	$K_a = \frac{F_a}{d_a} = \frac{0.67}{0.55} = 1.2181$	$K_s = \frac{F_s}{d_s} = \frac{0.649}{0.41} = 1.583$
Yellow Tip Limit:	$Y_a = \frac{100T_a}{A_a + 7E_a - 26.3O_{2a}} = \frac{100 \times 2.18}{9.53} = 22.87$	$Y_s = \frac{100T_s}{A_s + 7E_s - 26.3O_{2s}} = 20.62$

Finally, the indices can be calculated using the Equations B-3 through B-5 above:

- Lifting Interchangeability Index: 0.8389
- Flashback Interchangeability Index: 1.2642
- Yellow Tip Interchangeability Index: 1.236

Since $I_F = 1.2642 > 1.18$, this interchange parameter indicates that if 100 percent CH_4 is interchanged with a mixture of 70 percent CH_4 / 30 percent H_2, the device will experience flashback. Hence those two fuels are not interchangeable. On the other hand, the lifting and yellow-tipping indices indicate that these two fuels are interchangeable.

It is important to note that these indices were developed using laminar flames, and that they are designed to be used with systems that do not have any control systems. As a result, their applicability to systems that, for example, control heat input or firing temperatures is not really possible. Regardless, they will be considered and evaluated to the extent possible with data from the project in Chapter 4.

B.1.4 Schuster Index

The Schuster Index (Equation B-6) attempts to capture fuel impacts on combustion through inclusion of the laminar flame speed in conjunction with the Wobbe Index.

$$Sc = \frac{Wobbe\ Index}{S_L}$$ **Equation B-6**

Where

S_L is the laminar flame speed

The Schuster Index, when developed, was hard to implement due to lack of reliable laminar flame speed data. This has changed in recent years because researchers have more accurately measured flame speed. In this regard, the experimental measurements of individual flame speeds of single-component fuels have been particularly prolific and flame speed data are readily available. However flame speed measurements for alternative fuels such as coal-derived syngas, landfill gases, and imported LNG have not experienced the same level of evaluation (Ferguson et al. 2008). Since the flame speed captures a lot of information about the kinetics of the flame, and because some of the most important combustion parameters (such as equivalence ratio, preheating temperature, and pressure) have a direct effect on flame speed, Schuster Index is expected to be a more comprehensive single index parameter than Wobbe Index.

B.1.4.1 Example

The use of Schuster Index is, in principle, straightforward. The Wobbe Index is taken as above in Section B.1.2. What is then needed is the laminar flame speed. The laminar flame speed was one of the stated challenges for adoption of the Schuster Index in the time in which it originated. However, chemical kinetics programs like Cantera or CHEMKIN can now be (and are) used to calculate laminar flame speed for a given condition. Table provides examples of calculated laminar flame speeds and associated Shuster Index values. What is suggested here is that a "critical Schuster Index" may exist, below which flashback maybe an issue. This can be explored with existing and newly gathered flashback data.

Table B-8: Example Calculated Laminar Flame Speeds for Different Mixtures and Conditions

Fuel	Temperature (K)	Pressure (bar)	Laminar Flame Speed (cm/s)	Schuster Index
CH_4	300	1	19.81 (φ =0.7)	60.32
CH_4	500	1	55.91 (φ = 0.7)	21.37
CH_4	500	10	20.93 (φ = 0.7)	57.10
C_3H_8	500	10	27.75 (φ = 0.7)	65.12
H_2	500	10	197.3 (φ = 0.7)	5.49

B.1.5 Bureau of Mines

In the 1950s, while working for the U.S. Bureau of Mines, E. R. Weaver expanded the AGA indices on lifting, yellow tipping, and flashback by adding separate parameters for incomplete combustion, burner load, and air supply (NGC+ Interchangeability Work Group 2005). Weaver's main contribution was to include empirical correlations to take account of the effect of flame speed on each index. Those empirical correlations, used by Weaver in 1951, could be updated with more accurate results, given the important progress achieved in measuring the flame speed of fuel mixtures and the availability of flame speed predictions based on current kinetic models (Ferguson et al. 2008).

Similarly to AGA indices, Weaver Fuel interchangeability is predicted based on the limits that give a relative correlation of the "substitute" fuel to the "adjustment" gas. It is worth highlighting that the multiple index techniques have a history of widespread and satisfactory use in the industry; however, as empirical models, the multiple index methods also have limitations based on the burner designs and fuel gases tested in the development research (NGC+ Interchangeability Work Group 2005). Similarly to AGA indices, Weaver indices were never optimized for today's engines operating under lean pre-mixed combustion (Ferguson et al. 2008).

Table shows the formulas to calculate the Weaver interchangeability indices; the table also shows the values of the indices for exactly interchangeable fuels and the accepted ranges or the stability limits when two fuels do not match exactly.

Table B-9: Weaver Indices and Acceptable Ranges

Weaver Index	Formula	Exact Inter-change-ability	Acceptable Ranges (Wanneg et al. 2011; Ferguson et al 2008)
Air supply index (J_A)	$J_A = \frac{A_s\sqrt{d_a}}{A_a\sqrt{d_s}}$	$J_A = 1$	$0.8 \le J_A \le 1.2$
Weaver index for flashback (J_F)	$J_F = \frac{S_s}{S_a} - 1.4J_A + 0.4$	$J_F = 0$	$J_F \le 0.26$
Weaver index for burner load (J_H). This relation is equivalent to Wobbe Index ratio.	$J_H = \frac{H_s\sqrt{d_a}}{H_a\sqrt{d_s}}$	$J_H = 1$	$0.8 \le J_H \le 1.2$
Weaver index for incomplete combustion (J_I).	$J_H = J_A - 0.366\frac{R_s}{R_a} - .634$	$J_I = 0$	$J_I \le 0.05$
Weaver index for lifting (J_L).	$J_L = \frac{J_A\left(\frac{S_s}{S_a}\right)(100 - Q_s)}{(N_s - N_a)/100}$	$J_L = 1$	$J_L \ge 0.64$
Weaver index for yellow tipping (J_Y).	$J_Y = J_A - 1 + \frac{(N_s - N_a)}{100}$	$J_Y = 0$	$J_Y \le 0.05$

Similar to AGA calculations, the subscript "a" denotes the original adjust gas, and the subscript "s" denotes the new substitute gas.

Weaver used an empirical relation to obtain the flame speed of each fuel. The Weaver flame speed factor is presented below in Equation B-7:

$$S = \frac{\sum a_i B_i}{A + 1.0 + 5.0Z - 18.8Q}$$ **Equation B-7**

This empirical formula captures the effect of the content of oxygen in the fuel gas (Q), and the percent of inert components (Z), where:

a_i = is the mol fraction of the component *i.*

B_i = an empirical constant called the *flame factor.* The flame factor is assigned to each component in the fuel mixture.

A	=	stoichiometric volume of air required to complete the combustion of a unity of volumetric fuel.
d	=	relative density of gas expressed as specific gravity referred to air as unity.
S	=	maximum flame speed in a mixture of the gas with air, expressed as a fraction of the flame speed for hydrogen.
Q	=	is the molar fraction of oxygen in the mixture.
H	=	heating value of gas in Btu/scf.
R	=	ratio of number of atoms of hydrogen in all forms of combination in the fuel gas to the number of carbon atoms in the hydrocarbons. (Carbon monoxide is excluded.)
N	=	number of "readily liberated atoms" of carbon per hundred molecules of gas.
Z	=	is the molar fraction of inert components.

3.1.5.1 Example

In the context of Weaver indices, let's find out if the interchangeability of hydrogen (H_2) with pure methane (CH_4) is possible.

The properties of methane and hydrogen are presented in Table B-10:

Table B-10: Properties Needed for Example Weaver Index Calculation

Fuel mixture (vol.)	100% CH_4	100% H_2
Relative density	$d_a = 0.55$	$d_s = 0.07$
Stoichiometric air-to-fuel ratio (volume)	$A_a = 9.52$	$A_s = 2.38$

The Weaver air supply index (J_A) is shown in Equation B-8 (from Table B-9):

$$J_A = \frac{A_s\sqrt{d_a}}{A_a\sqrt{d_s}} \quad or \quad J_A = \frac{2.38\sqrt{0.55}}{9.52\sqrt{0.07}} = 0.7$$

Equation B-8

Since 0.7 is out of the stability range $0.8 \le J_A \le 1.2$, (recall Table B-9) these two fuels are not interchangeable with respect to the air supply criterion. This parameter can be evaluated in the context of data obtained throughout this project.

Similar to the AGA indices, the Weaver Indices were designed for laminar systems without controls. As a result, application to practical turbulent systems that incorporate some level of control on firing temperature or load will be inherently limited. Hence, additional concepts are desired for more general application.

B.2 Other Methodologies

In addition to the historical parameters, other work, both historic and more recent, touch on more general concepts for the prediction of fuel interchangeability using reduced-order methods. Generally, the historical parameters were derived empirically in the context of simple Bunsen-type flames with low Reynolds number conditions (i.e., emphasis on laminar behavior). Further, they emphasized only variation in natural gas (e.g., generally the fuel was mostly methane). In practice, burner configurations tend to be turbulent and generally feature a means of anchoring the reaction (e.g., with swirl, or other "aerodynamic" stabilization mechanisms). Also, it is of interest to understand the interchangeability of fuels with a wider range of compositions.

Hence, while these concepts have been generally derived from more general combustion theory and, while they are empirical in nature, they may be more generally applicable to practical lean premixed burner configurations.

B.2.1 Blowoff

Blowoff refers to the dynamic process of flame detachment and extinction. In general, blowoff has been represented as a competition between time scales associated with physical processes and kinetic processes. The ratio of the time scales is the Damköhler number (Da), shown in Equation B-9:

$$Da = \frac{\tau_{physical}}{\tau_{chemical}} \qquad \textbf{Equation B-9}$$

When the physical time scale (e.g., residence time,$\tau_{physical}$) falls below the kinetic time scale (e.g., reaction time, $\tau_{chemical}$), Da will reduce, and when it approaches 1.0, will be at a level where the combustion process will be prone to blowoff. Essentially, the mixture does not have enough physical time to chemically release the fuel energy. Generally, the physical time scale is dictated by the design of the combustion system. Parameters such as swirl strength and flame holder size dictate a residence time within the combustion zone. On the other hand, the kinetic time scale is strongly affected by temperature, pressure, and fuel composition. As a result, changing loads and/or fuels significantly impact the reaction times and, thus, the Damköhler number.

This intuitively appealing description of the mechanism triggering blowoff has resulted in decades of work essentially validating the concept (e.g., Chaudhuri et al. 2010; Rizk and Lefebvre 1986; Leonard and Mellor 1983; Ballal and Lefebvre 1979; Wright 1959; Zukoski and Marble 1955) This body of work has been largely summarized by Shanbhogue et al. (2010) and essentially concludes that a Damköhler number approach is effective in capturing the global blowoff behavior. As a result, this concept has gained widespread acceptance as a general approach to infer blowoff.

To apply this approach, the numerator and denominator in Equation B-9 must be determined. Each has subtleties that must be considered and which may be a function of the burner type and fuel type.

Early examples of blowoff correlations using this approach are in form of an equivalence ratio or fuel-to-air ratio at blowoff, as a function of geometry, velocity, and an effective reaction rate. Examples include that shown in Equation B-10 (Lefebvre 1983):

$$q_{LBO} = C\left\{\dot{m}_A/V_c P_3{}^{1.25} exp\left({T_3}/{100}\right)\right\}^{0.16}$$ **Equation B-10**

Where

q_{LBO}	=	fuel-to-air ratio at blowoff
C	=	constant (function of fuel type and geometry)
m_A	=	air mass flow rate
V_c	=	characteristics reaction volume
P_3	=	combustor inlet pressure
T_3	=	combustor inlet temperature

Equation B-10 was developed for gas turbine applications, and it reveals a time-scale ratio as follows:

- The air mass flow and the volume generate a *residence time*.
- The pressure and exponential terms form a reaction rate that is the inverse of the *chemical time* and that can be thought of as an ignition delay time.

Conceptually, ignition delay time could be considered "unrealistic" as it is a "sit and wait" time, not a time associated with convection or diffusion of radical species. Regardless, the similar form for reaction rate and delay time suggests this could be evaluated.

Another recent correlation is shown in Equation B-11 (Huelsekamp et al. 2011):

$$\emptyset_{blowoff} = 0.195\left\{\left({U}/{D}\right)^{0.1493} exp\left(\frac{361.4}{T}\right)/P^{0.2199}\right\}$$ **Equation B-11**

Equation B-11 also reflects a ratio of time scales similar to that noted in Equation B-10. It is noted that the authors developing Equation B-11 systematically considered numerous other non-dimensional groups such as Prandtl number, Schmidt number, Reynolds number, and Strouhal number. The noted lack of correlation with these other numbers was taken as further reaffirmation that Damköhler number is the appropriate group to correlate blowoff.

Choices can be made relative to the time scale of interest. One could be the ignition delay time, which is essentially captured in the form of Equation B-10 and Equation B-11 as the chemical time scale is an Arrhenius expression.[6] In both examples, however, fuel composition is not explicitly considered (as a result of the constants found in the exponential terms which should be a function of fuel); yet, as is discussed in Section 4.1, the ability to determine ignition delay

[6] An Arrehnius expression essential relates the reaction rate constant, k, to the temperature, T, and an "activation energy," E_A according to $k = Ae^{-E_A/RT}$.

time for a wide variety of fuels appears well in hand. A second chemical time scale expression, which is commonly used in the literature, is shown in Equation B-12:

$$\tau_{chem} = \alpha / S_L^2. \qquad \textbf{Equation B-12}$$

Where

α is the thermal diffusivity
S_L is the laminar flame speed

To apply Equation B-12, the thermal diffusivity of the mixture and the laminar flame speed are needed. Conceptually, to apply Equation B-12, the following steps would be taken to correlate data from the experiment using a Damköhler number approach (using the first two steps for the denominator, and the second two for numerator):

1. Obtain thermal diffusivity α of the fuel-air mixture using a transport properties calculator at blowoff conditions.
2. Calculate laminar flame speed S_L, either via kinetics software such as CHEMKIN, or obtain values from literature.
3. Establish a representative velocity for the system.
4. Establish a characteristic length scale applicable to the combustor in question.

Returning to the fundamental form of the Damköhler number given in Equation B-9, if a given combustion system is considered, it might be argued that the value in the numerator is a constant (e.g., constant recirculation zone size, constant bulk gas residence time). As a result, the key to considering fuel composition is the determination of the denominator. Hence, Equation B-12 could be used or an explicit ignition delay time could be used.

This essentially one-dimensional conceptual model may not fully capture the details of the processes occurring. Indeed, local behaviors may indicate blowoff ahead of any time ratio which may be responsible for the scatter in the data available. As fuel composition changes dramatically or inlet conditions reach levels that are outside of the conditions for which the numerous experimental studies have been carried out, refinements to the conceptualization of blowoff may be required. The impact of further transient response requirements may also require new thinking in this area.

B.2.1.1 Example

An example for applying these correlations is as follows:

For a given burner arrangement, consider the application of Equation B-10, which was developed with gas turbine applications in mind. In this example, the values summarized in Table B-11 are known as a result of a single experiment:

Table B-11: Values for Application of Equation B-10

Air mass flow	0.017 kilograms per second (kg/s)

Volume of Reaction Zone (from image or computational fluid dynamics, CFD)	$1.26E10^{-5}$ m^3
Temperature	300 K
Pressure	1 bar
Observed fuel-to-air ratio at blowoff	0.004

Using these parameters:

$$0.004 = C\{0.017/1.26E10^{-5} \times 1^{1.25}\ exp(^{300}/_{100})\}^{0.16}$$ **Equation B-13**

and solving for C:

C = 0.002

Now if the blowoff at another condition is needed, for example 10 bar and 600 K, these values are used in Equation B-10 to determine the fuel-to-air ratio at blowoff. Table B-12 summarizes the values for this example.

Table B-12: Application of Equation 20 for 10 bar, 600 K

Air mass flow	Unknown, kg/s
Volume of Reaction Zone (from image or CFD)	Unknown, m^3
Temperature	600 K
Pressure	10 bar
Observed fuel-to-air ratio at blowoff	Solved for

If it assumed that the pressure drop across the burner remains constant, the mass flow rate will scale by the density. In this case, the higher air pressure will lead to a factor of 10 higher mass flows, but the higher temperature will reduce this by a factor of 2, resulting in 5 times the air flow, or 0.085 kg/s. The volume of the reaction zone may change, but assume that the fraction of air participating is constant. In this case, the fuel to air ratio at blowoff can be determined using Equation B-14:

$$q_{LBO} = 0.002\{0.085/1.25 \times 10^{-5}(10)^{1.25} exp(^{600}/_{100})\}^{0.16}$$ **Equation B-14**

q_{LBO} = 0.002

Hence, the increased pressure and temperature leads to the ability to operate leaner mixtures as expected.

In this case, the fuel has not changed—only the operating condition has. If the fuel were to change, it is likely that the size of the reaction would change, but so would the constant, *C*, for a given geometry. As a result, one approach to using Equation B-10 would be to establish a correlation for the value of *C* for different fuels. This could be done with a series of tests with various fuels, but this would defeat the purpose of having the expression to predict the impact of the fuel composition. The tests to establish *C* for each fuel would generate the desired fuel composition effect without needing the expression to predict it. It would be helpful to have a more general approach to account for fuel variation. This is pursued in Section 4.2.

B.2.2 Flashback

Flashback can be an issue for the low-emission systems under consideration in this study that rely on premixing of the fuel and air prior to combustion. As summarized in Lieuwen et al. (2008), flashback has been classified to describe at least four different types of behavior:

1. Flashback into the core flow
2. Flashback along a boundary
3. Flashback associated with combustion induced vortex breakdown
4. Flashback associated with combustion dynamics

B.2.2.1 Core Flashback

Regarding *core flashback,* the simplest design rule requires that the flow field must not have strong local velocity deficits and that the flow velocity must be substantially above the reaction propagation rate. Figure B-5 illustrates the concept of core flashback. Essentially, when the reaction propagation rate exceeds the mixture velocity, flashback into the mixer can occur. This simple model suggests that a simple velocity ratio might be sufficient as a critical parameter.

a) Factors Influencing Core Flashback

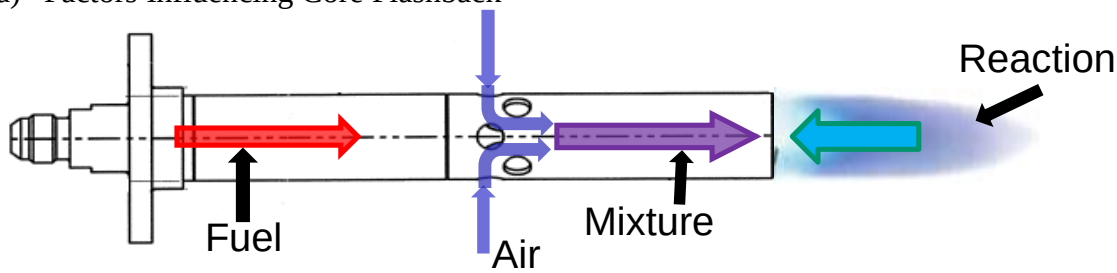

b) State at core flashback

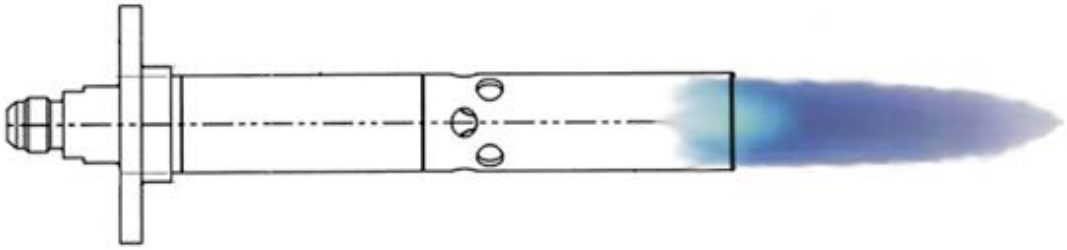

Figure B-5: Conceptual Model of Core Flashback

Equation 25 illustrates such an expression which involves a flame speed, S_L, and a bulk flow velocity, U_{flow}. Examination of this expression also suggests that a ratio of time scales (e.g., residence time and reaction rate) may also be an appropriate parameter). In other words, Equation B-15 can be considered a form of Equation B-9.

$$FB_i = S_L/U_{flow}.$$ **Equation B-15**

B.2.2.2 Boundary Layer Flashback

Boundary layer flashback is a result of the fact that, at a wall, the flow velocity is necessarily zero. Moving away from the wall, the velocity will increase until it reaches a value that is "isolated" from the wall, or the freestream velocity, designated as U_{ax} in Figure B-6. This distance is known as the *penetration depth* and is designated as d_{bl} in Figure B-6. Conceptually, because the velocity in the boundary layer will somewhere drop to a value below the flame propagation rate, S_T, the reaction can propagate upstream along a boundary. The final part of the concept is associated with the fact that the wall not only results in a zero velocity condition at its surface, it also serves as means of "quenching" the reaction by essentially terminating key propagation reactions. As a result, if the reaction gets to certain critical distance from the wall, the "quenching distance," d_q, it will not be able to propagate upstream.

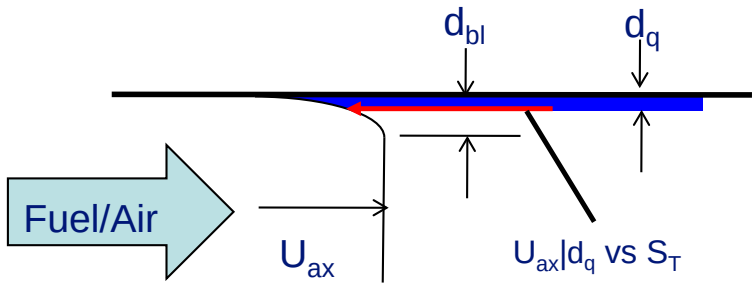

Figure B-6: Boundary Layer Flashback Illustration

From this simplified model, it can be seen that strategies to avoid boundary layer flashback would be to keep reaction out of the boundary layer by (1) reducing the amount of fuel in that location (i.e., "lean out" the boundary layer), (2) minimizing the thickness of the boundary layer /"penetration distance" (thereby ensuring $d_q > d_{bl}$), or (3) taking advantage of quenching distance differences. Figure B-7 shows quenching distances for various fuels. As shown, fuels such as hydrogen or acetylene have much smaller quenching distances than do propane or isooctane. This, combined with hydrogen's relatively high burning velocity, is a primary reason why hydrogen poses significant challenges for premixed operation.

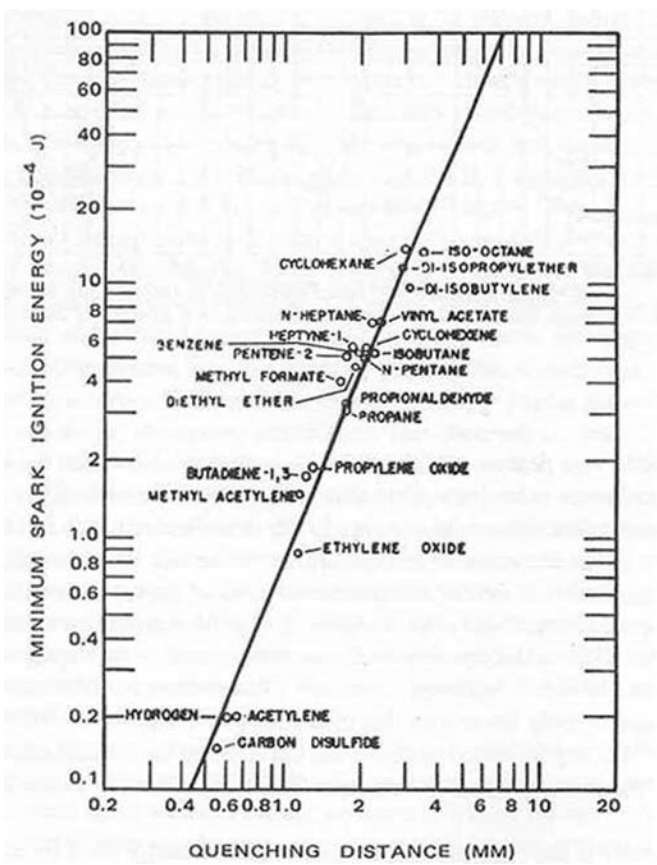

Source: Calcote et al. 1952

Figure B-7: Quenching Distances for Various Fuels

The conceptual model posed in Figure B-6 was reduced to practice in the 1940s by Lewis and von Elbe (1943)who considered a combination of the flame speed, the flow speed, and the distance from the wall at which flashback occurred. They termed this the critical gradient (Equation B-16):

$$g_c = \frac{S_L}{d_{bl}}$$ **Equation B-16**

The concept of the velocity gradient in their theory was devised for a *laminar stream* and sets that the velocity distribution of the injected fluid follows closely the Poiseuille parabola, shown in Equation B-17:

$$U = n\left(R^2 - r^2\right)$$ **Equation B-17**

where

U is the velocity at a distance r from the axis,
R is the radius of the tube, and
$n = \frac{-a}{4\eta}$, where η is the viscosity and a the hydrodynamic pressure gradient.

By adding assumptions regarding the state of the flow (e.g., fully developed laminar pipe flow), the relation was reduced to a form that could easily be calculated using the flow rate, *Q*, and geometry of the pipe, as shown in Equation B-18:

$$g_c = \frac{4Q}{\pi R^3}$$ **Equation B-18**

Hence Equation B-18 can be used as a design guide for interchangeability. If a given mixture exceeds the critical value, it will flashback. This is a very convenient form in that the geometry (via *R*) and the volume flow rate, *Q*, of the mixture is needed along with the critical velocity gradient for that condition. Thus, in principle, a tabulation or correlation that relates this critical velocity gradient to the conditions of interest would be beneficial. However, such a tabulation is not available. Also, Equation B-18 does not contain an explicit fuel effect, which implies that Equation B-16 is perhaps a more general and useful form. Unfortunately, this form requires laminar flame speeds and the penetration distance, both of which require some effort to determine and are not available in a tabular or correlation form. Figure B-8 shows an example of the concept to collapse data from various sources for atmospheric natural gas/air mixtures (Shaffer et al. 2013). As shown, if the equivalence ratio is known, the critical gradient to avoid flashback can be established, and then the flow rates and or velocities can be adjusted using Equation B-18 to ensure flashback is avoided. Of course, these results are only for natural gas, and furthermore, the conditions are laminar.

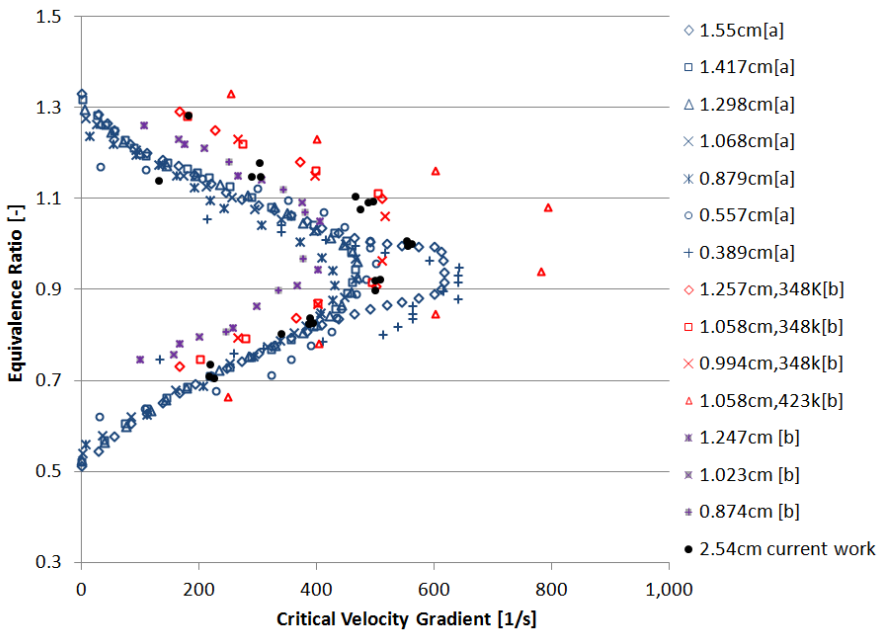

Source: Shaffer et al. 2013.

Figure B-8: Summary of Equivalence Ratio vs. Critical Velocity Gradient for Various Studies with Natural Gas

Just considering the laminar flame speeds of methane and hydrogen, one might expect a difference in the critical velocity gradient of about 7 (ratio of laminar flame speed of hydrogen to that of methane). However, this does not include any quenching effects, as characterized by d_{bl} in Equation B-16. As shown in, hydrogen can sustain reaction closer to the wall than can methane; hence, the critical velocity gradient is more than 7 times higher for hydrogen. This is for a laminar situation. Whether the critical wall gradient for the corresponding *turbulent boundary layer* is higher than that for the laminar case depends on the thickness of the quenching distance with respect to the laminar sub-layer (Wohl 1953). An alternative expression for the critical gradient at flashback for turbulent flow conditions is shown in Equation B-19:

$$g_c = 0.03955\, Re^{3/4}\, \bar{u}/d \qquad \textbf{Equation B-19}$$

Equation B-19 incorporates aspects of the fuel through density and viscosity contained within the *Re* term, and thus has promise for describing the relative flashback propensity of two given fuels. Interestingly, however, no direct connection to flame speeds or quenching is evident, again suggesting a lack of key physics in its ability to predict fuel compositional impacts.

In 1959, a method for predicting the interchangeability of arbitrary gas mixtures concerning only the flame stability was developed (Van Krevelen and Chermin 1959). Their work was based on the theory of stability of laminar atmospheric burner flames as defined by Lewis and Von Elbe. According to Lewis and Von Elbe, both flashback and blowoff are exclusively governed by the boundary velocity gradient and the air-fuel ratio (Lewis and von Elbe 1943). This was confirmed experimentally by Grumer et al. who found that the two stability limits (flashback and blowoff) are independent of the burner port diameter (Grumer et al. 1956). Grumer determined these stability limits for a large number of single-component gases and gas

mixtures. As mentioned, the theory of Lewis and Von Elbe applies well to laminar flame regimes. Consequently, Grumer used premixed laminar streams, flowing through single upright ports in free air, at room temperature and pressure. As a consequence, the method developed by Van Krevelen and Chermin is appropriate only for the interchangeability of premixed laminar flames. However, it is worth summarizing the details, however, as extension of the concept to turbulent flames may be possible.

Flame stability diagrams for hydrogen and methane are presented Figure B-9. The critical gradient can be calculated as Equation B-18 for a given value of *F*, the fuel-gas concentration as a fraction of the equivalence ratio. Hydrogen, with its reactivity, may flash back already at a boundary velocity gradient of 10,500 sec^{-1} but can hardly be blown off. However, methane flashes back only when the boundary velocity gradient has fallen to the low value of 400 sec^{-1}; whereas, blowoff occurs at 2,000 sec^{-1} (at stoichiometric gas concentration) (Van Krevelen and Chermin 1959).

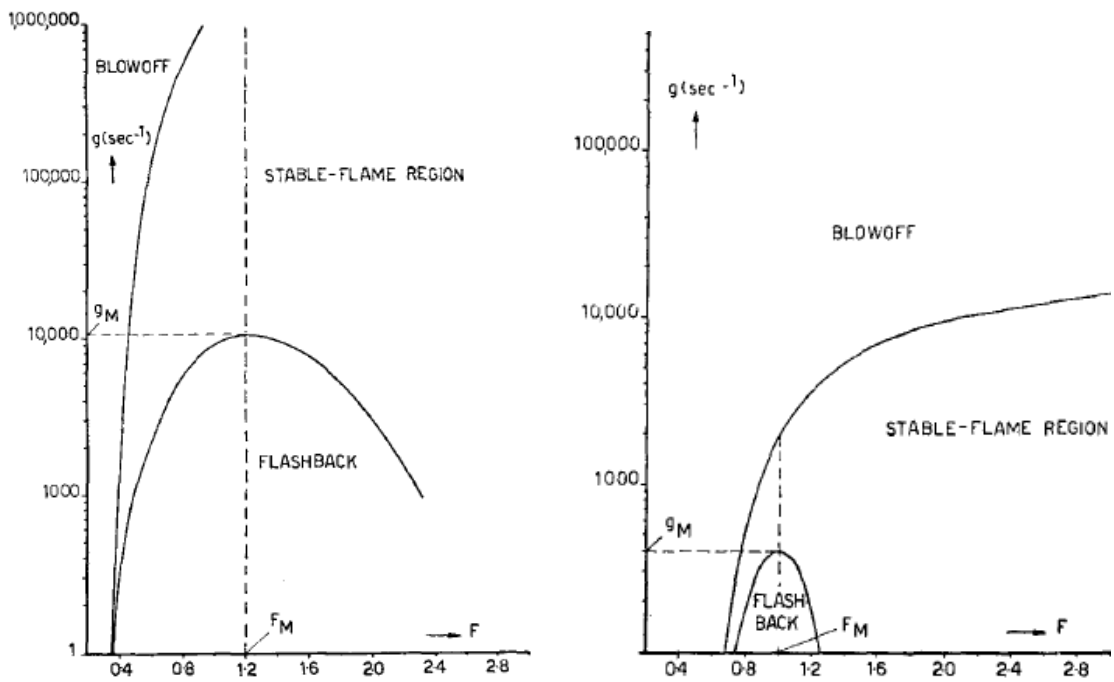

Source: Van Krevelen and Chermin 1959.

Figure B-9: Flame Stability Diagram of Hydrogen (left) and Methane (right)

Figure B-10 shows a schematic representation of the flame stability diagram. This diagram is characterized by the following data:

1. The coordinates of the peak of the flashback curve (g_M, F_M).
2. A quantity providing a measure of the width of the flashback curve.
3. The distance of the blow-off curve from the peak of the flashback curve characterized, for example, by the distances TP and TQ.

In principle, the flame stability diagram for any given gas or mixture (burning in air) is completely characterized by these three quantities.

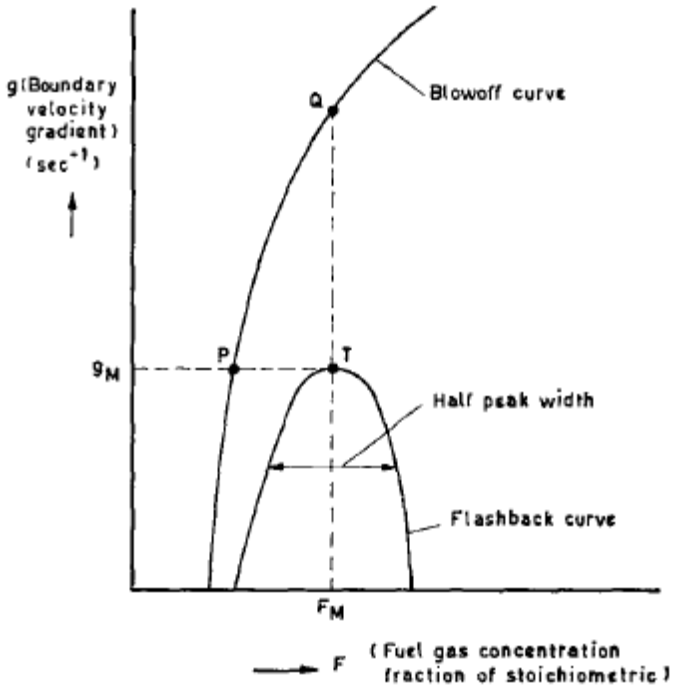

Source: Van Krevelen and Chermin 1959.

Figure B-10: Typical Flame Stability Diagram

Van Krevelen and Chermin (1959) found it possible to reduce all individual stability diagrams (of both pure and mixed gases) to a generalized diagram by using the following coordinates:

1. The dimensionless reduced boundary velocity gradient: $g_R = g/g_M$.
2. The reduced gas concentration, defined as $F_R = 1 + \varphi(F - F_M)$. Where $F$is the fuel gas concentration, fraction of stoichiometric; F_M is the position of the peak of the flashback curve; and φ is the reduction factor. This is a reciprocal measure of the width of the flashback curve and has been normalized in such a way that for methane $\varphi = 1$.

The generalized flame stability diagram is presented in Figure B-11. This comprises a bundle of blowoff curves that are exclusively determined by the percentage of hydrogen in the inert-free mixture.

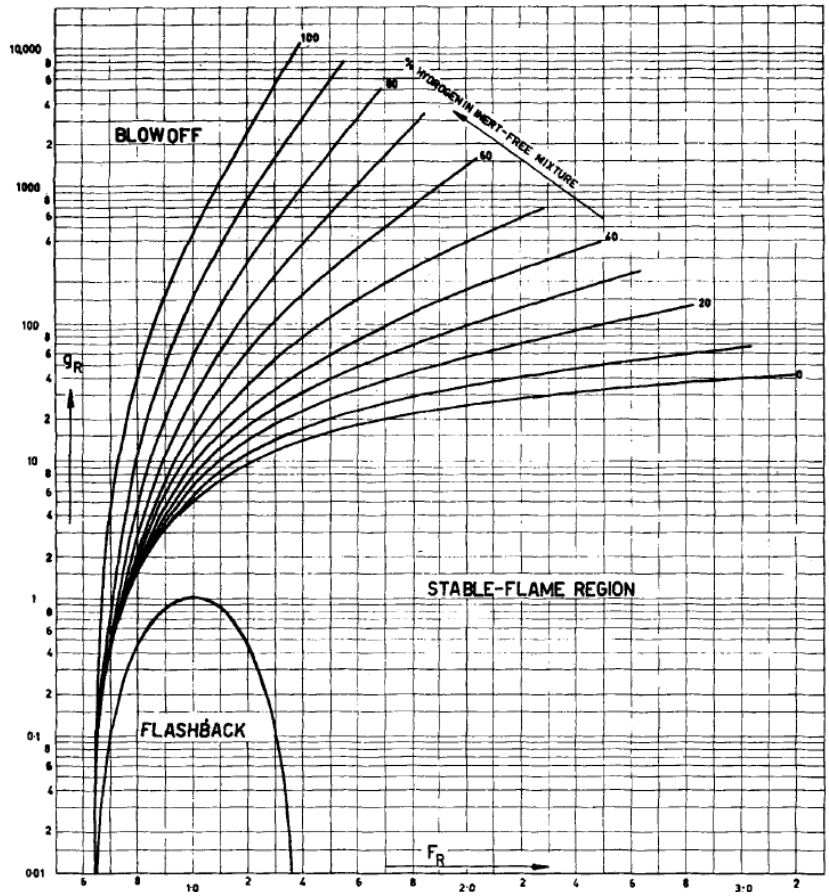

Source: Van Krevelen and Chermin 1959.

Figure B-11: Generalized flame stability diagram

The numerical values of F_M, g_M, and ϕ of pure fuel gases are given in Table B-13.

Table B-13: Values of g_M, F_M, and ϕ of Pure Fuel Gases

Fuel gas	g_M (sec^{-1})	F_M	ϕ
CH_4	400	1	1
C_2H_6 (ethane)	650	1.13	0.8
C_3H_8	580	1.12	0.6
C_2H_4 (ethylene)	1,400	1.1	0.63
C_6H_6 (benzene)	720	1.06	0.63
H_2	10,500	1.2	0.46

Of the characteristic parameters, the reduction factor ϕ is the only additive one. The other two, g_M and F_M, are only additive for mixtures of hydrocarbons. For other binary mixtures Grumer determined the corresponding maximum values, as presented in Figure B-12.

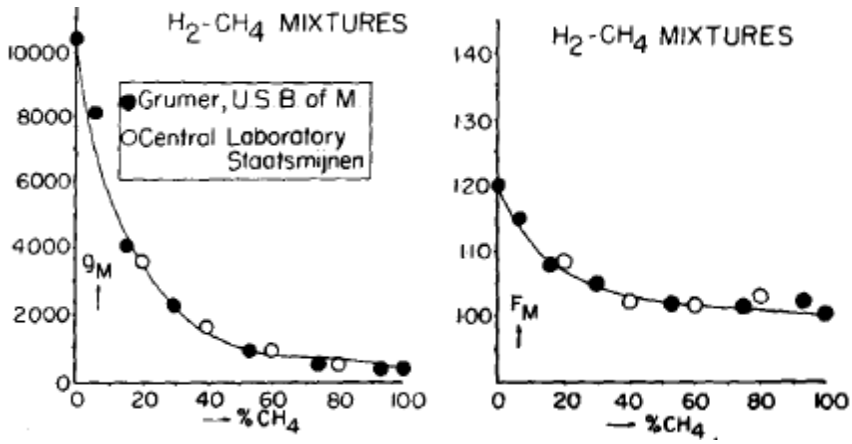

Source: Figure copied from Van Krevelen and Chermin 1959.

Figure B-12: Critical Gradient (left) and Equivalence Ratio (right) at the Flashback Maximum Point for Methane-Hydrogen Mixtures

For detailed descriptions about how to determine the parameters g_R, F_R, and ϕ for other fuel mixtures including inert gases, see Van Krevelen and Chermin (1959).

Finally, if a given gas or gas mixture A, is burning with a stable flame on a burner port, the coordinates relating this burner-fuel gas combination (the performance point of the burner for gas A) naturally lie within the stable flame region of the diagram. This gas is interchangeable with another gas (B) only if the coordinates of the performance point of the burner-fuel gas B combination also come within the stable flame region of the generalized diagram.

If the performance point of a burner with adjustment gas A is known, the performance of the same burner with a substitute fuel B can be calculated, as shown in equations B-20 and B-21:

$$g_B \approx g_A \left(\frac{P_B}{P_A} \right)$$ **Equation B-20**

$$F_B \approx F_A \left(\frac{W_B}{W_A} \right)$$ **Equation B-21**

Where P the gas-line pressure and W is the Wobbe Index of the gas.

B.2.2.3 Example

A burner has been adjusted for methane (A) and the coordinates of the performance point are:

$$g_A = 750\,\text{sec}^{-1};\ F_A = 1.2\ ;\ P_A = 1\,cm\,Hg$$

The performance point in the generalized stability diagram becomes:

$$g_{RA} = \frac{750\,\text{sec}^{-1}}{400\,\text{sec}^{-1}} = 1.88;\quad F_{RA} = 1 + 1 \times (1.2 - 1) = 1.2$$

The Wobbe Index of methane is:

$$W_A = 43818.8\frac{MJ}{m^3}$$

Now consider a mixture of 40 percent H_2 and 60 percent CH_4 (gas B). The method can be applied to establish if gas B can be interchanged for gas A without concern for flashback. Gas B has a Wobbe Index of:

$$W_B = 39153.1\frac{MJ}{m^3}\ .$$

Using equations 30 and 31, the values of g_B and F_B for the given injector are established. Assuming that the line pressure is the same for both gases:

$$g_B \approx g_A\left(\frac{P_B}{P_A}\right) = g_B \approx 750\,\text{sec}^{-1}$$

$$F_B \approx F_A\left(\frac{W_B}{W_A}\right) = F_B \approx 1.2\left(\frac{39153.1}{43818.8}\right) \approx 1.0722$$

$$\phi_B \approx 0.6 \times 1 + 0.4 \times 0.46 = 0.784$$

Now the values can be estimated using the reduced form. From Figure B-12, $g_{MB(60\%CH_4-40\%H_2)} \approx 882\,\text{sec}^{-1}$, and $F_{MB(60\%CH_4-40\%H_2)} \approx 1$. Therefore:

$$g_{RB} = g_B / g_{MB} = \frac{750}{882} = 0.8503.$$

$$F_{RB} = 1 + \phi_B(F_B - F_{MB}) = 1 + 0.784(1.0722 - 1) = 1.0566\ .$$

Since this point lies in the flashback region, this approach indicates that gas mixture B is not interchangeable with gas A (i.e., it will be prone to flashback. Again, although this approach was developed for laminar conditions, it could be possible to expand it to turbulent flow. But generally, it is designed for systems without controls, which may limit its applicability to advanced power generation systems that typically include controls to maintain power output or certain temperatures within the system.

B.2.2.4 Combustion Induced Vortex Breakdown (CIVB) Flashback

For swirling flames, the presence of the flame can alter the vortex breakdown behavior, which can lead to flashback. This work has been summarized in a number of works from Sattelmayer's research group at the Technical University of Munich (Kroner et al. 2003; Fritz et al. 2004; Kiesewetter et al. 2007; Konle and Sattelmayer 2010). That group has proposed several correlations that can be used to estimate the onset of combustion induced vortex breakdown. In this case, the relative mass and thermal diffusivity which are strong properties of the fuel can play a role in whether CIVB flashback occurs. This causes some additional design considerations to be required when considering fuel flexibility. Figure B-13 illustrates the concept of CIVB, where the system on the left represents the normal desired state of the reaction. In the right figure, the reacting recirculation region interacts with the mixture approaching it, causing a change in the stabilizing location of the reaction and allowing it to propagate upstream into the mixing tube.

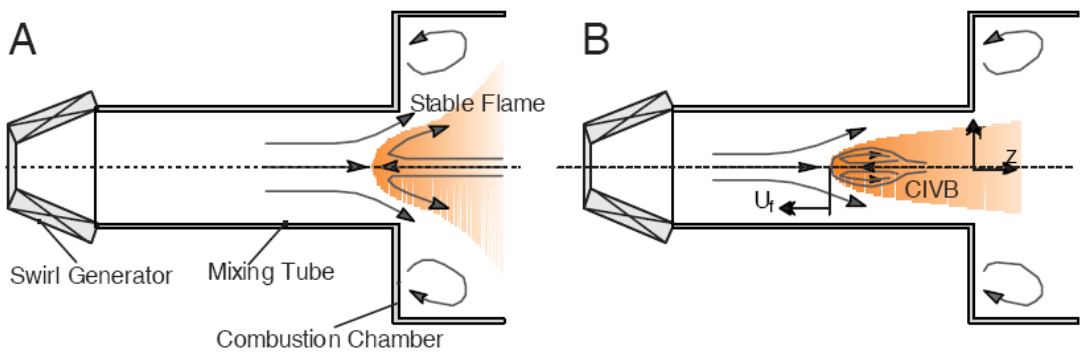

Source: Lieuwen et al. 2008.

Figure B-13: Conceptual Representation of CIVB.

The CIVB mechanism in flashback can be physically described as ability of the premixer zone to quench the combustion-induced bubble with negative axial velocity. If the conditions in the premixer zone are stable enough to quench the bubble and prevent it from entering the premixer zone, flashback does not occur; otherwise final flashback will take place and the bubble will enter the premixer zone and damage the hardware. A variable introduced to predict flashback is shown in Equation B-22:

$$C_{quench} = \frac{\tau_{chem}}{\tau_{res}}$$ **Equation B-22**

which upon inspection can be related to a Damköhler number (Equation B-23):

$$C_{quench} = \frac{1}{Da}$$ **Equation B-23**

As with blowoff, the strategy for determining τ_{chem} must be established. In the work of Sattelmayer, the use of a perfectly-stirred reactor (PSR) simulation was adopted, rather than $\tau_{chem} = \alpha / S_L^{\ 2}$. The rationale is that a PSR approach may capture the physics of the behavior near extinction, whereas $\tau_{chem} = \alpha / S_L^{\ 2}$ is more appropriate for complete reactions. Next, the

parameter in Equation B-24 is suggested as a promising parameter if it can be assumed that conditions at flashback will have a constant value of C^*_{quench} .

$$C^*_{quench} = Le_F \times C_{quench} = Le_F \times \tau_{PSR} \times \frac{\bar{u}}{d}$$ **Equation B-24**

The other parameters are:

$\bar{u}$ is the reference velocity.

d is the length reference.

$Le_F = \frac{a_m}{D_{Fm}}$ is the fuel Lewis number (ratio of the thermal-to-mass diffusion).

It is apparent that including Le_F in the correlation could, in principle, capture the impact of fuel composition. As a result, C_{quench} and C^*_{quench} can be calculated and used to assess flashback propensity via the CIVB mechanism. τ_{PSR} is calculated for the measured equivalence ratio at blowoff, and $\bar{u}$ and d are calculated based on air flow rates and dimensions of the particular burner configuration.

This general approach for estimating CIVB is evaluated for the high-swirl burner validation test bed, as described in Section 4.2.6.

B.2.2.5 Combustion Dynamics

In addition to the mechanisms above, if a system possesses combustion instability, it is possible that the pressure field within the system can couple with local variation in the fuel-to-air ratio and lead to a situation where the flow can essentially move up into the premixer under another mechanism. The challenge relative to the influence of fuel composition is that changing the fuel composition can influence the location of the heat release, which can then potentially couple with the acoustic field.

B.2.2.6 Comments on Flame Speed

As shown in a number of the equations above (e.g., Equation B-6, Equation B-7, Equation B-14, Equation B-15, Equation B-16, etc.) flame speed appears in many expressions. This warrants some discussion regarding flame speed. In many of the early parameter developments, the laminar flame speed is used. Often, the cases under consideration were, in fact, laminar. The laminar flame speed is an intrinsic property of the fuel/air mixture and the conditions of interest (i.e., mixture temperature and pressure). In these cases, laminar flame speeds could be available through tabulated data. However, the vast majority of these data are for stoichiometric conditions and for nominally room temperature mixtures at 1 atm. Data for mixtures of fuel components or for elevated temperature and pressure conditions are far more sparse and are generally beginning to appear in the literature only in the last decade (e.g., Natrajan 2005; Hu 2009). As a result, for concepts such as Shuster Index, it stands to reason that more complete and improved data on laminar flame speeds may now be available.

However, the more challenging issue facing the current applications is that the large majority of them are *turbulent*. Conceptually, turbulence enhances mixing, and thus the turbulent burning rate can far exceed the laminar rate. Hence applying laminar flame speeds to turbulent situations can be problematic. Considerable work in the literature has examined the relationship between turbulent and laminar flame speeds. Appendix E provides details regarding this subject. At first look, a rationale for using the laminar flame speed is apparent in that many researchers have proposed a form for the turbulent flame speed based on the laminar flame speed and the level of turbulence in the flow. Among the first equations developed for the calculation of turbulent flame speed was Equation B-25, developed theoretically by Damköhler (1950):

$$S_T = S_L + u' \qquad \textbf{Equation B-25}$$

where,

$$u' = fluctuating\ velocity\ component.$$

Other examples illustrate a similar form, such as Equation B-26 (Liue and Lenze 1992):

$$S_T = S_L + 5.3u'\sqrt{S_L} \qquad \textbf{Equation B-26}$$

and Equation B-27 (Bradley 1992):

$$\frac{S_T}{S_L} = 1.52\frac{u'}{S_L} \qquad \textbf{Equation B-27}$$

As will be explained in Appendix E, it is vital to consider the details of the nature of the flame speed considered. To this end, different definitions have been proposed to describe turbulent flame speed based on the different experimental methods used to measure it. Which definition best applies to flashback remains an open question, but conceptually, the local displacement rate is probably the best concept to use compared to the global consumption rate, which is derived from the most common types of measurements on Bunsen cone flames. To illustrate this, Figure B-14 presents measured turbulent flame speeds based on global consumption rates versus the local displacement rate (Kido et al. 2002). Both experiments shown were performed at atmospheric conditions (T = 298 K, P = 1 atm). As shown, major differences in the turbulent flame speed will result depending on which definition is used. The local displacement speed, $S_{T,LD}$, has been referenced often in turbulent flame speed discussions, yet available data may reflect the global consumption rate.

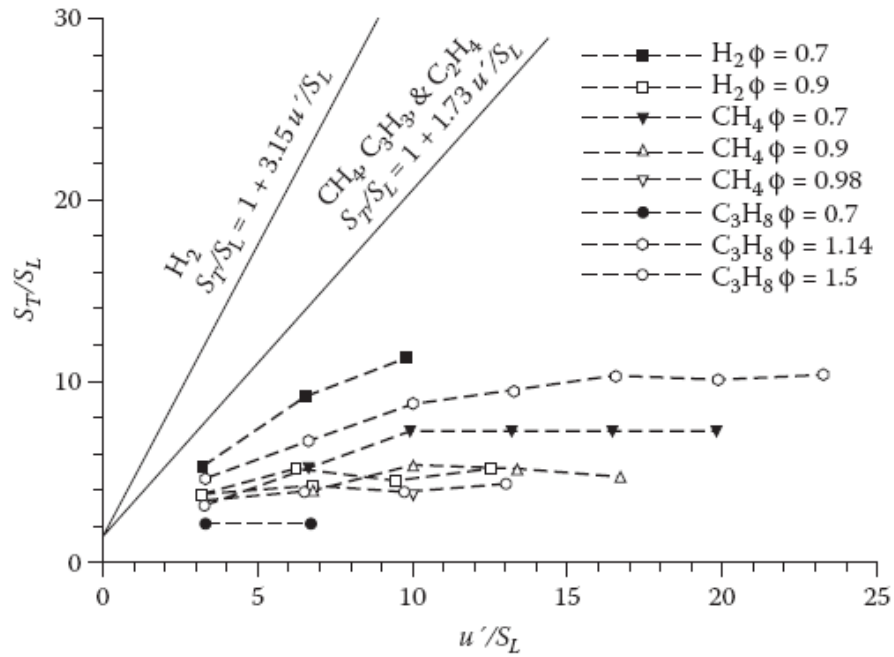

Source: Kido et al 2002; Cheng 2009.

Figure B-14: Kido et al. Data Collected Using Spark-Ignited Flame Kernel Shown Here with Symbols ($S_{T,GD}$). Correlations Obtained Using Low-Swirl Burner ($S_{T,LD}$) Are Shown as Solid Lines from Cheng.

In summary, flashback in practical systems is dependent upon turbulent flame speed, which in turn is fraught with challenges due to differences in definition and lack of validation data. For many practical burner configurations, those based on local displacement speed seem most appropriate, but even then discrepancy is evident and the role of pressure, temperature, and fuel mixtures is unclear (see Appendix E). Some general trends are: leaner conditions result in a slower S_T, higher hydrogen content causes an increase in S_T, increases in inlet bulk velocity lead to increased S_T, and the addition of diluents does not have a marked effect on S_T. Development of design tools for flashback (and blowoff) that are based on turbulent flame speeds remain works in progress. Data and analysis conducted for this project can help to progress these tools.

B.2.3 Autoignition

Like flashback, autoignition is primarily a concern for systems using some degree of premixing. It is particularly a concern for higher hydrocarbon and liquid fuels, such as lean premixed, pre-vaporized systems. For these lean premixed systems, it is apparent that a Damköhler expression exists (Equation B-28):

$$Da = \frac{\tau_{res}}{\tau_{ign}} \qquad \textbf{Equation B-28}$$

Equation B-28 describes the relative residence time to ignition time in the premixer. In this case, if *Da* approaches 1, the likelihood of ignition within the premixer increases. To apply this concept, all that is required is to determine the numerator and denominator. The numerator can be based on bulk parameters such as premixer volumes and volumetric flow rates. These can be ascertained from premixer geometry and flow rates. This may not capture any local separation

or boundary-layer effects. As a result, rather than a simple one-dimensional determination, something like CFD can be applied with "tracers" or a similar feature applied to generate a spectrum of possible fluid parcel residence times. In this case, it would be most conservative to use the longest residence time.

What remains then is to determine the ignition delay time. This can be determined in at least three ways which are becoming common.

B.2.3.1 Tabulated Values

Tabulated values for the spontaneous ignition temperature for many fuel/air mixtures are available in the literature. These include those from the Advisory Group for Aerospace Research and Development (AGARD) (Mullins 1955) and the U.S. Bureau of Mines (Zabetakis 1965). These values are also available from recent books (Glassman 1996). These tables include the temperature, and in some cases, the period of time at that temperature for which ignition occurred. Unfortunately, the delay time data are not comprehensive. As a result, these tables are difficult to use for general delay time.

B.2.3.2 Correlations

B.2.3.2.1 Natural Gas-Type Fuels

A comparison of selected autoignition delay time correlations for pure methane is shown in Figure B-15. Even for pure methane, the available correlations do not agree well.

Other Arrhenius-type expressions have been generated for use as design guides for numerous fuels. These are generally developed for ranges of fuel types based on measurements using different types of devices, such as flow reactors, shock tubes, or rapid compression machines. Spadaccini and Colket (1994) reviewed several shock tube experiments for methane. It is noted that shock tubes, while providing a highly repeatable and controlled environment, are best suited for high-temperature conditions. The correlation developed based on review of the literature is shown in Equation B-29:

$$\tau = 2.21 \times 10^{-14} \exp\left(\frac{22659}{T}\right) [O_2]^{-1.05} [CH_4]^{0.33}$$ **Equation B-29**

To address higher hydrocarbons, Spadaccinni and Colket proposed the correlation in Equation B-30 as a design tool. Note that the role of specific higher hydrocarbons is not explicitly indicated. Also, the temperatures for which this expression is valid are generally above 1,300 K.

$$\tau = 1.77 \times 10^{-14} \exp\left(\frac{18693}{T}\right) [O_2]^{-1.05} [CH_4]^{0.66} [\mathrm{HC}]^{-0.19}$$ **Equation B-30**

For lower-temperature regimes (most relevant to gas turbine premixers), correlations for autoignition delay time have been proposed by Cowell and Lefebvre (1986) and by Beerer et al. (2011) for the present project based on data from flow reactors. Cowell and Lefebvre concentrated on pure fuels; that is, methane and propane; while Beerer et al. looked at mixtures of methane, ethane, and propane.

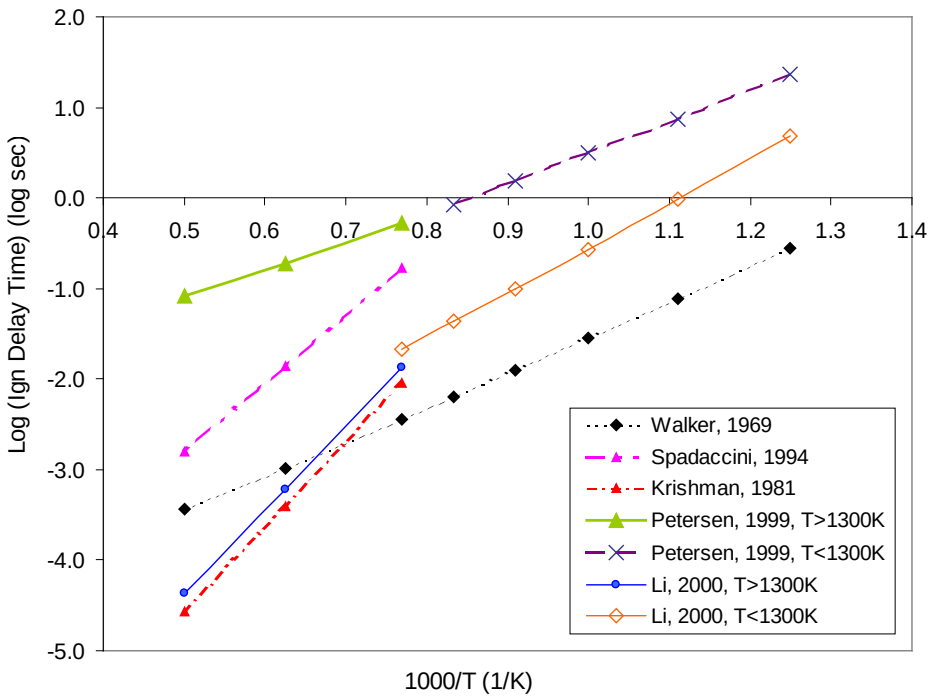

Figure B-15. Literature Autoignition Delay Time Correlations for Pure Methane (P = 1 atm, ϕ = 1.0)

The trend due to Equation B-30 is displayed as the solid line in Figure B-16. The dashed vertical lines in the figure represent the regions of typical gas turbine premixer and reheat burner inlet temperatures. Gas turbine premixer inlet temperatures are usually less than 900 K, which is on the far right of the plot. Inlet temperatures for reheat combustors are in between 900 and 1,300 K. As shown, the correlation presented in Equation B-30 does not capture the behavior in the lower temperature ranges. This is consistent with its recommended range of applicability for temperatures above 1,300 K.

Beyond correlations for ignition delay time, it may also be possible to correlate results using knock indices from automotive engines. Octane or cetane numbers are used to describe the relative resistance or relative ease with which gasoline or diesel fuels will autoignite. Conceptually this has been extended to gaseous fuels in the form of MN.

The MN is therefore somewhat related to the combustion properties of the fuel, such as reaction rate. It is analogous to the motor octane number (MON) defined for gasoline. While defined in the context of internal combustion engines for transportation, MN may also affect performance of power generation devices located in the same distribution region.

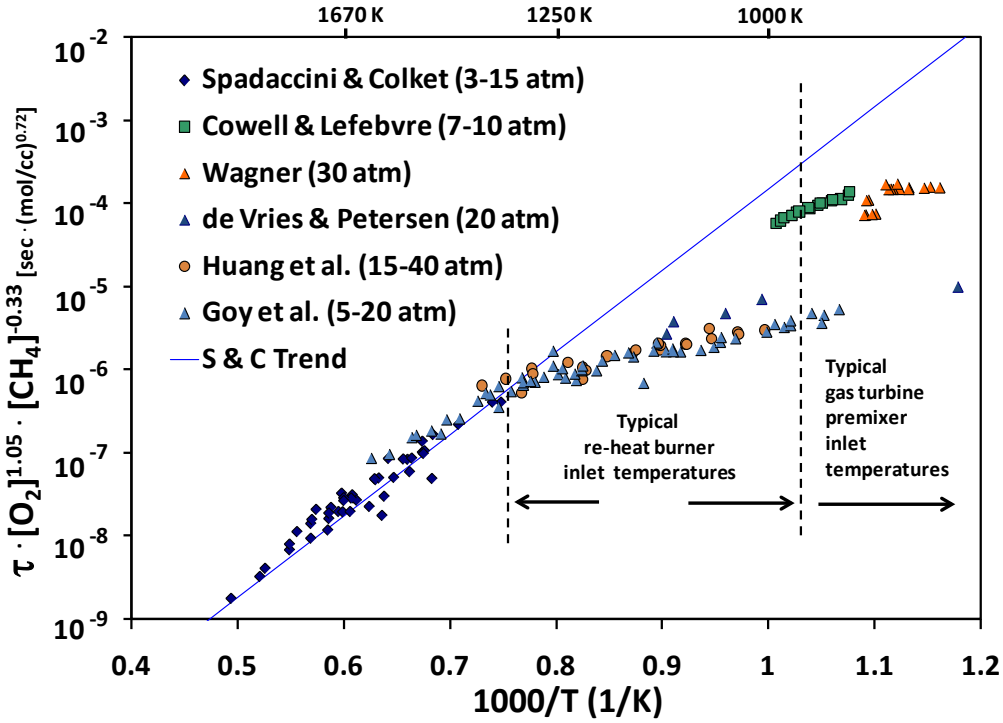

Source: Beerer et al. 2011.

Figure B-16: Ignition Delay Results of Methane/Air at Intermediate and High Temperature Conditions

The MON equivalent for natural gas is also related to the reactive hydrogen-to-carbon ratio $\left(\frac{H}{C}\right)$ of the fuel, as shown in Equation B-31:[7]

$$MON = -406.14 + 508.04\left(\frac{H}{C}\right) - 173.55\left(\frac{H}{C}\right)^2 + 20.17\left(\frac{H}{C}\right)^3$$

Equation B-31

Further, empirical correlations are available to relate MN to a MON "equivalent" of the gas as a measure of knock resistance according to Equation B-32:

$$MN = 1.624 * MON - 119.1$$

Equation B-32

Because knock (i.e., pre-ignition in an spark-ignited reciprocating engine) and ignition delay are likely related, it is possible that MN or MON can be used as an indicator of relative ignition times for alkane fuel mixtures.

B.2.3.2.2 Hydrogen-Containing Fuels

Significantly less work has been done for hydrogen-containing fuels compared to natural gas-type fuels. However, similar to the correlations produced for alkanes, some work has been

[7] California Air Resources Board. "Proposed Amendments to the California Alternative Fuels for Motor Vehicles Regulations." Appendix D.

done for hydrogen-containing fuels to produce design guides for ignition delay time. For the lean mixtures typically considered in the present low-emissions systems addressed by the present work, the expression in Equation B-33 from Peschke and Spadaccini (1985) is applicable (630–790 K; 12.5–23 atm; equivalence ratios from 0.3 to 0.6).

$$\tau(s) \cdot [O_2]^{0.50}[F]^{0.25} = 1.29 \times 10^{-7} \exp(\frac{3985}{T})$$ **Equation B-33**

B.2.3.2.3 Diluted Fuels

It is expected that some impact on ignition delay time may occur for fuels diluted with N_2 or CO_2, as might be found with landfill gas or gas from anaerobic digestion. Experimental results in the literature could provide a basis for a correlation. For example, Holton (2008) observed a 2 percent and 3 percent increase in ignition delay when he added 5 percent and 10 percent CO_2 to CH_4, respectively, at atmospheric pressures and inlet temperatures from 1,020 to 1,150 K.

B.2.3.3 Detailed Chemistry Calculations

Finally, with the advent of dramatically increased computational horsepower, numerical calculations with chemical kinetic software codes are feasible. The CHEMKIN code (Reaction Design, San Diego, California) can perform efficient calculations of combustion properties such as ignition delay times. General computational time for a calculation is on the order of seconds with a standard PC; therefore, large parameter studies can be performed in short periods of time. Several research groups have developed mechanisms that describe the chemistry, transport, and thermodynamics involved during ignition or any general combustion process. These mechanisms can be imported into software like CHEMKIN to perform the calculations. Open-source alternatives to CHEMKIN, such as Cantera, are also available and can be used to carry out the same calculations.

Because these comprehensive codes can be like a "black box," some experience is required to run them and get reliable results. Also, some, like CHEMKIN, can be quite expensive. As a result, some researchers with experience and access to these kinetics codes have applied them "as experiments" to produce simplified design guides that can then be used conveniently (e.g., in Excel).

B.2.3.3.1 Alkane-Type Fuels

One example of using detailed mechanisms to develop a correlation is provided in Chen et al. (2007). In this work, a statistically designed "experiment" was developed and detailed chemical kinetic simulations (in this case, Lawrence Livermore National Laboratory's "C5 Mechanism" (Ribacour et al. 2000) and solving for the delay time using CHEMKIN) carried out. Applying analysis of variance (ANOVA) to the calculated ignition delay times, a correlation for autoignition temperature prediction was obtained for higher hydrocarbons. The correlation is shown as Equation B-34.

$$
\begin{aligned}
T_{ign} = {} & \alpha_1 X_{CH_4} + \alpha_2 X_{C_2H_6} + \alpha_3 X_{C_3H_8} + \alpha_4 X_{CH_4} X_{C_2H_6} + \alpha_5 X_{CH_4} X_{C_3H_8} + \alpha_6 X_{CH_4} P + \alpha_7 X_{CH_4} \phi \\
& + \alpha_8 X_{C_2H_6} X_{C_3H_8} + \alpha_9 X_{C_2H_6} P + \alpha_{10} X_{C_2H_6} \phi + \alpha_{11} X_{C_3H_8} P + \alpha_{12} X_{C_3H_8} \phi + \alpha_{13} X_{CH_4} P^2 \\
& + \alpha_{14} X_{CH_4} \phi^2 + \alpha_{15} X_{C_2H_6} P^2 + \alpha_{16} X_{C_2H_6} \phi^2 + \alpha_{17} X_{C_3H_8} P^2 + \alpha_{18} X_{C_3H_8} \phi^2 + \alpha_{19} X_{CH_4} X_{C_2H_6} P \\
& + \alpha_{20} X_{CH_4} X_{C_2H_6} \phi + \alpha_{21} X_{CH_4} X_{C_3H_8} P + \alpha_{22} X_{CH_4} X_{C_3H_8} \phi + \alpha_{23} X_{CH_4} P\phi + \alpha_{24} X_{C_2H_6} X_{C_3H_8} P \\
& + \alpha_{25} X_{C_2H_6} X_{C_3H_8} \phi + \alpha_{26} X_{C_2H_6} P\phi + +\alpha_{27} X_{C_3H_8} P\phi + \alpha_{28} X_{CH_4} X_{C_2H_6} P^2 + \alpha_{29} X_{CH_4} X_{C_2H_6} \phi^2 \\
& + \alpha_{30} X_{CH_4} X_{C_3H_8} P^2 + \alpha_{31} X_{CH_4} X_{C_3H_8} \phi^2 + \alpha_{32} X_{C_2H_6} X_{C_3H_8} P^2 + \alpha_{33} X_{C_2H_6} X_{C_3H_8} \phi^2 \\
& + \alpha_{34} X_{CH_4} X_{C_2H_6} P\phi + \alpha_{35} X_{CH_4} X_{C_3H_8} P\phi + \alpha_{36} X_{C_2H_6} X_{C_3H_8} P\phi
\end{aligned}
$$

Equation B-34

Where,

T_{ign} - Autoignition Temperature, K

X_{CH_4} - Volumetric fraction of CH_4 in natural gas (0.80–1.00)

$X_{C_2H_6}$ - Volumetric fraction of C_2H_6 in natural gas (0.00–0.20)

$X_{C_3H_8}$ - Volumetric fraction of C_3H_8 in natural gas (0.00–0.20)

P - Pressure, atm

ϕ - Equivalence ratio

$\alpha_1, \cdots, \alpha_{36}$ - Effect coefficients

The effect coefficients of Equation B-34 were obtained using ANOVA, which generated a response surface to curve-fit the data simulated by the chemical kinetics modeling. These coefficients are listed in Equation B-35.

$$
\begin{array}{llll}
\alpha_1 = 8.04\times10^2; & \alpha_2 = -5.75\times10^2; & \alpha_3 = 5.46\times10^3; & \alpha_4 = 1.55\times10^3; \\
\alpha_5 = -4.99\times10^3; & \alpha_6 = -12.09; & \alpha_7 = -67.74; & \alpha_8 = -4.07\times10^3; \\
\alpha_9 = 3.49; & \alpha_{10} = 4.63\times10^3; & \alpha_{11} = 5.76\times10^2; & \alpha_{12} = -1.82\times10^4; \\
\alpha_{13} = 0.45; & \alpha_{14} = 27.70; & \alpha_{15} = -0.09; & \alpha_{16} = -3.15\times10^3; \\
\alpha_{17} = -33.58; & \alpha_{18} = 1.48\times10^4; & \alpha_{19} = -14.37; & \alpha_{20} = -5.31\times10^3; \\
\alpha_{21} = -8.80\times10^2; & \alpha_{22} = 1.94\times10^4; & \alpha_{23} = 0.02; & \alpha_{24} = -7.35\times10^2; \\
\alpha_{25} = 1.68\times10^4; & \alpha_{26} = -22.12; & \alpha_{27} = 2.52\times10^2; & \alpha_{28} = 0.39; \\
\alpha_{29} = 3.58\times10^3; & \alpha_{30} = 48.18; & \alpha_{31} = -1.59\times10^4; & \alpha_{32} = 44.52; \\
\alpha_{33} = -1.37\times10^4; & \alpha_{34} = 29.76; & \alpha_{35} = -2.78\times10^2; & \alpha_{36} = -3.60\times10^2.
\end{array}
$$

Equation B-35

Conceptually, Equation B-34 and Equation B-35 can be used to estimate ignition delay times for a range of alkane fuel mixtures over a range of conditions.

B.2.3.3.2 Diluted Fuels

Little information is available regarding the role of diluents on the impact on ignition delay time of gaseous fuels. However, it is reasonable to apply comprehensive kinetic calculations for such cases to understand the effect of diluents on autoignition.

B.2.3.3.3 Hydrogen/Carbon Monoxide Fuels

An approach similar to that presented in Section B.2.3.3.1 has also been presented for hydrogen/carbon monoxide fuel mixtures (Donato and Petersen 2008). In this work, rather than a polynomial expression such as those shown in Equation B-34 and Equation B-35, an Arrhenius-type expression (Equation B-36) was used.

$$\ln(\tau_{ign}) = \ln A + x\ln X_{H2} + y\ln(\varphi) + z\ln(P) + \frac{E}{RT}$$ **Equation B-36**

Where

X_{H2} is the hydrogen mole fraction
φ is the fuel-air equivalence ratio by mass
P is the system pressure
E, A, x, y, and z are constants

Because of the known "S" shape ignition delay behavior for hydrogen, the concept of a transition temperature is introduced in order to create a piecewise expression and to classify sets of coefficients for different parts of the ignition delay versus log T curve.

One of the possible issues with use of calculated ignition times using CHEMKIN or other kinetics packages are that they use an underlying assumption of homogeneous ignitions. With hydrogen, ignition is not homogeneous at low temperatures and lean conditions. However, in flowing mixtures of hydrogen and air, ignition can occur in a "spot-wise" manner which, if considered "Autoignition" can lead to ignition delay times that are considerably shorter than those predicted. To illustrate this, Figure B-17 presents comparisons of calculated and measured delay times for syngas/air mixtures. Of interest is the significant differences between the full kinetic estimate of ignition delay time with that from correlations which have been observed in other measurements (e.g., Petersen et al. 2007a). This observation has led to considerable effort to explain the reasons (e.g., Chaos et al. 2010) and also to illustrate that hydrogen, in particular, can develop inhomogeneity in the early ignition time. Hence the influence of hydrodynamic effects may be important in these systems. In spite of these discrepancies, both the model and correlations suggest that ignition delay times are on the order of tens to hundreds of milliseconds (for hydrogen) and hundreds to thousands of milliseconds (for alkanes) at conditions relevant to a gas turbine.

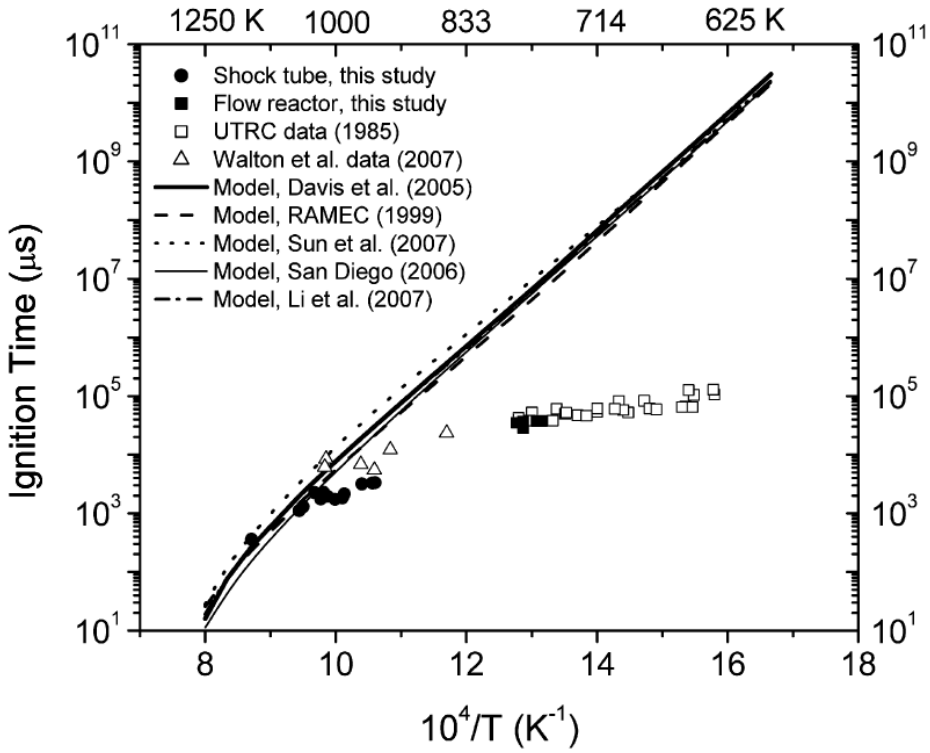

Source: Petersen et al. 2007a.

Figure B-17: Calculated and Measured Ignition Delay Times for Hydrogen/Air Mixtures

B.2.3.4 Summary of Autoignition Predictions

As shown above, despite the apparent simplicity of predicting autoignition, the agreement between simple correlations, as well as detailed kinetics modeling and experimental results, exhibit strong disagreement. A key factor contributing to this disagreement is the validity of assumptions used. For lean premixed combustion systems, generally high-pressure, low-temperature regimes are of interest. Generally speaking, the data to date do not cover this regime. Further, this regime has features which invalidate many of the assumptions required, such as homogeneous behavior. As a result, additional data are needed to capture the behavior in the range of interest. This has been accomplished as part of this project and is discussed in Section 4.1.

B.2.4 Emissions

Unburned hydrocarbon (UHC), CO, and NOx emissions are a function of the combustion conditions. In many state-of-the-art systems, however, the goal is to achieve very-well-mixed fuel/air, and thus the global basis can be a realistic approximation of the local behavior.

To this end, strategies to predict how fuel composition affects emissions have been developed and applied for combustion systems. For gaseous-fueled systems, the primary pollutants of interest are oxides of nitrogen, carbon monoxide, and unburned hydrocarbons. These are reviewed here.

B.2.4.1 Oxides of Nitrogen (NOx)

Oxides of nitrogen are pollutants emitted from all combustion processes, and are integral to the formation of photochemical oxidant, or smog, in metropolitan areas. The oxides of nitrogen, combined under the common heading *NO_x*, include nitric oxide (NO) and nitrogen dioxide (NO_2). In combustion devices, NO_x can be produced from atomic nitrogen contained in the fuel or from nitrogen present in the oxidizing agent. Fuel-bound nitrogen is normally a concern with solid and liquid fuels. In most combustion exhaust samples NO is the main contribution to the NO_x effluent (Correa 1992). The three primary mechanisms for NO emissions are summarized in the following sections.

B.2.4.1.1 The Zeldovich Mechanism

The first mechanism is called the *Zeldovich*, or *Thermal* mechanism. This mechanism typically becomes significant at temperatures above approximately 1,800 K. The Thermal mechanism consists of two reactions involving radical combustion species (Equations B-37 and B-38).

$$O + N_2 \leftrightarrow NO + N \qquad \textbf{Equation B-37}$$

$$N + O_2 \leftrightarrow NO + O \qquad \textbf{Equation B-38}$$

The reaction in Equation B-37 is relatively slow. Its large activation energy of 319,050 kilojoules per kilomole (kJ/kmol) leads to the strong temperature dependence characteristic of the mechanism (Turns 2012). Once the atomic nitrogen radical is formed, it immediately reacts with molecular oxygen to form another NO molecule in the reaction shown in Equation B-38. Therefore, two NO molecules are created for each oxygen molecule that is dissociated in the high-temperature environment. The mechanism can also be modified to include the reaction shown in Equation B-39.

$$N + OH \leftrightarrow NO + H \qquad \textbf{Equation B-39}$$

In which case, it is referred to as the *extended Zeldovich mechanism.* The kinetics of the Zeldovich mechanism often take place over a long residence time. Under traditional conditions the post-combustion gases remain at temperatures that allow NO to be formed by this route until the temperature is decreased by dilution jets or expansion in the turbine. Once formed, NO is said to be in a state of frozen equilibrium. After NO is formed in the reaction zone, reverse reactions *that lead to its destruction are inactive, due to slow reaction rates brought on by the decrease in temperature* (De Nevers 2000).

Evidence has shown that NO_x produced from this mechanism is proportional to pressure (Lefebvre 1983). NO_x emissions were seen to increase with pressure at equivalence ratios above 0.70 for natural gas flames. However, under 0.70, pressure did not have an effect on the NO_x levels; indicating that only the Thermal mechanism is dependent on pressure.

To mitigate NO_x produced from the Thermal mechanism, lean premixed combustion has developed as a suitable strategy. Figure 1 illustrates the effect of reducing the equivalence ratio to lower the flame temperature below the active range of NO production. In the case of hydrogen, a larger window of operation is available where lower reaction temperatures can be maintained before the occurrence of lean blow out (Therkelsen et al. 2009).

Improved mixing is also a recognized method for restricting peak reaction temperatures. A more completely mixed fuel-air mixture will have fewer rich pockets and thus fewer areas of locally high temperatures that will produce high NO levels. Thus enhanced premixing and lean burning has recently been the prominent strategy for direct mitigation of NO_x emissions formed in gas turbine combustors.

B.2.4.1.2 The Fenimore ("Prompt NO_X") Mechanism

It has been determined that under some conditions, NO can be found very early in the flame region. Forming very early in the combustion process, even before Thermal NO_X can form, "Prompt NO_X" (sometimes called "Fenimore NO_X," after the work performed by Fenimore (1970) is believed to be the result of radical concentrations that may significantly exceed equilibrium values. It is generally accepted that the mechanism for Prompt NO_X is initiated by the reaction in Equation B-40:

$$N_2 + CH \Rightarrow HCN + N \qquad \textbf{Equation B-40}$$

The remainder of the Prompt NO_X mechanism revolves around the oxidation of the N and HCN molecules. In the case of lean-premixed combustion, the path followed by HCN to NO is centered on a sequence of steps approximated by HCN → CN → NCO → NO. The oxidation of the N-atom is the same one described as being the third reaction in the Zeldovich mechanism listed above.

Currently, interest is increasing with regard to the amount of Prompt NO_X produced in combustion applications and finding methods to reduce its emissions levels. In the past, Prompt NO_X played only a relatively small role in the amount of overall NO_X produced from a typical combustion application, especially when compared to the emissions of Thermal NO_X. However, as combustion systems have continued to become cleaner, more efficient, and more complex—typically by focusing on the emissions of Thermal NO_X—the overall percentage of NO_X produced via the Prompt NO_X pathway has continued to rise.

The key reaction step in the formation of Prompt NO_X has been found to have activation energy in the range of ≈14 to ≈22 kcal/mol; relatively low compared to the ≈76 kcal/mol activation energy of the thermal mechanism. As a result, the rate of the Prompt NO_X mechanism does not fall as quickly with temperature as the thermal rate does, leaving the Prompt NO_X mechanism to continue to function at temperatures below 1,800 K. However, modeling work conducted indicates that the CH radical has a lifetime on the order of 0.1 millisecond (ms) in lean premixed combustion. The short lifetime of the CH radical and chemical reactor modeling indicate that Prompt NO_X is not a major source of NO_X in lean premixed combustion, unless the fuel-air ratio is greater than about 0.65, or the residence time of the combustion reactor is very short.

B.2.4.1.3 The N_2O Intermediate Mechanism

The N_2O Intermediate mechanism is important in lean premixed combustion. This mechanism is summarized by reactions shown in Equation B-41 through Equation B-43. The pressure influence on NO formed from this mechanism is seen in Equation B-41 with "M" representing a chemically unchanged third body species. As pressure increases, Equation B-41 is driven to the

right, forming more intermediate N_2O, which then forms NO via Equation B-42 and Equation B-43.

$$O + N_2 + M \leftrightarrow N_2O + M \quad \textbf{Equation B-41}$$

$$N_2O + H \leftrightarrow NO + NH \quad \textbf{Equation B-42}$$

$$O + N_2O \leftrightarrow NO + NO \quad \textbf{Equation B-43}$$

B.2.4.1.4 Nitrogen-Nitrogen-Hydrogen (NNH) Pathway

Bozzelli and Dean (1995) proposed a new chemical pathway of NO production through the NNH radical. The mechanism by which NO is formed is shown in Equation B-44 and Equation B-45. The NNH radical formed from molecular nitrogen is oxidized in Equation B-45 to form NO. According to Konnov et al. (2001), the NNH mechanism is important at all temperatures for residence times less than ~1 ms. Moreover, for lean hydrogen flames it was found that the contribution of this mechanism was important at temperatures up to ~1,900 K for all residence times.

$$N_2 + H \leftrightarrow NNH \quad \textbf{Equation B-44}$$

$$NNH + O \leftrightarrow NO + NH \quad \textbf{Equation B-45}$$

B.2.4.1.5 NO_2 Formation Chemistry

The use of hydrogen and its extensive lean flammability limit leads to the possibility of fairly low flame temperatures. Lower flame temperatures favor the production of NO_2. Thus NO_2 becomes a major contributor to overall NO_x emission for lean hydrogen flames. As such, its reaction chemistry is also included. NO_2 is formed from NO, as shown in Equation B-46. Equation The elementary reactions that are responsible for the destruction of NO_2 are fairly active at higher temperatures; thus NO becomes the main constituent of NO_x at higher flame temperatures (Turns 2012).

$$NO + HO_2 \leftrightarrow NO_2 + OH \quad \textbf{Equation B-46}$$

B3.2.4.1.6 NOx Prediction

NOx predictions using correlations have been done in the past. Examples can be found in Lefebvre and Ballal (2010). These generally take the form of a polynominal expression. An example that is germane to the current scope (lean premixed systems) is provided in Equation B-47 (Lewis 1991). This expression indicates that residence time does not play a significant role in NOx emissions, but rather temperature and pressure do.

$$NOx = 3.32\ x\ 10^{-6}\ \exp(0.008T_c)\ P^{0.5} \quad \textbf{Equation B-47}$$

Such correlations can provide guidance on how operation conditions affect emissions, however, it is evident that no direct connection to fuel composition is evident. Hence such expressions are not helpful in assessing the relative emissions behavior as fuel composition varies.

Related to such correlations are the notional "entitlement" plots, which provide an indication of the minimum NOx that can be expected for a given reaction temperature. An example is shown in Figure B-18. This plot is helpful in that it can be used to assess the relative emissions

performance for a given system at a given reaction temperature. Again, however, it does not imply how fuel composition impacts the expected emissions. There are other challenges with this approach as well, as discussed further in Section 5.3

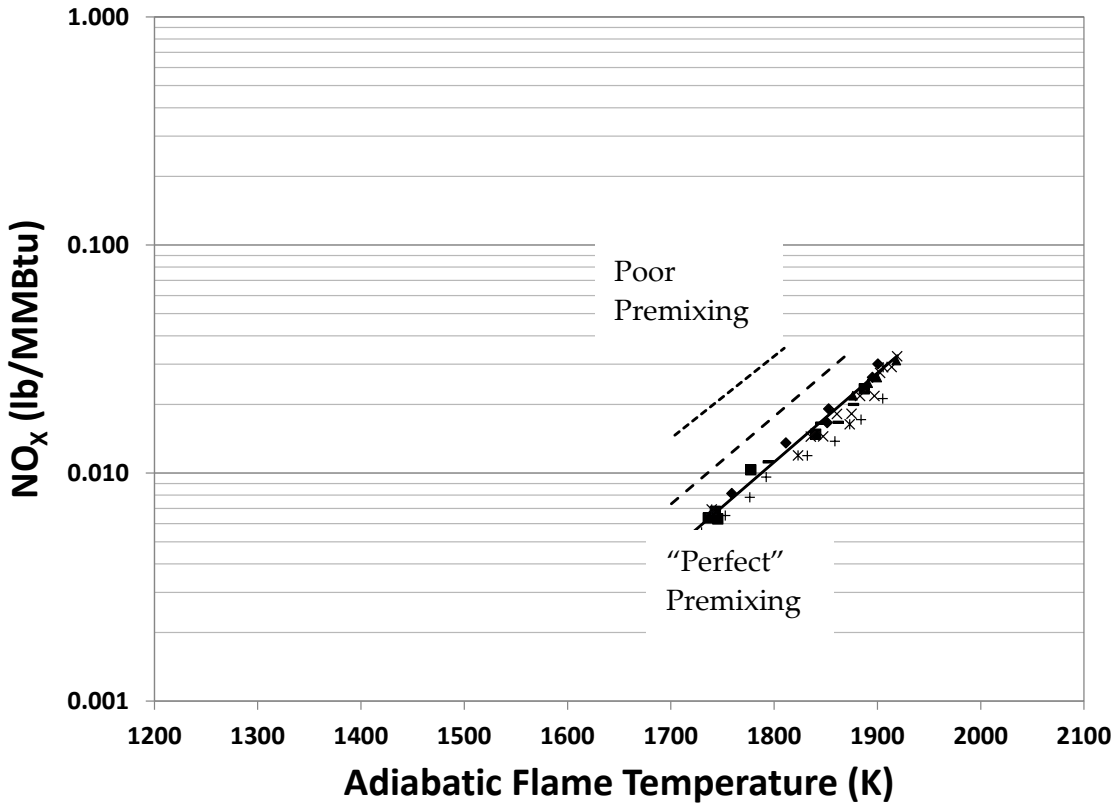

Source: Adapted from Leonard and Stegmaier 1994.

Figure B-18: NOx "Entitlement" Levels for Lean Premixed Natural Gas Combustion

Some research has suggested that the C/H ratio can be used as an estimate of NOx performance for lean premixed systems. An example is given Figure B-19, which shows a strong correlation between C/H ratio and NOx for a wide variety of hydrocarbon fuels operated in lean premixed combustion systems for a fixed firing rate. Two different residence times are shown, indicated by Long and Short SPP. While some scatter is evident, it seems that C/H ratio may be an attractive candidate to account for fuel composition variation.

Because Wobbe Index also scales with C/H ratio, it is not surprising to also find a relationship between NOx emission and Wobbe Index. However, as the fuel moves into the high hydrogen space, this correlation may not hold. Regardless, correlation of NOx with Wobbe Index or C/H ratio appears to hold some promise. Of course, this is likely to not hold for high-hydrogen-content fuels.

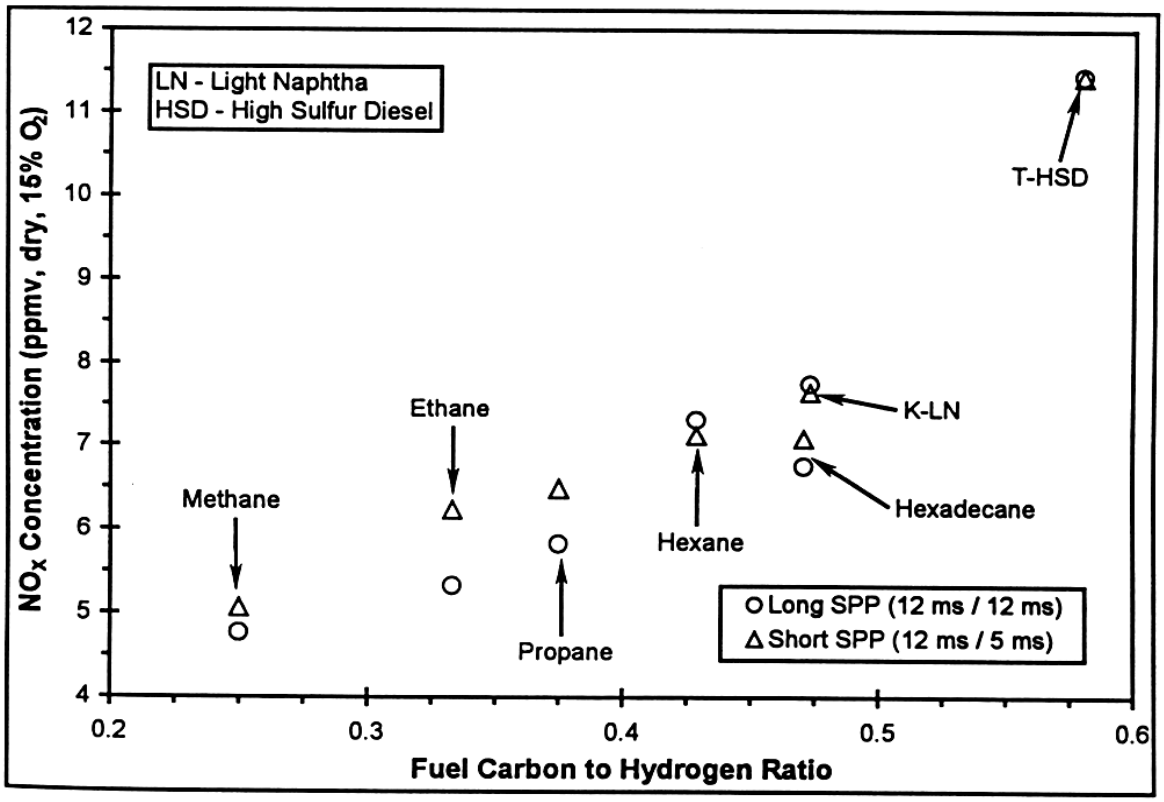

Source: Lee 2000.
T-HSD: Texaco High Sulfur Diesel; K-LN: Kern Light Naptha; SPP: Staged Prevaporizer-Premixer

Figure B-19: Relation between Fuel C/H Ratio and NOx Emissions for a Fixed Firing Temperature of 1,789 K

Beyond simple one-dimensional correlations shown above, higher-order approaches that can be considered include using computational fluid dynamics (CFD) to predict the full combustion system, including the pollutant emissions. However, due to the complex interaction between chemistry and turbulence in practical systems, the ability to use chemistry mechanisms that are large enough to capture subtle fuel composition effects may be limited.

Alternately, using CFD in conjunction with a chemical reactor network may be another approach that allows the sophistication of complex chemistry to be applied but in a one- or two-dimensional representation of the combustion system. In this approach, CFD is used with simple combustion chemistry to elucidate the details of the reaction behavior and location. Alternatively, an image of the reaction could be used. This information is used to develop a reactor network that can then be used to estimate how fuel composition impacts emissions. Figure B-20 illustrates this approach taken for a jet-stirred reactor.

The extension of this approach in general is an open question. It could be that most combustors/burners have a flame stabilization core that can be characterized somehow. In the example in Figure B-20 it is the main recirculation loop. In the low-swirl burner, it is the primary flame zone. All of these could be reduced first order to a Bragg Cell-type configuration

(Bragg 1953), which, with some information on post-flame time temperature history might be a first-order approach to NOx interchangeability. This needs to be evaluated.

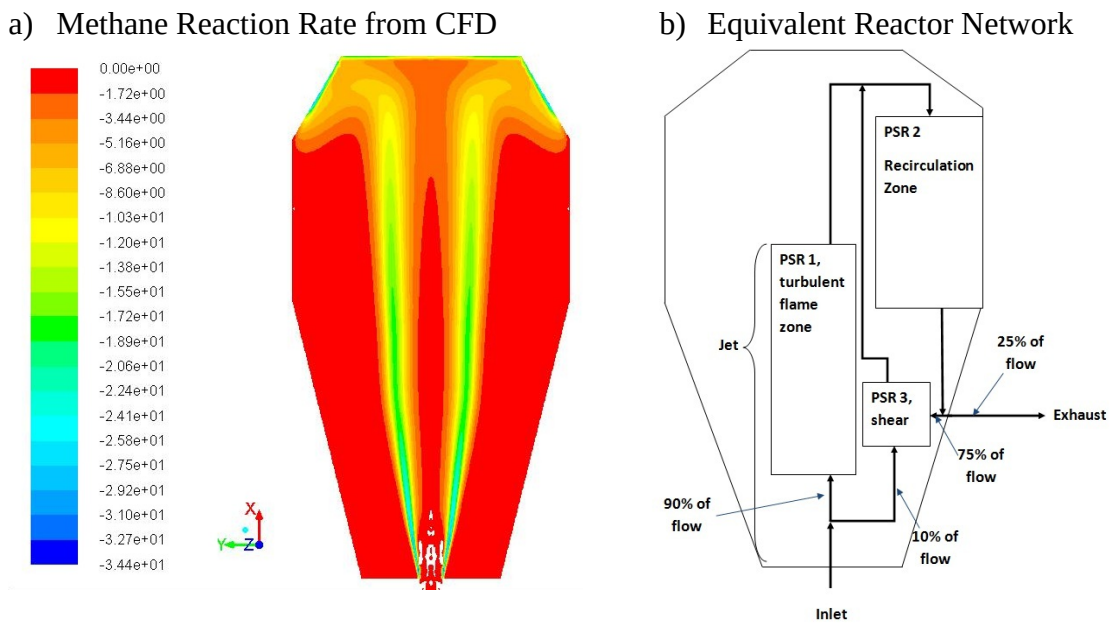

Figure B-20: Example of a Combustion System Divided into Several Chemical Reactors

B.2.4.2 Carbon Monoxide (CO)

In hydrogen fuel systems, carbon monoxide (CO) is, in principle, not an issue. However in any fuel where carbon is present, CO can be emitted. Carbon monoxide in lean premixed systems is due to two sources. The primary source is related to the termination of the overall fuel oxidation process. For example, methane oxidizes to CO_2 and water, but CO is an intermediate species in the process. Interestingly, the oxidation of methane to CO is relative fast compared to the subsequent oxidation of CO to CO_2. As a result, if combustion temperatures fall below 1,500 K, the CO to CO_2 oxidation step can be cut short, resulting in CO emissions. The second source of CO is associated with dissociation of CO_2 back into CO in the presence of oxygen. This occurs at high temperatures, generally at levels that are high enough to promote NOx emission. Hence, the key to minimizing CO emissions is to keep the temperature low enough to minimize NOx emission, but at the same time high enough to complete CO oxidation. The other implication is that sufficient oxygen is available and sufficient mixing with CO occurs. Finally, since the CO oxidation process can be slow, long residence times at these temperatures are needed.

B.2.4.2.1 CO Prediction

Examples of CO emission predictions can be found in the literature, but not nearly as widely as those for NOx. An example is shown in Equation B-48 (Lefebvre 1983).

$$CO = \frac{86\,\dot{m}_A T_{PZ} e^{-0.00345\cdot Tpz\cdot t}}{\left[V_c - 0.55\,\frac{f_{pz}\,\dot{m}_A\,D_o^2}{\rho_{pz}\,\lambda_{eff}}\right]\left[\frac{\Delta P_L}{P_3}\right]^{0.6} P_3^{1.5}}$$

Equation B-48

where

D_o	=	drop size (not relevant for gaseous fuels)
f_{pz}	=	fraction of total burner flow involved in combustion
m_A	=	combustor air mass flow
T_{PZ}	=	primary zone temperature
Δ_{PL}	=	liner pressure drop
V_c	=	combustion zone volume
ρ_{pz}	=	primary zone density
λ_{eff}	=	effective evaporation constant
P_3	=	reaction absolute pressure
t	=	time

Similar to NOx, CO can also be predicted using a chemical reactor network approach, as discussed above.

B.2.4.3 Unburned Fuel

When operating on a hydrocarbon fuel, UHCs can be emitted as a result of inefficient combustion that precludes the initial oxidation of the fuel into intermediate species such as CO. In hydrogen-fueled systems, it is possible for unburned hydrogen to be emitted, but the high reactivity of hydrogen helps to prevent this. In lean systems under consideration herein, UHCs can be manifested as methane species and non-methane species. Methane itself is an important climate change gas, due to its long lifetime. Predicting its emission is similar to that for CO. Non-methane hydrocarbon (NMHC) emission is considerably more difficult to predict, as complex chemistry is associated with the production and consumption of intermediate NMHC species. In lean systems, for example, evidence of aldehyde emissions has been observed. Prediction of the conditions and how fuel composition affect this takes considerable effort, and little existing work is available that seeks to do this in a simple fashion.

B.2.4.3.1 UHC Prediction

Due to the complexities of the NMHC emissions, the chemical reactor network (CRN) method may be the only real approach to consider for estimating speciation of UHC. In that case, the quality of the chemistry mechanism is the key to achieving correct results. Considerable validation would be needed, and generally the measurement of the NMHC is complex in its own right.

References

American Gas Association. 1946. *Research Bulletin #36: Interchangeablity of Other Fuels with Natural Gas.* AGA.

Ballal, D., and A. Lefebvre. 1979. "Weak Extinction Limits of Turbulent Flowing Mixtures." *Journal of Engineering for Gas Turbines and Power* 101: 343.

Beerer, D., V. McDonell, and S. A. L. Samuelsen. 2011. "An Experimental Ignition Delay Study of Alkane Mixtures in Turbulent Flows at Elevated Pressures and Intermediate Temperatures." *Journal of Engineering for Gas Turbines and Power* 133: 011502-1–011502-11.

Bozzelli, J., and A. Dean. 1995. O + NNH: A Possible New Route for NOx Formation in Flames. *International Journal of Chemical Kinetics* 27: 1090–1109.

Bradley, D. 1992. "How Fast Can We Burn?" *24th Symposium (International) on Combustion.* 24(1): 247–262.

Bragg, S. 1953. "Application of Reaction Rate Theory to Combustion Chamber Analysis." Aeronautical Research Council Publication, London.

Calcote, H. F., J. Gregory, C. Barnett, and R. Gilmer. 1952. "Spark Ignition Effect of Molecular Structure." *Industrial Engineering Chemistry* 44: 2656–2662.

Chaos, M., M. Burke, J. Ju, and F. Dryer. 2010. "Syngas Chemical Kinetics and Reaction Mechanisms." In: T. Lieuwen, V. Yang, and R. Yetter, eds. *Synthesis Gas Combustion: Fundamentals and Applications.* Boca Raton: CRC Press. 29–70.

Chaudhuri, S., S. Kosta, M. Renfro, and B. M. Cetegen. 2010. "Blowoff Dynamics of Bluff Body Stabilized Turbulent Premixed Flames." *Combustion and Flame* 157: 790–802.

Cheng, R. 2009. "Turbulent Combustion Properties of Premixed Syngas." In: T. Lieuwen, V. Yang, and R. Yetter, eds. *Synthesis Gas Combustion: Fundamentals and Applications.* Boca Raton: CRC Press. 129–168.

Chen, J., V. G. McDonell, and G. S. Samuelsen. 2007. "Autoignition Correlations for Pipeline Natural Gas and Low and Intermediate Temperatures." *AIAA Journal of Propulsion and Power* 23(3): 585–592.

Correa, S. 1992. "A Review of NOx Formation Under Gas Turbine Combustion Conditions." *Combustion Science and Technology* 87: 329–362.

Cowell, L., and A. Lefebvre. 1986. *Influence of Pressure on Autoignition Characteristics of Gaseous Hydrocarbon-Air Mixtures.* SAE.

Damköhler, G. 1950. "Influence of Turbulence on the Velocity of Flame in Gas Mixtures. *Z. Elektrochem* 46: 601–626.

De Nevers, N. 2000. *Air Pollution Control Engineering.* McGraw Hill.

de Vries, J., and E. Petersen. 2007. "Autoignition of Methane Based Fuel Blends under Gas Turbine Conditions." *Proceedings of the Combustion Institute* 31: 3163–3171.

Donato, N., and E. Petersen. 2008. "Simplified Correlation Models for CO/H_2 Chemical Reaction Times." *International Journal of Hydrogen Energy* 33: 7565–7579.

Fenimore, C. 1970. "Formation of Nitric Oxide in Premixed Hydrocarbon Flames." *Thirteenth Symposium (International) on Combustion* 13(1): 373–380.

Ferguson, D., G. Richard and D. Straub. 2008. "Fuel Interchangeability for Lean Premixed Combustion in Gas Turbine Engines." In *Proceedings of ASME Turbo Expo 2008: Power for Land, Sea and Air.* Berlin, Germany.

Fritz, J., M. Kroner, and T. Sattelmayer. 2004. "Flashback in a Swirl Burner with Cylindrical Premixing Zone." *Journal of Engineering for Gas Turbines and Power* 126: 276–283.

GE Power Systems. 2002. *GEI 41040G Specification of Fuel Gases for Combustion in Heavy-Duty Gas Turbines.* General Electric.

Glassman, I., 1996. *Combustion.* 3rd ed. San Diego: Academic Press.

Goy, C., A. Moran, and G. Thomas. 2001. *Paper 2001-GT-0051: Autoignition Characteristics of Gaseous Fuels at Representative Turbine Conditions.* New Orleans: American Society of Mechanical Engineers.

Grumer, J., M. E. Harris, and V. Rowe. 1956. *Fundamental Flashback, Blow-off and Yellow Tip limits of Fuel Gas-Air Mixtures.* Springfield, Virginia: Bureau of Mines Report of Investigation 5225.

Hack, R., and V. McDonell. 2008. "Impact of Ethane, Propane, and Diluent Content in Natural Gas on the Performance of a Commercial Microturbine Generator." *ASME Journal of Engineering for Gas Turbines and Power* 011509-1:7.

Halchuk, R., and R. D. Wilson. 2005. *AGA Bulletin#36 and Weaver Interchangeability Methods: Yesterday's Research and Today's Challenges.* Available at: http://www.aga.org. Accessed 2012.

Holton, M. 2008. Autoignition Delay Time Measurements for Natural Gas Fuel Components and Their Mixtures. M.S. Thesis. University of Maryland.

Hu, E. 2009. "Experimental and Numerical Study on Laminar Burning Characteristics of Premixed Methane-Hydrogen-Air Flames." *International Journal of Hydrogen Energy* 34(11): 4876–4888.

Huang, J., P. Hills, K. Bushe, and S. Munshi. 2004. "Shock-Tube Study of Methane Ignition Under Engine Relevant Conditions: Experiments and Modeling." *Combustion and Flame* 136: 25–42.

Huelskamp, B., et al. 2011. *Improved Correlations for Blowout of Bluffbody Stabilized Flames.* Orlando Florida: AIAA.

Kido, H., M. Nakahara, J. Hashimoto, and D. Barat. 2002. "Turbulent Burning Velocities of Two-Component Fuel Mixtures of Methane, Propane, and Hydrogen." *JSME International Journal Series B* 45(2): 355–362.

Kiesewetter, F., M. Konle, and T. Sattelmayer. 2007. "Analysis of Combustion Induced Vortex Breakdown Driven Flame Flashback in Premix Burner with Cylindrical Mixing Zone." *Journal of Engineering for Gas Turbines and Power* 129(4): 929–936.

Konle, M., and T. Sattelmayer. 2010. "Time Scale Model for the Prediction of the Onset of Flame Flashback Driven by Combustion Induced Vortex Breakdown." *Journal of Engineering for Gas Turbines and Power 1*32(4).

Konnov, A. 2000. "Development and Validation of a Detailed Reaction Mechanism for the Combustion of Small Hydrocarbons." *Proceedings of the Combustion Institute* 30: 317.

Kroner, M., J. Fritz, and T. Sattelmayer. 2003. "Flashback Limits for Combustion Induced Vortex Breakdown." *Journal of Engineering for Gas Turbines and Power* 125: 693–700.

Lee, J. 2000. *Reduction of NOx Emission for Lean Prevaporized-Premixed Combustors.* Seattle: University of Washington.

Lefebvre, A. 1983. *Gas Turbine Combustion.* 1st ed. London: Taylor and Francis.

Lefebvre, A., and D. Ballal. 2010. *Gas Turbine Combustion: Alternative Fuels and Emissions.* 3rd ed. Boca Raton: CRC Press.

Leonard, P., and A. Mellor. 1983. "Correlations of Lean Blowoff of Gas Turbine Combustors Using Alternative Fuels." *Journal of Propulsion and Power* 7(6): 729–732.

Leonard, G., and J. Stegmaier. 1994. "Development of Aeroderivative Gas Turbine Dry Low Emissions Combustion System." *Journal of Engineering for Gas Turbines and Power* 116: 542–550.

Lewis, B., and G. Von Elbe. 1943. "Stability and Structure of Burner Flames." *Journal of Chemical Physics* 11: 75–97.

Lewis, G. 1991. *A New Understanding of NOx Formation.* Nottingham, ISABE.

Lieuwen, T., V. G. McDonell, D. Santavicca, and T. Sattelmayer. 2008. "Burner Development and Operability Issues Associated with Steading Flowing Syngas Fired Combustors." *Combustion Science and Technology* 180: 1169–1192.

Liu, Y., and B. Lenze. 1992. "Investigation of Flame Generated Turbulence in Premixed Flames and Low and High Burning Velocities." *Experimental Thermal and Fluid Science* 5(3): 410–415.

B-Meier, J., W. Hung, and V. Sood. 1986. "Development and Application of Industrial Gas Turbines for Medium-BTU Gaseous Fuels." *Journal of Engineering for Gas Turbines and Power* 108(1): 182–190.

Mullins, H. 1955. "Spontaneous Ignition of Liquid Fuels." In: *AGARDograph No. 4.* London: Butterworth. Chapter 11.

Natrajan, J., et al. 2005. "Laminar Flame Speeds of Synthetic Gas Fuel Mixtures," Paper GT2005-68917, presented at ASME Turbo Expo, Reno, NV, June.NGC+

Peschke, W., and L. Spadaccini. 1985. *Determination of Autoigntion and Flame Speed Characteristics of Coal Gases Having Medium Heating Value.* Palo Alto: EPRI.Petersen 2007a

Ribacour, M., et al. 2000. "Ignition of Isomers of Pentane: An Experimental and Kinetics Modeling Study." *Proceedings of the Combustion Institute* 28: 1671–1678.Rizk and L (1986)

Shaffer, B., Z. Duan, and V. McDonell. 2013. "Study of Fuel Composition Effects on Flashback Using a Confined Jet Flame Burner." *Journal of Engineering for Gas Turbines and Power* 135: 011502-1–9.

Shanbhogue, S., S. Husain, and T. Lieuwen. 2010. "Lean Blowoff of Bluff Body Stabilized Flames: Scaling and Dynamics." *Progress in Energy and Combustion Science* 35: 98–120.

Singer, B. 2006. *Natural Gas Variability in California: Environmental Impacts and Device Performance.* California Energy Commission. CEC-500-2006-100.

Spadaccini, L., and M. Colket. 1994. "Ignition Delay Characteristics of Methane Fuels." *Progress in Energy and Combustion Science* 20: 431–460.

Therkelsen, P., T. Werts, V. McDonell, and G. Samuelsen. 2009. Analysis of NOx Formation in a Hydrogen Fuel Gas Turbine Engine. *Journal of Engineering for Gas Turbines and Power* 131: 031507-1:10.

Turns, S. 2012. *An Introduction to Combustion.* 3rd ed. New York: McGraw Hill.

Van Krevelen, D. W., and H. A. Chermin. 1959. "Generalized Flame Stability Diagram for the Prediction of the Interchangeability of Gases." *Proc Combust Institut* 7: 358–368.

Wagner, T. 1990. *Task 200—Ignition Delay Characterization, Report R90-252099-1.* East Hartford: United Technologies Research Center.

Walton, S., X. He, B. Zigler, and M. Wooldridge. 2007. "An Experimental Investigation of Ignition Properties of Hydrogen and Carbon Monoxide Mixtures for Syngas Turbine Applications." *Proceedings of the Combustion Institute* 31: 3147–3154.

Wanneng, D., Q. Chaokui, T. Jixu, and L. Zhaojian. 2011. "A Study on the Interchangeability of Biogas-LPG." *IEEE* 978-1-61284-752-8: 288–283.

Weaver, E., R. 1951, "Formulas and Graphs for Representing the Interchangeability of Fuel Gases." Journal of Research of the National Bureau of Standards, 46: 213-245.

Wohl, K. 1953. "Quenching, Flashback, Blowoff: Theory and Experiments." *Fourth Symposium (International) on Combustion* 68–89.

Wright, F. 1959. "Bluffbody Stabilization: Blockage Effects." *Combustion and Flame* 319–337.

Zabetakis, M. 1965. *Bulletin No. 627.* U.S. Bureau of Mines.

Zukoski, E., and F. E. Marble. 1955. "The Role of Wake Transition in the Process of Flame Stabilization on Bluff Bodies." *AGARD Combustion Research and Reviews* 167.

APPENDIX C:
Alkane Ignition Delay Correlations

C-1 Correlations for Specific Fuels Tested

Table C-1 provides empirical correlations for ignition delay time for the specific fuels tested. The nomenclatures used in Table C-1 is as follows:

τ - Ignition delay time (seconds)

T – Absolute mixture temperature (K)

R – Universal Gas Constant – 1.987×10^{-3} kcal/mol-K

P – Absolute pressure (atm)

E – Activation Energy (kcal/mol)

exp – e = 2.71828…

Correlated over range: 800 to 950 K, 7 to 15 atm, Equivalence ratios of 0.6

Turbulent Flows (Reynolds Number ~30,000)

Table C-1: Ignition Delay Correlations for Fuels Tested in this Study

a)	b) Composition	c) Ignition Delay Expression
a)	b) Methane	c) $\tau = 9.08 \times 10^{-5} \cdot \exp\left(\frac{18.425}{RT}\right) P^{-1.0}$
d)	e) Ethane	f) $\tau = 5.71 \times 10^{-9} \cdot \exp\left(\frac{33.540}{RT}\right) P^{-1.0}$
g)	h) Propane	i) $\tau = 3.29 \times 10^{-8} \cdot \exp\left(\frac{29.765}{RT}\right) P^{-1.0}$
j)	k) 90% Methane, 10% Ethane	l) $\tau = 1.66 \times 10^{-6} \cdot \exp\left(\frac{24.865}{RT}\right) P^{-1.0}$
m)	n) 85% Methane, 15% Ethane	o) $\tau = 1.19 \times 10^{-6} \cdot \exp\left(\frac{25.410}{RT}\right) P^{-1.0}$
p)	q) 70% Methane, 30% Ethane	r) $\tau = 2.41 \times 10^{-8} \cdot \exp\left(\frac{31.590}{RT}\right) P^{-1.0}$
s)	t) 95% Methane, 5% Propane	u) $\tau = 7.41 \times 10^{-6} \cdot \exp\left(\frac{21.750}{RT}\right) P^{-1.0}$
v)	w) 90% Methane, 10% Propane	x) $\tau = 2.30 \times 10^{-7} \cdot \exp\left(\frac{27.435}{RT}\right) P^{-1.0}$
y)	z) 70% Methane, 30% Propane	aa) $\tau = 2.76 \times 10^{-6} \cdot \exp\left(\frac{22.330}{RT}\right) P^{-1.0}$
bb)	cc) 70% Methane, 15% Ethane, 15% Propane	dd) $\tau = 8.05 \times 10^{-8} \cdot \exp\left(\frac{28.660}{RT}\right) P^{-1.0}$
ee)	ff) Simulated Natural Gas	gg) $\tau = 1.15 \times 10^{-8} \cdot \exp\left(\frac{33.120}{RT_{mix}}\right) P^{-1.0}$
hh)	ii) Irvine Natural Gas	jj) $\tau = 7.44 \times 10^{-7} \cdot \exp\left(\frac{25.750}{RT_{mix}}\right) P^{-1.0}$

C-2 General Correlation for Binary Blends

Interpolating the expressions developed for the methane/ethane and methane/propane binary blends, two general expressions were developed, as seen in Table C-2. These best-fit curves for the pre-exponential function, *A*, and the activation energy, *E*, based on the fraction of ethane or propane in the fuel, can be used to develop an expression for mixtures of methane/alkanes that were not specifically studied in this report. The expressions are valid over the range of testing, 800 to 950 K, 7 to 15 atm, and overall lean equivalence ratios. The expressions can be used for mole fraction of ethane or propane from 0 percent to 100 percent (f = 0 to 1). Figure C-1 and Figure C-2 show the curves with respect to experimental data.

τ - Ignition delay time (seconds)

T – Absolute mixture temperature (K)

R – Universal Gas Constant – 1.987×10^{-3} kcal/mol-K

P – Absolute pressure (atm)

f – Volumetric fraction of ethane or propane in fuel (from 0 to 1)

E – Activation energy (kcal/mol)

exp – e = 2.71828…

erf – Error function

Table C-2: Best Fit Values for A and E for Binary Blends of Methane with Ethane or Propane

d) Blend	e) Ignition Delay Expression
kk) General Expression	ll) $\tau = \mathrm{A} \cdot \exp\left(\frac{E}{RT}\right) P^{-1.0}$
mm) nn) Methane/Ethane	$E = 18.4 + 15 \cdot erf(4 \cdot f)$ $\log(A) = -4.04 + -4 \cdot erf(4 \cdot f) - (f/6)$
oo) pp) Methane/Propane	qq) rr) $E = 18.4 + 3.8 \cdot (f)^{0.08} + 7.3 \cdot (f)^{2.5}$ ss) tt) $\log(A) = -4.04 + -1.55 \cdot (f)^{0.13} - 1.9 \cdot (f)^{2.4}$

Example:

Method to find an expression for the ignition delay of a 85/15 (by mole or volume) mixture of Methane/Propane:

Fraction of propane in fuel: f = 0.15

$$E_{85/15} = 18.4 + 3.8 \cdot (0.15)^{0.08} + 7.3 \cdot (0.15)^{2.5} = 21.7 \frac{kcal}{mol}$$

$$\log(A) = -4.04 + -1.55 \cdot (0.15)^{0.13} - 1.9 \cdot (0.15)^{2.4} = -5.27$$

$$A_{85/15} = 10^{-5.27} = 5.37 \times 10^{-6}$$

Hence:

$$\tau_{85/15} = \mathrm{A} \cdot \exp\left(\frac{E}{RT}\right) P^{-1.0} = 5.37 \times 10^{-6} \cdot \exp\left(\frac{21.7}{RT}\right) P^{-1.0}$$

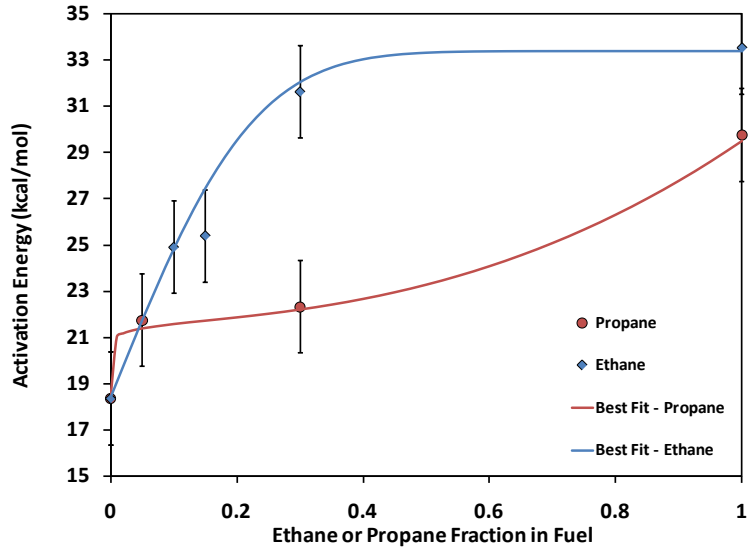

Figure C-1: Best-Fit Curves for Activation Energy, E, for Methane/Ethane and a Methane/Propane Blend Fitted to Experimental Data

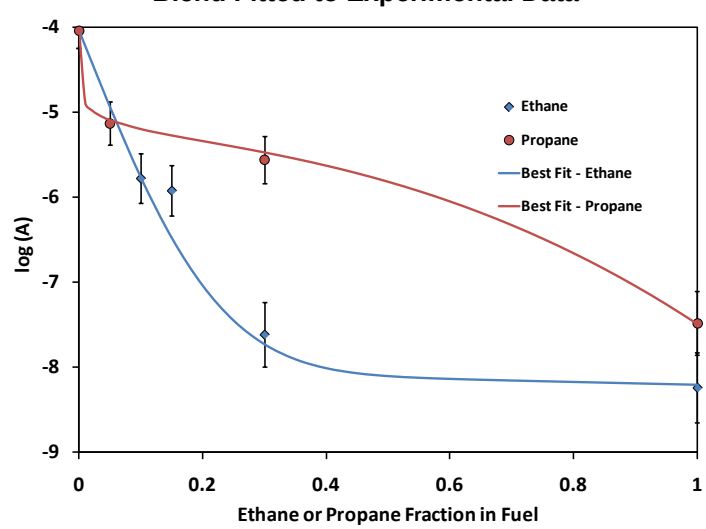

Figure C-2: Best-Fit Curves for Logarithm of Pre-Exponential Factor, A, for Methane/Ethane and a Methane/Propane Blend Fitted to Experimental Data

Example Problem:

Method to find an expression for the ignition delay of a 85/15 (by volume) mixture of methane and propane:

Fraction of propane in fuel: f = 0.15

$$E_{85/15} = 18.4 + 3.8 \cdot (0.15)^{0.08} + 7.3 \cdot (0.15)^{2.5} = 21.7 \ \frac{kcal}{mol}$$

$$\log_{10}(A) = -4.04 - 1.55 \cdot (0.15)^{0.13} - 1.9 \cdot (0.15)^{2.4} = -5.27$$

$$A_{85/15} = 10^{-5.27} = 5.37 \times 10^{-6}$$

Hence:

$$\tau_{85/15} = A \cdot \exp\left(\frac{E}{RT}\right) P^{-1.0} = 5.37 \times 10^{-6} \cdot \exp\left(\frac{21.7}{RT}\right) P^{-1.0} =$$

To find the ignition delay time of a 85/15 methane/propane mixture at 15 atm and 900 K, plug into the expression:

$$\tau_{85/15} = A \cdot \exp\left(\frac{E}{RT}\right) P^{-1.0} = 5.37 \times 10^{-6} [atm \cdot \sec] \cdot \exp\left(\frac{21.7\left[\frac{kcal}{mol}\right]}{1.987 \times 10^{-3}\left[\frac{kcal}{mol \cdot K}\right] \cdot 900[K]}\right) (15[atm])^{-1.0} =$$

$$\tau_{85/15} = 0.067 \sec = 67 \, m\sec$$

APPENDIX D:
Details and Heat Transfer Analysis of JSR

Experimental WSR designs have been constructed in many different ways, from a single jet impinging on a truncated cone to dozens of jets emerging from the center of a sphere. The basic idea is to have mixing occur as fast as possible. While the WSR is known as an experimental device, the idealized model is referred to as the *perfectly-stirred reactor* (PSR). The basic concept behind the PSR is that premixed fuel and air flow into a fixed volume at constant pressure and are instantaneously mixed with the combustion products. The reaction that occurs achieves a steady-state combustion temperature, and the mass flow leaving the reactor maintains this reaction temperature, as well as the species concentrations associated with the homogenous reactor volume (Glassman 1996). That is, the PSR is uniform in temperature and species concentrations. While the WSR attempts to achieve this homogeneity, there are typically two or more combustion regimes within the experimental device that are associated with the inlet reactant stream.

Throughout the years, many researchers have built experimental well-stirred reactors in hopes of approaching the ideal PSR. Longwell and Weiss (1955) were among the first to build such a reactor in which they studied reaction rates of hydrocarbon fuels near blowout. Their design incorporated a spherical reactor body with the premixed fuel and air being injected in the center of the body through a perforated ball. In the 1970s, Pratt and Malte (1974) studied NO_X formation in a single-jet-stirred reactor burning premixed CO and air. In the 1990s Zelina and Ballal constructed an experimental PSR that is toroidal in geometry in which the premixed reactants enter through 32 jets on the outer surface of the toroid (Zelina 1995). In the late 1980s, Thornton et al. (1987) developed a single-jet-stirred reactor that employs a cavity in the shape of a truncated cone. This WSR geometry is what many University of Washington (UW) researchers have been using to study LPM combustion kinetics, from the early 1990s through today. The reactor used in this study is of this same geometry and was constructed out of high-purity Greencast alumina by Lee (2000).

To properly model the NO_X data and compare it to data obtained from other fuels at various equivalence ratios, the true gas temperature must be measured. As mentioned above, the thermocouple loses heat mainly due to radiation to the colder reactor wall and also through conduction through the wires. To properly correct the temperature read by the thermocouple, the temperature of the inside reactor wall must be known with a reasonable degree of certainty.

Several experimental researchers at UW have reported some degree of heat loss from various jet-stirred reactors for both atmospheric (Lee 2000; Steele 1995)and high-pressure (Steele 1995; Shuman 2000) JSR experiments. In general, the high-pressure experiments were found to be more adiabatic than the atmospheric pressure tests; however, all experiments showed that the heat loss is minimized when the mass flow rate through the reactor is increased. A larger mass flow rate decreases the overall reactor residence time, as given in Equation D-1, where τ is the reactor residence time, ρ is the density of the fluid in within the reactor based on the combustion

temperature and pressure, *V* is the reactor volume, and $\dot{m}$ is the total mass flow rate through the reactor.

$$\tau = \frac{\rho V}{\dot{m}}$$ **Equation D-1**

Because the present study is concerned with the differences between a variety of fuels, the goal is to keep variations in residence time to a minimum, to help remove this parameter, since it does have a mild effect on emissions (Steele 1995). With the exception of the experiments investigating the effect of residence time, the air flow rate is kept constant at 1.08E-3 kg/s for all constant temperature experiments (1,800 K) for every fuel tested. For the blowout tests, the air flow rate is also set constant at 1.08E-3 kg/s. However, due to differences in blowout temperature (e.g., H_2 vs. CH_4), the residence time is larger due to an inherent increase in density when the reactor is colder.

Past JSR researchers have used an optical pyrometer to measure the reactor wall temperature. In the work by Shuman (2000), for a measured thermocouple temperature of 1,813 K, the measure wall temperatures ranges from 1,030°C to 1,220°C (1,890°F to 2,230°F). Lee (2000) reports a typical measured wall temperature of 1,602 K (Lee 2000). Steele (1995) reports a measured wall temperature of 1,563 K for the atmospheric tests conducted. Although all three experimentalists measured the wall temperature in order to properly correct their thermocouple measurements, none of them attempted to quantify the actual heat loss from the reactor.

The heat loss in the present reactor is quantified by two methods. In the first procedure, a First Law balance is performed on the JSR by taking the difference between the enthalpy of the premixed reactants coming into the reactor and that of the hot combustion products leaving the reactor, as shown in Equation D-2 and Equation D-3. The estimated heat loss from the first law balance is 440.6 W, which is about 20 percent of the incoming energy based on the LHV of the fuel. The inputs and outputs of the analysis are shown in **Table** D-1.

Table D-1: Inputs and Results from First Law Balance on the Heat Transfer

Input Parameters	Output Parameters	q_{out} (W)
$T_{preheat}$ = 571 K $\dot{m}$ = 4.62e-5 kg/s Φ = 0.718	T_{gas} = 1,800 K y_{O2} = 0.068 y_{CO2} = 0.079 y_{CO} = 0.00242	440.6

$$Q_{out} = \sum N_r (h_f^{\circ} + h - h^{\circ})_r - N_p (h_f^{\circ} + h - h^{\circ})_p$$ **Equation D-2**

$$q_{out} = \frac{Q_{out} m_{CH4}}{M_{CH4}}$$ **Equation D-3**

where,

- Q_{out} is the heat loss from the reactor (kJ/kmol_{CH4})
- N_r and N_p are the mole numbers of each species for reactants and products, respectively (kmoles)
- h_f° is the enthalpy of formation (kJ/kmole)
- h is the enthalpy of each species at elevated temperature in kJ/kmole
- q_{out} is the reactor rate of heat loss (W)
- m_{CH4} is the mass flow rate of CH_4 (kg/s)
- M_{CH4} is the molecular weight of CH_4 (kg/kmole)

The second approach to quantifying reactor heat loss involves a simple one-dimensional heat transfer model. As shown in **Figure** D-2, heat is transferred to the reactor wall from the gas via convection and radiation. The convective heat transfer coefficient is estimated as 200 W/m^2-K from using the boundary layer theory analysis of flow around a body of revolution, as outlined in Kays et al. (2005). The radiation to the reactor wall is quite insignificant, due to the small mean beam length (0.017 m) calculated for the JSR. The emissivity of the combustion products is determined as 0.009 from the charts in Incropera and DeWitt (2007), and 0.012 from a more refined algorithm presented by Modest (1993). For the remainder of this analysis, the gaseous radiation to the wall is neglected. The heat convected to the wall is then transferred through the reactor wall by conduction. The radiative losses through the exhaust ports and feed jet are assumed to be negligible due to the small area that these holes encompass. The conduction resistance is modeled as two concentric spheres, as given by Equation D-4.

$$R_{Conduction} = \frac{(1/r_1) - (1/r_2)}{4\pi k}$$ **Equation D-4**

where,

- $R_{Conduction}$ is the conduction resistance (K/W)
- r_1 and r_2 are the inside and outside radii, respectively (m)
- k is the thermal conductivity of the castable alumina (W/m-K) (average k for calculated wall temperatures is 2.3 W/m-K)

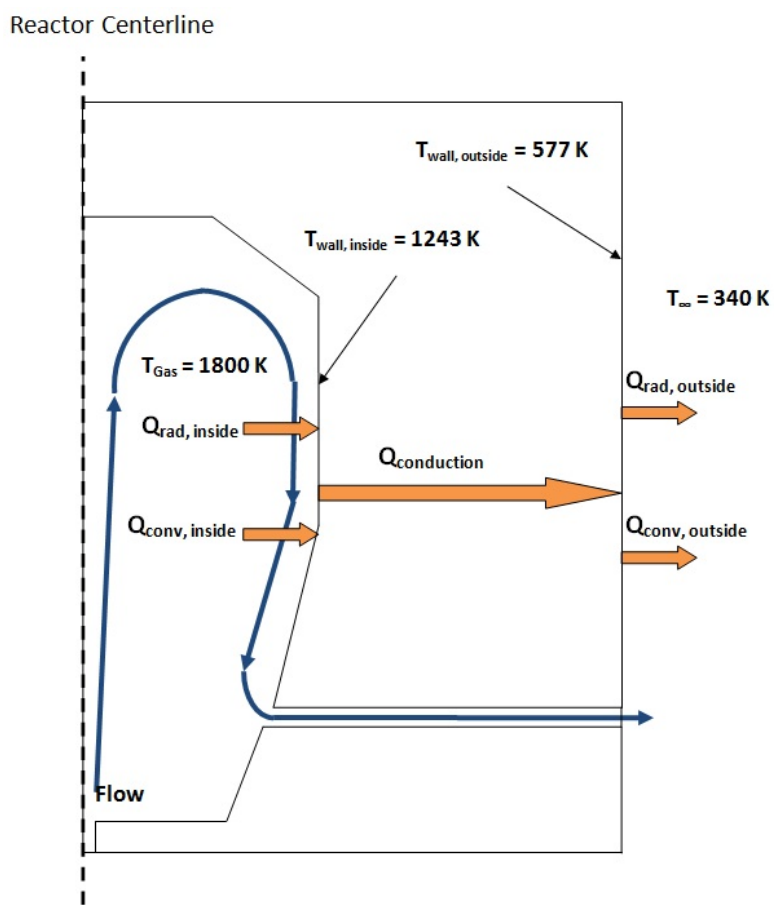

Figure D-1: Diagram Illustrating the Modes of Heat Transfer out of the JSR

The heat then is transferred to the ambient environment through natural convection and radiation. The temperature of the ambient environment is that of the plenum where the reactor exhausts. The one-dimensional thermal circuit used in this analysis is shown in **Figure** D-3. Note that the temperature of the gas and that of the ambient environment are measured; whereas, the inside and outside wall temperatures are calculated.

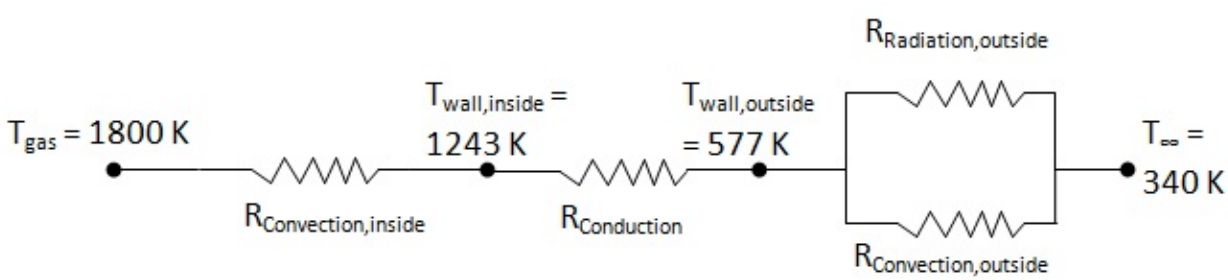

Figure D-2: One-Dimensional Thermal Circuit for the JSR

The total reactor heat loss calculated from this analysis is found to be 422 W, which is remarkably close to the heat loss calculated from the first law analysis shown above. A summary of the results are shown in **Table** D-2.

Table D-2: Measured and Calculated Temperatures, Thermal Resistances, and Heat Loss from the Thermal Model Illustrated by Figure D-1 and Figure D-2

Measured Temperatures	Calculated Temperatures	Thermal Resistances (W/K)	q_{out} (W)
T_{gas} = 1,800 K T_{∞} = 340 K $T_{wall,outside}$ = 563 K	$T_{wall,inside}$ = 1,243 K $T_{wall,outside}$ = 577 K	$R_{convection,inside}$ = 1.32 $R_{convection,inside}$ = 1.58 $R_{convection,outside}$ = 0.56	422

There are a couple of points that should be made about this one-dimensional heat transfer analysis. Each one of the thermal resistances is of the same order of magnitude; thus, there is no clear mode of heat transfer to focus on improvement. This being said, the reactor is run at the current flow rates to promote fast mixing and approach well-stirred condition. Decreasing the flow rates through the reactor will certainly increase the convective resistance on the inside wall of the reactor; however, this is not advised, since mixing will be compromised. Constructing the reactor body out of a material with a lower thermal conductivity will increase the conductive resistance of the reactor. Increasing the outside dimensions of the reactor will augment the conduction resistance; however, the increase in outside surface area reduces the convection/radiation resistance on the outside of the reactor at a quicker rate. It seems that constructing the reactor out of a material with a lower thermal conductivity or adding insulation to the outside (although this will also increase surface area) is the best method of making the reactor operate in a more adiabatic manner. Most of the materials that will tolerate these temperatures have a fairly large conductivity. This is why layered designs are often used.

References

Glassman, I., 1996. *Combustion.* 3rd ed. San Diego: Academic Press.

Incropera, F., and D. DeWitt. 2007. *Introduction to Heat Transfer.* New York: Wiley & Sons.

Kays, W., M. Crawford, and B. Weigand. 2005. *Convective Heat and Mass Transfer.* New York: McGraw-Hill.

Lee, J. 2000. *Reduction of NOx Emission for Lean Prevaporized-Premixed Combustors.* Seattle: University of Washington.

Longwell, J., and M. Weiss. 1955. "High Temperature Reaction Rates in Hydrocarbon Combustion." *Industrial & Engineering Chemistry* 47: 1634–1643.

Modest, M. 1993. *Radiative Heat Transfer.* New York: McGraw-Hill.

Malte, P., and D. Pratt. 1974. "The Role of Energy-Releasing Kinetics in NOx Formation: Fuel-Lean, Jet-Stirred CO-Air Combustion." *Combustion Science and Technology* 9: 221–231.

Shuman, T. 2000. *NOx and CO Formation for Lean Premixed Methane-Air Combustion in a Jet-Stirred Reactor Operated at Elevated Pressures.* Seattle: University of Washington.

Steele, R. 1995. *NOx and N_2O Formation in Lean-Premixed Jet-Stirred Reactors Operated from 1 to 7 atm.* Seattle: University of Washington.

Thornton, M., P. Malte, and A. Crittenden. 1987. "A Well-Stirred Reactor for the Study of Pyrolysis and Oxidation Kinetics: Carbon Monoxide and n-Pentane Oxidation." *Combustion Science and Technology* 54: 275–297.

Zelina, J. 1995. Combustion Studies in a Well-Stirred Reactor. Ph.D. Thesis. Dayton: University of Dayton.

APPENDIX E:
Topical Report: Flame Speed Test Results and Analysis

Public Interest Energy Research (PIER) Program

FINAL PROJECT REPORT

DEVELOPMENT AND EVALUATION OF GAS FUEL INTERCHANGEABILITY CRITERIA AND METHODOLOGIES

APPENDIX E

TOPICAL REPORT: Flame Speed Test Results and Analysis

Prepared for: California Energy Commission

Prepared by: Georgia Tech, under subcontract to the University of California, Irvine

JUNE 2013

Prepared by:

Primary Author(s):
Andrew Marshall
Prabhakar Venkateswaran
Tim Lieuwen

Georgia Tech University
270 Ferst Drive
Atlanta, GA 30332-0150

Contract Number: 500-08-034

Prepared for:

California Energy Commission

Marla Mueller
Contract Manager

Linda Spiegel
Office Manager
Energy Generation Research Office

Laurie ten Hope
Deputy Director
RESEARCH AND DEVELOPMENT DIVISION

Robert P. Oglesby
Executive Director

DISCLAIMER

This report was prepared as the result of work sponsored by the California Energy Commission. It does not necessarily represent the views of the Energy Commission, its employees or the State of California. The Energy Commission, the State of California, its employees, contractors and subcontractors make no warrant, express or implied, and assume no legal liability for the information in this report; nor does any party represent that the uses of this information will not infringe upon privately owned rights. This report has not been approved or disapproved by the California Energy Commission nor has the California Energy Commission passed upon the accuracy or adequacy of the information in this report.

ACKNOWLEDGEMENTS

The authors are grateful to Mr. Bobby Noble, Brad Ochs and Dave Shaw for their invaluable assistance in designing and installing the high pressure test facility. The authors also gratefully acknowledge Mr. Andrew Irby, Daniel Miller, Juan Camilo Pedroza, and Ramon Romero for their assistance in assembling the experimental facility and data collection. This research was also partially supported by the University Turbine Systems Research program, who provided financial assistance for Mr. Venkateswaran and facility development.

Chapter E-1: Introduction

There is significant interest in developing dry low NOx combustion technologies that can operate with synthetic gas (syngas) fuels derived from organic based feedstock [1]. Syngas fuels are typically composed primarily of H_2 and CO, and may also contain smaller amounts of CH_4, N_2, CO_2, H_2O, and other higher order hydrocarbons [2, 3]. However, the specific composition depends upon the fuel source and processing technique, leading to substantial variability in composition - one of the largest barriers towards their usage in lean, premixed combustion systems.

A variety of operability, emissions, and structural life issues must be addressed in evaluating the impact of fuel composition on a gas turbine combustor; e.g., NOx and CO emissions, liner and fuel nozzle thermal loading, blow-off and flashback limits, and combustion instabilities. The turbulent flame speed is an important parameter through which the fuel composition exerts influences on many of these issues, such as thermal loading, blow-off limits, flashback limits, and combustion instability [4]. For example, the turbulent flame speed has a direct impact on the flame length and its spatial distribution in the combustor. This, in turn, affects the thermal loading distribution on the combustor liners, fuel nozzles and other hardware. Furthermore, the flames proclivity to flashback is directly a function of how rapidly the flame propagates into the reactants, which is dependent on the turbulent flame speed. In addition, the turbulent flame speed has a leading order influence on combustion instability limits through its influence upon the flame shape and length [5]. For example, measurements from Santavicca [6] have clearly shown how combustion instability boundaries are influenced by changes in flame location, due to changes in H_2 content of the fuel or mixture stoichiometry.

The laminar flame speed, S_L, is a thermo-physical property of a fuel-oxidizer mixture that describes the speed at which a laminar flame front propagates into a reactive mixture. For a given mixture, it is a function of pressure, temperature and flame stretch rate [7]. The turbulent flame speed, S_T, while having an analogous definition for the average propagation speed of a turbulent front, does not uniquely depend on the mixture's thermal and chemical properties. As with turbulence itself, S_T is a function of the flow within which the flame resides; i.e., it is a function of laminar flame speed, turbulence intensity, turbulence length scales, etc. Correlations of turbulent flame speed of the form $S_T = S_{L,0} \cdot f(u'_{rms})$, where u'_{rms} denotes the root mean square (RMS) turbulence fluctuation, have been obtained from numerous studies [8].

However, u'_{rms} and $S_{L,0}$ alone do not capture many important characteristics of S_T, a point that has been made repeatedly in the literature [8]. Fuel composition is also known to significantly influence the turbulent flame speed. For example, the effect of fuel composition on the turbulent flame speed is well-documented in the literature [9, 10]. Kido *et al.* [11, 12] obtained data for mixtures of H_2, methane (CH_4), and propane (C_3H_8) where, by adjusting the dilution and stoichiometries of the different fuel blends, they obtained different mixtures with the same un-stretched laminar flame speed, $S_{L,0}$. Their data clearly show that these mixtures have substantially different turbulent flame speeds, with the high H_2 mixture having *an order of magnitude* larger S_T value than the propane mixture at the same turbulence intensity. Similarly, other data sets also exist showing strong sensitivities of S_T to fuel composition [9, 13-15]. In the same way, other data sets show sensitivities of S_T to pressure and fuel/air ratio that cannot be correlated with the corresponding laminar, un-stretched flame speeds of the mixtures [16, 17].

Prior studies have shown that the sensitivity of the turbulent flame speed to fuel composition is associated with the stretch sensitivity of the reactant mixture, which leads to variations in the local consumption speed along the flame front. In particular, the high mass diffusivity of H_2 makes syngas

mixtures highly stretch sensitive. Stretch effects can be manifested through both non-unity Lewis number and preferential diffusion effects [18]. While various modeling approaches have been put forth to capture these effects, conceptual models based on leading points concepts appear to be one of the most natural approaches for capturing these stretch sensitivities [9, 19-21]. Leading points are loosely defined as positively curved points on the flame front that propagate out farthest into the reactant mixture. It has been hypothesized that the velocity of these points controls the overall propagation velocity of the turbulent flame [9]; i.e., the turbulent flame speed can be written as:

$$S_T = \langle S_L \rangle_{LP} + \langle u'_{rms} \rangle_{LP} \tag{E-1}$$

where $\langle \ \rangle_{LP}$ denotes the ensemble averaged value of the quantity at the flame leading edge. This simplified expression should obviously be interpreted for scaling of local turbulent displacement speeds only [22], and not as a quantitative expression for turbulent flames in general. Thus, the ensemble averaged laminar burning velocity of the turbulent flame leading point, $\langle S_L \rangle_{LP}$, turns out to be a very significant way in which diffusive and kinetic mixture properties influence the turbulent flame speed, and is the focus of the rest of this introduction.

For negative Markstein length, l_M, mixtures, the burning velocity of this positively curved leading point is greater than the laminar un-stretched value [18]. Thus, we can write the inequality:

$$S_{L,0} < \langle S_L \rangle_{LP} < S_{L,\max} \tag{E-2}$$

where $S_{L,max}$ is the maximum possible burning velocity of a stretched flamelet. For example, $S_{L,max}$ is indicated in Figure E-5 for a positively stretched, H_2/CO stagnation flame. Using this inequality, we can write Eq. (E-1) as:

$$\frac{S_T}{S_{L,\max}} \le 1 + \frac{\langle u'_{rms} \rangle_{LP}}{S_{L,\max}} \tag{E-3}$$

The resulting expression is very similar to the classical Damköhler turbulent flame speed scaling [23], except the parameter arising from the analysis is $S_{L,max}$ [22]. Lipatnikov and Chomiak [24] argued that the flame leading points were "critically stretched flamelets", which basically suggests that $\langle S_L \rangle_{LP}$ should be scaled with the respective values of the mixture at very high stretch rates; i.e., that $\langle S_L \rangle_{LP} = S_{L,\max}$. This expression can be derived rigorously for an isothermal, negative Markstein length flame propagating into a quiescent mixture, where it can be shown that the leading edge of the flame accelerates until settling at the steady-state value where $S_{L,LP} = S_{L,\max}$ [22]. This result follows from the fact that $S_{L,0}$ is a 'repelling' point for thermodiffusively unstable (i.e., $l_M < 0$) flames, since a positively curved perturbation on a flat flame grows with increasing curvature and correspondingly increasing flame speeds. Moreover, $S_{L,max}$ is a stable 'attracting' point for constant density flames with positively curved wrinkles. Thus, in this limit, we can replace the inequality in Eq. (E-3) with:

$$\frac{S_T}{S_{L,\max}} = 1 + \frac{\langle u'_{rms} \rangle_{LP}}{S_{L,\max}} \tag{E-4}$$

Note the important caveats in the prior paragraph associated with the applicability of this expression; namely, that the flame leading point be quasi-steady, that gas expansion effects are negligible, and that the mixture has a negative Markstein length. For example, quasi-steadiness of the leading point implies that turbulent eddies must evolve over a time scale that is slow relative to that required for the leading points to be attracted to the $S_{L,max}$ point and for the internal chemical kinetic processes to equilibrate to the evolving flame stretch rate characteristics. In flames with fluctuating stretch rates the augmentation

of the laminar burning velocity by positive stretch decreases and the extinction stretch rate increases [25]. Thus, there are two important non-quasi-steady effects which influence this scaling; one related to the geometry of the turbulent flame brush and the other related to the internal flame structure.

In a prior paper, we showed excellent collapse of a range of H_2/CO data using $S_{L,max}$ values obtained from steady-state, detailed kinetics calculations of a premixed, opposed-flow flame [22]. This report further analyzes the scaling relation given by Eq. (E-3) as well as coupled pressure and fuel effects. Measuring pressure sensitivities of the turbulent flame speed is a convenient way to probe internal flame structure unsteady effects, as characteristic chemical kinetic times, t_{chem}, are generally inversely proportional to pressure. There are limited data of this kind in the literature and the results are not well understood. Kobayashi *et al.* [26] reported turbulent consumption speed measurements of $\phi = 0.9$ CH_4/air mixtures and showed that $S_{T,GC}/S_{L,0}$ increased with pressure due to decreases in $S_{L,0}$, but that $S_{T,GC}$ itself was independent of pressure. Kitagawa *et al.* [17] reported similar measurements on turbulent flame speeds of H_2/air mixtures at pressures from 1-5 atm; i.e., that $S_T/S_{L,0}$ was primarily sensitive to pressure through influences on $S_{L,0}$. However, the influence on S_T is unclear. Daniele *et al.* [16] reported $S_{T,GC}$ measurements of H_2/CO mixtures for pressures of 1-20 atm at 623 K. They found that $S_{T,GC} / S_{L,0}$ increased with pressure at each given H_2/CO ratio and $u'_{rms} / S_{L,0}$ value.

In this report, we describe measurements of $S_{T,GC}$ at 5 and 10 atm and compare them to previously obtained 1 atm measurements [22]. We show that data can be collapsed quite well using Eq. (E-4) for a given pressure, but that significant differences are observed across different pressures. Previously, Kobayashi *et al.* [26] suggested that the rise in $S_{T,GC}/S_{L,0}$ with pressure at low $u'_{rms}/S_{L,0}$ in their data was due to the amplification of the Darrieus-Landau (D-L) instability. They also suggest that the thinning of the flame and decreasing turbulent Gibson scale with pressure allows the flame to interact with a large range of turbulent length scales, resulting in finer scale wrinkling and, hence, larger flame area. However, the D-L instability probably does not have a dominant influence on the burning velocity at high turbulence intensities [26], where we also show that the pressure effect persists. Pressure also has strong impacts on mixture stretch sensitivities, such as Markstein length, l_M. However, the data presented in this report clearly shows that the mixture stretch sensitivity, as parameterized by the steady-state value of l_M or $S_{L,max}$, does not capture the pressure sensitivity of the S_T. We suggest that this scatter reflects non-quasi-steady effects and show that much of the scatter can be collapsed by a two-factor parameterization of S_T based on the mixture stretch sensitivity and chemical time. In other words, we suggest that pressure effects on the turbulent burning velocity are more a manifestation of its influence on relative values of turbulence and flame time scales than length scales.

Chapter E-2: Experimental Facility and Flow Field Characterization

E.2.1 Experimental Facility

The turbulent flame speed is a definition dependent quantity. It can be defined locally at a single point on the flame or globally averaged over the entire flame. In addition, the propagation rate can be defined based on a kinematic argument through the velocity at the flame front or a consumption rate. Through the International Workshop on Turbulent Premixed Flames [27], and in recent reviews [10, 28], four definitions of the turbulent flame speed have been proposed: local consumption speed, $S_{T,LC}$, global consumption speed, $S_{T,GC}$, local displacement speed, $S_{T,LD}$, global displacement speed, $S_{T,GD}$.

This study focuses upon measurements of $S_{T,GC}$ using a turbulent Bunsen flame, an $S_{T,GC}$ measurement approach recommended by Gouldin and Cheng [27]. The experimental facility has been detailed extensively in our previous work [22, 29], so only a short description is provided here. A schematic of the system is shown in Figure E-1. The burner is a smoothly contoured nozzle with high contraction ratio to inhibit boundary layer growth and achieve a top-hat exit velocity profile. Measurements were taken using a 12 mm exit diameter burner. An annular sintered plate is placed around the burner outlet to hold a premixed, methane-air pilot flame to stabilize the main flame. The total mass flow rate of the pilot does not exceed 5% of the main flow rate to ensure minimal impact of the pilot on the main flame.

Main fuel and pilot flow rates are metered using sonic orifices and the flows are controlled by varying the upstream gas pressure using air-loaded pressure regulators. The downstream pressure of the air-loaded pressure regulators is controlled using ER-3000 pressure controllers. Calibration of the sonic orifices was performed using a Ritter drum-meter calibrator with an accuracy of ± 0.2%. The main and co-flow (used to pressurize the vessel and assist in cooling) air flow rates are metered using sub-critical orifices by measuring the upstream pressure and temperature and the differential pressure across the orifice.

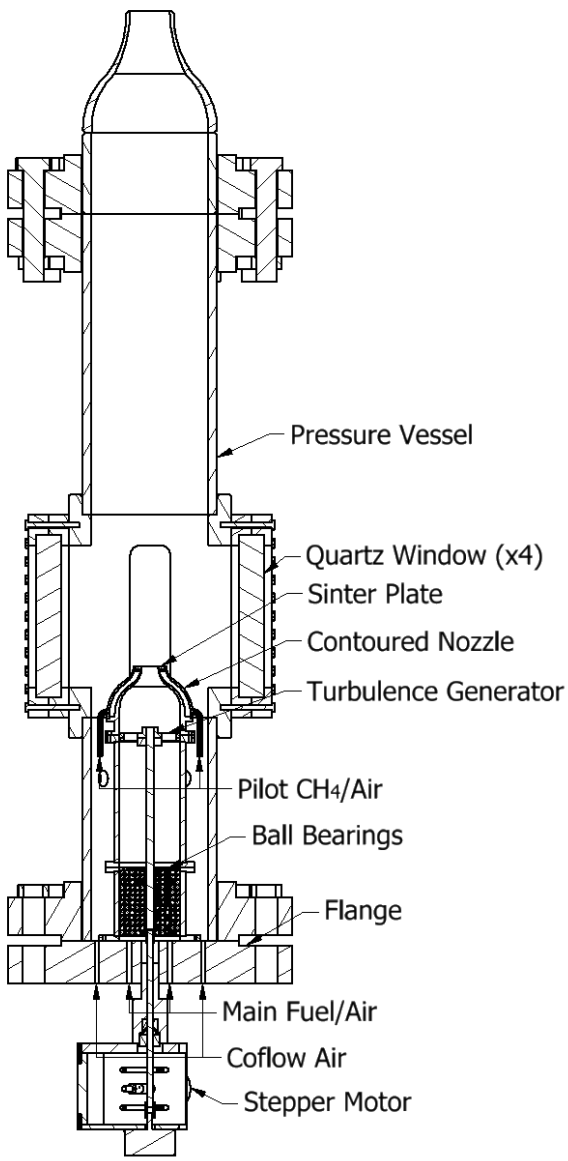

Figure E-1: Schematic of the experimental facility.

The burner is placed inside a pressure vessel with four orthogonal quartz windows each providing viewing areas of 7″ x 2″. The pilot flame is lit using a hydrogen torch that is ignited using a high voltage spark.

The turbulence intensity is varied independently of the mean flow velocity using a remotely operable turbulence generator. Further description of the turbulence generator can be found in Marshall *et al.* [29].

E.2.2 Flow Field Characterization

This section presents results illustrating the flow field characteristics over a range of operating pressures and preheat temperatures. Data were obtained with a TSI 3-component Laser Doppler Velocimetry (LDV) system. The air flow was seeded using 5 µm alumina (Al_2O_3) particles. The LDV transmitter probes were mounted on a computer-controlled, three-axis traverse to enable axial and radial scanning across the burner exit along three orthogonal directions. The LDV system is comprised of an Innova 90C 2.4 W, 514.5 nm continuous wave argon-ion laser with an FBL-3 multicolor beam generator. The multicolor beam generator has a Bragg cell that shifts one beam of each of the three pairs by 40 MHz. Two fiber optic transceiver probes were mounted 90° apart and operated in backward-scatter mode. The signal from the transceiver probe was connected to a PDM 1000-3 three-channel photodetector module. The output frequencies were downmixed and sent through a bandpass filter before being processed by an FSA 3500-3 signal processor to record three components of velocity in non-coincidence mode. The amount of downmixing and the range of the bandpass filter varied depending on the channel and the expected measurement velocity range. Approximately 30,000 realizations, divided roughly equally among the three channels, were used to generate the quoted velocity statistics. Data were taken in two perpendicular radial cuts 3 mm above the nozzle exit to verify azimuthal symmetry in the flow. Profile results presented in the report will be shown for a single cut, since there was no noticeable difference between the two traverse directions.

Data were obtained at mean flow velocities from $U_0 = \dot{m}/\rho A$ = 10-50 m/s, which correspond to geometric Reynolds numbers of $Re_D = U_0 D/\nu$ = 23,000-206,000 and turbulent Reynolds numbers of $Re_l = u'_{rms}\, l/\nu$ = 220-9,000.

Figure E-2 presents representative profiles of the mean and fluctuating axial, radial, and azimuthal velocities as a function of radial distance from the center of the burner. All velocities have been normalized by the mean axial velocity calculated in a region including all points within ±3 mm around the center of the burner. Total turbulence intensity is calculated from $u'_{rms} = \sqrt{(u'_{ax})^2 + (u'_{rad})^2 + (u'_{azi})^2}$. The solid lines correspond to a chamber pressure of 5 atm, while the dashed lines correspond to atmospheric data reported previously [29]. These results show little effect of pressure on the time-averaged or fluctuating velocity characteristics. The data show a well-defined top-hat axial velocity profile and low radial and azimuthal velocities. These profile results are typical for other mean flow velocities, pressures, and preheat temperatures.

Figure E-2 also shows that the turbulent fluctuations in the axial direction are about half of the fluctuations in the transverse directions. This is due to vortex stretching through a contraction [30, 31]. Our area contraction ratio is 40 for the 12 mm diameter nozzle. The high area contraction ratio produces radially uniform velocity profiles as shown, as well as flashback-resistant burners, but also necessarily leads to this anisotropy in turbulence intensity at the burner outlet.

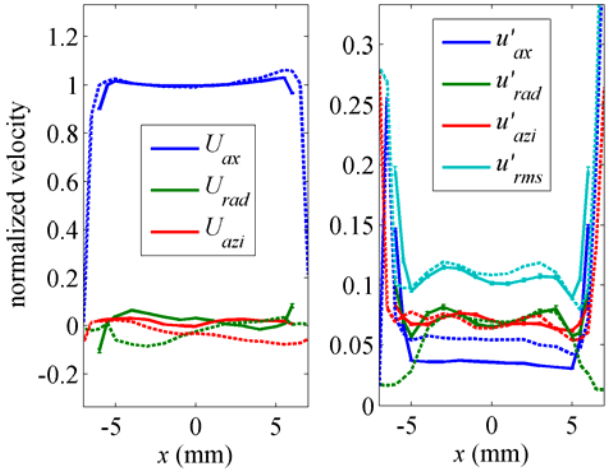

(a) (b)

Figure E-2: (a) Mean axial, radial and azimuthal velocities and (b) RMS of the fluctuating axial, radial, azimuthal, and total velocities as a function of radial distance from the center of the burner for U_0 = 30 m/s and *BR* = 69%. Dashed and solid lines correspond to pressures of 1 and 5 atm, respectively.

Figure E-3 summarizes the performance of the turbulence generator over the pressure range of 1-20 atm by plotting the total centerline turbulence intensity, u'_{rms}/U_0 as a function of blockage ratio (defined as the amount of area blocked by the turbulence generator over the total area). The turbulence intensity monotonically increases with blockage ratio and follows the same general trend for all of the tested conditions.

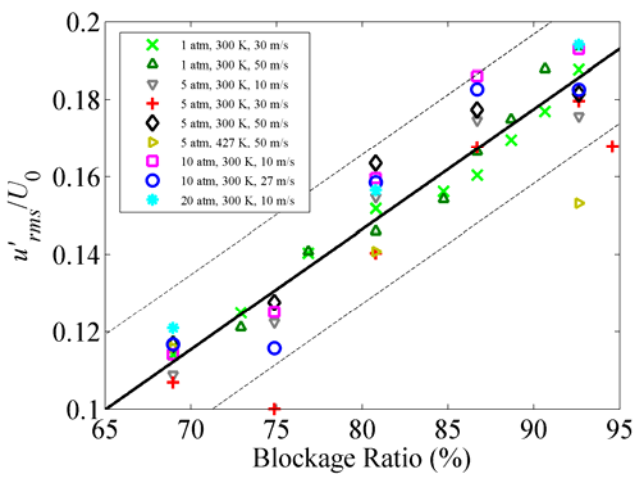

Figure E-3: Dependence of the burner centerline total turbulence intensity on blockage ratio. The solid line corresponds to the linear fit of the data, and the dashed lines correspond to the 95% confidence level.

Figure E-3 also presents the linear best fit of the combined data with the associated 95% confidence levels that was used in the subsequent measurements to specify the turbulence intensity. Some of the scatter in the data is likely due to Reynolds number effects on the turbulence generator performance, and some is due to uncertainty in mass flow rate, which is about ±4%. This uncertainty in the turbulence intensity translates to a horizontal uncertainty bar for the consumption speed data. In order to avoid clutter, these uncertainties are not displayed in the presentation of the consumption speed data.

E.2.3 Image Analysis

The image processing methodology has been extensively documented in [22], but is briefly overviewed here. Global consumption speeds were calculated using Eq. (5) whose key measurement input is the progress variable surface area, $\bar{A}_{<c>}$:

$$S_{T,GC} = \frac{\dot{m}_R}{\rho_R \bar{A}_{\langle c \rangle}} \qquad \text{(E(5)}$$

Digital images of the flame emission were captured with a 16-bit intensified charge-coupled device (ICCD) camera. Line-of-sight images of the flame were obtained over 5 seconds and time-averaged. To estimate the time-averaged flame brush location from the line-of-sight images, a three-point Abel deconvolution scheme [32] was used. The axial distribution of the centerline intensity was then fit to a Gaussian curve, from which the location of the maximum intensity was identified. This point is associated with the most probable location of the flame, and defined as the <*c*> = 0.5 progress variable contour. The estimated uncertainty in identifying this point is 1-2%. Straight lines are then drawn from this point to the two flame anchoring points and rotated about the line of symmetry to generate a cone; i.e., the "angle method" [26, 33, 34]. The overall uncertainty in the $S_{T,GC}$ value is estimated to be 3%.

Chapter E-3: Experimental Conditions and Kinetic Calculations

E.3.1 Experimental Conditions

Measurements of $S_{T,GC}$ were obtained at 1, 5, and 10 atm as a function of $u'_{rms}/S_{L,0}$ using the 12 mm diameter burner. Data were acquired at mean flow velocities from 20-50 m/s and volumetric H_2/CO ratios from 30/70-90/10, keeping $S_{L,0}$ and reactant temperature fixed at 34 cm/s and 300 K, respectively. $S_{L,0}$ was kept nominally constant for one data set by adjusting the stoichiometry at each H_2/CO ratio and pressure. $S_{L,0}$ estimates were determined using the PREMIX module [35] in CHEMKIN with the Davis H_2/CO mechanism for H_2/CO mixtures [36]. The parameter ranges explored in this study along with the symbol type and color scheme are summarized in Table E-1. Figure E-4 summarizes where the measured data are located on a Borghi-Peters diagram [37].

Table E-1: Investigated parameter space (cell colors for ϕ indicate the symbol fill color)

	Constant $S_{L,0}$			
U_0 (m/s)	20, 30, 50			
H_2 (%)	30	50	70	90
Symbol	○	◁	▷	◇
ϕ, 1 atm	0.61	0.55	0.51	0.48
ϕ, 5 atm	0.75	0.68	0.63	0.59
ϕ, 10 atm		0.75		
$S_{L,0}$ (m/s)	0.34			

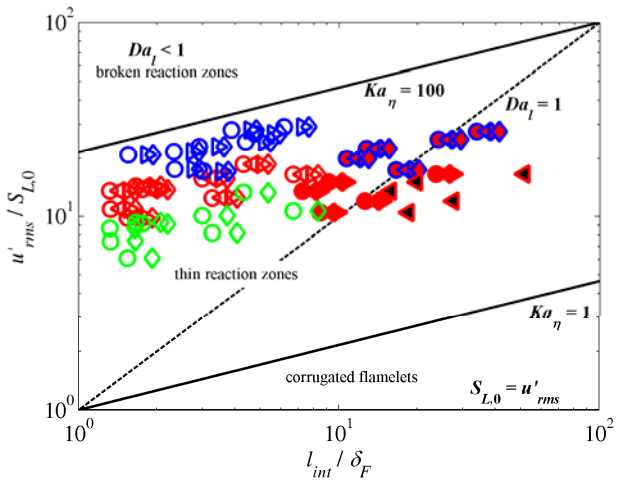

Figure E-4: Borghi-Peters diagram showing location of constant $S_{L,0}$ study data points for the 12 mm burner at 1, 5 and 10 atm.

E.3.2 Stretch Sensitivity Calculations

Stretch sensitivity calculations were performed for the mixtures in Table E-1. Stretch sensitivities were calculated using an opposed-flow calculation of two premixed flames with a nozzle separation distance of 20 mm using the OPPDIF [38] module in CHEMKIN. An arc length continuation method was used to determine the extinction point. From these calculations, various stretched properties of the mixture were extracted. In this work the displacement laminar flame speed is considered, determined from the minimum velocity upstream of the reaction zone, as suggested by Wu and Law [39]. These calculations are performed using detailed kinetics and transport properties which naturally incorporate both non-unity Lewis number and differential diffusion effects.

Figure E-5 plots a typical steady-state calculation showing the stretch sensitivity of a 30/70 H_2/CO mixture whose $S_{L,0}$ is kept constant at 34 cm/s across the pressures by adjusting the equivalence ratio. At least three global parameterizations of the mixtures stretch sensitivity can be deduced from Figure E-5 - the Markstein length, l_M, the extinction stretch rate, κ_{ext}, and the maximum stretched laminar flame speed, S_{Lmax}. Note the different pressure sensitivities of these three quantities. For example, if pressure is increased by a factor of 5, the extinction stretch rate and Markstein length increase and decrease by a factor of approximately 5, respectively. This can be explained by the thinning of the flame with pressure. In fact, these two effects appear to nearly compensate each other with the result that $S_{L,max}$ is relatively insensitive to pressure. In fact, $S_{L,max}$ remains almost constant above 5 atm and actually decreases beyond 12.5 atm. Although not shown, l_M, S_{Lmax}, and κ_{ext} all increase with H_2 content of the fuel at a given pressure for the constant $S_{L,0}$ sweeps.

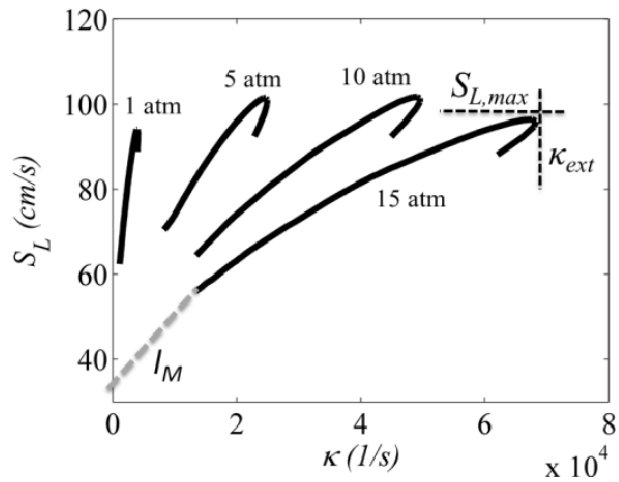

Figure E-5: Pressure effect on mixture stretch sensitivity for 30% H_2 mixtures at constant $S_{L,0}$.

Chapter E-4: Results and Analysis

E.4.1 H_2/CO Sweeps at Constant $S_{L,0}$

This section presents new $S_{T,GC}$ data acquired at 5 and 10 atm, supplementing the 1 atm data previously presented in Ref. [22]. The 1 atm data will be shown alongside this new data in following sections. As described earlier, all data were acquired for mixtures where the H_2/CO ratio and equivalence ratio were simultaneously adjusted to maintain the same $S_{L,0}$ value of 34 cm/s. Figure E-6 plots $S_{T,GC}$ as a function of u'_{rms} normalized by $S_{L,0}$ for the range of conditions reported in Table E-1.

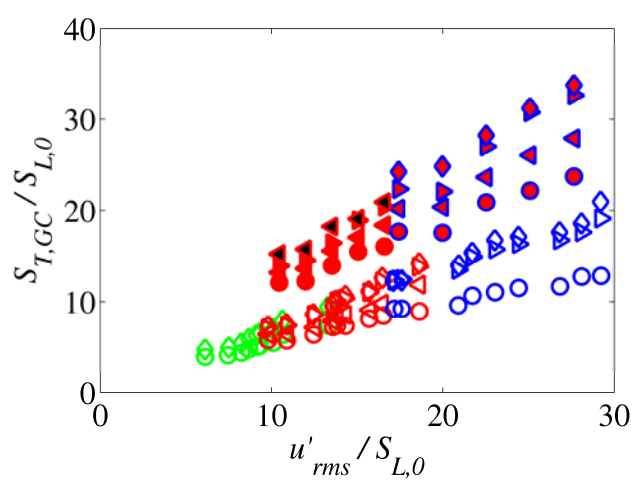

Figure E-6: $S_{T,GC}$ as a function of u'_{rms} normalized by $S_{L,0}$ at various mean flow velocities, H_2/CO ratios, and pressures for the 12 mm diameter burner (See Table E-1 for the legend of mixture conditions, flow velocities and pressures).

Several important observations can be made from Figure E-6 . First, fuel effects are clearly present at the elevated pressure conditions, i.e., different H_2/CO blends at constant $S_{L,0}$ and u'_{rms} have different turbulent consumption speeds. For example, at 5 atm and $u'_{rms}/S_{L,0} = 28$, $S_{T,GC}/S_{L,0}$ increases by about 50% as the H_2 content increases from 30% to 90%. A second important observation is the pressure effects. Specifically, $S_{T,GC}$ at 5 atm is approximately double its value at 1 atm, and increases slightly further at 10 atm. This increase is quantified in Figure E-7, which plots the ratio of $S_{T,GC}/S_{L,0}$ at 5 and 10

atm to 1 atm for each mixture and mean flow velocity as a function of turbulence intensity. The figure shows that this ratio has values of about 1.8 and 2.2 at 5 and 10 atm, respectively. Note that this is not an $S_{L,0}$ effect, as $S_{L,0}$ is fixed at 34 cm/s. Furthermore, note that the corresponding low stretch sensitivity of these mixtures, as quantified by l_M actually decreases with pressure, while the high stretch sensitivity, as quantified by $S_{L,max}$ stays relatively constant with pressure. These points will be considered more fully in the next section.

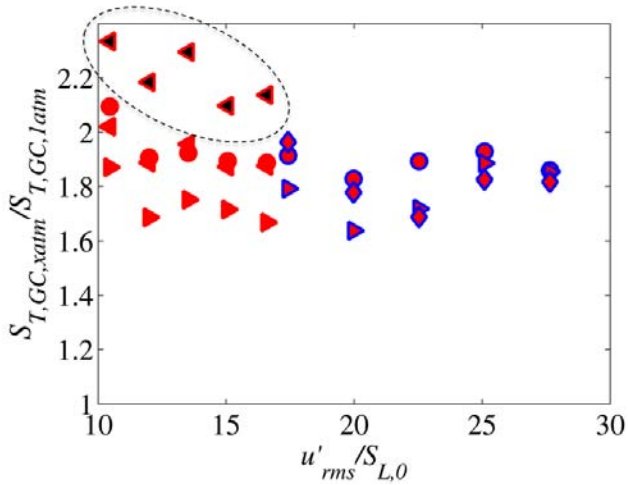

Figure E-7: Ratio of $S_{T,GC}$ at 5 and 10 atm to 1 atm across the range of turbulence intensities investigated. The 10 atm ratio is circled, while the rest are 5 atm ratios.

E.4.2 Analysis: $S_{L,max}$ Scaling of Data

In this section, the data in Figure E-6 and previously reported 1 atm data are correlated using the quasi-steady scaling law, Eq. (E-4). Similar calculations as shown in Figure E-5 were performed to normalize the measured turbulent flame speed data, as shown in Figure E-8. This figure shows that both the 1 and 5 atm datasets collapse quite well individually, but that there are systematic differences between them.

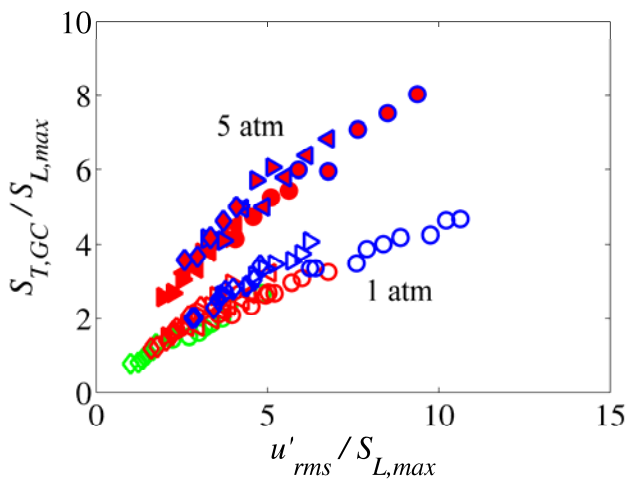

Figure E-8: $S_{T,GC}$ as a function of u'_{rms} normalized by $S_{L,max}$ at various mean flow velocities, H_2/CO ratios and pressures using the 12 mm diameter burner (See Table E-1 for the legend).

E.4.3 Analysis: Chemical Time Scaling of Data

In interpreting the factors leading to both the collapse of some data and scatter in others when scaled using Eq. (E-4), it is important to recall the limitations of this expression summarized in Chapter 1. We

believe that the scatter shown in these data stems from the fact that $S_{L,max}$ is not a fundamental property of the mixture. For example, the burning velocity of highly stretched flames is a function of the manner in which the flame is stretched, i.e., by tangential flow straining or curvature [40], as well as the stretch profile through the flame (manifested by, for example, variation in quantities such as $S_{L,max}$ or κ_{ext} with opposed-flow nozzle separation distance or velocity profile [41]). Note that our calculations derive $S_{L,max}$ from a tangentially strained flame, while the actual flame leading points are both curved and strained. We are currently analyzing this further with curved flame computations. In addition, very different $S_{L,max}$ values are obtained when using consumption and displacement based burning velocities [42]. Finally, $S_{L,max}$ is a frequency dependent quantity [25]; the steady-state values used here are only appropriate if the internal structure of the leading point is quasi-steady. We have analyzed several of these points, but do not reproduce the different analyses for sake of space. Instead, we focus on the non-quasi-steady chemistry point, as analysis indicates that the observed trends are most consistent with this effect.

In unsteady opposed-flow calculations, Im and Chen [25] show that the absolute value of the Markstein length and $S_{L,max}$ both decrease as the frequency of the imposed strain rate is increased. This dependency can be incorporated into Eq. (E-1) by replacing $S_{L,max}$ with $S_{L,\max}(\omega)$, which is the frequency dependent $S_{L,max}$. The resulting expression can then be divided by the steady-state $S_{L,max}$ to give:

$$\frac{S_T}{S_{L,\max}} = \frac{S_{L,\max}(\omega)}{S_{L,\max}} + \frac{\langle u'_{rms} \rangle_{LP}}{S_{L,\max}} \qquad \text{(E-6)}$$

The degree of non-quasi-steadiness can be determined using the time scale ratio, $\tau_{S_{L,\max}} / \tau_{flow}$, where $\tau_{S_{L,\max}}$ is a chemical time scale associated with the highly stretched flamelets and τ_{flow} is a characteristic fluid mechanic time scale; i.e., $S_{L,\max}(\omega)/S_{L,\max} \to 1$ as $\tau_{S_{L,\max}} / \tau_{flow} \to 0$. The chemical time scale, $\tau_{S_{L,\max}}$, is given by $\tau_{S_{L,\max}} = \delta_F\big|_{S_{L,\max}} / S_{L,\max}$ where $\delta_F\big|_{S_{L,\max}}$ is the flame thickness at $S_{L,\max}$ calculated using $\delta_F = (T_b - T_u)/(dT/dx)_{\max}$.

The variation in the chemical time scale across H_2/CO mixtures and pressures is shown in Figure E-9. The point corresponding to 0% H_2 is a pure CH_4/air. These data show that pressure exerts the strongest influence on the chemical time. For example, at a fixed H_2 content of 30%, there is a factor of about 12 reduction in $\tau_{S_{L,\max}}$ associated with a corresponding pressure increase from 1 to 10 atm. In contrast, $\tau_{S_{L,\max}}$ increases by about a factor of 3.5 as the H_2 content is increased from 30% to 90% at 1 atm.

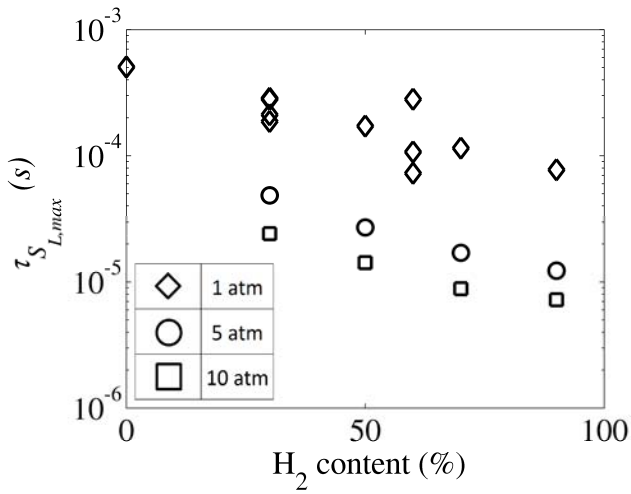

Figure E-9: Variation in $\tau_{S_{L,\max}}$ as a function of H_2 content for the different mixtures and conditions investigated. 0% H_2 corresponds to the pure CH_4 mixture.

Figure E-10 plots $S_{T,GC}/S_{L,\max}$ as a function of $\tau_{S_{L,\max}}/\tau_{flow}$, where $\tau_{flow} = D/U_0$, at fixed turbulence intensities, $u'_{rms}/S_{L,\max}$ = 3 and 6.5 for the 12 mm burner data. For reference, the straight lines indicate a power law fit to the data given by $S_{T,GC}/S_{L,\max} \sim \left(\tau_{S_{L,\max}}/\tau_{flow}\right)^b$ where $b \sim -0.33$.

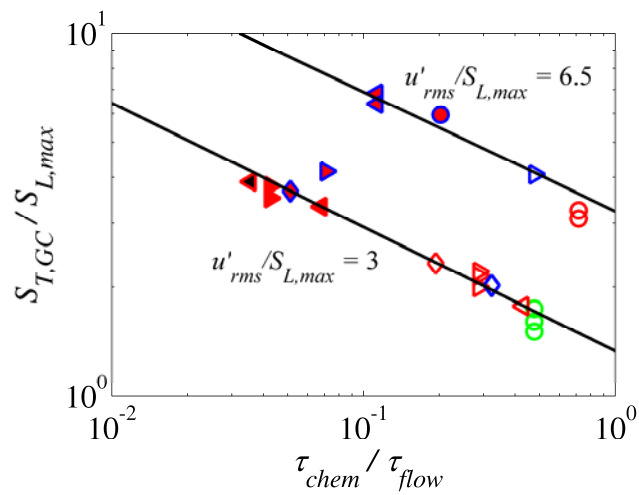

Figure E-10: Dependence of $S_{T,GC}/S_{L,\max}$ upon $\tau_{S_{L,\max}}/\tau_{flow}$ at a fixed turbulence intensity, $u'_{rms}/S_{L,\max}$ = 3 and 6.5 for the 12 mm diameter burner.

Note the clear correlation between turbulent flame speed and time scale ratio across the entire range of pressure and fuel composition. Slower chemistry is associated with lower values of the normalized turbulent flame speed, possibly since the effective $S_{L,\max}$ value of the non-quasi-steady flame is lower than its quasi-steady value, as expected from Eq. (E-6). While the time scale ratios are much less than unity (indicating that the chemistry is actually quasi-steady with respect to the large scales), the corresponding ratios calculated using Kolmogorov time scales range from 20-95 for the same data. In other words, significant non-quasi-steady chemistry effects would be expected for small flow length scale-flame interactions.

Chapter E-5: Conclusions and Future Work

This report describes turbulent consumption speed measurements of H_2/CO blends at 5 and 10 atm. Experiments were conducted for mean flow velocities of 30 and 50 m/s for H_2/CO blends ranging from 30/70 to 90/10 by volume. It was found that at the same $S_{L,0}$ when the pressure was increased by a factor of 5, the consumption speed increased by almost a factor of 2.

The data were then normalized with $S_{L,max}$ as per the scaling law derived in our earlier work. These data show that, at a given pressure, different fuel compositions and equivalence ratio data collapse. However, systematically different trends are observed with the 5 and 10 atm data. There is some evidence that these systematic differences are more fundamentally due to non-quasi-steady effects, as the pressure differences can be reasonably correlated with a computed chemical time scale for the 12 mm burner. In particular, if these pressure effects are fundamentally due to non-quasi-steady effects, then the faster chemistry associated with higher pressure flames suggests that the turbulent flame speed should cease to exhibit a pressure sensitivity at pressures where the flame is internally quasi-steady.

Future work is aimed at extending the $S_{T,GC}$ measurements to mixtures that simulate process and refinery gases, landfill and biomass gases, and gasified coal/petcoke. These mixtures are simulated using different mixtures of CH_4, C_3H_8, H_2, CO and CO_2. Measurements of mixtures that contain C_3H_8 and CO_2 will be performed at atmospheric conditions due to complications associated with maintaining these components in the gas phase at high pressures. For the other mixtures, measurements of $S_{T,GC}$ will be performed at 5 and possibly 10 atm over a range of turbulence intensities.

References

1. T. Lieuwen, Yang, V., Syngas Combustion, CRC Press, 2009, p.^pp.
2. J. Klimstra, SAE transactions 95 (6) (1986) 962-972
3. M. Moliere, ASME Paper# GT-2002-30017 (2002)
4. T. Lieuwen, McDonell, V., Petersen, E., Santavicca, D., Journal of Engineering for Gas Turbines and Power 130 (2008) 011506
5. T. C. Lieuwen, Yang, V., Progress in Astronautics and Aeronautics (2005)
6. L. Figura, Lee, J.G., Quay, B.D., Santavicca, D. , in: *ASME Paper # GT2007-27298*, 2007.
7. C. M. Vagelopoulos, Egolfopoulos, F. N., Symposium (International) on Combustion 25 (1) (1994) 1317-1323
8. A. N. Lipatnikov, Chomiak, J., Progress in Energy and Combustion Science 28 (1) (2002) 1-74
9. A. Lipatnikov; J. Chomiak, Progress in Energy and Combustion Science 31 (1) (2005) 1-73
10. J. F. Driscoll, Progress in Energy and Combustion Science 34 (1) (2008) 91-134
11. M. Nakahara; H. Kido, AIAA Journal 46 (7) (2008) 1569-1575
12. H. Kido; M. Nakahara; K. Nakashima; J. Hashimoto, Proceedings of the Combustion Institute 29 (2) (2002) 1855-1861
13. D. Littlejohn; R. K. Cheng, Proceedings of the Combustion Institute 31 (2) (2007) 3155-3162
14. R. Cheng; D. Littlejohn; P. Strakey; T. Sidwell, Proceedings of the Combustion Institute 32 (2) (2009) 3001-3009
15. M. Fairweather; M. P. Ormsby; C. G. W. Sheppard; R. Woolley, Combustion and Flame 156 (4) (2009) 780-790
16. S. Daniele; P. Jansohn; J. Mantzaras; K. Boulouchos, Proceedings of the Combustion Institute 33 (2) (2011) 2937-2944
17. T. Kitagawa; T. Nakahara; K. Maruyama; K. Kado; A. Hayakawa; S. Kobayashi, International Journal of Hydrogen Energy 33 (20) (2008) 5842-5849
18. C. K. Law, Combustion Physics, Cambridge University Press, New York, 2006, p.^pp.
19. V. R. Kuznetsov; V. A. Sabel'nikov, in: Turbulence and Combustion, V. R. Kuznetsov; V. A. Sabel'nikov; P. A. Libby, (Eds.) Hemisphere Publishing Corporation: Moscow, 1986; p 362.
20. V. P. Karpov; A. N. Lipatnikov; V. L. Zimont, in: Advances in Combustion Science: In honor of Ya. B. Zel'dovich, W. A. Sirignano; A. G. Merzhanov; L. De Luca, (Eds.) AIAA: Reston, VA, 1997; Vol. 173, pp 235-250.
21. F. Dinkelacker; B. Manickam; S. P. R. Muppala, Combustion and Flame 158 (9) (2011) 1742-1749
22. P. Venkateswaran; A. Marshall; D. H. Shin; D. Noble; J. Seitzman; T. Lieuwen, Combustion and Flame 158 (8) (2011) 1602-1614
23. G. Damköhler, Zeitschrift Electrochem 46 (1940) 601-626
24. A. N. Lipatnikov; J. Chomiak, Combustion Science and Technology 137 (1-6) (1998) 277-298
25. H. G. Im; J. H. Chen, Proceedings of the Combustion Institute 28 (2) (2000) 1833-1840
26. H. Kobayashi; T. Tamura; K. Maruta; T. Niioka; F. A. Williams, Proceedings of the Combustion Institute 26 (1) (1996) 389-396
27. F. Gouldin; R. K. Cheng International Workshop on Premixed Turbulent Flames. http://eetd.lbl.gov/aet/combustion/workshop/workshop.html
28. R. K. Cheng, in: Synthesis Gas Combustion: Fundamentals and Applications, T. C. Lieuwen; V. Yang; R. A. Yetter, (Eds.) CRC Press: 2009; p 403.

29. A. Marshall; P. Venkateswaran; D. Noble; J. Seitzman; T. Lieuwen, Experiments in Fluids 51 (3) (2011) 611-620
30. L. Prandtl, (1932)
31. G. Taylor, ZAMM-Journal of Applied Mathematics and Mechanics/Zeitschrift für Angewandte Mathematik und Mechanik 15 (1-2) (1935) 91-96
32. C. Dasch, Applied Optics 31 (8) (1992) 1146–1152
33. D. Ballal; A. Lefebvre, Proceedings of the Royal Society of London. Series A, Mathematical and Physical Sciences 344 (1637) (1975) 217-234
34. G. Smallwood; Ö. Gülder, Combustion and Flame 101 (4) (1995) 461-470
35. R. J. Kee; J. F. Grcar; M. Smooke; J. Miller, Sandia National Laboratories Report SAND85-8240, Sandia National Laboratories, Livermore (1983)
36. S. G. Davis; A. V. Joshi; H. Wang; F. Egolfopoulos, Proceedings of the Combustion Institute 30 (1) (2005) 1283-1292
37. N. Peters, Journal of Fluid Mechanics 384 (1999) 107-132
38. R. J. Kee; J. A. Miller; G. H. Evans; G. Dixon-Lewis, Proceedings of the Combustion Institute 22 (1) (1989) 1479-1494
39. C. K. Wu; C. K. Law, Proceedings of the Combustion Institute 20 (1) (1985) 1941-1949
40. W. Peiyong; S. Hu; J. A. Wehrmeyer; R. W. Pitz, in: *42nd AIAA Aerospace Sciences Meeting and Exhibit*, AIAA: AIAA-2004-148, Rena, NV, 2004.
41. F. N. Egolfopoulos, Proceedings of the Combustion Institute 25 (1) (1994) 1375-1381
42. T. Poinsot; D. Veynante, Theoretical and Numerical Combustion, RT Edwards, Inc., Philadelphia, 2005, p.^pp.

APPENDIX F:
Topical Report: Diffusion Transport Property Calculator

Public Interest Energy Research (PIER) Program

FINAL PROJECT REPORT

DEVELOPMENT AND EVALUATION OF GAS FUEL INTERCHANGEABILITY CRITERIA AND METHODOLOGIES

APPENDIX F

TOPICAL REPORT: Diffusion Transport Property Calculator

Prepared for: California Energy Commission

Prepared by: University of California, Irvine – Combustion Laboratory

MAY 2013

UCI COMBUSTION LABORATORY

UNIVERSITY of CALIFORNIA · IRVINE

Prepared by:

Primary Author(s):
Matthew Clarey
Brendan Shaffer
Vince McDonell

UCI Combustion Laboratory
University of California, Irvine
131 Engineering Laboratory Facility
Irvine, California 92697-3550
Tel: (949) 824-5950 x121
Fax: (949) 824-7423
www.ucicl.uci.edu

Contract Number: 500-08-034

Prepared for:

California Energy Commission

Marla Mueller
Contract Manager

Linda Spiegel
Office Manager
Energy Generation Research Office

Laurie ten Hope
Deputy Director
RESEARCH AND DEVELOPMENT DIVISION

Robert Oglesby
Executive Director

DISCLAIMER

This report was prepared as the result of work sponsored by the California Energy Commission. It does not necessarily represent the views of the Energy Commission, its employees or the State of California. The Energy Commission, the State of California, its employees, contractors and subcontractors make no warrant, express or implied, and assume no legal liability for the information in this report; nor does any party represent that the uses of this information will not infringe upon privately owned rights. This report has not been approved or disapproved by the California Energy Commission nor has the California Energy Commission passed upon the accuracy or adequacy of the information in this report.

F.1 Introduction

Diffusive transport can be very important within flames especially those with non-unity Lewis numbers (ratio of thermal diffusivity to mass diffusivity of a mixture). Therefore, it is important to be able to calculate the properties associated with diffusive transport. Currently, Chemkin calculates these properties for any flame speed calculations performed, however, their extraction is clumsy and time consuming. Efforts were made to write Fortran scripts that interfaced directly with the Fortran modules within Chemkin to extract these properties in a more time efficient manner. However, this proved difficult. It was then determined that it may be easier to implement the transport model in a platform that is well known at the UC Irvine Combustion Lab using the literature from which Chemkin developed its methodologies (Dixon-Lewis 1968) (Kee, Coltrin and Glarborg 2003) (Monchick and Mason November 1961).This program can calculate the following:

1. Thermal Diffusivity
2. Pure Species Thermal Conductivity
3. Mixture Thermal Conductivity (multicomponent and mixture averaged)
4. Thermal Diffusion Coefficients
5. Binary Diffusion Coefficients
6. Pure Species Viscosity
7. Mixture Viscosity
8. Species Densities
9. Mixture Density
10. Species Specific Heat Capacity (constant pressure)
11. Mixture Specific Heat Capacity (constant pressure)

F.2. Instructions

This Matlab script calculates the transport properties of various gas mixtures at different temperatures and pressure. The user need only place the input file in the appropriate folder (Transport Code) with the appropriate name (INPUT.xls), delete the existing OUTPUT.xls file, and run the PROPS.m file. An example of the INPUT.xls and OUTPUT.xls format is shown in Table F-1 and F-2, respectively. The output properties can be formatted in any way you would like, you only need to change the "OUTPUT" section at the bottom of the PROPS.m file.

This program can calculate the following:

1. Thermal Diffusivity
2. Pure Species Thermal Conductivity
3. Mixture Thermal Conductivity (multicomponent and mixture averaged)
4. Thermal Diffusion Coefficients
5. Binary Diffusion Coefficients
6. Pure Species Viscosity
7. Mixture Viscosity
8. Species Densities
9. Mixture Density
10. Species Specific Heat Capacity (constant pressure)
11. Mixture Specific Heat Capacity (constant pressure)

There are also several other properties not listed here that are calculated in order to calculate the above properties.

Comparing results with http://navier.engr.colostate.edu/tools/diffus.html for a sample set shows that this code produces workable data. This can be seen in the verification.xls file. The only issue is that some of the thermal diffusivity values show discrepancies. For certain gases, namely CO and N2, the thermal conductivities are much different than the "accepted" value from the website. Other than that the rest of the data show a percent error less than 5% from the website.

Table F-1 INPUT.xls Format

	A	B	C	D	E	F	G	H	…
1	Pressure [PA]	Temp [K]	H2	CO	CH4	C2H6	O2	N2	…
2	101325	562.1111	0.1152	0	0	0	0.1858	0.6988	…
3	101325	555.3889	0.1185	0	0	0	0.1851	0.6962	…
…	…	…	…	…	…	…	…	…	…

Pressure must be in Pascals, temperature in Kelvin. Under each molecule is the mole fraction for that case. The user can either enter moles of each component or the mole fraction.

This code is built to accept as many mixtures (i.e., rows) as desired. Be sure to use the full chemical symbol exactly as it appears in the transport file from Chemkin.

Table F-2 OUTPUT.xls Format

	A	B	C	D	E	F	G
1	$C_{p,mix}$ $\left[\frac{J}{kgK}\right]$	ρ $\left[\frac{kg}{m^3}\right]$	ν $\left[\frac{m^2}{s}\right]$	$Thermal\ Conductivity$ $\left[\frac{W}{mK}\right]$	$Thermal\ Diffusivity$ $\left[\frac{m^2}{s}\right]$	$Mix\ Diffusivity\ Gas\ 1$ $\left[\frac{m^2}{s}\right]$	$Mix\ Diffusivity\ Gas\ N$ $\left[\frac{m^2}{s}\right]$
2	…	…	…	…	…	…	…

F.3 Mechanism Transport File

Each kinetic mechanism includes a file that includes information important for modeling the diffusive transport of the various molecules included in the particular mechanism. This file typically has the word "tran" or "transport" located somewhere within its name specifying that it contains the transport information. The mechanism used in this particular model is from the National University of Ireland, Galway, http://c3.nuigalway.ie/mechanisms.html, "Natural Gas to/including C5 (2007/08)". These mechanism files are located within the EXCEL_FILES folder. The format of these files were prepared in accordance to the format needed for Chemkin. The Chemkin Input Manual (CHEMKIN/CHEMKIN-PRO15101: Input Manual 2010) discusses the specifics of this format. This manual is included as the Input.pdf in the PDF folder. The formatting of the mechanism transport file will be discussed here. The nC5_44_HighTempMech_tran.xls file under the EXCEL_FILES folder contains the molecular data necessary for modeling diffusive transport in this format (by column):

1. Molecule symbol (first column)
2. An index indicating whether the molecule is monatomic, linear or nonlinear. If the index is 0, the molecule is a single atom. If the index is 1 the molecule is linear, and if it is 2, the molecule is nonlinear. (second column)
3. The Lennard –Jones potential well depth ϵ/k_B in Kelvins. (third column)
4. The Lennard –Jones collision diameter σ in angstroms. (fourth column)
5. The dipole moment μ in Debye. (fifth column)
6. The polarizability α in cubic angstroms. (sixth column)
7. The rotational relaxation collision number Z_{rot} at 298 K. (seventh column)

By knowing the formatting of this file, the transport can be modified or replaced with relative ease.

The thermodynamic mechanism file must also be used to model the diffusive transport of the molecules. Galway is again used for this file, nC5_44_HighTempMech_therm.xls. For specifics on the format of the transport library that Chemkin uses reference their Input Manual (CHEMKIN/CHEMKIN-PRO15101: Input Manual 2010). This Matlab code uses an excel file made from the mechanism. Every character of the mechanism corresponds to a separate column in the excel file.

If a different mechanism is used a new 'Period Table.xls' might need to be created based upon the new molecules that might appear in the file. The Matlab script only cares about the two left columns of this file. The heading must remain the same, and the molecule symbol must be exactly as it appears in the mechanism. The second column is the molecular weight in grams per mole. The first row must have "Molecule" and "Molecular Mass" for the first two indices, respectively.

F.4 Collision Integral Tables

The collision integral tables were copied from Monchick and Mason (Monchick and Mason November 1961). They were placed into an excel file and depend on the reduced dipole moment of the collision and the reduced temperature Equations (4) and (5) respectively. If a collision integral is needed a quadratic interpolation is taken on the table.

F.5 Theory

The theory for the calculations comes from a combination of sources. For the most part all equations were taken from Chemically Reacting Flow (Kee, Coltrin and Glarborg 2003). Dixon-Lewis (Dixon-Lewis 1968) and CHEMKIN Theory Manual (CHEMKIN Theory Manual 2010) were also used in the construction of this program.

Reduced Molecular Mass

$$m_{ij} = \frac{m_i m_j}{m_i + m_j} \qquad [kg] \qquad \textbf{(F-1)}$$

$$m_i \quad = \quad molecular\ mass \qquad [kg]$$

Reduced Collision Diameter

$$\sigma_{ij} = \frac{\sigma_i + \sigma j}{2} \qquad [m] \qquad \textbf{(F-2)}$$

$$\sigma_k \quad = \quad collision\ diameter \qquad [m]$$

Interaction Well Depth

$$\epsilon_{ij} = \sqrt{\epsilon_i \epsilon j} \qquad [] \qquad \textbf{(F-3)}$$

$$\epsilon_i \quad = \qquad []$$

Reduced Dipole Moment of the Collision

$$\delta_{ij}^* = \frac{1}{2}\frac{\bar{\mu}_\iota \bar{\mu}_J}{\epsilon_{ij}\sigma_{ij}^3} \qquad \textbf{(F-4)}$$

$$\bar{\mu}_\iota \quad = \quad dipole\ moment \qquad [Cm]$$

For the case of a polar molecule interacting with a nonpolar molecule:

$$\epsilon_{ij} \quad = \quad \xi^2\sqrt{\epsilon_i \epsilon j}$$

$$\sigma_{ij} \quad = \quad \frac{\sigma_i + \sigma j}{2}\xi^{-1/6} \qquad [m]$$

$$\xi \quad = \quad 1 + \frac{1}{4}\alpha_i^* \overline{\mu_J^*}\sqrt{\frac{\epsilon_j}{\epsilon_i}}$$

$$\alpha_i^* \quad = \quad \frac{\alpha_i}{\sigma_i^3}$$

$$\overline{\mu_J^*} \quad = \quad \frac{\bar{\mu}_J}{\sqrt{\epsilon_j \sigma_j^3}}$$

Reduced Temperature

$$T^* = \frac{T k_B}{\epsilon} \tag{F-5}$$

Pure Species Viscosity

$$\mu_k = \frac{5}{16}\frac{\sqrt{\pi m_k k_B T}}{\pi \sigma_k^2 \Omega_{kk}^{(2,2)\star}} \qquad \left[\frac{kg}{m\ s}\right] \tag{F-6}$$

Boltzmann Constant	k_B	$= 1.380648813 \times 10^{-23}$	$[J/K]$
	T	$= temperature$	$[K]$
	σ_k	$= collision\ diameter$	$[m]$
	$\Omega_{kk}^{(2,2)\star}$	$= collision\ integral$	

The collision integral depends on the reduced temperature T^* and the reduced dipole moment of the collision δ_{ij}^* equations (5) and (6), respectively. Collision integrals are quadratic interpolations of the appropriate table (IV through VIII) from Monchick and Mason (Monchick and Mason November 1961).

Pure Species Thermal Conductivity

$$\lambda_k = \frac{\mu_k}{W_k}\left(f_{trans} C_{v,trans} + f_{rot} C_{v,rot} + f_{vib} C_{v,vib}\right) \tag{F-7}$$

$$f_{trans} = \frac{5}{2}\left(1 - \frac{2}{\pi}\frac{C_{v,rot}}{C_{v,trans}}\frac{A}{B}\right)$$

$$f_{rot} = \frac{\rho\, \mathcal{D}_{kk}}{\mu_k}\left(1 + \frac{2}{\pi}\frac{A}{B}\right)$$

$$f_{vib} = \frac{\rho\, \mathcal{D}_{kk}}{\mu_k}$$

$$A = \frac{5}{2} - \frac{\rho\, \mathcal{D}_{kk}}{\mu_k}$$

$$B = Z_{rot} + \frac{2}{\pi}\left(\frac{5}{3}\frac{C_{v,rot}}{R} + \frac{\rho\, \mathcal{D}_{kk}}{\mu_k}\right)$$

$$Z_{rot}(T) = Z_{rot}(298)\frac{F(298)}{F(T)} \tag{F-8}$$

$$F(T) = 1 + \frac{\pi^{3/2}}{2}\left(\frac{\epsilon/k_B}{T}\right)^{1/2} + \left(\frac{\pi^2}{4} + 2\right)\left(\frac{\epsilon/k_B}{T}\right) + \pi^{3/2}\left(\frac{\epsilon/k_B}{T}\right)^{3/2} \tag{F-9}$$

$$C_{v,vib} = C_v - C_{v,trans} - C_{v,rot}$$

Linear Molecule:	Nonlinear Molecule:	Monatomic Molecule
$\frac{C_{v,trans}}{R} = \frac{3}{2}$	$\frac{C_{v,trans}}{R} = \frac{3}{2}$	$\frac{C_{v,trans}}{R} = \frac{3}{2}$
$\frac{C_{v,rot}}{R} = 1$	$\frac{C_{v,rot}}{R} = \frac{3}{2}$	$\frac{C_{v,rot}}{R} = 0$
$C_{v,vib} = C_v - \frac{5}{2}R$	$C_{v,vib} = C_v - 3R$	$C_{v,vib} = 0$

Binary Diffusion Coefficient

$$\mathcal{D}_{jk} = \frac{3}{16}\frac{\sqrt{2\pi k_B^3 T^3/m_{jk}}}{P\pi\sigma_{jk}^2\Omega_{jk}^{(1,1)\star}} \qquad \textbf{(F-10)}$$

T	=	$temperature$	$[K]$
P	=	$pressure$	$[Pa]$
σ_{ij}	=	$reduced\ collsion\ diameter$	$[m]$
$\Omega_{jk}^{(1,1)\star}$	=	$collsion\ integral$	
m_{jk}	=	$reduced\ molecular\ mass$	
$Boltzmann\ Constant$ k_B	=	$1.380648813 \times 10^{-23}$	$[J/K]$

$$\mathcal{D}_{kk} = \frac{3}{8}\frac{\sqrt{\pi k_B^3 T^3/m_k}}{P\pi\sigma_k^2\Omega_{kk}^{(1,1)\star}} \qquad \textbf{(F-11)}$$

T	=	$temperature$	$[K]$
P	=	$pressure$	$[Pa]$
σ_k	=	$collsion\ diameter$	$[m]$
$\Omega_{kk}^{(1,1)\star}$	=	$collsion\ integral$	
m_k	=	$molecular\ mass$	$[kg]$
$Boltzmann\ Constant$ k_B	=	$1.380648813 \times 10^{-23}$	$[J/K]$

The collision integral depends on the reduced temperature T^* and the reduced dipole moment of the collision δ_{ij}^* equations (5) and (6), respectively. Collision integrals are quadratic

interpolations of the appropriate table (IV through VIII) from Monchick and Mason. (Monchick and Mason November 1961)

Species Density

$$\rho_k = \frac{PW_k}{RT} \tag{F-12}$$

Mixture Density

$$\rho = \sum_{i=1}^{K} X_i \rho_i \tag{F-13}$$

Mixture –Averaged Properties

Mixture Viscosity

$$\mu = \sum_{k=1}^{K} \frac{X_k \mu_k}{\sum_{j=1}^{K}\left(X_j \Phi_{kj}\right)} \qquad \textbf{(F-14)}$$

$$\Phi_{kj} = \frac{1}{\sqrt{8}}\left(1 + \frac{W_k}{W_j}\right)^{-1/2}\left(1 + \left(\frac{\mu_k}{\mu_j}\right)^{1/2}\left(\frac{W_j}{W_k}\right)^{1/4}\right)^2$$

K = $number\ of\ gas\ species$

X_k = $mole\ fraction\ of\ species\ k$

W_k = $molecular\ weight$ $\left[\frac{kg}{mol}\right]$

μ_k = $viscosity\ of\ species\ k$

Mixture Kinematic Viscosity

$$\upsilon = \frac{\mu}{\rho} \qquad \textbf{(F-15)}$$

Mixture –Averaged Thermal Conductivity

$$\lambda = \frac{1}{2}\left(\sum_{k=1}^{K} X_k \lambda_k + \frac{1}{\sum_{k=1}^{K} \frac{X_k}{\lambda_k}}\right) \qquad \textbf{(F-16)}$$

K = $number\ of\ gas\ species$

X_k = $mole\ fraction\ of\ species\ k$

λ_k = $thermal\ conductivity\ of\ species\ k$

Specific Heat

$$C_p = \sum_{k}^{K} X_k C_{p,k} \qquad \textbf{(F-17)}$$

$C_{p,k}$ = $species\ specific\ heat$

Species specific heat is calculated using the coefficients from the thermo mechanism.

Multicomponent Properties

All equations, unless otherwise noted, were taken from Chapter 12 of Chemically Reacting Flow(Kee, Coltrin and Glarborg 2003).

$$\begin{pmatrix} L^{00,00} & L^{00,10} & 0 \\ L^{10,00} & L^{10,10} & L^{10,01} \\ 0 & L^{01,10} & L^{01,01} \end{pmatrix} \begin{pmatrix} a_{00}^{1} \\ a_{10}^{1} \\ a_{01}^{1} \end{pmatrix} = \begin{pmatrix} 0 \\ X \\ X \end{pmatrix} \qquad \textbf{(F-18)}$$

$$X = \text{mole fraction vector}$$

$$L_{jk}^{00,00} = \frac{16T}{25P}\sum_{l=1}^{K}\frac{X_l}{m_j\mathcal{D}_{jl}}\{m_kX_k(1-\delta_{jl}) - m_jX_j(\delta_{jk}-\delta_{kl})\} \qquad \textbf{(F-19)}$$

$$L_{jk}^{00,10} = \frac{8T}{5P}\sum_{l=1}^{K}X_kX_l(\delta_{jk}-\delta jl)\frac{m_l(1.2C_{kl}^{*}-1)}{(m_k+m_l)\mathcal{D}_{kl}} \qquad \textbf{(F-20)}$$

$$L_{jk}^{10,00} = L_{kj}^{00,10} \qquad \textbf{(F-21)}$$

$$L_{jk}^{01,00} = L_{kj}^{00,01} = 0 \qquad \textbf{(F-22)}$$

$$L_{jk}^{10,10} = \frac{16T}{25P}\sum_{l=1}^{K}\frac{m_j}{m_k}\frac{X_jX_l}{(m_j+m_l)\mathcal{D}_{jl}} \times\left\{(\delta_{kl}-\delta_{jk})\left[\frac{15}{2}m_k^2+\frac{25}{4}m_l^2-3m_l^2B_{jl}^{*}\right] - 4m_km_lA_{jl}^{*}(\delta_{kl}-\delta_{jk})\left[1+\frac{5}{3\pi}\left(\frac{C_{j,rot}}{R\xi_{jl}}+\frac{C_{l,rot}}{R\xi_{jl}}\right)\right]\right\} \qquad \textbf{(F-23)}$$

$$L_{jk}^{10,01} = \frac{32T}{5\pi PC_{k,int}}\sum_{l=1}^{K}\frac{m_kA_{kl}^{*}}{(m_k+m_l)\mathcal{D}_{kl}}(\delta_{jl}+\delta_{jk})X_kX_l\frac{C_{k,rot}}{\xi_{kl}} \quad (*) \qquad \textbf{(F-24)}$$

$$L_{jk}^{0110} = L_{kj}^{10,01} \qquad \textbf{(F-25)}$$

$$L_{jj}^{01,01} = -\frac{8R^2}{\pi C_{j,int}^2}\frac{m_jX_j^2}{R\mu_j}\frac{C_{j,rot}}{R\,\xi_{jj}} - \frac{4RT}{C_{j,int}P}\left\{\sum_{l=1}^{K}\frac{X_jX_l}{[\mathcal{D}_{j\,int,l}]} + \sum_{l\neq j}^{K}\frac{12X_jX_l}{5\pi C_{j,int}}\frac{m_j}{m_l}\frac{A_{jl}^{*}}{\mathcal{D}_{jl}}\frac{C_{j,rot}}{\xi_{jj}}\right\} \qquad \textbf{(F-26)}$$

$$L_{jk}^{01,01} = 0\ (j \neq k) \qquad \textbf{(F-27)}$$

(*) Equation differs from Kee(Kee, Coltrin and Glarborg 2003) but instead follows Dixon-Lewis(Dixon-Lewis 1968). Within Chemically Reacting Flow the units did not seem to work out because there was an addition of another R. In Dixon-Lewis this was omitted.

	K	$=$	*number of gas species*		
	X_k	$=$	*mole fraction of species k*		

	m_k	$=$	$molecular\ mass$	$[kg]$	
	T	$=$	$temperature$	$[K]$	
	P	$=$	$pressure$	$[Pa]$	
	R	$=$	8.3144621	$\left[\frac{J}{molK}\right]$	
	δ_{jl}	$=$	$Kronecker\ Delta\ (1\ if\ j = l, 0\ if\ j \neq l)$		
	$C_{k,int} = C_p - \frac{3}{2}R$				
	C_p	$=$	$total\ heat\ capacity$		

The total heat capacity C_p if found using the polyfit described in the CHEMKIN Theory Manual (CHEMKIN Theory Manual 2010) where the coefficients are found using the thermo mechanism.

The relaxation collision number ξ_{jk} depend only on the species j ($all\ \xi_{jk} = \xi_{jj}$). These are the Z_{rot}'s described in Equation (8); Equation (9) gives it's temperature dependence (Kee, Coltrin and Glarborg 2003).

Binary Diffusion Coefficients for Internal Energy

$$\mathcal{D}_{j\ int,k} = \mathcal{D}_{jk}$$

The above equation is an approximation given in Chemically Reacting Flow (Kee, Coltrin and Glarborg 2003). For collisions between two polar molecules there is a correction factor, which is also given in Chemically Reacting Flow.

$$\mathcal{D}_{p\ int,p} = \frac{\mathcal{D}_{pp}}{1 + \delta'_{pp}}$$

$$\delta'_{pp} = \frac{2985}{\sqrt{T^3}}$$

Multicomponent Diffusion Coefficients

$$D_{jk} = X_j \frac{16T}{25Pm_k} \bar{W}\left(P_{jk} - P_{jj}\right) \tag{F-28}$$

$$(P) = (L^{00,00})^{-1}$$

Thermal Conductivity

$$\lambda_0 = \lambda_{0,trans} + \lambda_{0,int} \tag{F-29}$$

$$\lambda_{0,trans} = -4\sum_{k=1}^{K} X_k a_{k01}^1$$

$$\lambda_{0,int} = -4\sum_{k=1}^{K} X_k a_{k10}^1$$

Thermal Diffusivity

$$\alpha = \frac{\lambda}{\rho \frac{C_p}{W_{ave}}} \tag{F-30}$$

Thermal Diffusion Coefficients

$$D_k^T = \frac{8 m_k X_k}{5R}\ a_{k00}^1 \tag{F-31}$$

Mixture Diffusion Coefficients

$$D_{km} = \frac{1 - Y_k}{\sum_{j \neq k}^{K} \frac{X_j}{D_{jk}}} \tag{F-32}$$

Mass Fraction

$$Y_k = \frac{X_k W_k}{W_{ave}} \tag{F-33}$$

References

"CHEMKIN Theory Manual." Reaction Design, San Diego, 2010.

"CHEMKIN/CHEMKIN-PRO15101: Input Manual." Reaction Design, San Diego, 2010.

Dixon-Lewis, G. "Flame Structure and Flame Reaction Kinetics II. Transport Phenomena in Multicomponent Systems." *Proceedings of the Royal Society of London, Series A, Mathematical and Physical Sciences* 307, no. 1488 (1968): 111-135.

Kee, Robert J., Michael E. Coltrin, and Peter Glarborg. *Chemically Reacting Flow: Theory and Practice.* Hoboken: John Wiley & Sons Inc., 2003.

Monchick, L., and E. A. Mason. "Transport Properties of Polar Gases." *The Journal of Chemical Physics* 35, no. 5 (1961): 1676-1697.

APPENDIX G:
Topical Report: Flame Structure Tests and Interpretation

Public Interest Energy Research (PIER) Program

FINAL PROJECT REPORT

DEVELOPMENT AND EVALUATION OF GAS FUEL INTERCHANGEABILITY CRITERIA AND METHODOLOGIES

APPENDIX G
Topical Report: Flame Structure Tests and Interpretation

Prepared for: California Energy Commission

Prepared by: Department of Mechanical Engineering

University of Washington

MAY 2013

Prepared by:

Primary Author(s):
K.B. Fackler
Megan F. Karalus
Igor V. Novosselov
John C. Kramlich
Philip C. Malte

Department of Mechanical Engineering
University of Washiington
Box 352600
Seattle, WA 98195-2600

Contract Number: 500-08-034

Prepared for:

California Energy Commission

Marla Mueller
Contract Manager

Linda Spiegel
Office Manager
Energy Generation Research Office

Laurie ten Hope
Deputy Director
ENERGY RESEARCH AND DEVELOPMENT DIVISION

Robert P. Oglesby
Executive Director

DISCLAIMER

This report was prepared as the result of work sponsored by the California Energy Commission. It does not necessarily represent the views of the Energy Commission, its employees or the State of California. The Energy Commission, the State of California, its employees, contractors and subcontractors make no warrant, express or implied, and assume no legal liability for the information in this report; nor does any party represent that the uses of this information will not infringe upon privately owned rights. This report has not been approved or disapproved by the California Energy Commission nor has the California Energy Commission passed upon the accuracy or adequacy of the information in this report.

ACKNOWLEDGEMENTS

Support for this project was provided by the California Energy Commission through Agreement No. 500-08-034 through the University of California-Irvine. We wish to acknowledge Marla Mueller, Technical Lead, who is the Technical Project Officer at the California Energy Commission, and Vincent McDonell, who is the Project Manager at UC Irvine.

CHAPTER G.1: Introduction

G.1.1 Overview

Lean-premixed (LPM) combustion technology is utilized in state of the art gas turbines to provide extremely efficient power generation with low emissions. Traditionally, natural gas has been used almost exclusively in LPM combustion. While extensive research on natural gas-fueled LPM combustion has been reported, much less research has been conducted on the use of alternatives to natural gas for LPM combustion devices. In the future, gas turbines will be run with a variety of fuel compositions ranging from syngases with high H_2 content to landfill and digester gas, which are mainly composed of CH_4, CO_2, and N_2. Alternative fuel blends will have a wide range of heating values, flame speeds, and chemical composition. It is important to study the behavior of these fuels under LPM conditions to maximize performance efficiency, while minimizing the overall emissions. In order to use alternative fuels effectively, knowledge must be gained pertaining to the expected emissions at comparable combustion temperatures as well as the relative resistance to blowout.

The range of fuel compositions studied in this work is shown below in Table G-1. It is the goal of this research to study fuel blends that will typify the composition of future fuels. Five fuel categories are studied: (1) pure H_2, (2) process and refinery gas, including combinations of H_2, CH_4, C_2H_6, and C_3H_8, (3) oxygen blown gasified coal/petcoke composed of H_2, CO, and CO_2, (4) landfill and digester gas composed of CH_4, CO_2, and N_2, and (5) liquified natural gas (LNG)/shale/associated gases composed mainly of CH_4, C_2H_6, and C_3H_8. The baseline fuel for which all blends are compared is CH_4. In addition to the blends outlined in Table G-1, it is of both academic and general interest to perform parameterized studies within each fuel blend. Parameterized studies allow one to track differences that arise from variations in composition. As an example, we study mixtures of H_2/CH_4 that have limited application (e.g., 80/20). However, the study of this fuel blend provides useful chemical kinetic information that helps generalize the results of other more practical mixtures.

G.1.2 Report Outline

In order to avoid redundancy, many aspects of the first report: "Well-stirred Reactor Test Results and Interpretation" will not be included in the current one. Among the information found in the prior report is the following:

1. A literature review of recent work from other researchers that have studied LPM combustion of various alternatives to natural gas is presented in Chapter 1.
2. Chapter 2 provides a general overview of LPM combustion in industrial gas turbines, and the basic concepts of NO_X formation follows this discussion.
3. In Chapter 3, the details of the experimental setup are presented.
4. The zero dimensional chemical kinetic model that is used to interpret the experimental data is developed in Chapter 4.

5. The major experimental findings as well as modeled interpretation of the data are presented in Chapter 5.

Table G-1: Summary of gas composition used in this study

Category	Source		H_2	CO	CH_4	CO_2	N_2	C_2	C_3
1	High H_2	Range in Field	90 - 100						
		Nominal Fuel	100						
		Alternative Fuel	90			10			
2	Process and Refinery	Range in Field	25 - 55	10	30 - 65	5		0 - 25	0 - 25
		Nominal Fuel	25		50			25	
		Alternative Fuel 1	25		50				25
		Alternative Fuel 2	25		65			10	
		Alternative Fuel 3	55		35			10	
3	Gasified Coal/Petcoke (O_2 Blown)	Range in Field	35 - 40	45 - 50		10 - 15			
		Nominal Fuel	40	50		10			
		No Alternatives							
4	Landfill and Digester Gas	Range in Field			35 - 65	35 - 55	0 - 20		
		Nominal Fuel			50	35	15		
		Alternative Fuel 1			50	50			
		Alternative Fuel 2			50		50		
5	LNG	Range			75 - 95			5 - 25	
		See below							
	Shale Gas	Range			82 - 97	2.5		0 - 14	1
		See below							
	Associated Gas	Range			75 - 95			5 - 25	
		See below							
	LNG/Shale/ Associated Gases	Nominal Fuel			95			5	
		Alternative Fuel 1			90			10	
		Alternative Fuel 2			75			25	
		Alterntative Fuel 3			75				25

This report focuses only on new material and will serve as a supplement to the information presented in the previous report. This document is organized as follows:

1. In Chapter G.2, detailed reactor scans are presented for each alternative fuel category outlined in Table G-1.
2. CFD modeling results including both simplified global chemistry as well as modeling results from more detailed chemical mechanisms are presented in Chapter 3.
3. Finally, general conclusions and future research goals are outlined in Chapter 4.

CHAPTER G.2:
Experimental Flame Structure Measurements

In the following chapter, detailed reactor scans are presented for the fuel compositions outlined in Table G-1.

G.2.1 Reactor Scans

Detailed reactor scans are conducted for each fuel category at 2/3 of the reactor height as shown in Figure G-1. In all cases, the plots include the scan for pure CH_4 as a comparison point.

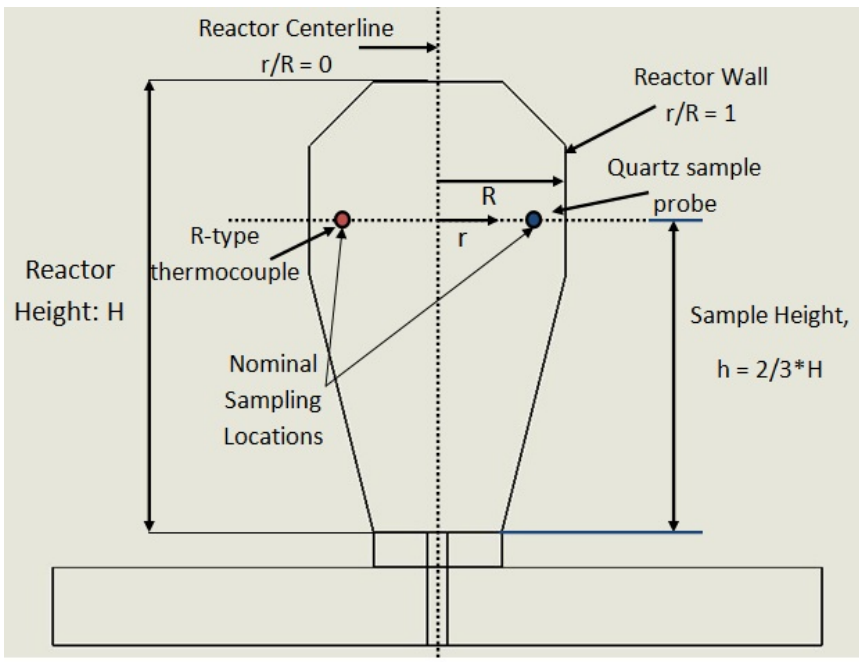

Figure G-1: Sampling locations within the JSR.

Both temperature and major species concentrations are measured radially from the reactor centerline to the reactor wall in order to gain perspective on the structure of the LPM flame for each fuel blend.

G.2.1.1 Pure H2

The temperature and NO_X profiles for H_2 and CH_4 are shown below in Figure G-2 and Figure G-3. Although these two fuels have the same temperature within the

recirculation zone, H_2 is far more reactive along the centerline in comparison to the CH_4 and all other pure alkane fuels. Despite a significantly higher temperature on LPM H_2 combustion is found to produce about 35% less NO_X in comparison to CH_4 measured at the nominal temperature of 1800 K within the recirculation zone.

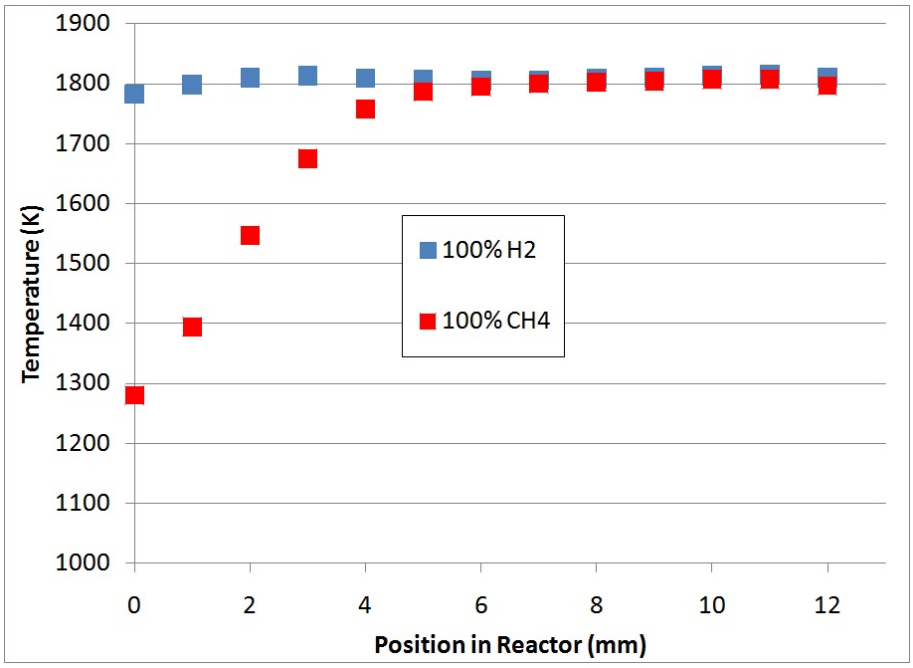

Figure G-2: Temperature profile across the JSR for LPM CH_4 and H_2 combustion.

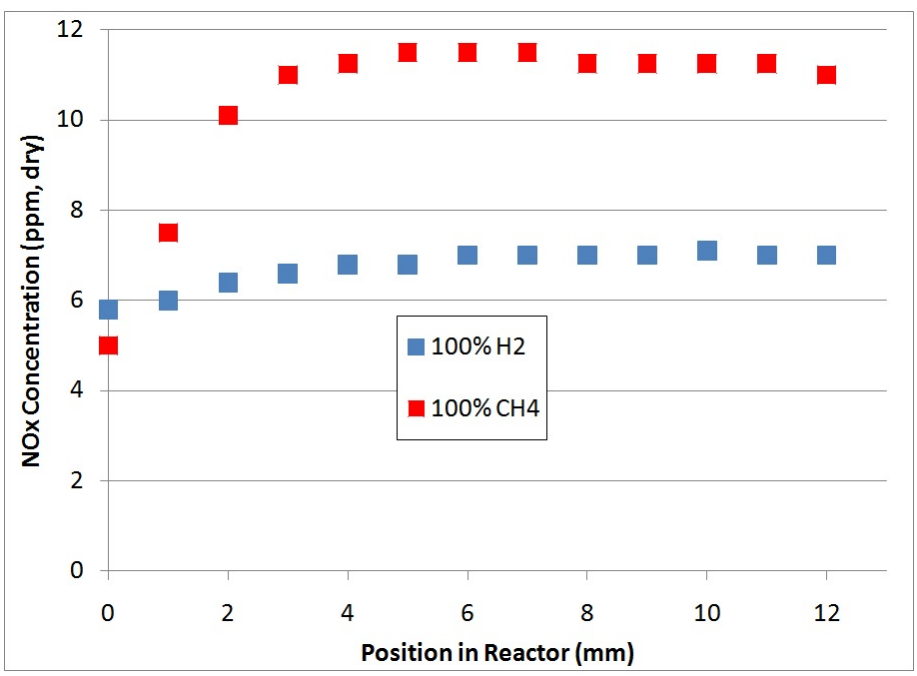

Figure G-3: NO_X concentration profile across the JSR for LPM CH_4 and H_2 combustion

G.2.1.2 Process and Refinery Blends

As mentioned above, process and refinery blends are composed mainly of H_2, CH_4, and other higher order hydrocarbons. Similar to the trend shown above, the addition of H_2 seems to increase reactivity on centerline while decreasing overall NO_X emissions. The temperature, CO, and NO_X profiles are shown in Figure G-4 through Figure G-6. The increase in reactivity is especially evident looking at the CO profiles in Figure G-6. While, the fuel blends with H_2 and C_2H_6 addition have CO profiles that peak on centerline, pure CH_4 combustion actually peaks off of centerline at a radial location that is slightly larger than the radius of the jet.

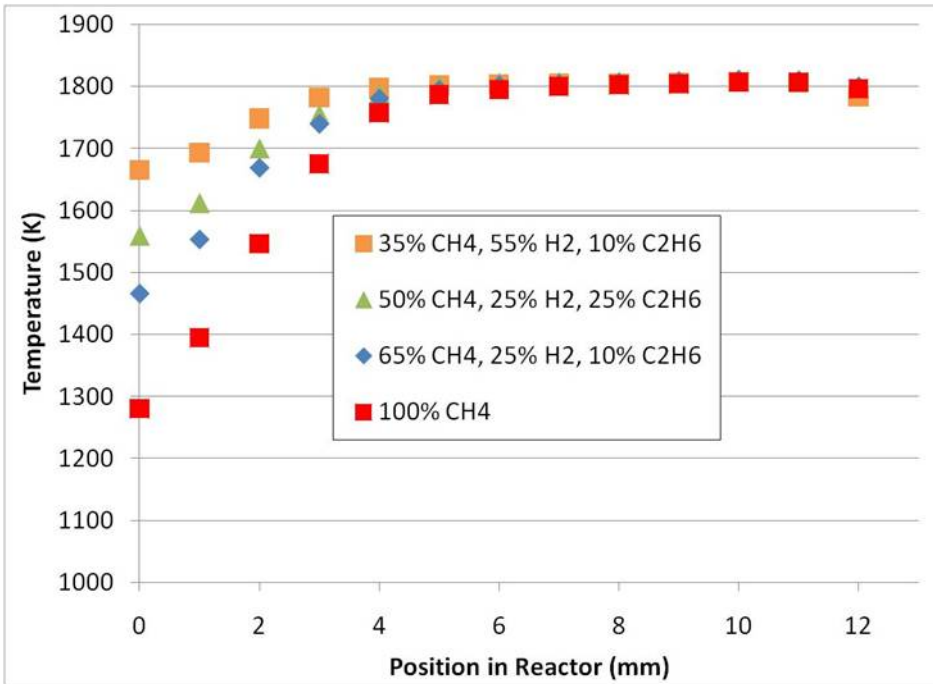

Figure G-4: Temperature profile across the JSR for the Process and Refinery Fuel

It is interesting to note the effect of C2H6 addition. Table G-1 shows that both the nominal process and refinery blend and alternative blend 2 contain 25% H_2. However, the nominal blend has 15% more C_2H_6 and this is replaced by CH_4 in the alternative fuel. While both of these blends are more reactive than pure CH_4 on centerline, the addition of C_2H_6 actually increases this reactivity and temperature by about 100 K. In Figure G-5 the NO_X profiles are almost identical within the accuracy of the measurements with more C_2H_6. As mentioned above, this result is consistent with previous studies showing that NO_X emissions increase with increasing fuel mole fraction of heavier hydrocarbons [1], [2], [3].

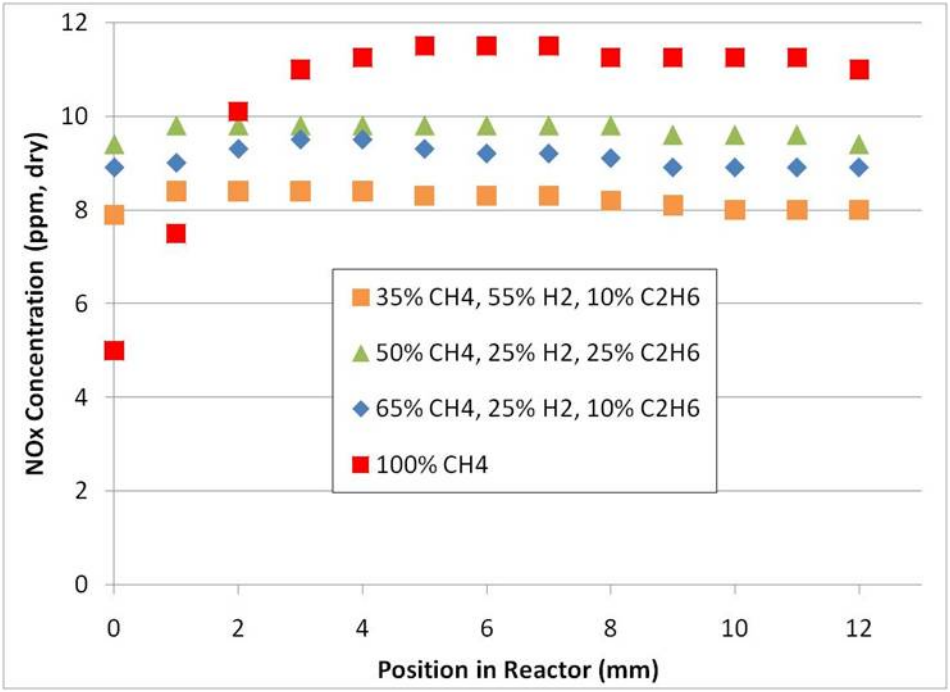

Figure G-5: NO_X concentration profile across the JSR for the Process and Refinery Fuel Blends.

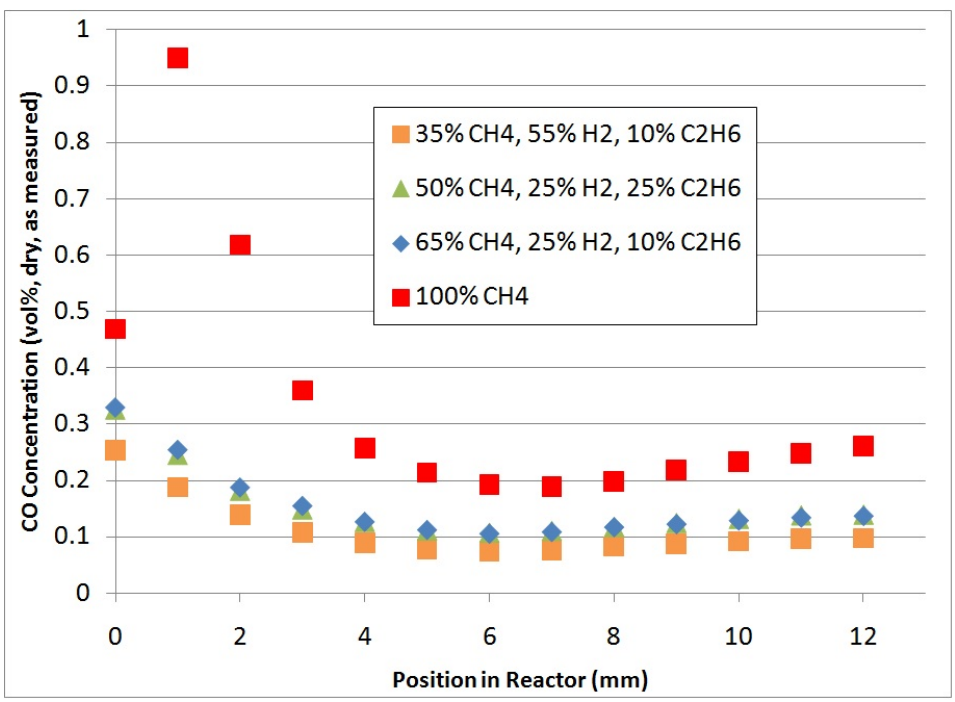

Figure G-6: CO concentration profile across the JSR for the Process and Refinery Fuel Blends.

G.2.1.3 Gasified Coal/Petcoke (O2 Blown)

Category 3 is a product of the gasification process. As outlined above, it is primarily composed of H_2 and CO with small concentrations of CO_2 but without any hydrocarbon species. The temperature, CO, and NO_X profiles are shown in Figure G-7 through Figure

G-9.

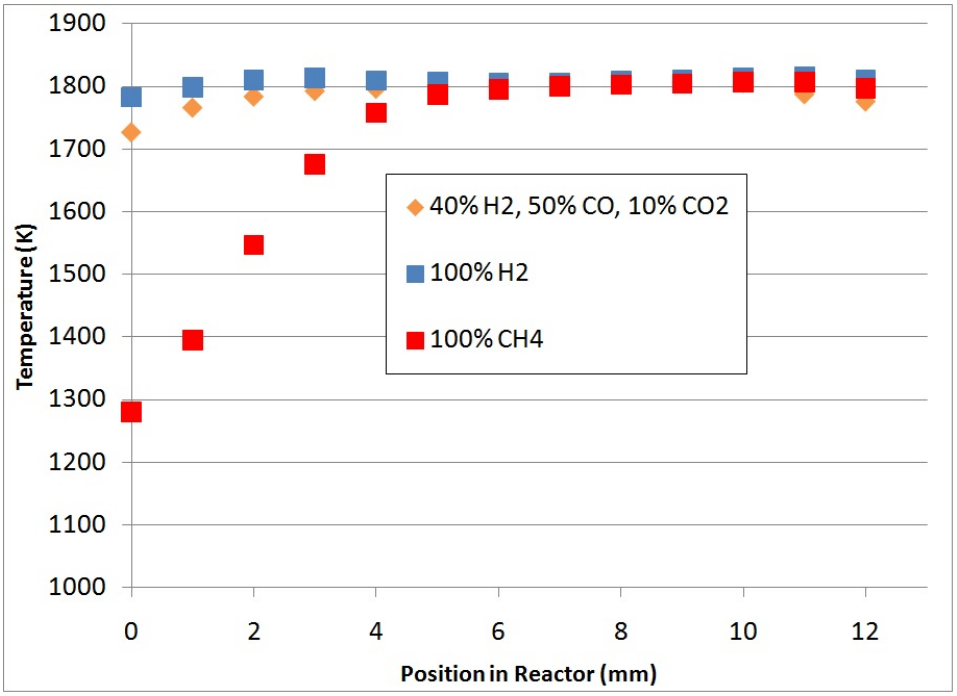

Figure G-7: Temperature profile across the JSR for the Gasified Coal/Petcoke blend with pure CH_4 and H_2 shown for reference.

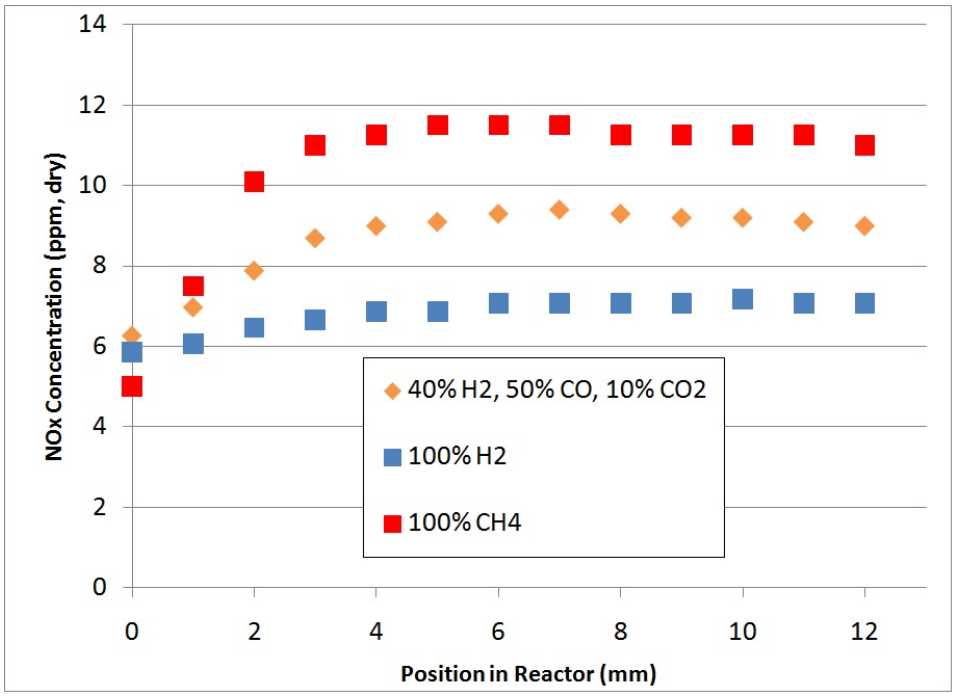

Figure G-8: NO_X concentration profile across the JSR for the Gasified Coal/Petcoke blend with pure CH_4 and H_2 shown for reference.

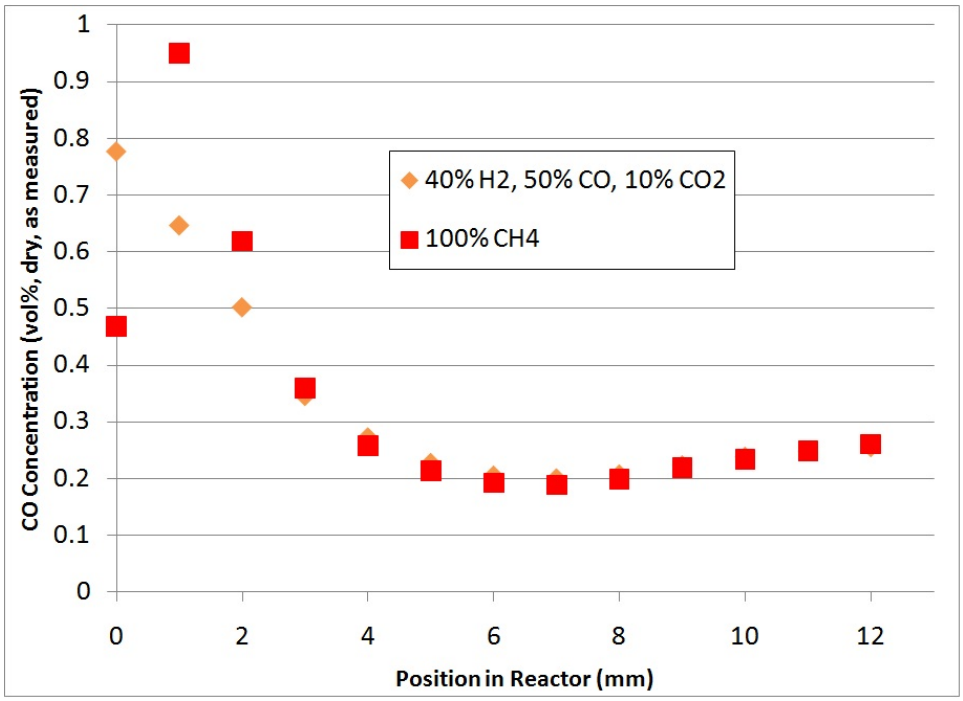

Figure G-9: CO concentration profile across the JSR for the Gasified Coal/Petcoke blend with pure CH_4 shown for reference.

The temperature profiles for the gasification blend and pure H_2 are almost identical. Since H_2 is so highly reactive it dominates the relatively low reactivity of the CO. Despite the small temperature difference, the gasification blend actually produces about 2 ppm more NO_X .

G.2.1.4 Landfill and Digester Gas

Landfill and digester gas is mainly composed of CH_4 and CO_2 with varying levels of N_2. The profiles for temperature, CO, and NO_X are shown in Figure G-10 through Figure G-12.

Although the temperature profiles for each landfill blend and pure CH_4 are practically indistinguishable, the CO and NO_X profiles are quite different. Shown in Figure G-11, the addition of diluent seems to spread out the reaction zone with the CO concentration peaking at 2 mm away from the centerline instead of 1 mm for CH_4 combustion. This trend makes sense since the addition of diluent will slow the flame speed of the mixture; thus, spreading out the turbulent flame brush region.

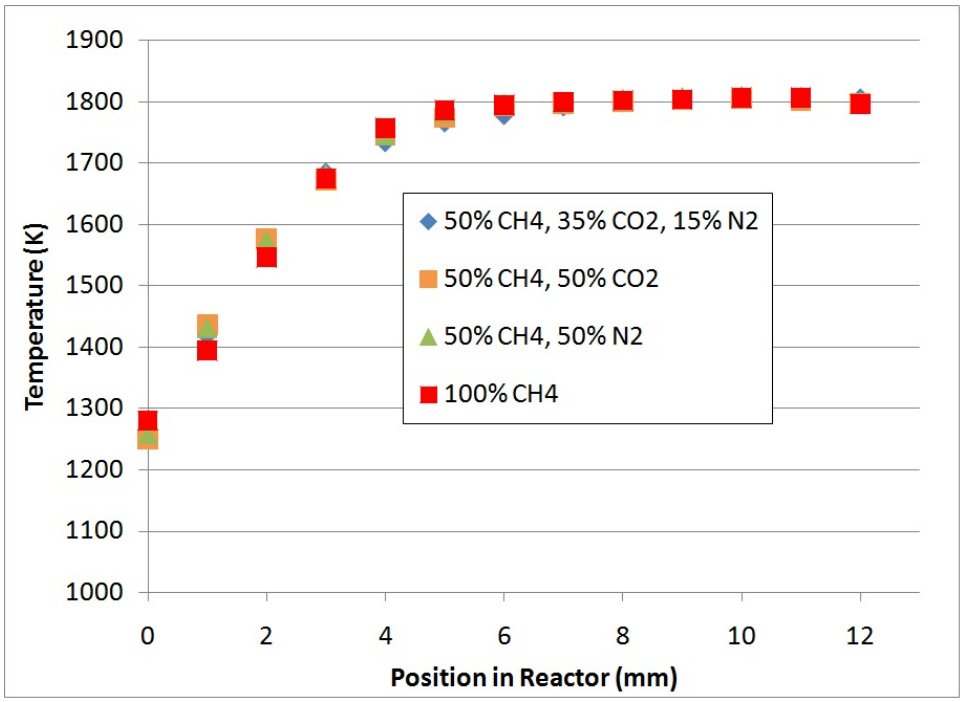

Figure G-10: Temperature profile across the JSR for the Landfill and Digester Gases with pure CH_4 shown for reference.

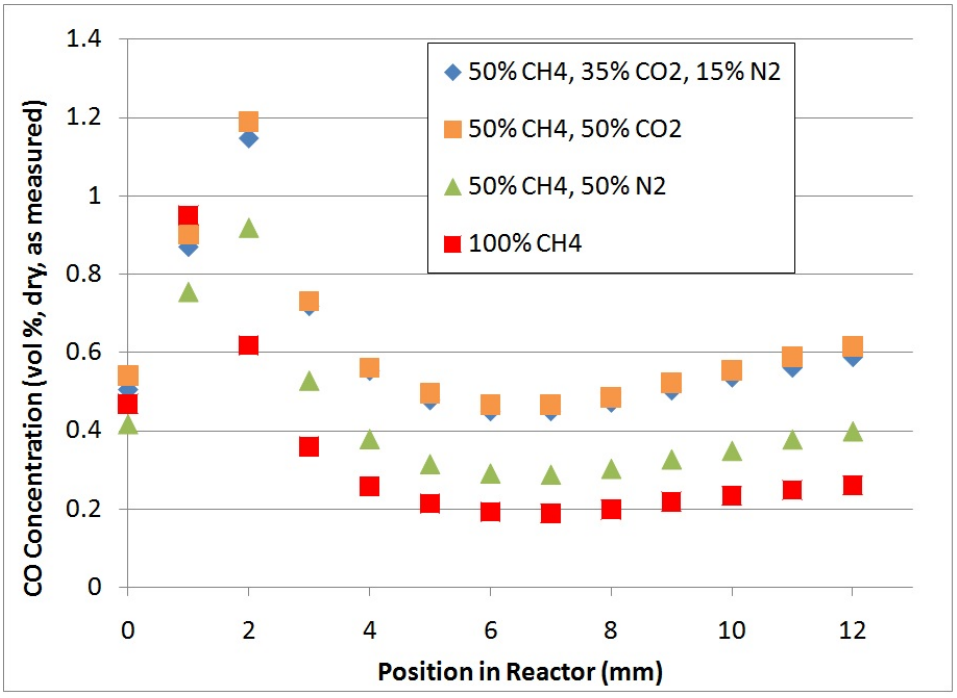

Figure G-11: CO concentration profile across the JSR for the Landfill and Digester Gases with pure CH_4 shown for reference.

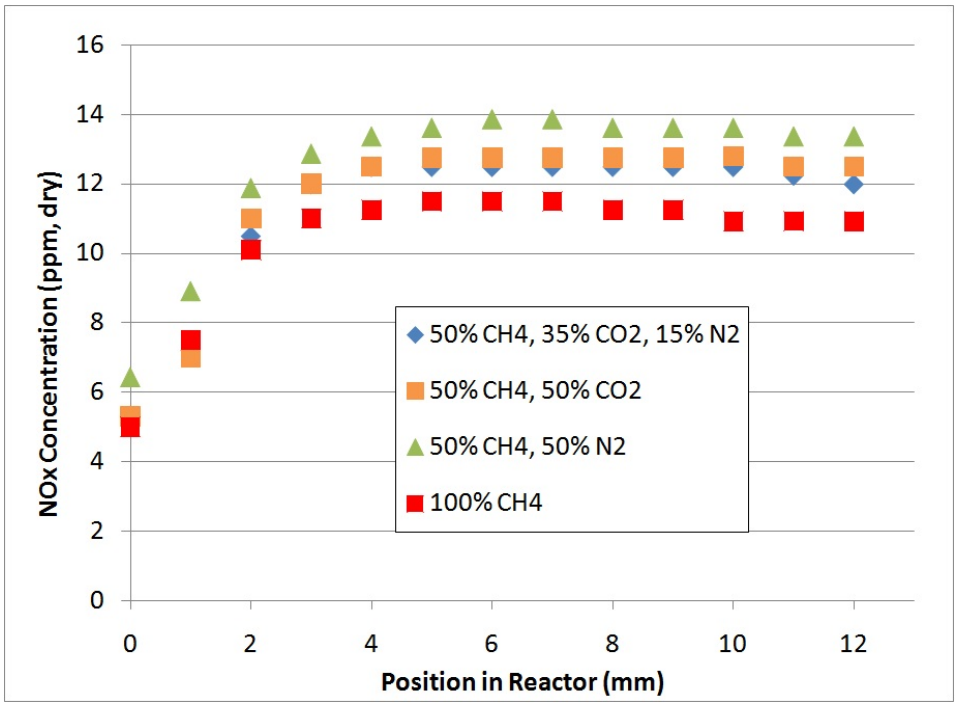

Figure G-12: NO_X concentration profile across the JSR for the Landfill and Digester Gases with pure CH_4 shown for reference.

Note that the CO concentration within the recirculation zone is larger for the landfill gases than for pure CH_4. Within the recirculation zone, the landfill mixtures that contain CO_2 actually have a CO concentration that is more than double that of pure CH_4. As discussed in Section 5.3.1 in the previous report, the rise in CO emissions for landfill gas blends is partially due to an increase in the equivalence ratio required to maintain temperature (since air flow rate is kept constant). This effect is relatively unaffected by the diluent since both N_2 and CO_2 have approximately the same specific heat within the range of preheat and combustion temperatures used in this study. The larger increase in CO emissions for the landfill blends containing CO_2 can possibly be attributed to a competition between CO_2 and O_2 for H-atom, which will lead to increased CO formation through the reaction $CO_2 + H \leftrightarrow CO + OH$ [4]. Since CO_2 could be consuming H-atom, an important reactant in the primary chain branching reaction $H + O_2 \leftrightarrow O + OH$, the presence of CO_2 is expected to result in a smaller radical pool. A smaller radical pool, especially a smaller O-atom radical pool, will lead to reduced NO_X production. This is thought to be the main reason for the lower NO_X emissions for the landfill gas blends diluted with CO_2 as opposed to N_2.

G.2.1.5 LNG, Shale, and Associated Gas

LNG, Shale, and Associated Gases are mainly composed of CH_4 with varying levels of C2 and C3 hydrocarbons. The profiles for temperature, CO, and NO_X are shown in Figure G-13 through Figure G-15.

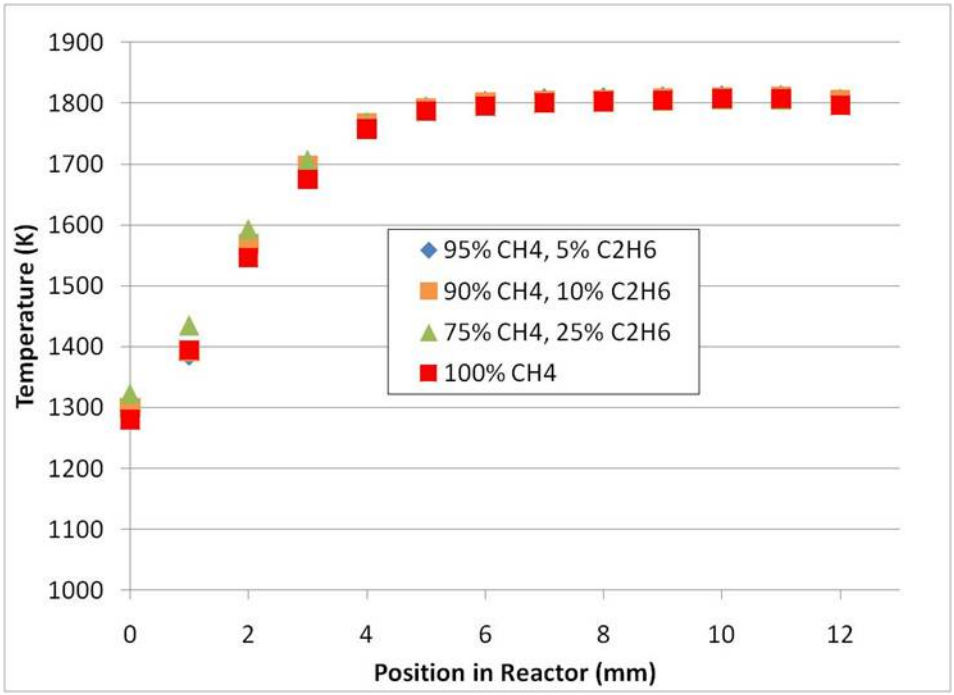

Figure G-13: Temperature profile across the JSR for the LNG, Shale, and Associated Gases with pure CH_4 shown for reference.

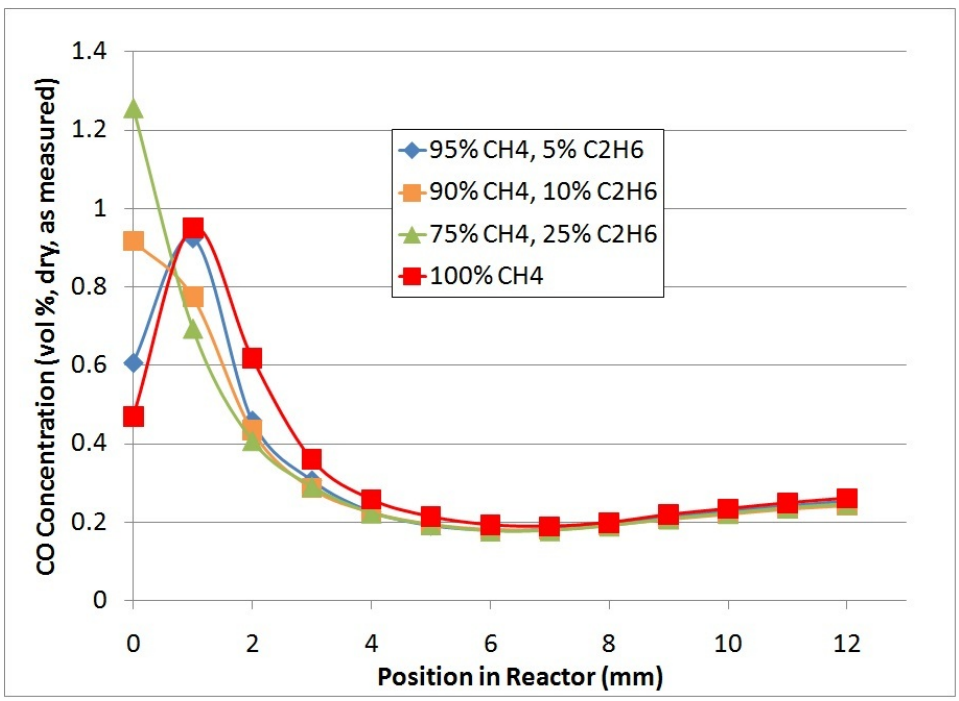

Figure G-14: CO concentration profile across the JSR for the LNG, Shale, and Associated Gases with pure CH_4 shown for reference

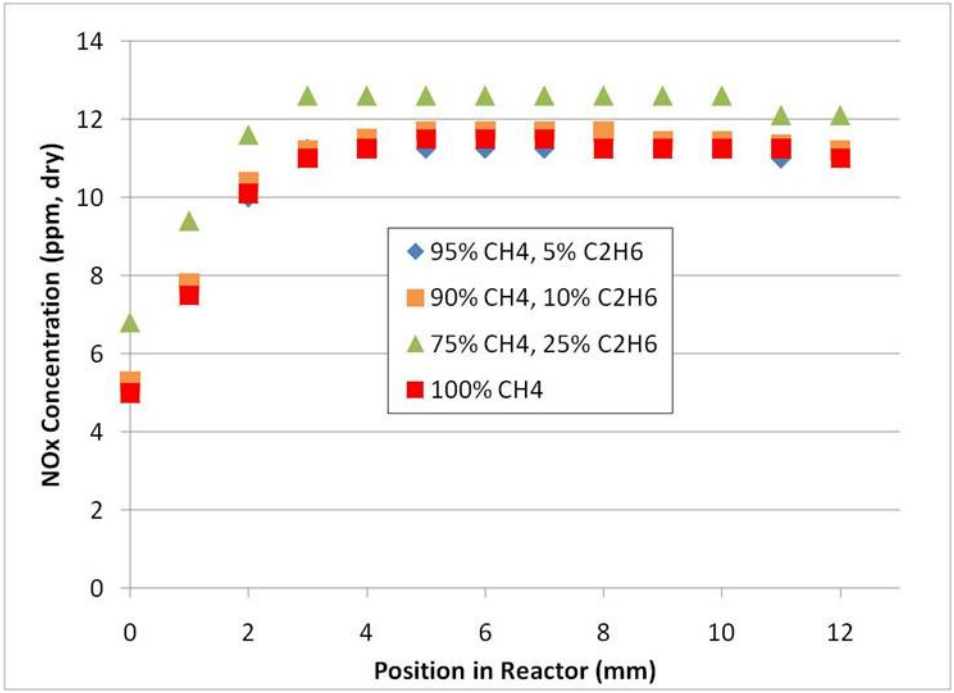

Figure G-15: NO_X concentration profile across the JSR for the LNG, Shale, and Associated Gases with pure CH_4 shown for reference.

Since each of the nominal fuel blends in this category are composed mainly of CH_4, the fact that the temperature profiles are similar is not surprising. The addition of C2H6 promotes an increased reactivity on centerline as indicated by the rise of CO concentration shown in Figure G-14. This added reactivity is also thought to be the main reason for the larger NO_X emissions produced by fuels containing larger amounts of C_2H_6 as shown in Figure G-15.

Chapter G.3:
CFD Modeling

In this chapter, the results of both two and three dimensional CFD simulations are presented to illustrate the general flow, temperature, and species structure within the reactor. At this time only the CFD results from the LPM combustion of CH_4 and H_2 are presented. The simulations are run employing chemical mechanisms of increasing levels of sophistication.

First, the computational grid, the heat transfer, and turbulence models used for both the two and three dimensional simulations are presented. Next, the three dimensional CFD results from LPM CH_4 combustion employing a simplified global mechanism are shown. This model is then used to initialize both LPM CH_4 and H_2 three dimensional combustion models employing detailed oxidation chemistry. Lastly, the results of LPM H_2 combustion incorporating full NO_X chemistry are presented.

G.3.1 Grid, Fluid Dynamics and Heat Transfer Models

For both the two and three dimensional CFD models a structured hexagonal grid is generated encompassing both the solid and fluid portions of the JSR. One quarter of the physical domain is modeled in three dimensions; whereas the two dimensional domain is axisymmetric. The fluid dynamic and heat transfer models are the same for both the two and three dimensional models.

G.3.1.1 Grid

The three dimensional CFD simulations are conducted with a structured domain of about 1,000,000 cells encompassing both the solid and fluid portion of the JSR. We found it necessary to model the solid portion of the domain in order to properly incorporate heat transfer from the reactor. The grid and a blow up of the reactor region for the three-dimensional model are shown in Figure G-16.

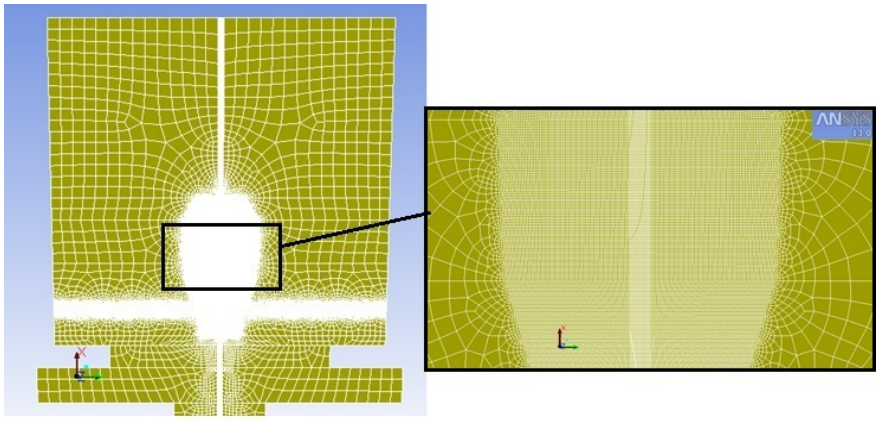

Figure G-16: Grid used in Three Dimensional CFD simulations.

Use of a structured hexagonal domain is absolutely necessary to avoid convergence issues. The refined portion of the grid is concentrated within the combustion chamber and has a nominal cell length of 0.158 mm. Approximately, 71% of the cells in the entire domain are fluid cells with the remaining composed of solid cells. The only reason there are so many solid cells is due to the required growth around the boundary layer of the combustion chamber.

The two dimensional CFD simulations are conducted with a structured domain of about 35,000 cells encompassing both the solid and fluid portion of the JSR as shown in Figure G-17. Similar to the three dimensional grid, about 70% of the domain is made up of fluid cells; however, in the refined portion of the combustion chamber the nominal cell length is about 0.065 mm.

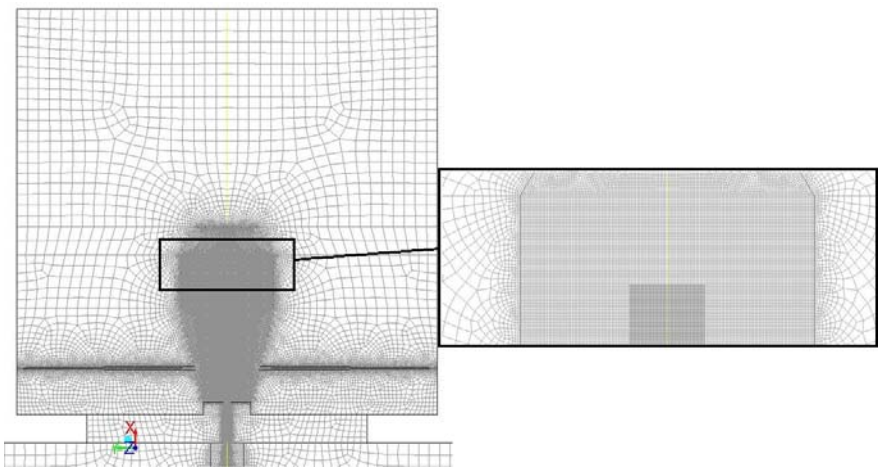

Figure G-17: Grid used in Two Dimensional CFD simulations.

G.3.1.2 Fluid Dynamics and Heat Transfer Models

The flow of reactants going through the nozzle block is choked; thus the density within the fluid portion of the domain is modeled with the ideal gas equation. Since the flow within the JSR is compressible, a velocity or mass flow inlet will not converge. Instead, the inlet and outlet are set as pressure boundaries. The correct stagnation properties are set for both boundaries and the mass flow rate through the reactor will adjust. For all modeled conditions, the mass flow rate difference between the model and experiment is less than 1%.

Due to the highly recirculating nature of the flow within the combustion chamber, model convergence was not attainable for either the standard [5] or realizable [6] k-ε models. Instead, the Reynolds stress model [7] is employed due to its inherent ability to handle the highly recirculating nature of the flow inside the JSR.

A multidimensional heat transfer model is utilized that accounts for convection on both the inner and outer surfaces of the JSR, conduction throughout the entire domain, and radiation on both the inner and outer surface of the JSR. The radiation on the inner surface is modeled using the Discrete Ordinates Model [8], while the radiation on the outer surface is modeled

as the actual ceramic surface with a temperature dependant emissivity and a view factor equal to unity. The partial differential equations that govern both flow and heat transfer within the JSR are solved using the ANSYS Fluent software package [9].

G.3.2 LPM CH_4 combustion model with global chemistry

Both to aid in the development of the CRN from Chapter 4 of the previous report and to initialize CFD simulations incorporating complex chemistry, a simple 3 step global chemistry mechanism is used to model LPM CH_4 combustion [10]. The simplified chemistry within the reactor is modeled with the finite rate/eddy-dissipation model [11]. In this model, the reaction rate is computed by both an Arrhenius expression and an expression that incorporates turbulent effects. The turbulent mixing, or eddy-dissipation reaction rate is governed by the the large eddy mixing time scale: k/ε , while the chemical rate is generally governed by one or two global Arrhenius steps [9]. The net reaction rate is computed as the smaller of the two rates. The global chemistry does a reasonably good job of predicting CH_4 and CO oxidation as shown in Figure G-18 and Figure G-19.

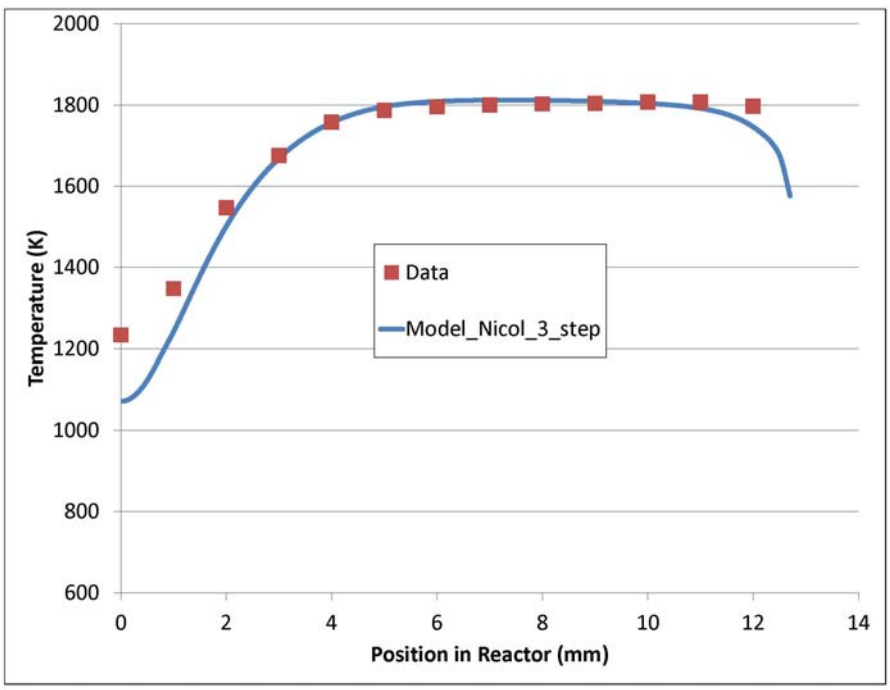

Figure G-18: Profile of temperature from reactor centerline to wall, measured and predicted by CFD for CH_4 combustion for exit gas O_2 of 6.6% (mole %, dry)

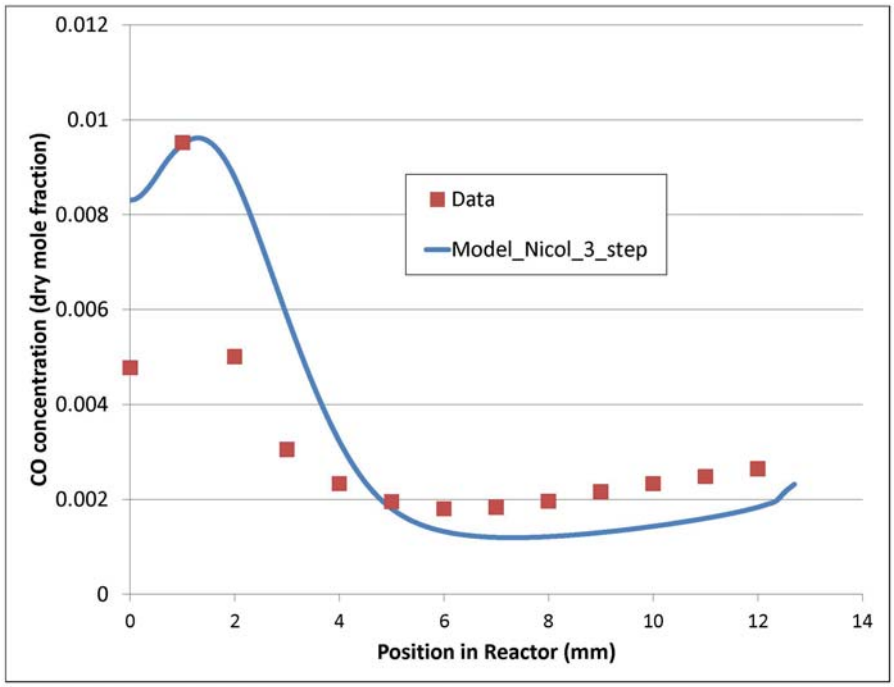

Figure G-19: Profile of CO from reactor centerline to wall, measured and predicted by CFD for CH_4 combustion for exit gas O_2 of 6.6% (mole %, dry)

The contours of temperature and CO concentration are shown in Figure G-20. This figure illustrates the two zone combustion behavior of the JSR. The highly turbulent flame zone is anchored around the nozzle, which is outlined by the region of high CO concentration.

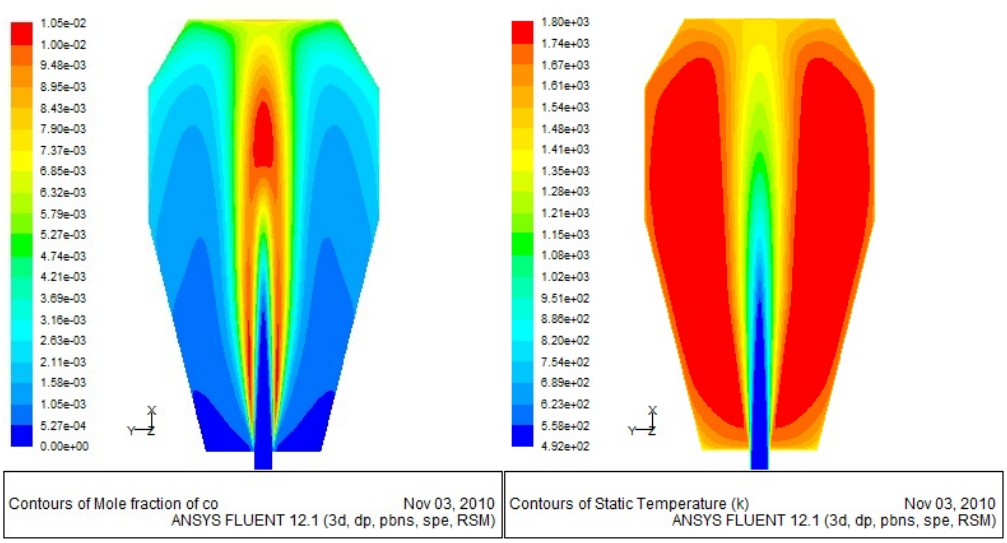

Figure G-20: CO and temperature contours by CFD for JSR fired on CH_4 computed by global chemistry. The nominal recirculation zone temperature is 1800 K.

This flame zone is then followed by a super-equilibrium post flame recirculation zone, where the radicals (indicated by CO concentration) are starting to relax and the temperature is fairly uniform. Although this CFD model does not predict intermediate radicals and NO_X, the CO contours and flow field can be used as guidelines to develop a chemical reactor network (CRN), which can incorporate detailed chemistry. In addition, this model runs quickly enough that it is a good way to initialize the temperature and flow field for a simulation that incorporates more complex chemistry.

G.3.3 CH_4 and H_2 combustion model with detailed oxidation chemistry

This section presents the results of CFD simulations with detailed oxidation chemistry. The same grid is used in these simulations as described above. Detailed chemistry for both H_2 and CH_4 combustion is incorporated into this previously described model. While the CH_4 model predicts temperature pretty well, it does not do as well at capturing the CO profile. The model does, however, provide a look into the flame structure and radical concentration differences between LPM H_2 and CH_4 combustion. In the future these models will be fine tuned to capture the CO concentrations for CH_4 combustion as well as NO_X concentrations for H_2 combustion and hopefully CH_4 combustion. For now this Section will provide insight into the flame; however it should be thought of as a work in progress.

The chemistry within the reactor is modeled using the eddy-dissipation-concept (EDC) model [12]. The EDC model is an extension of the eddy-dissipation model that can employ detailed chemistry into turbulent reacting flows [13]. The chemistry for both fuels is obtained from a truncated version of the GRI 3.0 mechanism [14]. For H_2 combustion, all C and N-containing species are removed resulting in 9 species and 21 reactions. For CH_4 combustion, the GRI 3.0 mechanism has been systematically reduced to capture the major chemistry associated with CH_4 oxidation. The skeletal mechanism was developed by applying the Direct Relational Graph (DRG) method of Lu and Law [15] to a sample of perfectly stirred reactors (PSRs) using GRI 3.0 without NO_X chemistry. The parameter space was chosen to include a single pressure of 1 atm, equivalence ratios from 0.4 to 1.0, preheat up to 600 K, and mean PSR residence times from near blowout to 3 ms [16]. The resulting mechanism contains 14 species and 49 reactions.

G.3.3.1 CH_4 Combustion

The temperature and CO profiles for CH_4 combustion are shown below in Figure G-21 and Figure G-22. Both the extended mechanism developed by Karalus [16], and the 3 step global mechanism developed by Nicol et al. [10] are shown for comparison. As shown in Figure G-21, the more detailed CH_4 mechanism appears to predict the temperature in the recirculation zone fairly accurately; however, it under predicts the data near the jet, and at that point seems to be less accurate than the 3-step mechanism.

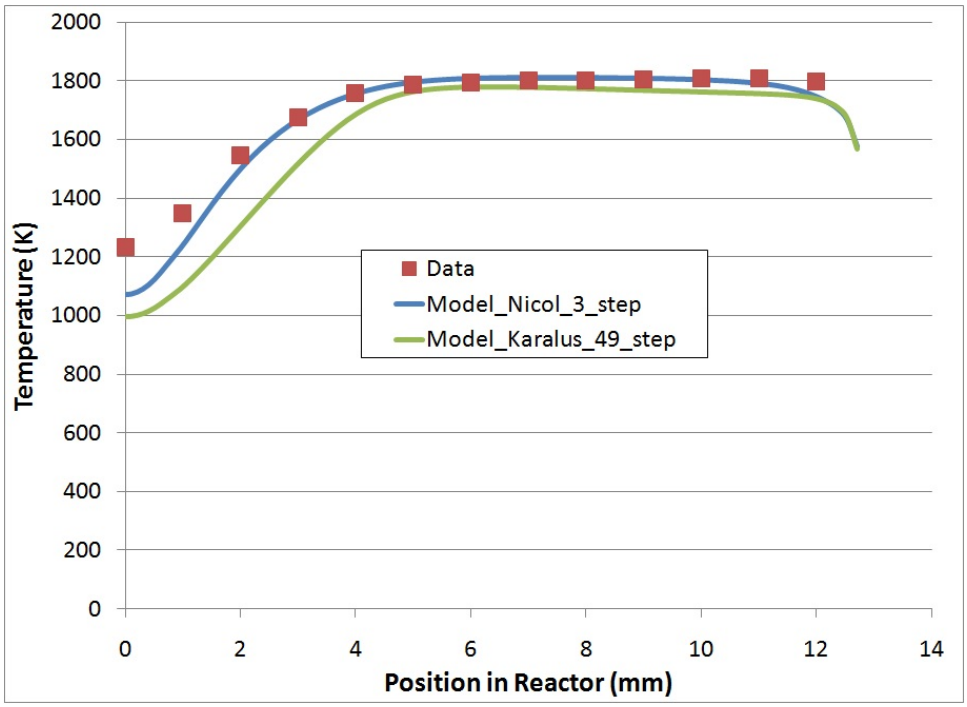

Figure G-21: Profile of temperature from reactor centerline to wall, measured and predicted by CFD for CH_4 combustion (w/o diluents) for exit gas O_2 of 6.6% (mole %, dry).

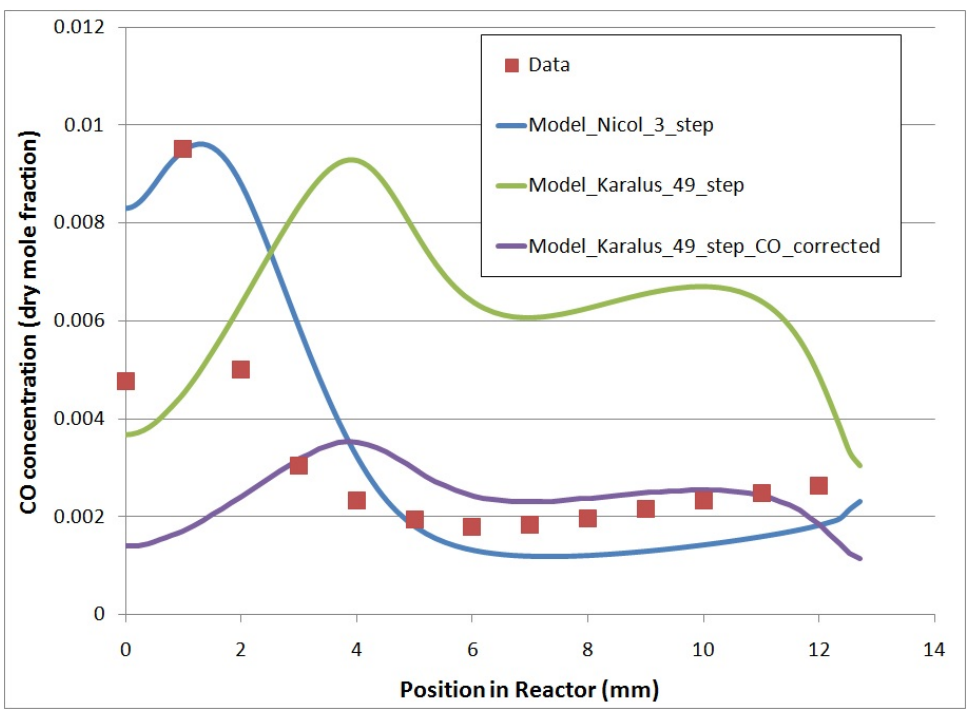

Figure G-22: Profile of CO from reactor centerline to wall, measured and predicted by CFD for CH_4 combustion (w/o diluents) for exit gas O_2 of 6.6% (mole %, dry).

The CO contour predicted by the 49-step mechanism seems to be even less accurate than the temperature prediction. Although the CO peak is of the same magnitude as the data

and the 3-step model, it is shifted about 3 mm away from the jet relative to the other two. In addition, the computed CO concentration in the recirculation zone is considerably higher than both the data and the concentration predicted by the 3-step mechanism. The 49-step mechanism does, however, predict the concentration on centerline fairly accurately.

Previous JSR researchers have reported that approximately 62% of the sampled CO oxidizes in the probe for LPM CH_4 combustion at atmospheric pressure and 1800 K in the recirculation zone [17]. For comparison, the CO profile predicted by the 49-step mechanism is debited 62% as shown in Figure G-22. The corrected CO profile correlates quite well with the measured data in the recirculation zone; however, the peak is far too low. Clearly, this correction would not apply where there is not sufficient OH radical to push the reaction. In fact, the probe chemistry may very well produce CO via CH_4 oxidation in the near jet region of the reactor. The probe chemistry should be evaluated for a variety of inlet conditions encountered along the reactor traverse. With a properly formulated probe model, it is quite possible that the CO profile predicted by the 49-step mechanism will match the measured data.

Shown by Steele, CO is primarily oxidized in the probe through reaction with OH- radical; however, he does not investigate any probe chemistry on reactor centerline. The predicted concentrations of CO, OH, and CH_4 are shown below in Figure G-23.

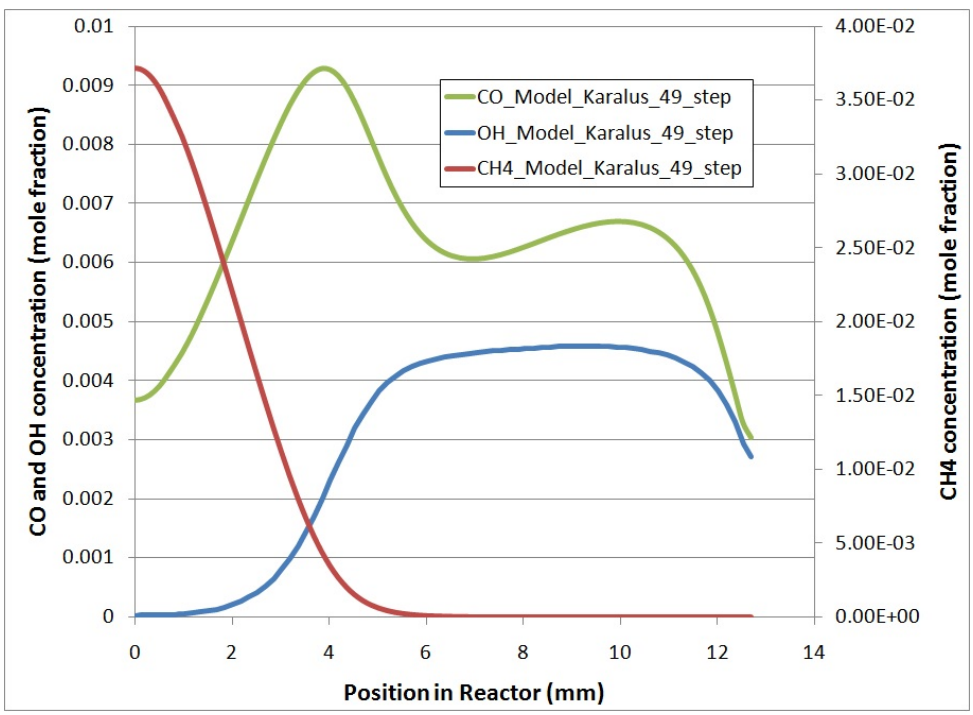

Figure G-23: Profiles of CO, OH, and CH_4 from reactor centerline to wall, predicted by CFD for CH_4 combustion for exit gas O_2 of 6.6% (mole %, dry).

The OH concentration does not rise significantly until the beginning of the recirculation zone, where the CO peak has already begun to fall. At the same time, the CH_4 concentration is quickly falling as the probe traverses away from the jet. It should also be noted that the

CH_4 concentration is an order of magnitude larger than the CO concentration on centerline. Further investigation of these phenomena is definitely a high priority for future research.

The two zone behavior of the JSR is well illustrated by looking at the rate of CH_4 destruction as shown in Figure G-24. The CH_4 starts being consumed at the shear layer of the jet, where the cold reactants meet the hot recirculating products. The CH_4 is not completely consumed until it hits the upper wall stagnation point and turns the corner toward the drain holes. This is precisely where the radical peak in concentration as shown below in Figure G-25 through Figure G-27. The near jet region is shown to be largely unreactive, while the recirculation zone contains quite high radical concentrations. These radical concentrations start to relax as flow moves towards the drain hole exhaust. We expect that when detailed NO_X chemistry is incorporated into this model, the bulk of the NO_X production from both the Zeldovich and N_2O pathways will occur within this region.

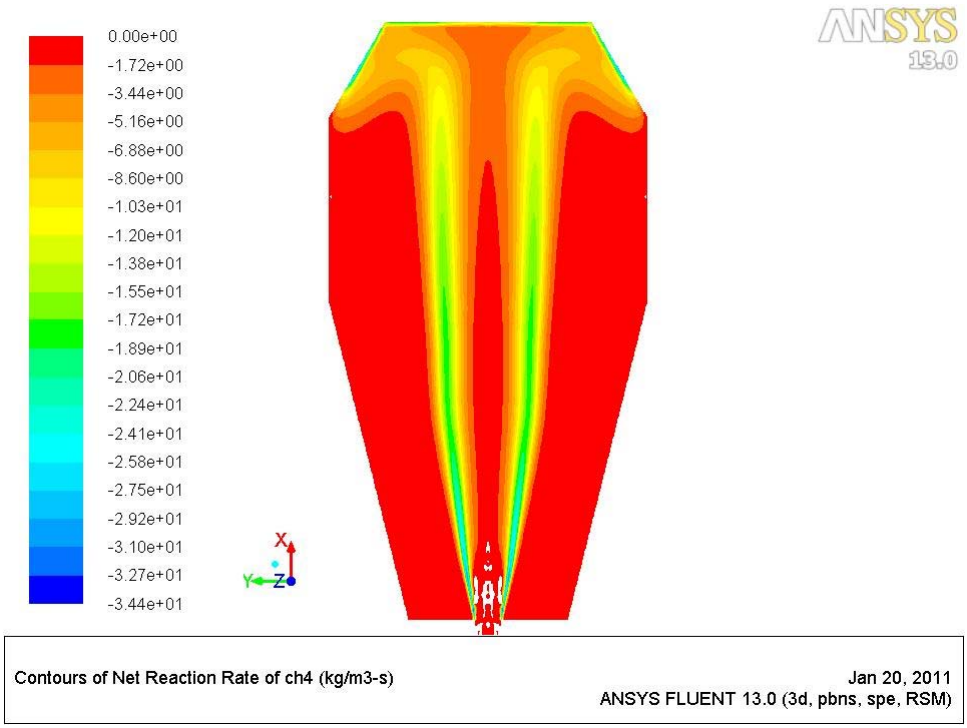

Figure G-24: Contours of CH_4 destruction predicted by CFD for CH_4 combustion for exit gas O_2 of 6.6% (mole %, dry).

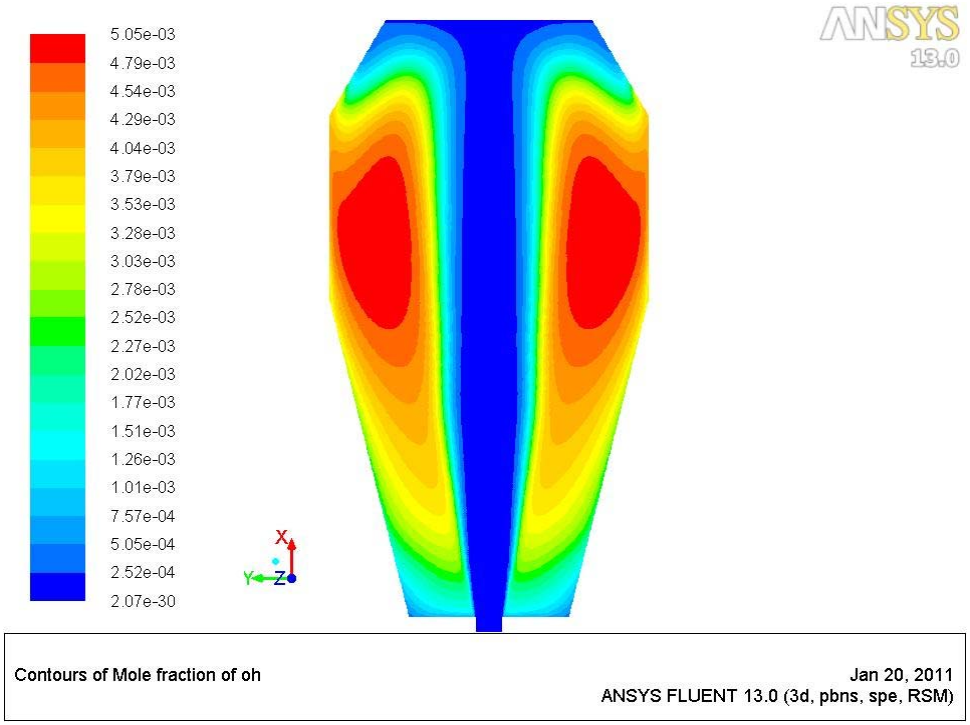

Figure G-25: Contours of OH predicted by CFD for CH_4 combustion for exit gas O_2 of 6.6% (mole %, dry).

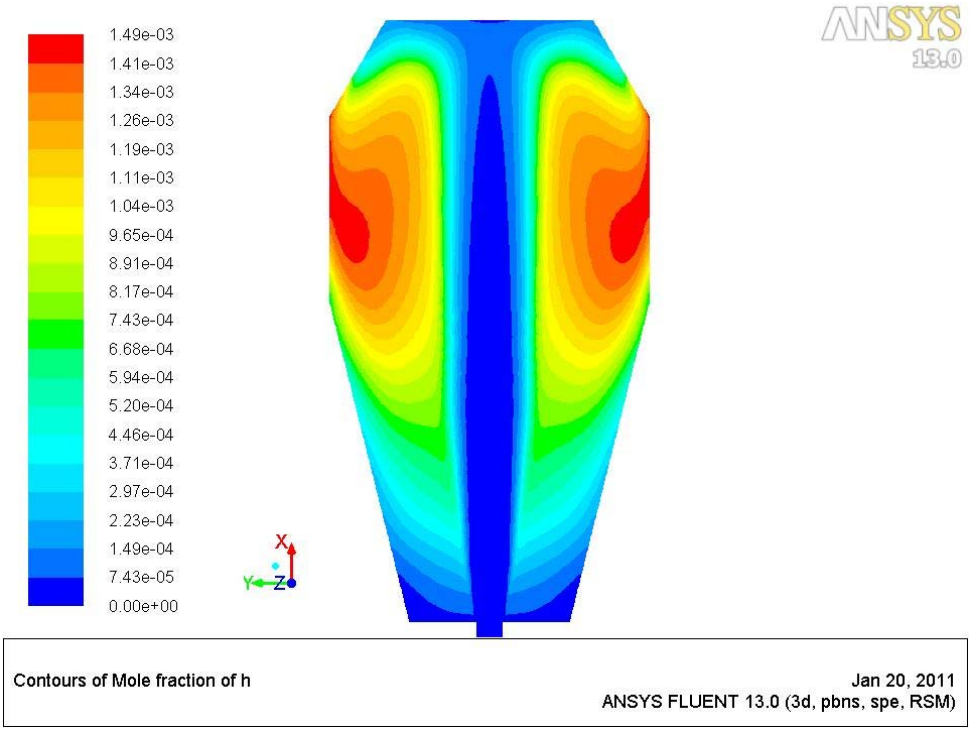

Figure G-26: Contours of H predicted by CFD for CH_4 combustion for exit gas O_2 of 6.6% (mole %, dry).

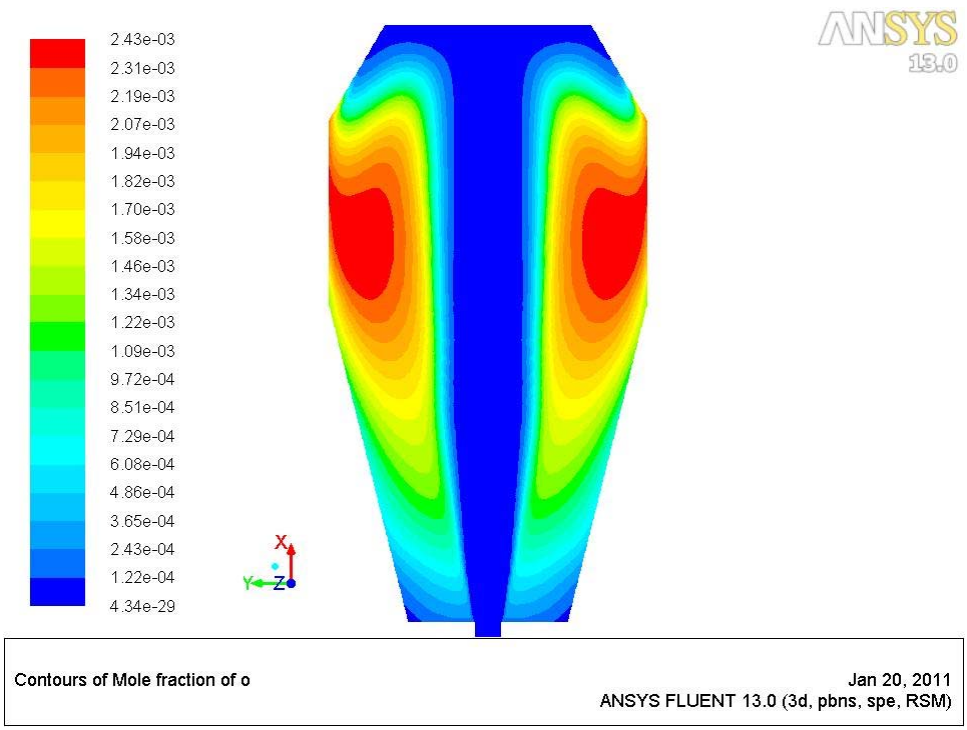

Figure G-27: Contours of O predicted by CFD for CH_4 combustion for exit gas O_2 of 6.6% (mole %, dry).

G.3.3.2 H_2 Combustion

Both the measured and predicted temperature profiles for H_2 combustion are shown below in Figure G-28. Similar to the CFD results shown above for CH_4 combustion, the model does a good job of predicting temperature in the recirculation zone; however, it under predicts temperature in the near jet region. There must be some issue with the model that is not capturing the oxidation right on centerline. We suspect that the turbulence/chemistry interaction is not odeled properly within this region. This is a region of very high turbulent kinetic energy, and it is possible that the turbulence/chemistry coupling via the Eddy Dissipation Concept may not be accurate under these extreme conditions. We are continuing to work on this issue. Nevertheless, it is assumed that the model predicts H_2 destruction as well as the radical fields with reasonable qualitative accuracy for purposes of comparing the behavior with CH_4, and they are shown below in Figure G-29 through Figure G-32. Unlike the CH_4 destruction shown in Figure G-24, all of the H_2 is consumed before the jet meets the upper wall. Unsurprisingly, the highest concentration of radicals is found in and around the jet, near the top of the reactor.

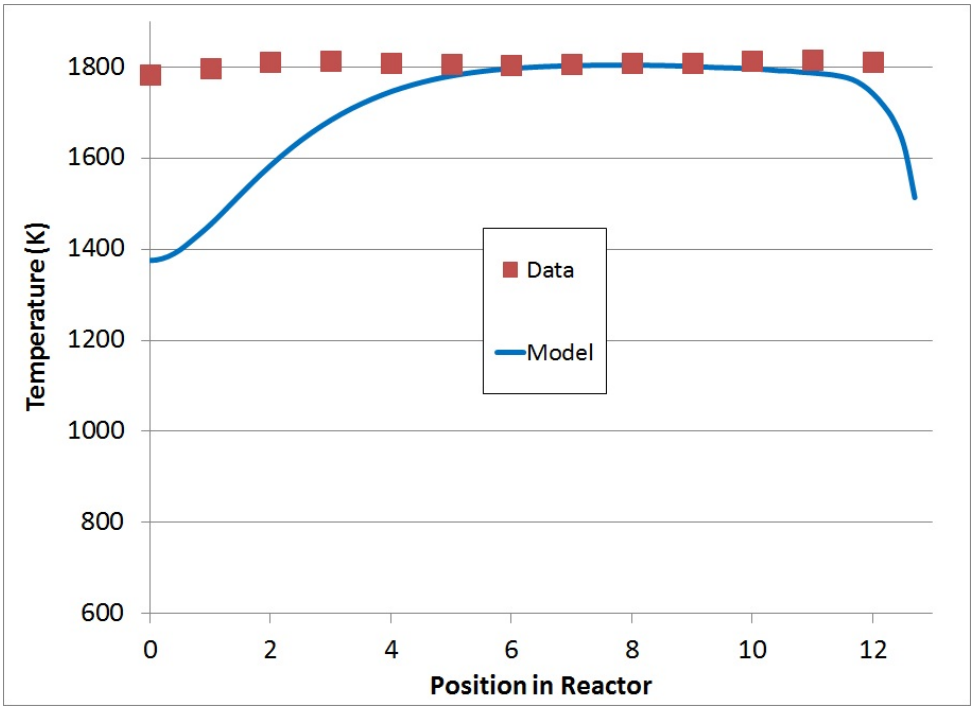

Figure G-28: Profile of temperature from reactor centerline to wall, measured and predicted by CFD for H_2 combustion.

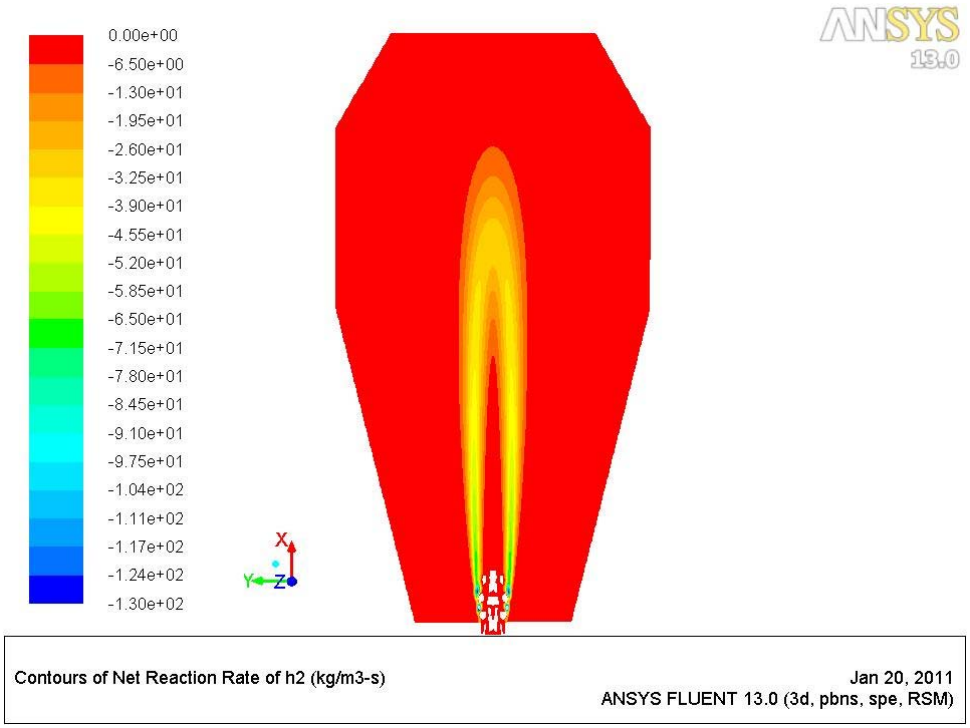

Figure G-29: Contours of H_2 destruction predicted by CFD for H_2 combustion.

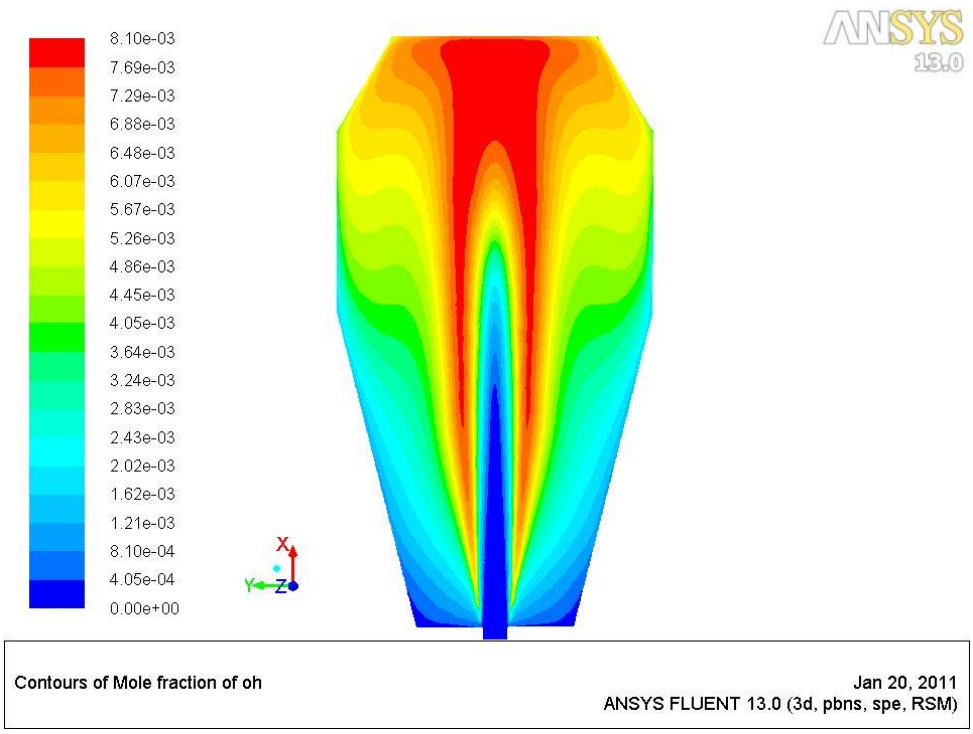

Figure G-30: Contours of OH predicted by CFD for H_2 combustion.

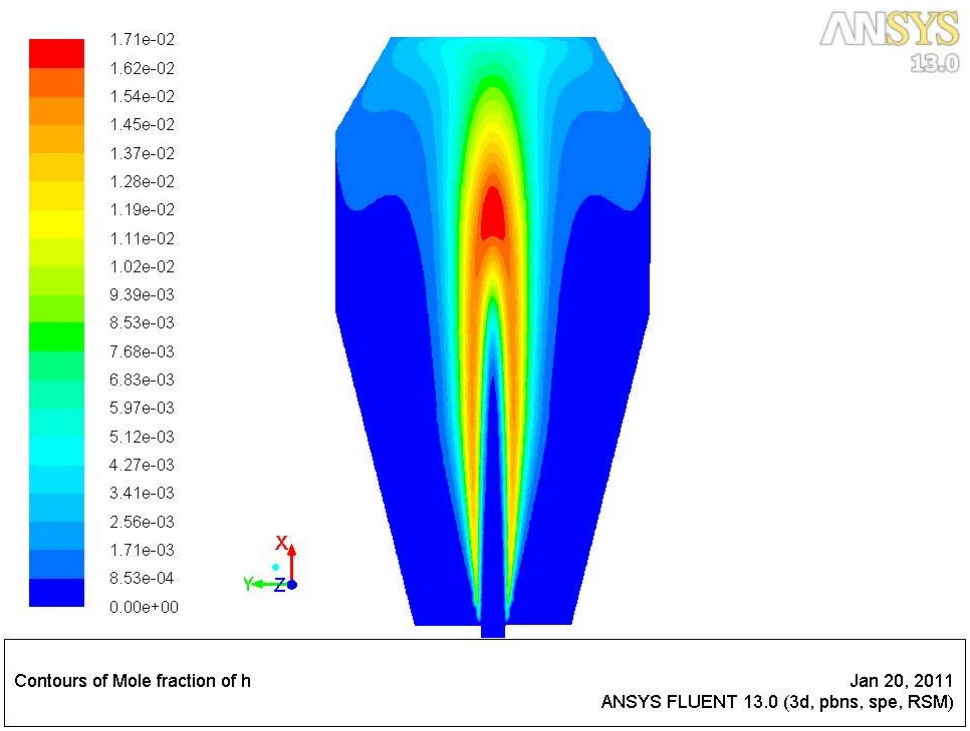

Figure G-31: Contours of H predicted by CFD for H_2 combustion.

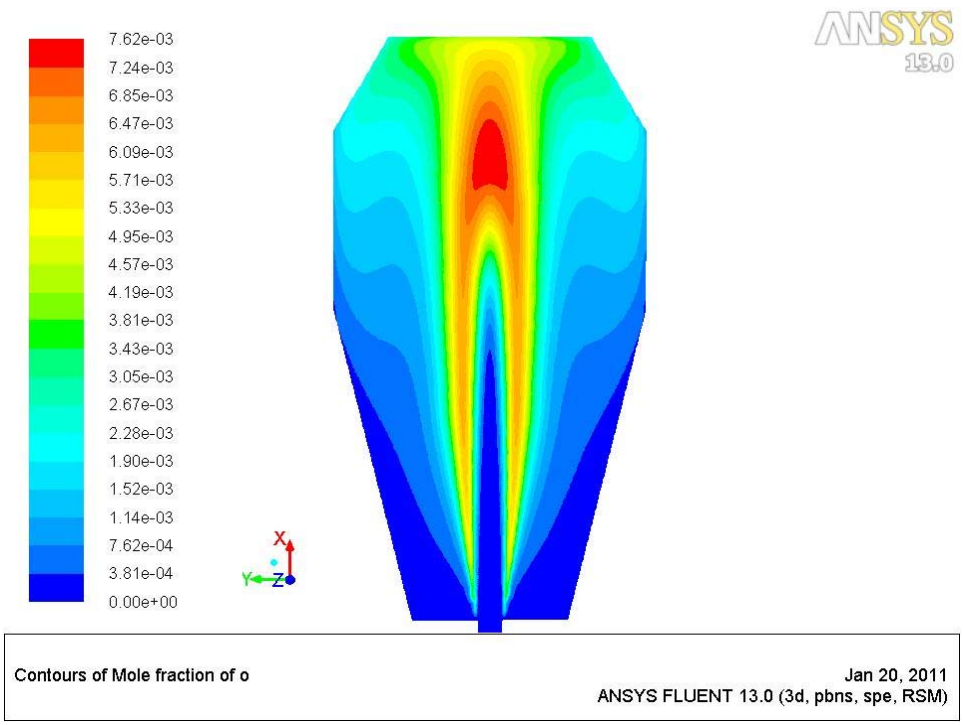

Figure G-32: Contours of O predicted by CFD for H_2 combustion.

G.3.4 H_2 Combustion with NO_X Formation Chemistry

In the following section, results from both two and three dimensional CFD simulations are shown modeling H_2 combustion with full NO_X chemistry. Since the prompt NO_X mechanism is absent from H_2 combustion, modeling full NO_X chemistry is feasible in both the two and three dimensional models. In the following CFD results, the GRI 3.0 mechanism [14] is used without any C containing species. The reduced mechanism with NO_X formation is composed of 18 species with 69 reactions. Note that this mechanism is barely larger than the reduced CH_4 oxidation mechanism used above.

Although a three dimensional solution is tractable with a convergence time of about 10 days, we decided to use the two dimensional model since the convergence time is only 1-2 days. The radial temperature and NO_X predictions are shown for both the two and three dimensional models are shown in Figure G-33 and Figure G-34.

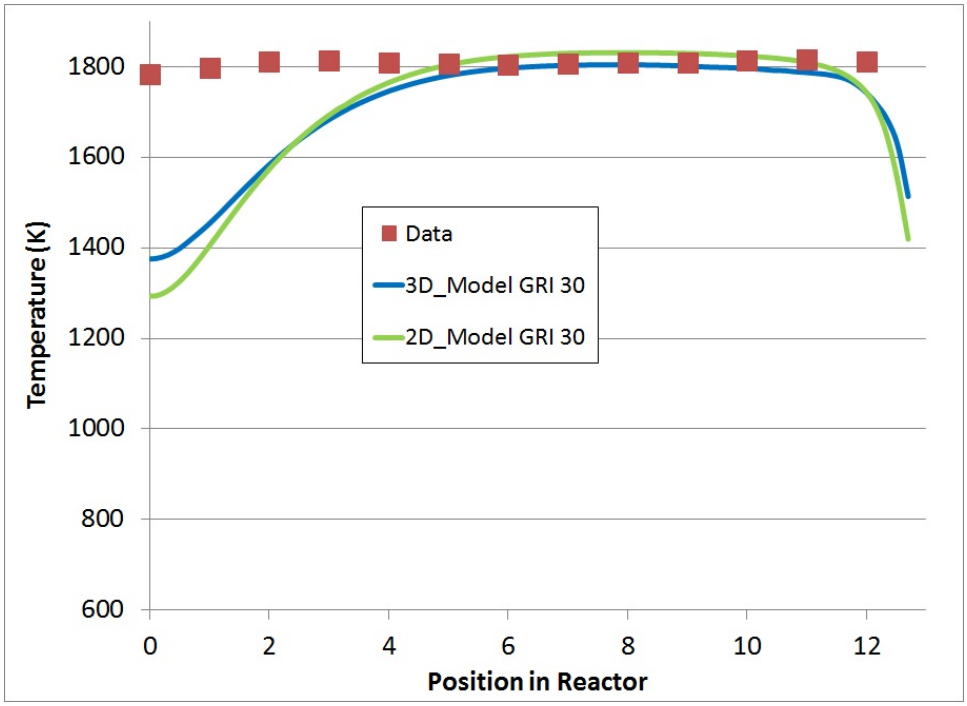

Figure G-33: Profile of temperature from reactor centerline to wall, measured and predicted by CFD for H_2 combustion with NO_X formation chemistry in two and three dimensions.

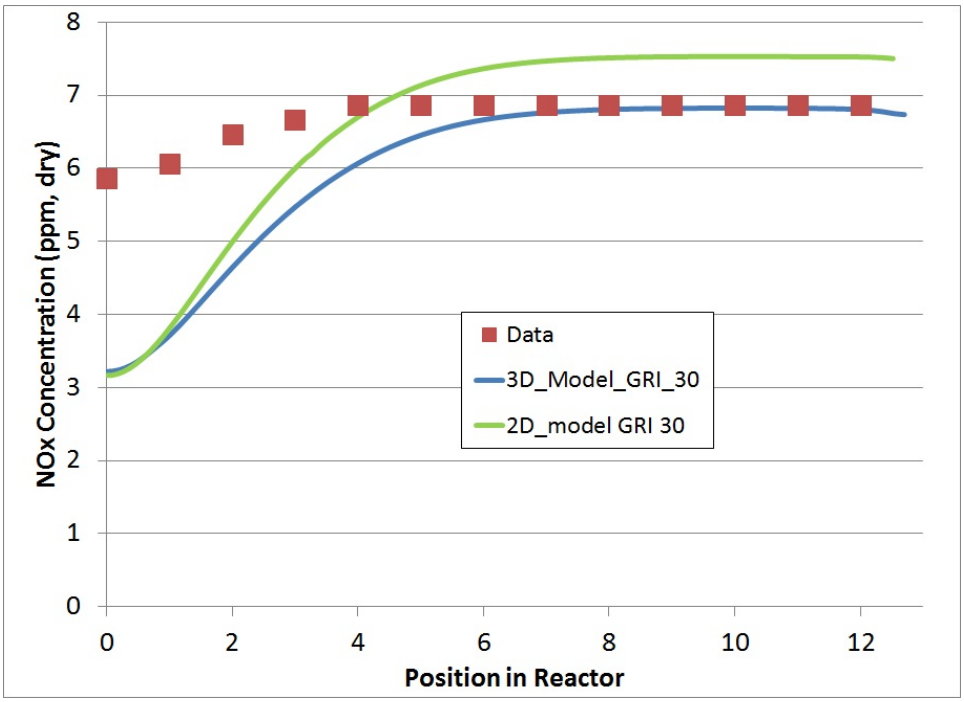

Figure G-34: Profile of NO_X concentration from reactor centerline to wall, measured and predicted by CFD for H_2 combustion with NO_X formation chemistry in two and three dimensions.

As seen in the above figures, both the two and three dimensional models predict the data in the recirculation zone with reasonable accuracy. There are still problems on centerline, which is most likely due to the issue with the turbulence-chemistry interaction in the turbulent jet region that was noted above. The 2D model predicts a slightly higher NO_X concentration and temperature in the recirculation zone than the 3D model. The slightly larger NO_X prediction is likely due to the larger temperature prediction. The difference in temperature is thought to be due to a difference in the manner that heat transfer is handled in the different models. This discrepancy will definitely be explored further in the future. Since the 2D model has a far faster convergence time and still does a reasonable job of predicting both temperature and NO_X concentration in the recirculation zone, it is decided to use it to dig further into the various pathways of NO_X production in LPM H_2 combustion.

The NO contribution from each pathway is determined by commenting out the limiting reactions from two pathways and running the model again. For example, to determine the contribution to NO_X production from only the Zeldovich pathway, the rate limiting reactions for both the NNH and N_2O pathways are removed from the mechanism. More details of this procedure can be found in the previous report. The results of the breaking down the NO_X formation mechanism into the specific pathway contributions are shown in Figure G-35.

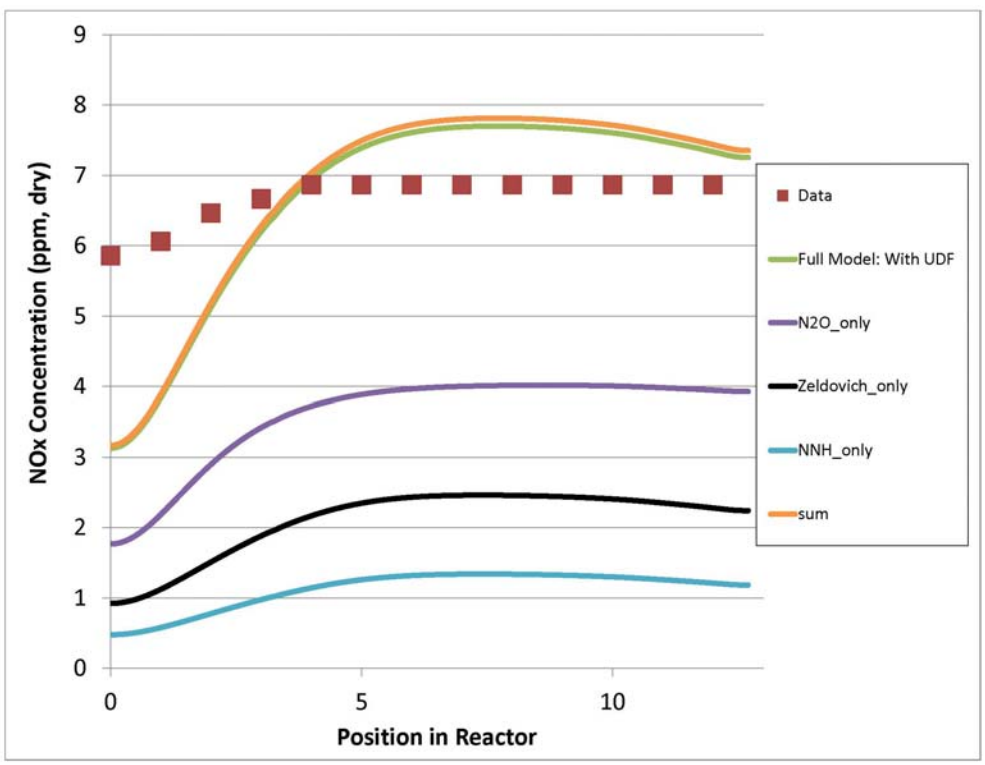

Figure G-35: Profile of NOX concentration from reactor centerline to wall, measured and predicted by CFD for H2 combustion with NOX formation chemistry in two dimensions for each NOX pathway.

Shown above, the N_2O pathway is the the most significant pathway to NO_X formation followed by the Zeldovich and NNH pathways. The rate of NO_X production for the full mechanism as well as the rate of NO_X production for each of the three pathways is shown in Figure G-36 through Figure G-39.

Figure G-36: Contours of the rate of NO_X production for the full GRI 3.0 mechanism.

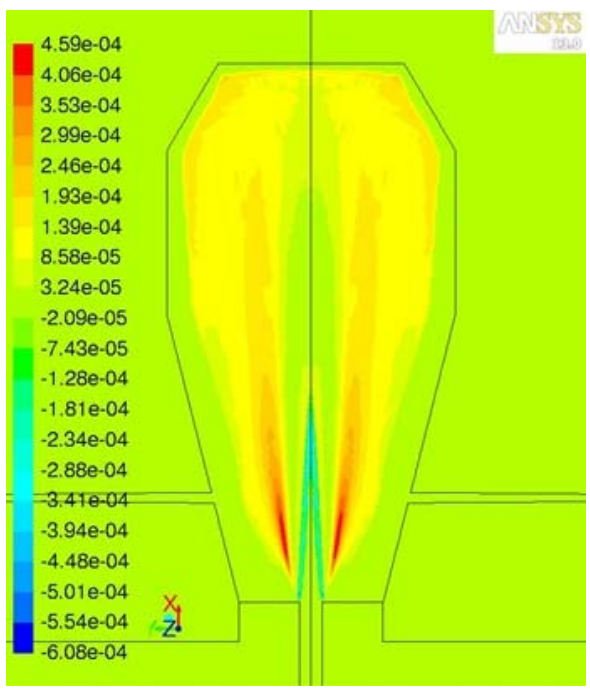

Figure G-37: Contours of the rate of NO_X production from the Zeldovich pathway only.

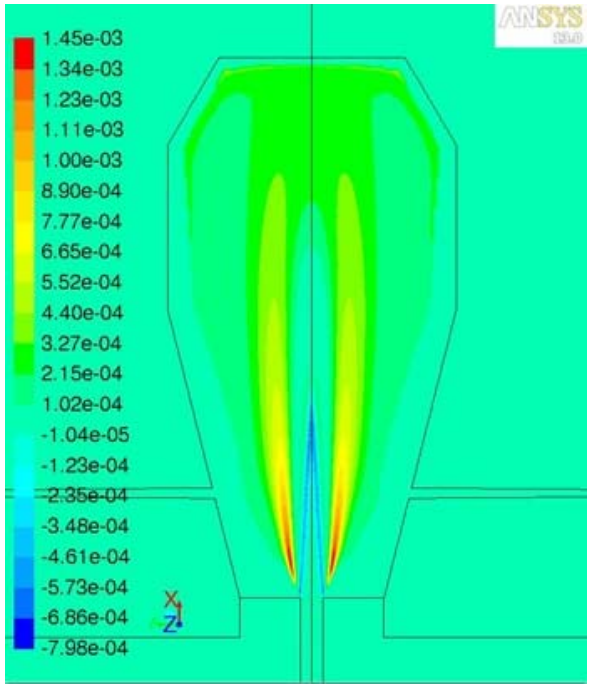

Figure G-38: Contours of the rate of NO_X production from the N_2O pathway only.

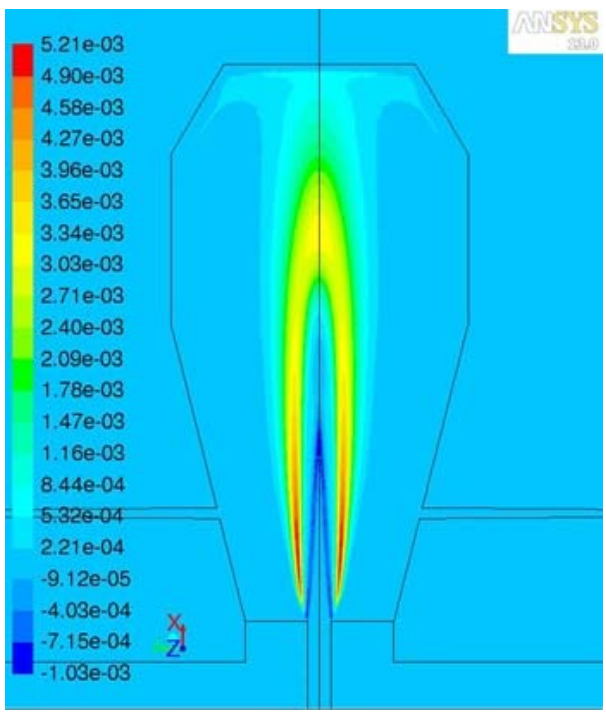

Figure G-39: Contours of the rate of NO_X production from the NNH pathway only.

Shown in the above Figures, most of the NO_X production occurs in and around the turbulent flame brush with the most productive portion of the reactor being located within the shear layer of the jet just as it enters the reactor. NO_X production from the Zeldovich pathway is the largest in the shear region, but extends well into the high temperature region of the reactor. Peak production from the N_2O and NNH pathways is also anchored around the jet

shear layer. There is some production out in the recirculation zone for the N_2O pathway since this pathway is both sensitive to temperature and O radical, which peaks at the top of the jet as shown in Figure G-32. The NNH pathway has a weak temperature dependance; thus, the contours of peak NO_X production are found around the jet where H radical is the largest. There is almost no production due to the NNH pathway out in the recirculation zone.

Chapter G.4:
Summary and Conclusions

A high intensity, single-jet stirred reactor, JSR, is used to study both pollutant formation and resistance to blowout for CH_4 and a variety of gaseous fuel alternatives to CH_4 as displayed in Table G-1. The JSR is intended to act as an idealized lean, premixed combustor. NO_X measurements are taken at a nominal combustion temperature of 1800 K, atmospheric pressure, and a reactor residence time of 3 ms. This ensures that the results focus on the effect of fuel chemistry by removing temperature, residence time, and pressure as variables.

G.4.1 Reactor Scan Experiments

At the nominal temperature and residence time, the experimental results show the following trends for flame structure and NO_X emissions as a function of fuel type:

1. Pure H_2 is far more reactive in comparison to CH_4 and all other pure alkane fuels. This results in relatively flat NO_X and temperature profiles; whereas, the alkane fuels drop in both temperature and NO_X production on centerline.

2. For category 2 (the Process and Refinery blends), H_2 addition increases reactivity on centerline while decreasing overall NO_X emissions. The increased reactivity is especially evident in the CO profiles where the fuels blended with C_2H_6 and H_2 have CO peaks on centerline and CO for pure CH_4 peaks slightly off centerline.

3. For category 3 (the O_2 blown gasified coal/petcoke), the temperature profiles for the gasification blend and pure H_2 are nearly identical, which is likely due to the high reactivity of H_2 dominating the relatively low reactivity of CO. Despite a small temperature difference, the addition of CO causes an increase in NO_X production.

4. For category 4 (the landfill gas), the temperature profiles are virtually indistinguishable. However, the addition of diluent decreases reactivity and spreads out the reaction zone with the CO concentration peaking at 2 mm off of centerline instead of 1 mm. Diluent addition increases NO_X production in comparison to pure CH_4 for reasons explained in the previous report.

5. For category 5 (the LNG, shale, and associated gases), the temperature profiles are all very similar. The increased reactivity of C_2H_6 is evident from looking at the CO profiles. Increased C_2H_6 addition erases the CO trough characteristic of pure CH_4 and causes a large CO peak on centerline which is indicative of the hydrocarbon material breaking down earlier in the jet.

G.4.2 CFD Modelling

The results of both two and three dimensional CFD simulations are presented to illustrate the general flow, temperature, and species structure within the reactor. At this time only the CFD results from the LPM combustion of CH_4 and H_2 are presented. The simulations are run employing chemical mechanisms of increasing levels of sophistication.

A three dimensional CFD simulation is run for LPM CH_4 combustion that uses a global CH_4 oxidation mechanism. While this model does not predict intermediate radicals and NO_X, the CO contours and flow field can be used as guidelines to develop a chemical reactor network (CRN), which can incorporate detailed chemistry. In addition, this model runs quickly enough that it is a good way to initialize the temperature and flow field for a simulation that incorporates more complex chemistry.

Three dimensional CFD models are constructed for modelling LPM CH_4 and H_2 combustion incorporating detailed oxidation chemistry. Both models predict temperature well within the recirculation zone; however, the models under predict temperature in the near jet region. This is possibly due to an incorrect implementation of the turbulence-chemistry interaction within the jet region. Although, there are still bugs to be worked out in the simulations, the preliminary results do a good job illustrating the vast difference in combustion behavior between the two fuels. In particular, the geometric location of the super-equilibrium radical field is anchored in and around the top of the jet for H_2 combustion; whereas, the radical fields are formed within the recirculation zone for CH_4 combustion.

The CFD model for CH_4 combustion with detailed chemistry does mispredict the measured CO within the JSR. It is hypothesized that there is significant CO oxidation within the sample probe for measurements taken within the recirculation zone, and there may be CO formation via CH_4 oxidation as the probe traverses into the jet. Both two and three dimensional CFD models are utilized to simulate LPM combustion with full NO_X chemistry. Both models predict the NO_X concentration in the recirculation zone with reasonable accuracy. The two dimensional model is used to breakdown NO_X formation into each of the three pathways. It is found that the N_2O route is the most important followed by Zeldovich and the NNH.

References

1. Hack, R.L. and V.G. McDonell, *Impact of Ethane, Propane, and Diluent Content in Natural Gas on the Performance of a Commercial Microturbine Combustor.* Journal of Engineering for Gas Turbines and Power, 2008. **130**.
2. Lee, J.C.Y., *Reduction of NO_X Emission for Lean Prevaporized-Premixed Combustors*, 2000, University of Washington.
3. Rutar, T., et al., *NO_X formation pathways in lean-premixed-prevaporized combustion of fuels with carbon-to-hydrogen ratio between 0.25 and 0.88.* Proceedings of the IMechE. Part A: Journal of Power and Energy, 2007. **221**: p. 387-398.
4. Glarborg, P. and L.L.B. Bentzen, *Chemical Effects of a High CO_2 Concentration in Oxy-Fuel Combustion of Methane.* Energy \& Fuels, 2008. **22**: p. 291-296.
5. Launder, B.E. and D.B. Spalding, *Lectures in Mathematical Models of Turbulence*. 1972: Lectures in Mathematical Models of Turbulence.
6. Shih, T.H., et al., *A New k-ε Eddy-Viscosity Model for High Reynolds Number Turbulent Flows - Model Development and Validation.* Computers Fluids, 1995. **24**: p. 227-238.
7. Launder, B.E., *Second-Moment Closure: Present... and Future?* International Journal of of Heat and Fluid Flow, 1989. **10**: p. 282-300.
8. Raithby, G.D. and E.H. Chui, *A Finite-Volume Method for Predicting a Radiant Heat Transfer in Enclosures with Participating Media.* Journal of Heat Transfer, 1990. **112**: p. 415-423.
9. *ANSYS® Fluent, Academic Research, Release 12.0*.
10. Nicol, D.G., et al. *Development of a Five-Step Global Methane Oxidation-NO Formation Mechanism for Lean-Premixed Gas Turbine Combustion*. in *Proceedings of the International Gas Turbine and Aeroengine Congress and Exhibition: Stockholm, Sweden*. 1998.
11. Magnussen, B.F. and B.H. Hjertager. *On mathematical models of turbulent combustion with special emphasis on soot formation and combustion*. in *Proceedings of the 16th International Symposium on Combustion*. 1976.
12. Magnussen, B.F. *On the Structure of Turbulence and a Generalized Eddy Dissipation Concept for Chemical Reaction in Turbulent Flow*. in *Nineteeth AIAA Meeting, St Louis*. 1981.
13. Gran, I.R. and B.F. Magnussen, *A numerical study of a bluff-body stabilized diffusion flame. part 2. influence of combustion modeling and finite-rate chemistry.* Combustion Science and Technology, 1996. **119**.
14. Smith, G.P., et al., *GRI-Mech 3.0*.
15. Lu, T.F. and C.K. Law, *A directed relation graph method for mechanism reduction.* Proceedings of the Combustion Institute, 2005. **30**: p. 1333-1341.
16. Karalus, M.F., *Skeletal Mechanism Development for Alternative Gaseous Fuels in Lean-premixed Combustion*.
17. Steele, R.C., *NO_X and N_2O Formation in Lean-Premixed Jet-Stirred Reactors Operated from 1 to 7 atm*, 1995, University of Washington.

APPENDIX H:
Topical Report: Reduced Order Kinetic Mechanisms for Alternative Fuels

Public Interest Energy Research (PIER) Program

FINAL PROJECT REPORT

DEVELOPMENT AND EVALUATION OF GAS FUEL INTERCHANGEABILITY CRITERIA AND METHODOLOGIES

APPENDIX H

Topical Report: Reduced Order Kinetic Mechanisms for Alternative Fuels

Prepared for: California Energy Commission

Prepared by: Department of Mechanical Engineering

University of Washington

MAY 2013

Prepared by:

Primary Author(s):
Megan F. Karalus
K. B. Fackler
Igor V. Novosselov
John C. Kramlich
Philip C. Malte

Department of Mechanical Engineering
University of Washington
Box 352600
Seattle, WA 98195-2600

Contract Number: 500-08-034

Prepared for:

California Energy Commission

Marla Mueller
Contract Manager

Linda Spiegel
Office Manager
Energy Generation Research Office

Laurie ten Hope
RESEARCH AND DEVELOPMENT DIVISION

Robert. P. Oglesby
Executive Director

DISCLAIMER

This report was prepared as the result of work sponsored by the California Energy Commission. It does not necessarily represent the views of the Energy Commission, its employees or the State of California. The Energy Commission, the State of California, its employees, contractors and subcontractors make no warrant, express or implied, and assume no legal liability for the information in this report; nor does any party represent that the uses of this information will not infringe upon privately owned rights. This report has not been approved or disapproved by the California Energy Commission nor has the California Energy Commission passed upon the accuracy or adequacy of the information in this report.

ACKNOWLEDGEMENTS

Support for this project was provided by the California Energy Commission through Agreement No. 500-08-034 through the University of California-Irvine. We wish to acknowledge Marla Mueller, Technical Lead, who is the Technical Project Officer at the California Energy Commission, and Vincent McDonell, who is the Project Manager at UC Irvine.

Chapter H.1: Introduction

Lean-premixed (LPM) combustion technology is utilized in state of the art gas turbines to provide extremely efficient power generation with low emissions. Traditionally, natural gas has been used almost exclusively in LPM combustion. While extensive research on natural gas-fueled LPM combustion has been reported, much less research has been conducted on the use of alternatives to natural gas for LPM combustion devices. In the future, gas turbines will be run with a variety of fuel compositions ranging from syngases with high H_2 content to landfill and digester gas, which are mainly composed of CH_4, CO_2, and N_2. Alternative fuel blends will have a wide range of heating values, flame speeds, and chemical composition. It is important to study the behavior of these fuels under LPM conditions to maximize performance efficiency, while minimizing the overall emissions. In order to use alternative fuels effectively, knowledge must be gained pertaining to the expected emissions at comparable combustion temperatures as well as the relative resistance to blowout.

The range of fuel compositions studied in this work is shown below in Table H-1. It is the goal of this research to study fuel blends that will typify the composition of future fuels. Five fuel categories are studied: (1) pure H_2, (2) process and refinery gas, including combinations of H_2, CH_4, C_2H_6, and C_3H_8, (3) oxygen blown gasified coal/petcoke composed of H_2, CO, and CO_2, (4) landfill and digester gas composed of CH_4, CO_2, and N_2, and (5) liquefied natural gas (LNG)/shale/associated gases composed mainly of CH_4, C_2H_6, and C_3H_8. The baseline fuel for which all blends are compared is CH_4. In addition to the blends outlined in Table H-1, it is of both academic and general interest to perform parameterized studies within each fuel blend. Parameterized studies allow one to track differences that arise from variations in composition. As an example, we study mixtures of H_2/CH_4 that have limited application (e.g., 80/20). However, the study of this fuel blend provides useful chemical kinetic information that helps generalize the results of other more practical mixtures.

This study focuses on the formation of NO_X in LPM combustion devices with an emphasis on the effects of varying fuel composition. Additionally, the effects of reactor residence time and post-flame combustor temperature are also investigated for a selected set of fuels. An atmospheric pressure jet-stirred reactor (JSR) is the research tool used in this study, and both experimental and modeling results are presented for LPM combustion within this combustor. In addition to the study of emissions, the effect that fuel composition has on the resistance to lean blowout is also investigated.

An integral part of this study is the use of Computational Fluid Dynamic (CFD) modeling to understand how NO_x and flame stability are influenced by the use of alternative fuels. Because of the significant computational costs associated with using detailed chemical kinetic mechanism in CFD, it is necessary to use reduced (i.e., truncated) mechanisms for fuels that are more complex than CO and H_2. This means reduced mechanisms must be developed for CH_4, C_2H_6, C_3H_8, etc. This report presents the results of the work to find the optimum mechanism reduction methodology for these fuels.

Table H-1: Summary of gas composition used in this study

Category	Source		H_2	CO	CH_4	CO_2	N_2	C_2	C_3
1	High H_2	Range in Field	90 - 100						
		Nominal Fuel	100						
		Alternative Fuel	90			10			
2	Process and Refinery	Range in Field	25 - 55	10	30 - 65	5		0 - 25	0 - 25
		Nominal Fuel	25		50			25	
		Alternative Fuel 1	25		50				25
		Alternative Fuel 2	25		65			10	
		Alternative Fuel 3	55		35			10	
3	Gasified Coal/Petcoke (O_2 Blown)	Range in Field	35 - 40	45 - 50		10 - 15			
		Nominal Fuel	40	50		10			
		No Alternatives							
4	Landfill and Digester Gas	Range in Field			35 - 65	35 - 55	0 - 20		
		Nominal Fuel			50	35	15		
		Alternative Fuel 1			50	50			
		Alternative Fuel 2			50		50		
5	LNG	Range			75 - 95			5 - 25	
		See below							
	Shale Gas	Range			82 - 97	2.5		0 - 14	1
		See below							
	Associated Gas	Range			75 - 95			5 - 25	
		See below							
	LNG/Shale/ Associated Gases	Nominal Fuel			95			5	
		Alternative Fuel 1			90			10	
		Alternative Fuel 2			75			25	
		Alterntative Fuel 3			75				25

Chapter H.2: Literature Review

The review by Tomlin et al. (1997) identifies three main mechanism reduction strategies: (1) Mechanism Reduction without time-scale analysis, (2) Reduction considering time-scales, and (3) Fitted kinetic models. While the terms skeletal, reduced, and global have been used interchangeably to describe various simplified mechanisms in the literature, the following definitions will be employed when discussing mechanism reduction here.

1. *Skeletal mechanism:* from an established full mechanism without time-scale analysis and without alteration of the elementary Arrhenius reaction rates in which redundant reactions have been removed.

2. *Reduced mechanism:* from a skeletal or full mechanism with time-scale analysis, employing

the Quasi Steady State Approximation (QSSA) and Partial Equilibrium (PE) Assumption.

3. *Global mechanism:* derived using intuition and the 'fitting' of parameters for one or more reactions to experimental data or detailed kinetic simulations.

The following provides a brief description of the methods employed for each level of mechanism simplification, advantages, disadvantages, and literature references. The final section summarizes the findings and offers insights directly related to our current work to assist in choosing a simplification method.

H.2.1 Mechanism reduction without time-scale analysis

If one begins with a comprehensive chemical mechanism, the first level of simplification is to a skeletal mechanism. This is accomplished by first determining the parameters of interest, (typically heat release, or important species concentration profiles) and second, identifying and eliminating redundant species and elementary reactions. There are two basic methods for identifying the redundant species: detailed reduction and sensitivity analysis. The detailed reduction method, developed by Wang and Frenklach (1997) identifies reactions which do not contribute to the accumulation/depletion of the important species by comparing individual reaction rates with a reference reaction, typically the rate limiting step or fastest reaction. They further proposed that the computations used to obtain the data required for this analysis did not need to be performed with a fully coupled fluid-dynamic/chemical- kinetic model, but simplified 0-D and 1-D models would suffice. The method is based on the assumption that if a skeletal reaction mechanism can accurately describe the time evolution characteristics of both thermal and chain reaction processes of a more complex mechanism, then it will describe the chemical processes to the same degree of accuracy in reactive flow simulations.

Nicol (1995) applied the detailed reduction method of Wang and Frenklach, but pointed out that the generalization of this method to processes of varying chemical time scales (i.e. the inclusion of NO_x formation) had not been demonstrated. Nicol modified the method, including results from both a 0-D Chemical Reactor Network Model (CRM) and a Laminar One-Dimensional Model (L1DM) to eliminate redundant species. As reactions were subsequently combined, the Arrhenius rate coefficients of the final reactions were modified slightly to improve agreement between the skeletal and full mechanism, resulting in more of a quasi-global rather than true skeletal mechanism.

In keeping with the idea of the detailed reduction but applying an alternative mathematical technique, the redundant species can also be determined by investigating the Jacobian of the kinetic system of ODEs. The Jacobian and normed Jacobian will show information about the concentration of species in relation to the rate of production of important species. The detailed method of Wang and Frenklach requires several simulations of different reduced order models each time a species is eliminated, while the alternative mathematical approach requires a single simulation of the original model with the Jacobian calculated at several reaction times. While the alternative method may be more computationally efficient it cannot be used to investigate the effects on other important features such as ignition time (Tomlin et al., 1997).

Sensitivity analysis is the formal and mathematically rigorous approach to simplifying mechanisms. It is used to investigate the output of models as a function of parameters. For

example, the local sensitivity coefficients are defined as the partial derivatives of each species concentration with respect to the chemical rate constants (the parameters of interest). A rate is then perturbed at time t_1 and the resulting change in species concentrations studied at time t_2 (Tomlin et al., 1997). The normalized sensitivity coefficients indicate the relative importance of each reaction to species concentration (Law et al., 2003). The CHEMKIN-II post-processing program KINALC includes SENKIN which provides sensitivity analysis functionality. ChemkinPro provides the ability to evaluate first-order sensitivity coefficients of the gas temperature, and species fractions.

H.2.2 Mechanism reduction with time-scale analysis

Further reduction requires two assumptions - quasi-steady state for species, and partial equilibrium for reactions - which generally allow some species to be related by algebraic equations. There are three basic reduction methods applying these assumptions: Quasi-Steady State Approximation (QSSA), Computational Singular Perturbation (CSP), and the slow manifold approach (intrinsic low-dimensional manifold, ILDM). All three of these methods rely on the idea that there are certain modes in the model equations which work on a faster time-scale than others, and therefore may be decoupled. Separating the time-scales reduces both the size and stiffness of the reaction mechanism.

The QSSA method is a well established technique, relying on both chemical intuition and mathematical analysis for the identification of quasi-steady state species and reactions in partial equilibrium. Peters has produced a number of reduced mechanisms for different fuels based on this method (Paczko et al., 1986; Peters and Williams, 1987). Reduced mechanisms based on the QSSA method are derived from homogeneous systems but applied to spatially distributed systems where error propagation can be important. Yannacopoulos et al. (1996) give a qualitative description of these possible errors. They find that the error introduced depends significantly on the spatial gradients, with larger gradients introducing larger errors. They also comment that the error will significantly increase for some nonlinearities and some advection velocities. Law et al. point out that these errors, the result of the deterioration or failure of the QSS assumption in certain regions of the computational domain (i.e. the low temperature flame zone), can lead to convergence problems in CFD simulations (Law et al., 2003).

While the QSSA method was introduced in the early twentieth century, the CSP and ILDM methods have only been in use for the last 20 to 30 years. Unlike QSSA, the latter methods establish partial-equilibrium and quasi-steady state relationships without using any chemical intuition or expertise, but rather provide complex numerical methods to automate the process. The CSP method produces a reduced mechanism of a similar form to that found with the QSSA method. Lu and Law point out several flaws in how QSS species are identified empirically in the QSSA method and claim that by using CSP to rigorously identify QSS species, some of the numerical difficulties discussed above can be abated (Lu and Law, 2008). It should be noted however that the reduced mechanism developed with this method also has the fewest number of species identified as QSS and therefore should have a wider range of applicability by nature.

The goal of ILDM is slightly different than CSP. Rather than trying to reduce the stiffness of the system of equations by introducing algebraic relations, ILDM reduces the “state space” of the system to facilitate the creation of a species concentration look-up table (Maas and Pope, 1992).

This couples nicely with the standard ISAT (In situ adaptive tabulation) algorithm for the generation of these lookup tables in CFD simulations. A presumed probability density function (PDF) approach using the tabulated chemistry is typically combined with RANS modeling of the turbulence. Lu and Law (2003) point out that ILDM still relies on the QSS assumption and therefore the reduced mechanisms still suffer from the same numerical difficulties described above. Recently, extended versions of ILDM have attempted to remedy this problem. The Flame Prolongation of ILDM (FPI) (Gicquel et al., 2000) and the Flame-Generated Manifold (FGM) (Oijen and De Goey, 2000) method both tabulate chemistry effects for unstrained premixed laminar flamelets. While ILDM mechanism reduction can be an automated process, a new lookup table must be generated for each fuel mixture under investigation. Table H-2 provides a brief summary of some of the various reduced mechanisms identified in the literature.

Table H-2: Sample of reduced mechanisms for CH_4/air combustion found in the literature

Name	Species	Reactions	Reference	Full Mech	Reduction Method
15-step	19 (21)	15 (17)	Tianfeng and Law (2008)	GRI 3.0	CSP
10-step	10 (15)	7 (10)	Belcadi et al. (2007)	GRI 3.0	CSP
12-step ARM	16 (19)	12 (15)	Sung et al. (2001)	GRI 3.0	QSSA
4-step	8	4	Paczko et al. (1986)	See paper	QSSA

H.2.3 Fitted kinetic models

Fitted kinetic models have a long history, being used before detailed kinetic models were developed. Even the comprehensive GRI 3.0 mechanism in common use today has been optimized by fitting the parameters of some reaction steps to bulk experimental data (Tomlin et al., 1997). The fitting strategies used to reduce detailed mechanisms fall into two basic categories: Quasi-Global Kinetic Models which tend to include a subset of the original mechanism as a base such as the H_2 / CO, while fitting one or more fuel oxidation steps; and Fitted Global Kinetic Models which fit a set of data to a small global reaction scheme.

H.2.3.1 Quasi-Global Kinetic Models

Edelman and Fortune (1969) were probably the first to combine global and elementary kinetics. The oxidation of the hydrocarbon to CO and H_2 was represented by a global reaction while the oxidation of CO and H_2 was the described by the elementary steps. Tomlin et al. (1997) point out that in reality, the hydrocarbon, CO and H_2 oxidation will compete for the radicals. The oxidation of CO and H_2 is over predicted without this coupling.

Gokulakrishnan et al. (2006) applies this method to develop a quasi-global mechanism to

predict the ignition delay time and laminar flame speed measurements of CH_4, H_2, CH_4 / H_2, CH_4 / CO, and CO / H_2 mixtures. The oxidation of methane to CH_2O and H_2 is represented as a global rate and then a detailed CH_2O / H_2 / O_2 mechanism is used to include the intermediate combustion radicals. The claim is that these radical concentrations are necessary to predict ignition and extinction phenomena simultaneously in order to properly account for flame-holding and stability. The resulting quasi-global mechanism consists of 15 species and 40 reactions which includes prediction of NO emissions. This mechanism is employed in a 2D simulation of a backward-facing step combustor, burning CH_4 /air at atmospheric pressure at equivalence ratios ranging from 0.5 to 1.5.

H.2.3.2 Fitted Global Kinetic Models

The fitted global kinetic models rely on first identifying the overall global scheme to be used. Hydrocarbon oxidation takes place in several steps. Tomlin et al. identifies them as the following:

1. Hydrocarbons decompose to olefins (endothermic)
2. Oxidation of H_2 (exothermic)
3. Oxidation of olefins to CO (endothermic)
4. Oxidation of CO to CO_2 (exothermic)

The scheme of Hautman et al. (1981) includes all of these stages:

$$C_nH_{2n+2} \rightarrow (n/2)\ C_2H_4 + H_2 \qquad \text{(H-1)}$$

$$C_2H_4 + O_2 \rightarrow 2CO + 2H_2 \qquad \text{(H-2)}$$

$$CO + (1/2)\ O_2 \rightarrow CO_2 \qquad \text{(H-3)}$$

$$H_2 + (1/2)\ O_2 \rightarrow H_2O \qquad \text{(H-4)}$$

Duterque et al. (1981) developed a global mechanism for high temperature propane flames based on the above scheme. They concluded that the reverse reactions were needed to account for CO and H_2 as stable products and to aid in achieving numerical stability, therefore the Hautman scheme was extended to eight steps.

Jones and Lindstedt (1988) developed their global scheme for hydrocarbon combustion by looking at a two-reaction zone flame model. In the primary zone, the fuel is converted to CO and H_2, and in the secondary zone these are oxidized to H_2O and CO_2.

$$C_nH_{2n+2} + (n/2)\ O_2 \rightarrow n\ CO + (n + 1)\ H_2 \quad \text{(H-5)}$$

$$C_nH_{2n+2} + n\ H_2O \rightarrow n\ CO + (2n + 1)\ H_2 \quad \text{(H-6)}$$

$$H_2 + (1/2)\ O_2 \rightarrow H_2O \quad \text{(H-7)}$$

$$CO + H_2O \rightarrow CO_2 + H_2 \quad \text{(H-8)}$$

The rate of each of these reaction steps is given in Arrhenius form with various powers of species concentrations, present or not present in the reaction. Early global reaction rates using the above schemes were derived directly from experimental results. The work of Nicol et al. (1999). and Novossolov and Malte (2008) aimed to simplify known detailed mechanisms for use in CFD applications, fitting the global reaction rates to data from Chemical Reactor Network Modeling (CRM) employing the detailed mechanism. This resulted in 5-step and 8-step reaction schemes, respectively, with the 8-step accounting for all four NO_x formation pathways. Pressure dependence is accounted for in the exponents of the species concentrations.

While all of the global kinetic schemes discussed so far were developed from simple intuition, Jiang et al. (1995) used QSSA and partial equilibrium assumptions to first develop a reduced mechanism. Then, rather than leaving the rates of the reduced mechanism as algebraic relations of the elementary steps, they created new global Arrhenius rates for each reaction, both forward and backward, in the following reduced scheme.

$$CH_4 + OH \rightarrow CO + H_2 + H \quad \text{(H-9)}$$

$$H_2 + M \rightarrow 2\ H + M \quad \text{(H-10)}$$

$$H + OH \rightarrow H_2O \quad \text{(H-11)}$$

$$CO + OH \rightarrow CO_2 + H \quad \text{(H-12)}$$

The alternative fitted kinetic model for use in a CFD code is known as the 'response modelling technique.' This combustion chemistry approach was developed at NASA Glenn Research Center by Molnar and Marek (2003). It begins by considering that reaction rates are controlled by either kinetics or mixing. The mixing time is determined in the turbulence modelling, while

the kinetic time is developed as an expression of the ignition delay time as a function of equivalence ratio, temperature, and pressure. Lamnaouer et al. (2009) also employ this method, and describe the reasoning for using the ignition delays times. To summarize their logic: the goal is to model gas turbine combustors - this combustion can be represented by adiabatic, constant pressure, well-stirred reactors; these reactors correspond to the post-shock conditions of shock heating a fuel/oxidizer mixture at constant enthalpy and constant pressure conditions; and finally, modeling the kinetic times based on an isothermal process instead does not affect the results appreciably. Although CO and NO_x were included in the method development, the ability of the model to accurately predict these species is still unclear.

H.2.4 Choosing a method

The ultimate goal of the mechanism work is to develop simplified mechanism(s) for use in CFD simulations of the combustion of various fuel mixtures consisting of methane, ethane, propane, CO, CO_2, and H_2. Ideally there would be one mechanism (although this may not be possible), and it would adequately predict CO and NO_x emissions. Although there is quite a bit of information in the literature on simplifying detailed mechanisms, most of this is directed at single hydrocarbon fuels. Very few authors, except for Gokulakrishnan et al. (2006) and Slavinskaya et al. (2008) discuss multicomponent fuels. Both of these authors ultimately use quasi-global techniques in their work to develop mechanisms that can be employed in CFD simulations.

Choosing a reduction method (or a global scheme) requires defining a reasonable number of species for CFD simulations. Law et al. (2003) suggests that 10 to 20 lumped reactions with the corresponding number of species could be reasonably incorporated into current 3-D, CFD simulations. Skeletal and reduced mechanisms are preferred in the literature because of the rigor employed in their development. This range for species count can preclude using skeletal mechanisms if the set of operating conditions is large (i.e. temperature, pressure, equivalence ratio), and while the species count of reduced mechanisms often fall in this range, there are significant numerical convergence issues when implemented in CFD models.

Table H-3 summarizes the simplification methods and their advantages and disadvantages:

Table H-3: Summary of Simplification Methods

Reduction Method	Advantages	Disadvantages
Without Time-Scale Analysis • detailed reduction • sensitivity analysis	• retains elementary reaction rates • mathematically rigorous • automated (KINALC & CheminPro)	• mechanism remains 'stiff' • mechanism remains large (removal of 10 − 15 species)
With Time-Scale Analysis	• reduce 'stiffness' (or generate a lookup table)	• all methods require QSS assumption

• QSSA • CSP • ILDM	• reduce species count to less than 20 • mathematically rigorous • automated • retains some elementary reaction in- formation	• failure of QSS assumption in low temperature zones creates numerical problems in CFD applications • repeat reduction for each new fuel mixture
Fitted Kinetic • quasi-global • global fitted	• significant reduction in species count • reduced 'stiffness' • possible to develop one for multiple fuel mixtures • numerical stability in CFD	• not rigorous • basis for establishing global reaction scheme?

Our suggestion is to pursue a global or quasi-global simplification. If we choose global, we should begin by establishing our global scheme. This should include at a minimum the inclusion of an H_2 oxidation step in the current global methane scheme. It may also include tracking one or more radicals and the oxidation of the other two hydrocarbons if a single mechanism/scheme can be developed. Fitting the scheme should begin at atmospheric pressure, with just methane as a fuel. Then we investigate and see if we can tune the scheme to include CH_4 / CO / H_2 mixtures, and then attempt to include the other hydrocarbons. When one or more atmospheric schemes have been developed we proceed to do the same for elevated pressures.

Since this fitting will be done against an established detailed mechanism we should determine if GRI 3.0 is the best option. This would be approached by developing an adequate CRN for the Jet Stirred Reactor and running our three mechanism options (USC, San Diego, and GRI 3.0) to see how they fit the experimental data. If we are interested in both NO_x and CO emissions we also need to resolve the possibility of CO oxidation in the probe.

In summary, three levels of reduction are identified and are described here as global, reduced (with time-scale analysis), and skeletal (without time-scale analysis). Previous restrictions on the number of species (□ 6) in a simulation favored global mechanisms, in which rate parameters for several global reactions are fit using results from detailed kinetic simulations (Nichol et al., 1999; Novosselov and Malte, 2008). As computational resources increased, implementation of reduced mechanisms became feasible. In their development, intuition and mathematical analysis are used to identify species in quasi-steady state, and reactions in partial equilibrium in order to relate some species by algebraic equations. Schemes for methane combustion with 10 to 19 independent species without NO_x (15 to 21 with NO_x) have been developed (Sung et al., 2001; Belcadi et al., 2007; Lu and Law, 2006, 2008). Lu and Law (2008) state however that simulations of turbulent combustion can currently incorporate 20-30 species, making it possible to reduce only to the skeletal mechanism for which unimportant species and elementary reactions are removed from a detailed mechanism. There are numerous methods, reviewed in

the articles above, for identifying the unimportant species and reactions. Lu and Law (2005) point out that the method of Directed Relation Graph (DRG) has 3 advantages over its competitors:

1. It features the fastest reduction algorithm for large mechanisms.
2. It can identify all candidate skeletal mechanisms sorted by accuracy in a single run.
3. It provides the ability to specify an upper error bound on the resulting mechanism.

It is therefore the chosen method for this study.

Chapter H.3: Description of Mechanism Reduction Procedure

The goal of the present study is to predict emissions of CO and NO_x, in addition to describing heat release and other major species concentrations in CFD modeling of LPM combustion with a mechanism of 30 species or less. The focus is on the industrial atmospheric combustor and high pressure gas turbine for $CH_4/H_2/CO_2$ fuel mixtures. Homogeneous systems provide expedient sampling for the development of skeletal mechanisms and it is appropriate to apply skeletal mechanisms developed from 0-D modeling to problems with transport provided some pre-validation is performed. In addition Perfectly Stirred Reactors (PSRs) capture the high temperature flame chemistry and kinetic extinction relevant to LPM combustion. While including auto-ignition modeling would increase the comprehensiveness of the resulting skeletal mechanism, it is not important in predicting emissions from steady, LPM combustion and therefore is not included. Thus the parameter space is chosen to include pressures from 1 to 30 atm, equivalence ratios from 0.4 to 1.0, and mean PSR residence times from slightly greater than blowout to 3ms. The preheat temperature is from 300 to 500 K for atmospheric combustion and is set for higher pressures as the outlet temperature of the compression process. (This assumes compression from 1 atm and 300 K to the pressure of interest with an 85% efficiency.)

The following describes the method of Directed Relation Graph (DRG) for finding a skeletal mechanism and the extended Directed Relation Graph Sensitivity Analysis 17 (DRGASA). The application of DRG to develop a skeletal oxidation mechanism for methane is described. This is followed by a discussion of the application of DRGASA to develop a skeletal NO_x mechanism to append to the methane mechanism. Finally the skeletal oxidation and NO_x mechanisms are validated against the full GRI-3.0 mechanism in both PSR and Laminar Flame Speed calculations.

H.3.1 Background of the Method

The detailed mechanism GRI-3.0 (Smith et al., 2000) has 35 (36 with Ar) species and 219 reactions describing fuel oxidation and an additional 17 species and 106 reactions describing NO_x production. It was designed and optimized to describe natural gas combustion and it is still in standard use today. The mechanism reduction used here is guided by a database of solutions of 0-D, adiabatic, homogeneous reactors (PSRs) in the parameter space of interest. The

variables of this space are residence time, preheat temperature, equivalence ratio, and pressure. Each is varied independently and the final matrix is found in Appendix A. A PSR is run under each set of conditions, for a total of 108 data points, and the results of species concentrations and rates of production are saved in text files for post-processing. These detailed chemical kinetic simulations are completed using CHEMKIN-PRO, and post-processing and implementation of the reduction algorithm is accomplished using SAGE (Stein et al., 2010), a Python based, open-source mathematics software package. The Python language is adept at string manipulation allowing for the integration of post-processing and reduction.

Eliminating unimportant species and reactions from the detailed mechanism requires an understanding of the pairwise relationship among the species. Graphs, the abstract representation of objects (nodes) and their connections (edges), are well suited to this type of analysis. More specifically, directed graphs with weighted edges provide the level of detail necessary to rigorously remove unimportant species. The method of Directed Relation Graph (DRG) developed by Lu and Law (2005), maps species couplings to a directed graph, weights these couplings, and removes weak couplings based on a user specified error tolerance. Species strongly coupled to the major ones, such as fuel or oxidizer, are then discovered through a graph search. The method of DRG by itself does not guarantee the smallest possible skeletal mechanism for the desired error tolerance since it retains species if their removal has a non-negligible effect on any of the other species in the mechanism. It is still possible then to further reduce the mechanism by removing species that have only a minor effect on the major species of interest or other global parameters. This is accomplished through DRG-aided sensitivity analysis (DRGASA), which is similar to traditional sensitivity analysis except that it evaluates the error induced by the elimination of species instead of the perturbation of species concentration. Details of both the DRG method and its extension, DRGASA, are discussed in the following.

H.3.2 Skeletal Reduction with DRG

A simple, but abstract mechanism can be used to illustrate the concept of skeletal reduction with DRG. Assume a reaction mechanism of the form below with fuel and product species *A, B, C, D, E, F* and reaction progress rates of q_1 to q_5.

(R1)	$A \longleftrightarrow B,$	q_1
(R2)	$B \longleftrightarrow D,$	q_2
(R3)	$B + D \longleftrightarrow C,$	q_3
(R4)	$E \longleftrightarrow C,$	q_4
(R5)	$E \longleftrightarrow F,$	q_5

An unweighted, directed graph (digraph) showing the coupling of all species can be drawn and is shown in Figure H-1, with the nodes corresponding to the species and the edges, connections through reactions. The graph illustrates the problem of removing species from a mechanism; because of the strong coupling of the species through the many reactions, removal of one

species may significantly affect the concentration prediction of another species even if they never appear together in any elementary reaction (i.e. removing species *D* may significantly affect the prediction of *A* although they are not directly connected). A weighted edge is needed to quantify the error induced by the removal of a species, so that a new digraph can be drawn in which the edge between *A* and *B* (for example), is kept if and only if the removal of species *B* would directly induce significant error to the production/destruction of species *A*.

Figure H-1: Digraph Example.

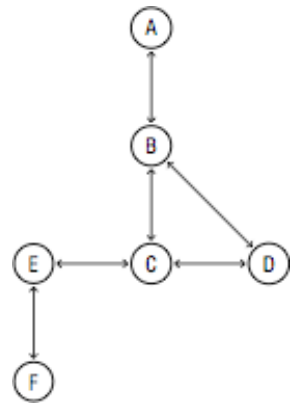

The production rate of *A*, R_A, in a mechanism with N reversible reactions can be expressed as

$$R_A = \sum_{i=1,N} \nu_{A,i} q_i \tag{H-13}$$

$$q_i = k_{fi} \prod_{j=1}^{K} [X_j]^{\nu'_{ji}} - k_{ri} \prod_{j=1}^{K} [X_j]^{\nu''_{ji}} \tag{H-14}$$

$$k_{fi} = A_i T^{\beta_i} \exp\left(\frac{-E_i}{RT}\right) F_i \tag{H-15}$$

$$k_{ri} = \frac{k_{fi}}{K_{ci}} \tag{H-16}$$

where the subscripts *i* and *j* refer to the ith elementary reaction and j^{th} species, ν_{Ai} is the stoichiometric coefficient of *A* in reaction *i*, q_i is the rate of progress of reaction *i*, *k* is the reaction rate, and the subscripts *f* and *r* refer to forward and reverse rates respectively. Furthermore ν' and ν'' refer to the stoichiometric coefficients of the reactants and products respectively, *C* is the molar concentration of a species, *A*, β, and *E* are the Arrhenius reaction rate parameters and *F* the correction factor for special effects. Finally *T* is the temperature and K_c is the equilibrium constant.

The production of species *j* by reaction *i* is given by ω_{ji}

$$\omega_{ji} = \upsilon_{ji} q_i \tag{H-17}$$

To quantify the direct influence of one species on another, a normalized contribution of species *B* to species *A* is defined as r_{AB}. Influence on both net production and net destruction is accounted for by using the absolute value of the contributing terms. Lu and Law (2006) explore

two alternate definitions for this normalized contribution but find that the definition given by Equation 18 performs correctly for mechanisms involving both Quasi-Steady State (QSS) species and Partial Equilibrium (PE) reactions.

$$r_{AB} = \frac{\sum_{i=1,N} |\omega_{Ai}\delta_{Bi}|}{\sum_{i=1,N} |\omega_{Ai}|} \tag{H-18}$$

$$\delta_{Bi} = \{1 \text{ if the } i^{th} \text{ reaction involves species } B\text{, or 0 otherwise}\} \tag{H-19}$$

With r_{AB} defined to measure the extent of the coupling of A to B as the relative error induced to species A by the elimination of B, Figure 1 can be redrawn such that an edge is kept if and only if $r_{AB} > \varepsilon$, where ε is a user specified threshold relative error. A possible resulting digraph is shown in Figure 2.

Figure H-2: Digraph example after edge removal.

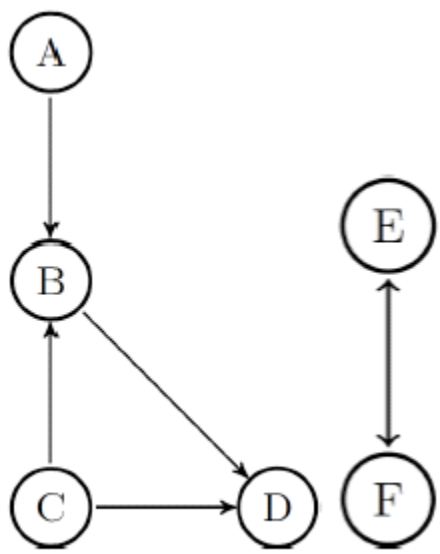

With the graph formed, species for the starting set are selected. This is typically a single species such as the fuel through which the oxidizer and all products of interest are coupled. Note that because third body species are not accounted for in the definition of the relative error, any inert species of interest should also be included in the starting set to ensure they remain in the skeletal mechanism. For each starting species, A, a depth first search (DFS) is applied to the digraph to identify the dependent set of A. The union of the dependent sets of species for each starting species is then the skeletal mechanism. The elementary reactions kept are all those from the detailed mechanism which include only the species from the now defined skeletal mechanism.

With some relative error ε the group $E - F$ is decoupled from the group $A - B - C - D$. While the intra-group coupling of E and F may be strong, the inter-group coupling of $E - F$ and $A - B - C - D$ is relatively weak. This sort of behavior accounts for sudden jumps in the number of species retained as ε is varied.

H.3.3 Further Skeletal Reduction with DRGASA

Because of the highly non-linear coupling of the species in a reaction mechanism, the error caused by the removal of a set of species is not necessarily the sum of the errors caused by the removal of each species individually. DRGASA is an iterative procedure that attempts to obtain a final skeletal mechanism with the required overall accuracy. To apply DRGASA, the following procedure is used:

1. A DRG analysis is applied to obtain the critical value of ε for each species, and any species with a smaller than user-specified level is eliminated as described above.
2. The sensitivities E_i, defined as the worst-case relative error induced to the parameters of interest (i.e. NO concentration) due to the elimination of each species i, are then computed for each species with ε greater than the user specified tolerance and still under consideration for removal.
3. The species are sorted by their E_i values in ascending order, and starting with the species with the smallest E_i, are eliminated one at a time.
4. A new reduced mechanism is created with just one of these species eliminated, the models re-run, and the sensitivities re-calculated.

The relative error is defined by Equation 20, where x_0 is the species concentration with the reduced mechanism and x is the species concentration with the detailed mechanism. The sensitivity E_i is the maximum δ in the parameter space.

$$\delta = \frac{|x - x_0|}{x} \tag{H-20}$$

The skeletal mechanism obtained by a DRGASA analysis is considered to be a minimal size, such that further elimination of any species would result in larger than acceptable error.

H.3.4 Mechanism Reduction Procedure

Detailed chemical kinetic simulations are completed using CHEMKIN-PRO with a 0-D, adiabatic, homogeneous reactor (PSR) to create a database of solutions in the parameter space of interest. The variables of this space are residence time, preheat temperature, equivalence ratio, and pressure. Each is varied independently and the final matrix is found in Appendix A. A PSR is run under each set of conditions, for a total of 108 data points, and the results of species concentrations and rates of production are saved in a text-file for post-processing. GRI-3.0 is chosen as the detailed mechanism but fuel oxidation and NO_x formation are treated separately resulting in the generation of two databases: one using full GRI-3.0 and the other using GRI-3.0 without the NO_x chemistry.

Post-processing and implementation of the reduction algorithm is accomplished using SAGE (Stein et al., 2010), a Python based, open-source mathematics software. The Python language is adept at string manipulation, allowing for the integration of post-processing and reduction. The reduction algorithm is outlined below:

1. A single result file from a PSR calculation is taken and post-processed: a list of species (nodes) is extracted and a list of r_{AB} is calculated (weighted edges). This is then repeated for all result files in the parameter space, and a master list of weighted edges for each graph from each results file is compiled.
2. A threshold value is chosen.
3. A graph (results file) is chosen and each of its weighted edges (r_{AB}) is compared to the chosen threshold value. If the weighted edge is less than the threshold, it is removed. A new digraph is then constructed using the list of species and the new list of weighted edges greater than the chosen threshold. A DFS is performed starting with the species of interest (either the fuel, CH_4), or NO here) which returns a list of species to be saved (the dependent set of CH_4 or NO).
4. Step 3 is repeated for each graph, corresponding to each results file, to compile a master list of species to be saved.
5. Steps 3 and 4 are then repeated for each new threshold value chosen such that a new master list of species to be saved is compiled.

The results of the application of this algorithm are described in what follows.

H.3.4.1 Methane Oxidation

Figure H-3 shows the dependence of the number of species in the skeletal mechanism on the value of the threshold ε. It is seen that there exist jumps in the number of species retained. This occurs most prominently at $\varepsilon = 0.025$ in which 10 species are removed (mostly C_2 species). Smaller jumps occur at $\varepsilon = 0.225$ and 0.335 at which 3 and 4 species are removed. These jumps, as mentioned above, are due to the elimination of strongly coupled groups of species. Since these groups should be kept together, the threshold should be chosen either right before or right after one of these jumps. Choosing a threshold slightly larger than the first jump, $\varepsilon = 0.03$ removes the largest strongly coupled group while retaining species crucial for the description of prompt.

Figure H-3: Dependence of the number of species in a skeletal mechanism on the threshold value ε for DRG. The blue line indicates a chosen threshold value and the red line shows species retained by the given skeletal mechanism.

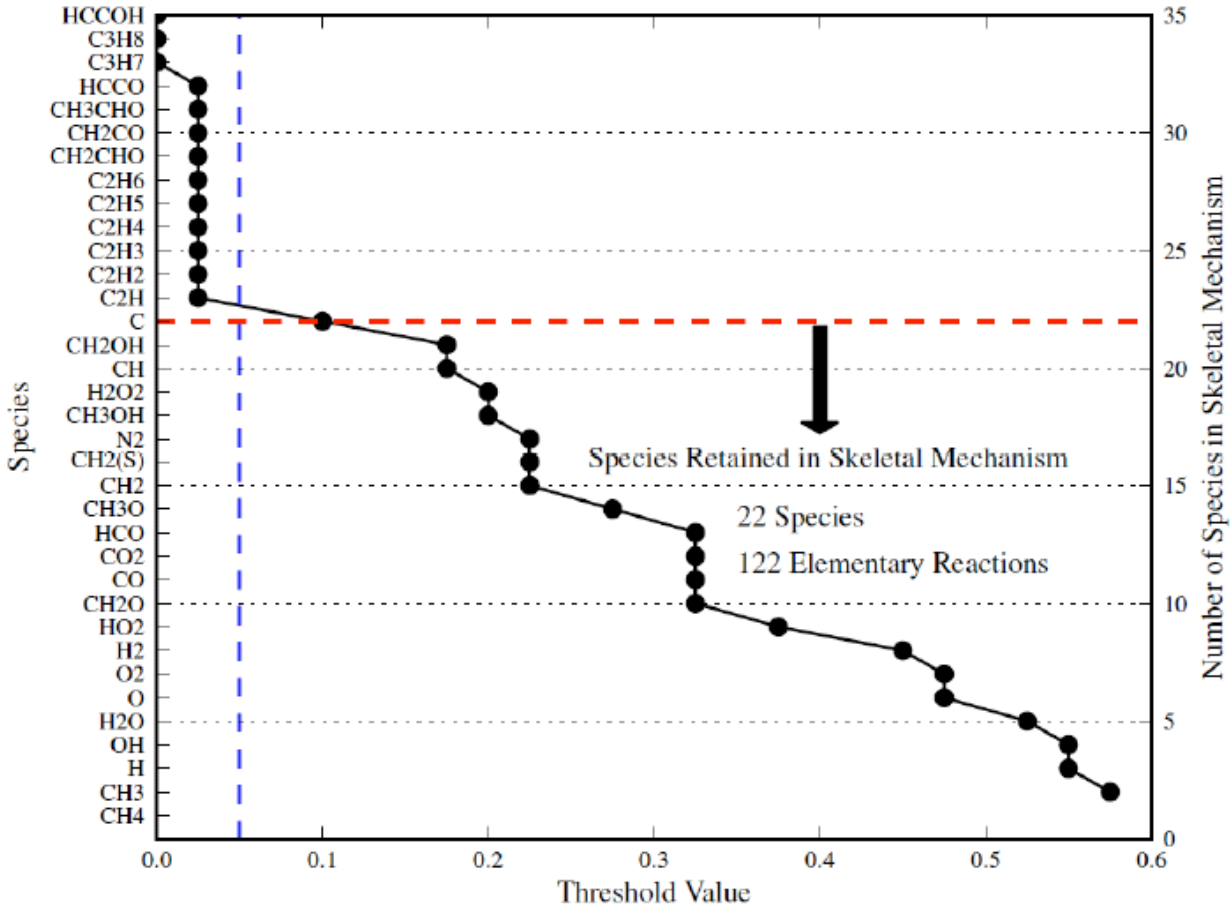

NO_x formation. The resulting skeletal mechanism retains 22 species: H_2, H, O, OH, H_2O, HO_2, H_2O_2, O_2, CO, HCO, CO_2, CH_4, CH_3, C, CH, CH_2OH, CH_3OH, $CH_2(S)$, CH_2, CH_3O, CH_2O, N_2. In addition, the skeletal mechanism retains 122 reactions by eliminating all elementary reactions in GRI-3.0 with any reactant or product not contained in this set of species. It should also be noted that all species and reactions of the H_2/CO submechanism are retained.

Lu and Law (2008) applied the method of DRG to generate a skeletal mechanism with a database of both PSR and auto-ignition behavior. Their parameter space included pressures of 1-30atm, equivalence ratios of 0.5-1.5, and initial temperatures of 1000-1600K for autoignition and 300 K for PSR. They chose a threshold of 0.13, resulting in a mechanism with 30 species and 184 reactions. In addition to the species included in the skeletal mechanism derived in this work, their mechanism included C_2H_2, C_2H_3, C_2H_4, C_2H_5, C_2H_6, CH_2CHO, CH_2CO, and HCCO.

H.3.4.2 NO_x

With the skeletal oxidation mechanism defined, the reduction of NO_x chemistry can now be evaluated. Because of the very small NO_x concentrations near blowout the same parameter space is used except that the blowout residence times are replaced with residence times 15%

larger than blowout (these residence times will be referred to as being "near blowout" in the following text). This is then run with full GRI including NO_x chemistry. A plot similar to Figure H-3 is created using NO as the starting species rather than CH_4, but only nitrogen containing species are plotted for clarity since the oxidation mechanism will not be altered. We see from Figure H-4 that at a threshold of 0.2, nine additional species including NO are retained. The resulting mechanism is considered the baseline for NO_x reduction for a total of 32 species.

Figure H-4: DRG applied to GRI with full NO_x chemistry. Threshold values are plotted for N containing species only for clarity. The blue line indicates a chosen threshold value and the red line shows the NO_x species retained by the given skeletal mechanism.

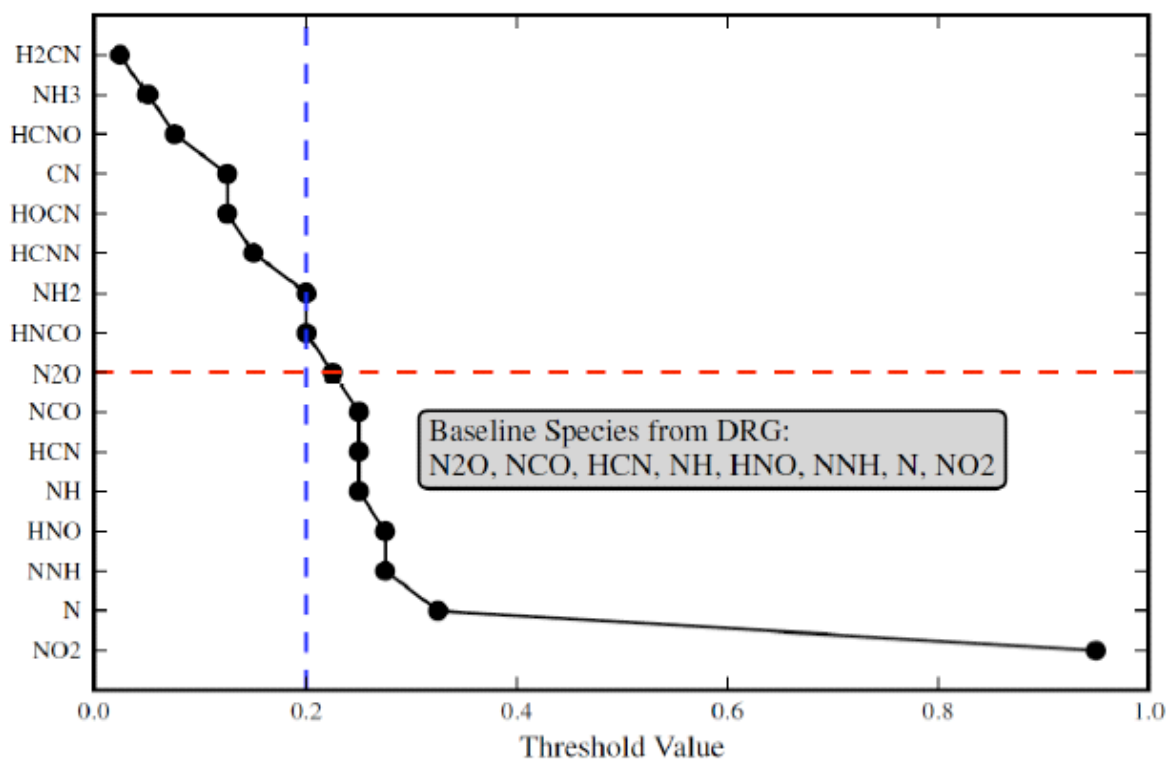

In an effort to reduce the mechanism further however, DRGASA is applied with NO chosen as the species of interest. Figure 5 shows the relative error of NO concentration as compared to full GRI across the full parameter space for the baseline case (32 species) and then the baseline case with each of the listed species removed one at a time. Although all baseline case N containing species were tested in this way, those listed in the figure were the only ones which induced small enough errors to be considered for removal. Also, as the concentration of NO decreased, the error significantly increased therefore two lower limits were considered, 5 and 10 ppm. If the NO concentration was below the chosen limit the error was not included in determining the maximum relative error. In addition, the maximum errors are shown for residence times near blowout and 3ms separately.

The results of Figure 5 indicate that NO_2 and HNO are possible candidates for removal. Removal of NO_2 has a more significant effect on results near blowout than at 3ms. The removal of HNO seems to have an equal effect on results at both blowout and 3ms. In addition there is

very little change in the maximum relative errors of the baseline case and that with NO_2 removed, therefore NO_2 is the only species chosen for removal. The fact that NO_2 was a candidate for removal at all may come as a surprise considering the results of Figure 5 which show removal of NO_2 to be possible only under the largest threshold value when DRG alone is applied. NO_2 can often be assumed to be a quasi-steady state species as most reactions involving NO_2 are simply shuffling NO to NO_2 and vice versa. This is an excellent illustration of the fact that the application of DRG alone does not necessarily result in the smallest skeletal mechanism possible. It also indicates that, contrary to the suggestion in Zheng et al. (2007) to only choose a range of thresholds (i.e. 0.2 to 0.4) over which to apply DRGASA, further reduction is still possible by looking at species with minimum removal thresholds as large as 0.95. Finally it should be noted that NO_2 is a candidate for removal because we are unconcerned with the distinction between NO and NO_2 in predicting NO_x emissions and assume NO is an acceptable surrogate for both NO_x species.

The final skeletal oxidation mechanism with skeletal NO chemistry has 30 species, the N containing species being N_2O, NCO, HCN, NH, HNO, NNH, N, NO, N_2. This ensures that a truncated version of each NO formation pathway is still present: NCO and HCN for the prompt route, NH and NNH for the NNH route, N_2O for the nitrous oxide route, and N for Zeldovich.

Figure H-5: Relative error of NO concentration (compared to full GRI) when each of the listed species is removed individually from the baseline skeletal mechanism, which was developed using only DRG.

(a) NO > 5ppm

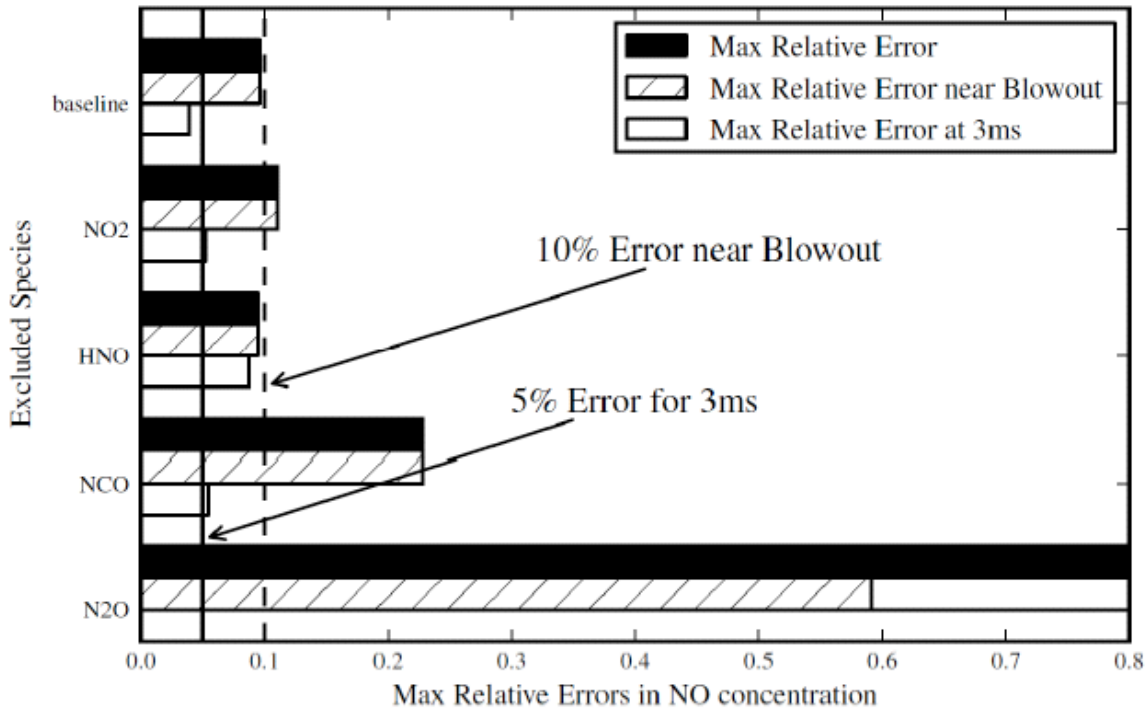

(b) NO> 10ppm

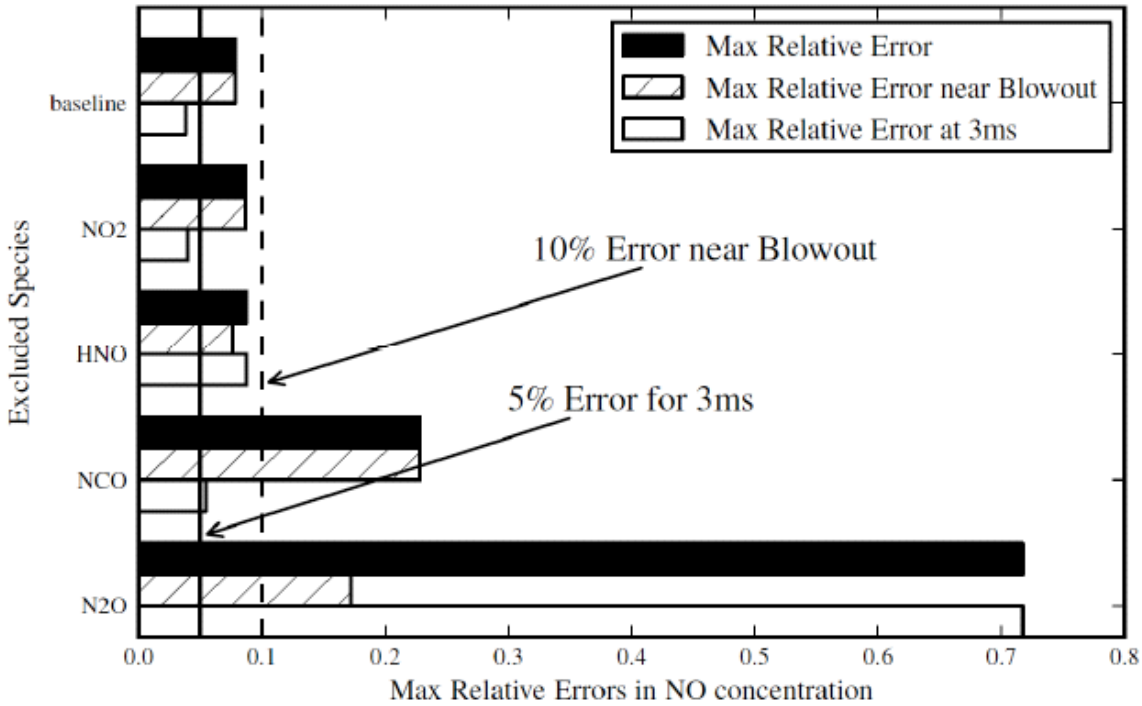

H.3.4.3 Validation

To verify the applicability of the skeletal mechanism with NO chemistry, prediction of the blowout residence time, and NO concentrations in a PSR and are compared against that predicted with full GRI-3.0. This is done for the full parameter space over which DRG was originally applied (although only to near blowout residence times for NO concentrations and only for concentrations greater than 5ppm). In addition, laminar flame speeds calculated using the two mechanisms are compared to ensure the skeletal mechanism can be extended to multi-dimensional models. Agreement between the full and skeletal mechanisms is quantified using the relative error given by Equation 20 above. The color scheme used to indicate the chosen pressure is the same among the following figures in this chapter with the dashed blue line indicating an inlet temperature of 500K and the solid blue line an inlet temperature of 300K.

Figure 6 illustrates the ability of the skeletal oxidation mechanism to capture extinction. The two sets of calculations for atmospheric pressure lie on top of each other at less than 5% error, and the calculations at higher pressures all tend to agree as well trending to larger errors as equivalence ratio decreases. This is hypothesized to be due to the increased importance of the C_2 pathways at extending stability at lower equivalence ratios and higher pressures. As a result the skeletal mechanism tends to under predict the blowout residence time. Figures 7 and 8 shows the increasing relative error in the prediction of NO concentrations as pressure increases, however errors are still reasonable, being consistently below 10%. It should be noted that the skeletal mechanism tends to over predict NO concentrations as compared to GRI. Finally Figure 9 shows the applicability of the skeletal mechanism to multidimensional models. The skeletal mechanism tends to overpredict the laminar flame speed and errors increase with lower equivalence ratios and higher pressures.

Figure H-6: Relative error in the prediction of residence time near blowout, detailed vs. skeletal mechanism.

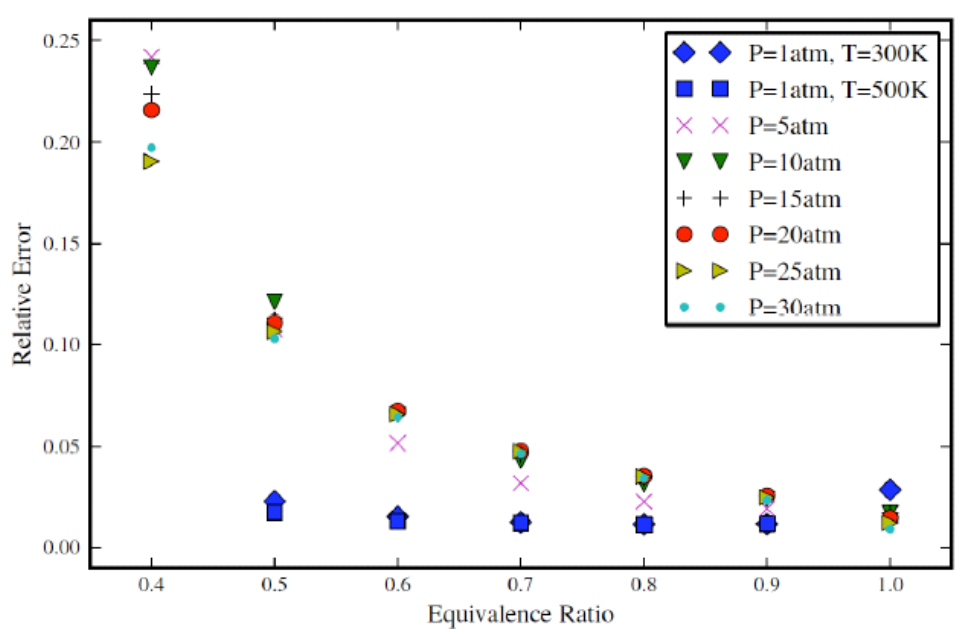

Figure H-7: Validation of NO prediction by the skeletal mechanism in a PSR near blowout, for all pressures in the parameter space, through plots of both magnitude and relative error.

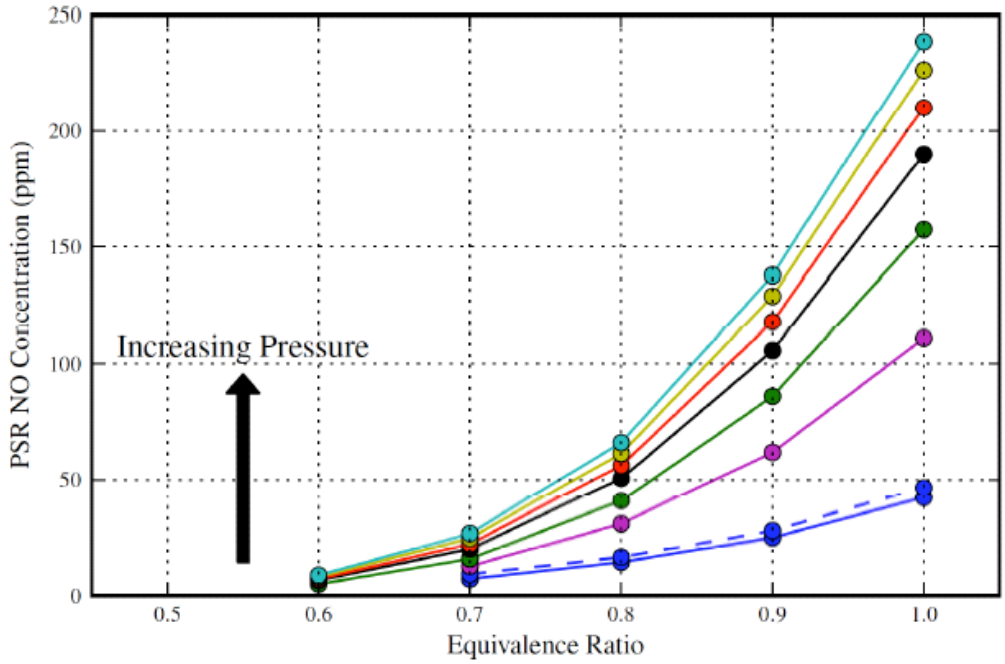

(a) NO concentration near blowout, detailed mechanism

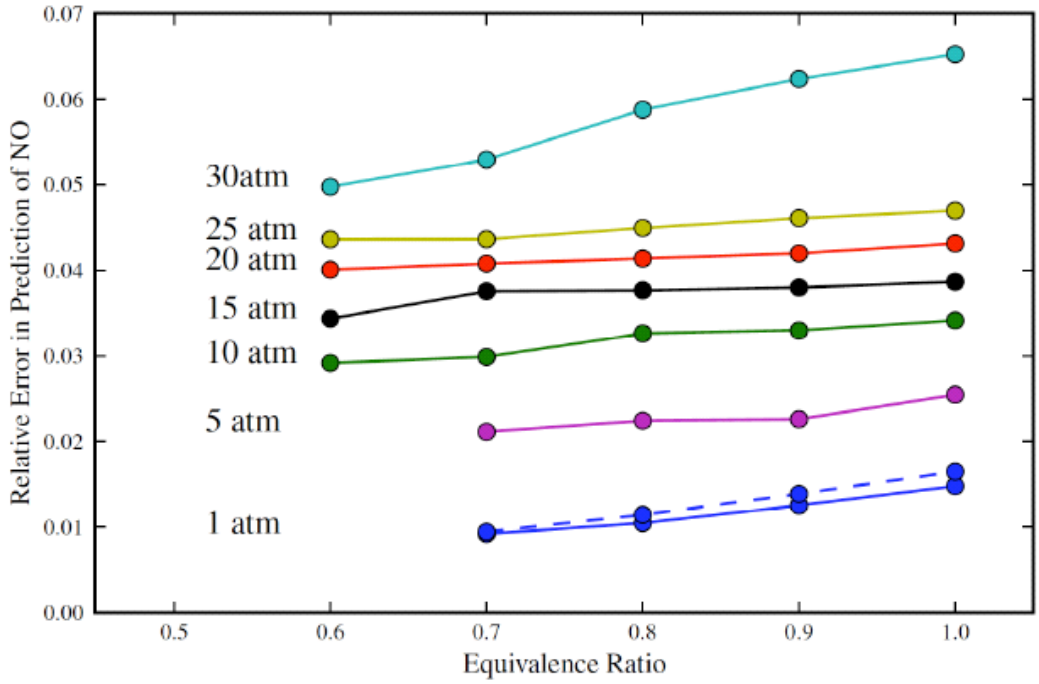

(b) Relative error in prediction of NO near blowout by skeletal mechanism

Figure H-8: Validation of NO prediction by the skeletal mechanism in a PSR at a residence time of 3ms, for all pressures in the parameter space, through plots of both magnitude and relative error.

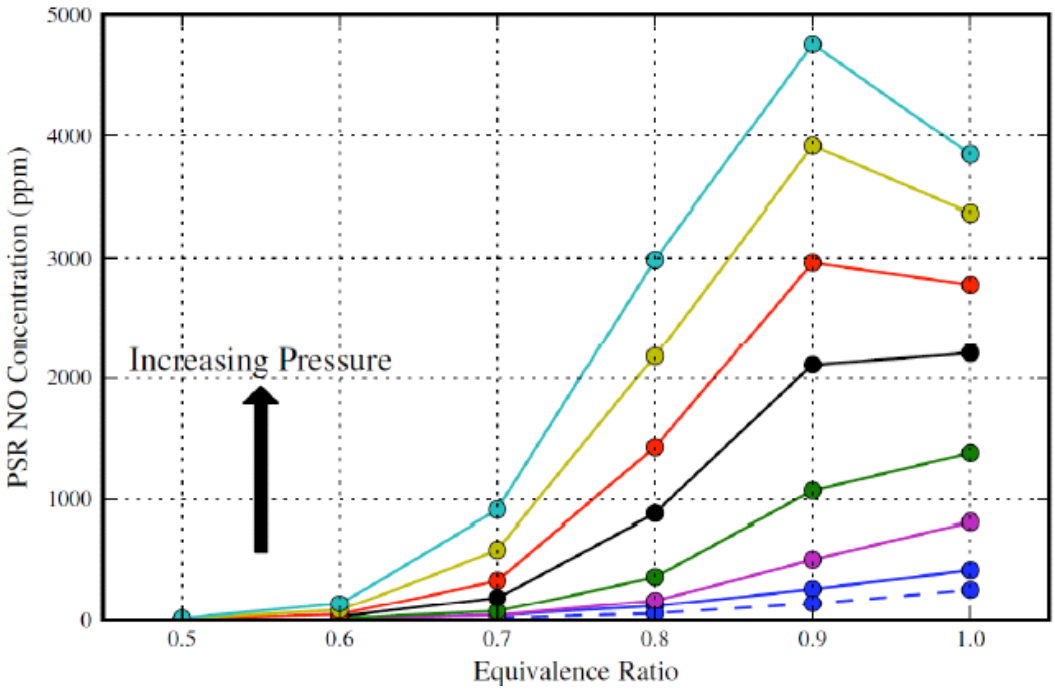

(a) NO concentration at 3ms, detailed mechanism

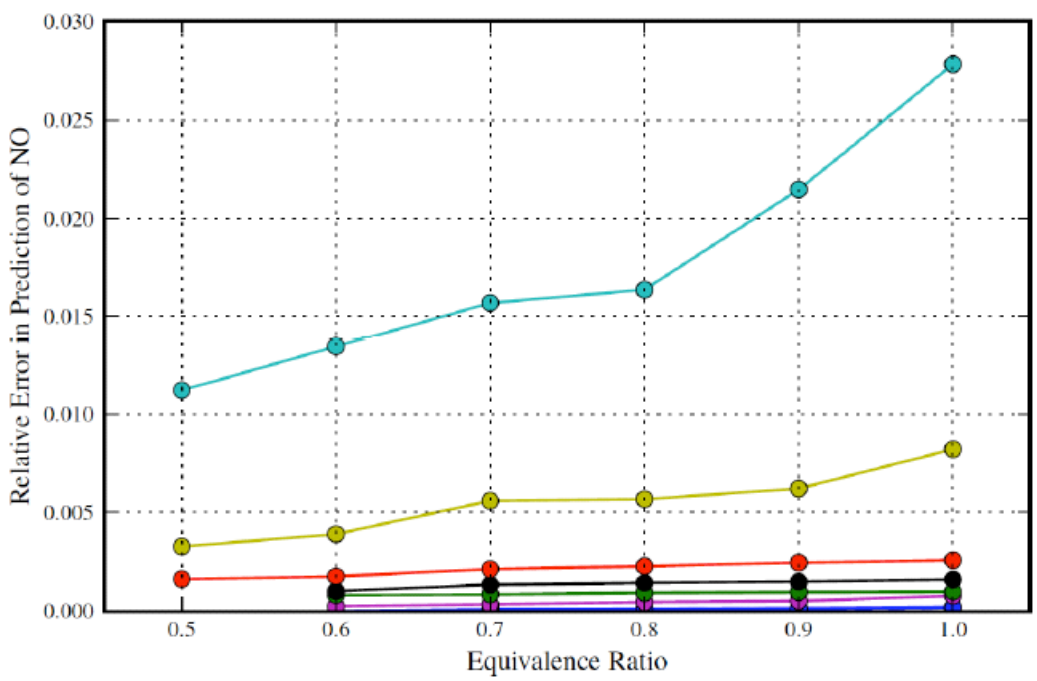

(b) Relative error in prediction of NO at 3ms by skeletal mechanism

Figure H-9: Validation of laminar flame speed calculations with the skeletal mechanism through plots of both magnitude and relative error.

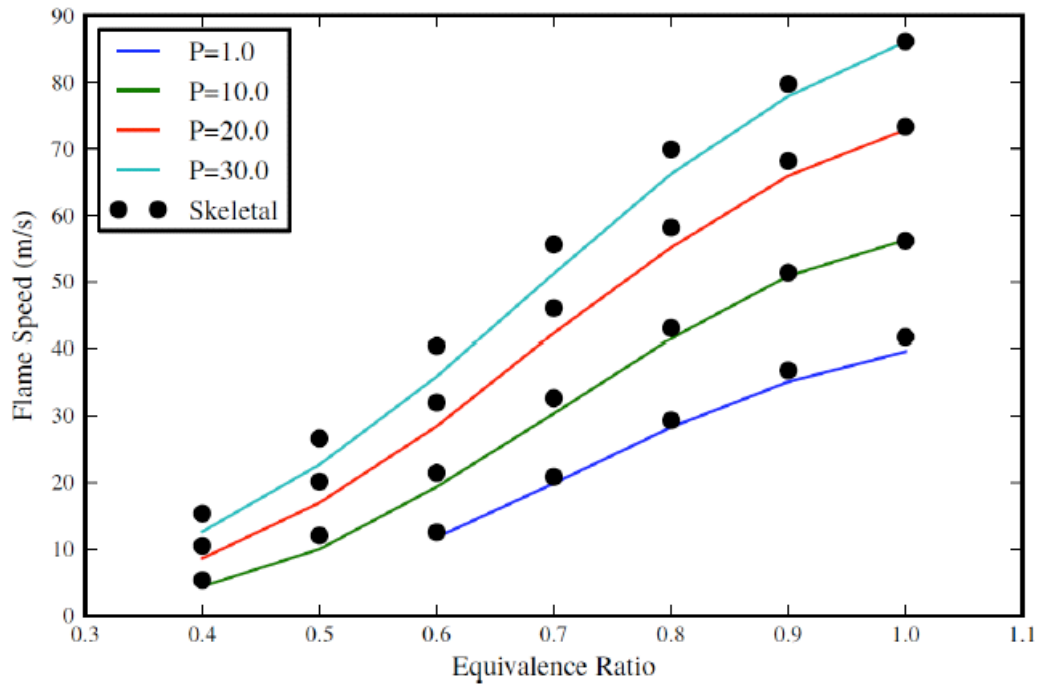

(a) Prediction of laminar flame speed (skeletal (points) versus detailed (lines)

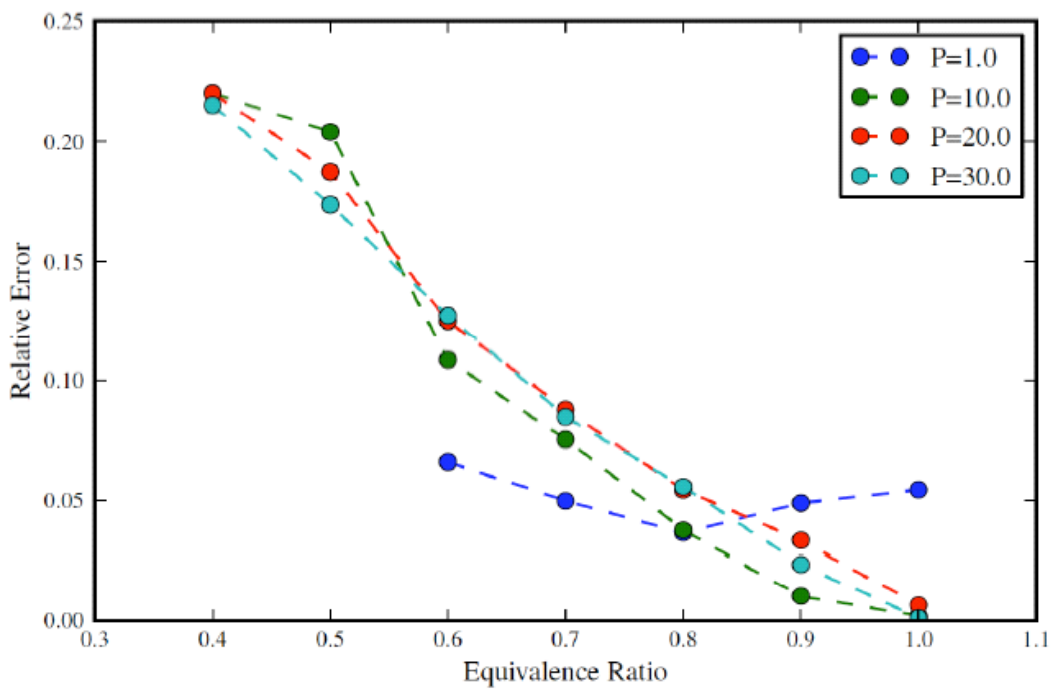

(b) Relative error in the prediction of laminar flame speed

Chapter H.4: Conclusions

The overall goal of this work is the development of a methodology that allows an estimation of the impact of the substitution of alternative fuels on flame stability and NOx emissions of lean, premixed combustors. An important component in the methodology development is the use of computational fluid dynamic (CFD) modeling, including coupled combustion chemistry. The use of detailed chemical kinetic mechanisms in these calculations is not presently feasible, except for the most simple fuels. The principal options for developing these reduced mechanisms include:

1. *Skeletal mechanisms:* from an established full mechanism without time-scale analysis and without alteration of the elementary Arrhenius reaction rates in which redundant reactions have been removed.
2. *Reduced mechanisms:* from a skeletal or full mechanism with time-scale analysis, employing the Quasi Steady State Approximation (QSSA) and Partial Equilibrium (PE) Assumption.
3. *Global mechanisms:* derived using intuition and the 'fitting' of parameters for one or more reactions to experimental data or detailed kinetic simulations.

Following a detailed review of the literature, the specific method chosen for the present work is the method of Directed Relation Graph (DRG), a *skeletal mechanism* method. This has three principal advantages over its competitors:

1. It features the fastest reduction algorithm for large mechanisms.
2. It can identify all candidate skeletal mechanisms sorted by accuracy in a single run.
3. It provides the ability to specify an upper error bound on the resulting mechanism.

The method was exercised to develop a reduced mechanism for CH_4 combustion, including NO_x formation, that includes 30 species. This mechanism was compared with a detailed mechanism for a series of flame calculations focusing on blowout, NOx formation, and laminar flame speed. The mechanism performed extremely well on all these tasks, and future work will use this method for developing reduced mechanisms for the more complex fuels used in the experimental studies.

References

Belcadi, A., M. Assou, E. Affad, and E. Chatri. Construction of a reduced mechanism for modelling premixed combustion of methane-air. Combustion Theory and Model ling, 11(4):603–613, 2007.

Duterque, J., R. Borghi, and H. Tichtinsky. Study of quasi-global schemes for hydrocarbon combustion. Combustion Science and Technology, 26:1–15, 1981.

Edelman, R. B., and O. F. Fortune. A quasi-global chemical kinetic model for the finite rate combustion of hydrocarbon fuels with application to turbulent burning and mixing in hypersonic engines and nozzles. AIAA Paper, (86), 1969.

Gicquel, O., N. Darabiha, and D. Thevenin. Laminar premixed hydrogen/air counterflow flame simulations using flame prolongation of ILDM with differential diffusion. Proceedings of the Combustion Institute, 28:1901–1908, 2000.

Gokulakrishnan P., S. Kwon, A.J. Hamer, M.S. Klassen, and R.J. Roby. Reduced kinetic mechanism for reactive flow simulation of syngas/methane combustion at gas turbine conditions. pages 513–521, Barcelona, Spain, 2006.

Hautman, D. J., F. L. Dryer, K. P. Schug, and I. Glassman. A multiple-step overall kinetic mechanism for the oxidation of hydrocarbons. Combustion Science and Technology, 25:219–235, 1981.

Jiang,B., D. Ingram, D. Causon, and R. Saunders. A global simulation method for obtaining reduced reaction mechanisms for use in reactive blast wave flows. Shock Waves, 5:81–88, 1995.

Jones, W. P., and R. P. Lindstedt. Global reaction schemes for hydrocarbon combustion. Combustion and Flame, 73:233–249, 1988.

Lamnaouer, M., R. C. Ryder, A. Brankovic, and E. L. Petersen. Reduced combustion time model for methane gas in gas turbine flow fields. Journal of Natural Gas Chemistry, 18:145–155, 2009.

Law, C. K., C. J. Sung, H. Wang, and T. F. Lu. Development of comprehensive detailed and reduced reaction mechanisms for combustion modeling. AIAA Journal, 41(9):1629–1646, 2003.

Lu, T. F., and C. K. Law. A directed relation graph method for mechanism reduction. Proceedings of the Combustion Institute, 30:1333–1341, 2005.

Lu, T. F., and C. K. Law. On the applicability of directed relation graphs to the reduction of reaction mechanisms. Combustion and Flame, 146:472–483, 2006.

Lu, T. F., and C. K. Law. A criterion based on computational singular perturbation for the identification of quasi steady state species: A reduced mechanism for methane oxidation with no chemistry. Combustion and Flame, 154:761–774, 2008.

Maas, U., and S. B. Pope. Simplifying chemical kinetics: Intrinsic low-dimensional manifolds in composition space. Combustion and Flame, 88:239–264, 1992.

Molnar, M., and C. J. Marek. Reduced equations for calculating the combustion rates of jet-A and methane fuel. Technical Report TM-212702, NASA, 2003.

Nicol, D. G., P. C. Malte, A. J. Hamer, R. J. Roby, and R. C. Steele. Development of a five-step global methane oxidation-NO formation mechanism for lean-premixed gas turbine combustion. Journal of Engineering for Gas Turbines and Power, 121(2):272–280, 1999.

Nicol, D. A Chemical Kinetic and Numerical Study of NO_x and Pollutant Formation in Low-Emission Combustion. PhD dissertation, University of Washington, 1995.

Novosselov, I. V., and P. C. Malte. Development and application of an eight-step global mechanism for CFD and CRN simulations of lean-premixed combustors. Journal of Engineering for Gas Turbines and Power, page 021502, 2008.

Van Oijen, J. A., and L.P.H. De Goey. Modeling of premixed laminar flames using flamelet-generated manifolds. Combustion Science and Technology, 161:113–137, 2000.

Paczko, G., P. M. Lefdal, and N. Peters. Reduced reaction schemes for methane, methanol, and propane flames. Proceedings of the Combustion Institute, 21:739–748, 1986.

Peters, N., and F. A. Williams. The asymptotic structure of methane-air flames. Combustion and Flame, 68:185–207, 1987.

Slavinskaya, N., M. Braun Unkhoff, and P. Frank. Reduced reaction mechanisms for methane and syngas combustion in gas turbines. Journal of Engineering for Gas Turbines and Power, 130:021504, March 2008.

Sung, C. J., C. K. Law, and J. Y. Shen. Augmented reduced mechanism for no emission in methane oxidation. Combustion and Flame, 125:906–919, 2001.

Tomlin, A. S., T. Turanyi, and M. J. Pilling. Comprehensive Chemical Kinetics: Low-Temperature Combustion and Autoignition, volume 35, chapter 4: Mathematical tools for the construction, investigation and reduction of combustion mechanisms. Elsevier Science, 1997.

Wang, H., and M. Frenklach. A detailed kinetic study of aromatics formation in laminar premixed acetylene and ethylene flames. Combustion and Flame, 110:173–221, 1997.

Yannacopoulos, A. N., A. S. Tomlin, J. Brindley, J. H. Merkin, and M.J. Pilling. Error propagation in approximations to reaction-diffusion-advection equations. Physics Letters A, 223:82–90, 1996.

Zheng, S. L., T. F. Lu, and C. K. Law. Experimental Counterflow Ignition Temperatures and Reaction Mechanisms of 1,3-Butadiene. Proceedings of the Combustion Institute, 31(1):367–375, 2007.